Understanding and controlling CO_2 permeation across dual-phase membranes with tailored, multi- or single-pore microstructures

SOTIRIA TSOCHATARIDOU

A thesis submitted for the degree of Doctor of Philosophy (PhD) in Engineering at Newcastle University

SCHOOL OF ENGINEERING

September 2021

Abstract

The importance of finding new ways of CO_2 separation or improving the existing ones, has increased significantly in recent years, because CO_2 emissions have become a serious environmental concern. CO_2 separation from different process streams, such as flue gases, has been researched extensively over the past few years. One way of separating CO_2 is through molten carbonate dual-phase membranes, which consist of a porous ceramic support infiltrated with a molten salt. They can operate continuously at elevated temperatures (400-900 °C) with high selectivity and low energetic penalties as opposed to other separation methods, such as absorption. One of the key challenges is understanding the contribution of various factors towards CO_2 permeation, such as operating conditions, membrane structure and gas phase composition. In this thesis, dual-phase membrane systems consisting of a zirconia or alumina support with various pore geometries and an alkali metal carbonate eutectic mixture were investigated. It was found that below 600 °C, CO_2 permeation is largely controlled by the geometry of the support material rather than its composition. Therefore, multi- or single-pore channels were laser drilled in dense polycrystalline and single crystal materials, and the geometry of the channels was tailored with high precision. By using an Al_2O_3 –carbonate multiple-pore system, it was found that at around 700 °C, CO_2 permeation is generally limited by the diffusion in the melt, while at temperatures around 550 °C, the rate is limited by reactions at the gas-melt interface. In single-pore systems, an effect of permeation was visualised by equilibrating the internal gas phase (gas phase behind the meniscus) to the external gas phase and observing the displacement of the molten salt meniscus. Permeation rates were extracted at low driving forces, necessary for real applications. To enhance permeation, the use of humidified gas streams was investigated. It was found that above 550 °C, CO_2 permeance was on the order of 10^{-7} mol m^{-2} s^{-1} Pa^{-1} compared to 10^{-9} mol m^{-2} s^{-1} Pa^{-1} under dry conditions. Furthermore, by coupling the permeation of CO_2 with H_2O, CO_2 could be permeated against its own chemical potential difference. This work provides an understanding on membrane performance by unprecedented control over pore geometry and the effect of water with well-defined chemical potential gradients across the membrane.

Acknowledgments

I would like to express my sincere gratitude to those who encouraged and supported me along this journey.

I would like to thank my PhD supervisors, Professor Ian Metcalfe and Dr Evangelos Papaioannou, for their support, encouragement and guidance given throughout my PhD. I am very grateful for the opportunity they have given me to do an exciting and challenging research. I would also like to express my gratitude to Dr Dragos Neagu and Dr Greg Mutch, my post-doctoral fellows, for their help and intellectual input given during our discussions.

Additionally, I would like to offer my thanks to Professor Victor Orera, Dr Rosa Isabel Marina and Dr Marisa San Juan, from the University of Zaragoza, for their contribution on the drilling and visualisation part of this work and for making my 6-month stay in Zaragoza so enjoyable. I am so grateful for our collaboration and the enjoyable working environment. I am also grateful to Professor Jose M. Serra and Juan Escribano, from the University of Valencia, for our collaboration on the freeze-casted membranes.

A special acknowledgment goes to all the group members for the fun moments spent together. Special thanks to Kelly, George, Ana and Maria for their friendship and support, and for making my stay in Newcastle more enjoyable.

To my dearest friends Maria Athanasiou, Keti Trachanatzi, Nikoleta Spasou, Francisco Luquin, Sisi Zheng, Gosia Chmielecka, George Varelis and Maria Vrahimi for their amazing support and unforgettable moments we spent together.

I would like to express my deepest gratitude to my family, particularly my parents, brothers and sisters, for believing in my potential and for their unconditional love and support. Thank you for always listening to me and standing by my side. This thesis is dedicated to you.

I would also like to acknowledge financial support provided by EPSRC under the European Union's Seventh Framework Programme (FP/2007-2013) / ERC Grant Agreement Number 320725.

Publications

- Tsochataridou S., Mutch G. A., Neagu D., Papaioannou, E. I., Sanjuan M. L., Ray B., Merino R. I., Orera V. M., and Metcalfe I. S., *Measuring Membrane Permeation Rates through the Optical Visualization of a Single Pore.* ACS Appl. Mater. Interfaces, 2020. **12** (14**)**: p.16436–16441. - Published

- Tsochataridou S., Papaioannou E. I., Gaudillere C., Serra J.M., Metcalfe I.S., *Enhanced CO_2 separation via molten-carbonate dual-phase membranes based on freeze-casted structures.* Journal of Membrane Science. - Under review

- Tsochataridou S., Papaioannou E. I., Neagu D., Mutch G. A. and Metcalfe I. S., *Humidity-driven membrane separation of CO_2 from air via a 'chemical potential handshake'.* – Under preparation

Conferences

- Tsochataridou S., E.I. Papaioannou, J. Escribano, G. A. Mutch, J. M. Serra and I.S. Metcalfe, Dual-phase membranes for CO_2 permeation: effect of pore geometry. ChemEngDayUK2017, University of Birmingham, 27-28 March 2017

- Tsochataridou S., M. S. Juan, R. I. Merino, G. A. Mutch, D. Neagu, E. I. Papaioannou, D. Sola, G. Triantafyllou, V. Orera, I. S. Metcalfe, Novel methods for investigating dual phase molten salt-ceramic gas separation membranes. Molten Salt Discussion Group (MSDG), University of Nottingham, 4-6 July 2017.

- Tsochataridou S., M. S. Juan, R. I. Merino, G. A. Mutch, D. Neagu, E. I. Papaioannou, D. Sola, G. Triantafyllou, V. Orera, I. S. Metcalfe, Novel methods for investigating dual phase molten salt-ceramic gas separation membranes. AIP/CAM-IES Conference, Perrin Lecture Theatre, London, 21 September 2017.

Contents

List of figures

List of tables

List of Acronyms and Abbreviations

Al_2O_3 - Aluminium oxide

CO_2 - Carbon dioxide

CO_3^{2-}- Carbonate ion

DMSO - Dimethyl sulphoxide

e^- - Electron

OH^- - Hydroxide ions

Li_2CO_3 - Lithium carbonate

O^{2-} - Oxygen ion

K_2CO_3 - Potassium carbonate

$C_2O_5^{2-}$ - Pyrocarbonate ions

Na_2CO_3 - Sodium carbonate

CGO - Cerium gadolinium oxide

LSCF6428 – Lanthanum strontium cobalt ferrite ($La_{0.6}Sr_{0.4}Co_{0.2}Fe_{0.8}O_{3-\delta}$)

MgO - Magnesium oxide

PESf - Polyethersulfone

SDC - Samarium doped ceria

BYS - Samarium–yttrium–bismuth oxide

YSZ - Yttria-stabilized zirconia

ZRA - Zirconium acetate complex

MIEC - Mixed ionic-electronic conductor

SOFC - Solid oxide fuel cell

<u>Methods/Instruments</u>

DSC - Differential scanning calorimetry

GC - Gas chromatograph

QMS - Quadrupole mass spectrometer

MFC - Mass flow controller

SEM - Scanning electron microscopy

TCD - Thermal conductivity detector

TG–MS - Thermogravimetric–mass spectrometry

Greek Letters

α - Activity

γ - Activity coefficient

γ_{SV} - Solid-vapor interfacial energy [J/m^2]

γ_{SL} - Solid-liquid interfacial energy [J/m^2]

γ_{LV} - Liquid-vapor interfacial energy [J/m^2]

ε – Porosity

z - Charge [C]

η - Electrochemical potential [J mol^{-1}]

θ - Contact angle [°]

λ - Decay constant [min^{-1}]

μ - Chemical potential [J mol^{-1}]

σ - Conductivity [Ω^{-1} m^{-1}]

τ - Tortuosity

φ - Phase volume fraction

x - Mole fraction

Other symbols

G - Conductance [S]

A - Cross-sectional area [m^2]

D - Diffusivity [m^2 s^{-1}]

ΔH - Enthalpy change [kJ mol^{-1}]

ΔS - Entropy change [kJ mol^{-1} K-1]

K - Equilibrium constant

F - Faraday constant [96485 C mol^{-1}]

J - Flux [ml min^{-1} cm^{-2}]

R - Gas constant [8.314 J mol^{-1} K^{-1}]

ΔG - Gibbs free energy change [kJ mol^{-1}]

k_H - Henry's constant [Pa m^3 mol^{-1}]

I - Laser intensity

m - Mass [g]

L - Membrane thickness [m]

M_w - Molecular weight [g mol^{-1}]

n - Number of moles [mol]

PR - Permeation rate [mol s^{-1}]

P - Pressure [Pa]

Q - Reaction quotient

T - Temperature [K]

t - Transport number

W - Work of adhesion [J/m^2]

Superscripts

′ - Feed-side outlet

″ - Permeate-side outlet

^{eff} - Effective

^{feed} - Feed-side inlet

^{permeate} - Permeate-side inlet

Subscripts

amb - Ambipolar

cap - Capillary

c - Carbonate phase

p - Partial (refers to the partial conductivity of each phase)

s - Solid phase (support)

i - Species

t - Total

Chapter 1
Introduction

1.1 The need for CO_2 separation and capture

Rapid economic growth, financial development, employment and population have contributed to today's increasing demand for energy [1]. It is predicted that the global population will rise to 9 billion by 2050, and it is expected that the world demand for energy will increase by 50% [2]. An obvious consequence of this is the abundant use of fossil fuels (petroleum, coal and natural gas), which are the primary sources of energy since the industrial revolution. The burning of the fossil fuels together with intensive farming and deforestation, results in the release of greenhouse gases (GHGs) into the atmosphere while limiting the natural carbon sink that absorbs carbon dioxide [3]. This has resulted in an increase of the surface temperature of the Earth with several consequences, including the spread of diseases, ecosystem changes, sea level rise, effects on ocean life, impact on agriculture etc. One of the major anthropogenic GHG is carbon dioxide (CO_2), and after the industrial revolution the atmospheric CO_2 increased more than 44%, from around 280 ppm to 405 ppm in November 2017 [4]. It is predicted that in 2030 the atmospheric CO_2 will increase to as much as 600–1550 ppm [5] and it was estimated that as much as 5 $GtCO_2$ will need to be removed from the atmosphere and locked underground every year until 2050 [6].

Various countries adopted the 2015 Paris climate agreement and have considered different climate action plans to reduce their CO_2 emissions [7]. This includes the increase usage of low carbon fuels (natural gas, hydrogen, nuclear power), the improvement of energy efficiency, the promotion of energy conservation, the development and usage of renewable energy (solar, wind, hydropower, bioenergy), increase afforestation and reforestation and CO_2 capture and storage (CCS) [8]. CCS can reduce CO_2 emissions by capturing or separating CO_2 from flue/fuel gases, transporting and then either storing permanently or reutilizing industrially (CCUS).

1.2 Overview of CO_2 capture and separation technologies

CO_2 capture systems include several technologies, associated with combustion processes where CO_2 is captured at different stages of the process. The three main CO_2 capture systems are shown in Figure 1-1; post-combustion, pre-combustion and oxyfuel combustion [9, 10].

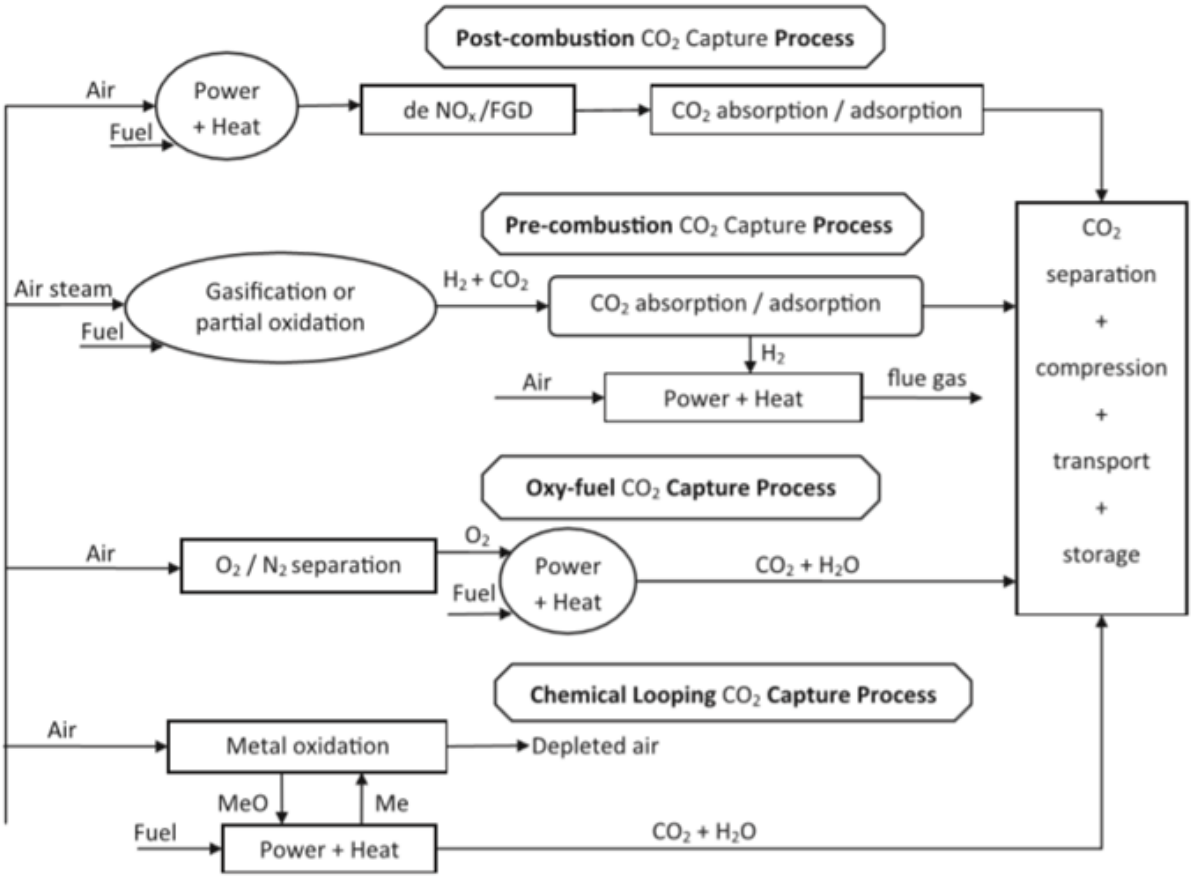

Figure 1-1. Process diagram/overview of leading CO_2 capture technologies. Retrieved from [8].

Post-combustion involves the separation of CO_2 from flue gas after combustion has taken place, where CO_2 level is around 7–14% for coal-fired combustion and 4% for gas-fired combustion. This low level of CO_2 along in large volumes of flue gas results to elevated energy penalties and cost for separating [11, 12]. In pre-combustion capture, the fuel is pre-treated by reacting with oxygen, air or steam (gasification or partial oxidation), to give mainly carbon monoxide (CO) and hydrogen (H_2). The content of H_2 is increased by passing the syngas through a catalytic reactor and CO reacts with steam forming CO_2 and H_2 [13]. The CO_2 (>20%) is then separated and the H_2 can be used as a clean fuel in a gas turbine. Finally, in oxyfuel combustion capture, the fuel is combusted in high oxygen concentration, resulting in high CO_2 concentrations in the flue gas (>80%) [14]. Gibbins and Chalmers [15] compared

the cost of the three CO_2 capture systems and reported that the pre-combustion technology shows the lowest cost per tonne of CO_2 avoided for coal-fired plants, while the other two capture systems have similar costs. On the other hand, for gas-fired plants, the cost per tonne of CO_2 avoided using the post-combustion capture was almost 50% lower than the pre-combustion and oxyfuel technology [16].

CO_2 separation technologies must be facilitated by a CO_2 capture process. These have been the focus of intense study in recent years. The current CO_2 separation technologies are cryogenic, absorption (with aqueous amine solutions), adsorption (with porous solids which have high adsorbing properties such as active carbon or zeolite) and membranes [17-19].

Cryogenic technology can separate gas mixtures by fractional condensation and distillation at low temperatures. This technology is widely used for high CO_2 concentrations (>90%) and it involves the cooling of gases to very low temperatures (lower than -73.3 °C) [12]. The process has the advantage that it allows recovery of pure CO_2 in the form of a liquid, which can be transported conveniently, and it achieves very high purities [12]. The most important disadvantages are that the water has to be removed before the cooling of the gas steam to avoid blockages and it requires a lot of energy [17].

Solvent absorption is a process in which CO_2 is absorbed from a gas mixture into a liquid e.g. amine. The most common amine-based absorption is with an aqueous monoethanolamine solution because it achieves high level of CO_2 capture (more than 90%) from flue gas [20]. However, the corrosion and degradation of the ammines and the large amount of power which is used to regenerate the solvent are the main disadvantages of this technology [17].

Adsorption is a technique in which CO_2 is adsorbed from a gas mixture into a solid, e.g. zeolite or carbon-based sorbents, and it involves either physical (physisorption) or chemical (chemisorption) interactions between the surface of the solid and the gas molecules [21]. The CO_2-loaded solid will then need to be purified, and this can be succeeded by using differences in pressure or in temperature in order to remove the carbon dioxide [17]. The main disadvantages of this technology are that it is not able to handle large CO_2 concentrations and it also adsorbs gases that are smaller than CO_2 [20].

Membranes for gas separation are considered the most energy-efficient technology for CO_2 capture [22, 23]. Membrane technology does not involve any moving parts, making it a less energy consumptive process, and it is a continuous process, which makes it more attractive for factory retrofitting. Another advantage of this technology, it uses solubility and diffusivity differences between the chemicals to be separated, which could result to higher selectivities

for a specific separation [23]. The gas permeation through membranes is mainly driven by the partial pressure difference of CO_2 between the two sides of the membrane.

Different types of membranes are available, such us organic (polymeric) or inorganic (carbon, zeolite, ceramic or metallic) membranes. The first commercially available membrane which has been recently developed is a polymeric membrane used for CO_2 separation from syngas [24]. The mechanism that can describe the gas permeation through these membranes is the solution-diffusion model. The diffusion of the gas is associated to the size of penetrants, the free volume in the polymers (space between polymer chains) and the solubility of the gas, which is related to the sorption of gas molecules in the polymers [25, 26]. However, most of the polymeric membranes are not chemically stable in an acid environment, cannot operate at high temperatures (above 200 °C), and suffer from low CO_2/N_2 selectivities (<less than 100) as compared to inorganic membranes [27, 28]. Moreover, plasticization which causes changes to the properties of the polymeric membrane due to the depression of the glass transition temperature, is one of the main issues of the polymeric membranes [29]. On the other hand, ceramic membranes show high thermal and chemical stability. It has been demonstrated that these membranes generally show high selectivities and permeabilities at temperatures above 400 °C [30, 31].

1.3 Ceramic dual-phase membranes for CO_2 separation

Much work has been done in searching for good ceramic membranes for the separation of CO_2: the concept of dual-phase membranes was first studied in 1992 by Mazanec et al. Dual-phase membranes for CO_2 separation are dense membranes consisting of a solid ceramic phase and a molten carbonate phase. Those membranes are ideal candidates for CO_2 separation because they can operate at high temperatures with high selectivity and the two phases can be separately adapted according to the requirements of a given application [32]. Perovskites, such as $La_{0.6}Sr_{0.4}Co_{0.8}Fe_{0.2}O_{3-\delta}$ (LSCF6428) and yttria stabilised zirconia (YSZ), are very good candidates for CO_2 separation due to their mechanical strength, high conductivity and catalytic properties with a carbonate eutectic mixture as the liquid phase. They have been studied extensively during the last 10 years [33].

However, membrane technology has many challenges related to the composition of gases and temperature for separation in large scale applications and can be sensitive to sulphur compounds or other trace gases [12, 17]. To improve this technology, it is important to understand the CO_2 transport mechanism through these membranes and study the parameters influencing CO_2 permeation. The operation principle of the dual-phase membranes for CO_2

permeation and the analysis of the parameters that can influence it, will be analysed in the next sections.

1.3.1 Operation principle

Dual-phase membranes are inorganic porous membranes, where the pores of the membrane are filled with a liquid, which is permeable for certain compounds. Molten carbonate dual-phase membranes usually consist of an oxygen-ionic-conducting ceramic phase or a mixed ionic-electronic contacting phase with a molten carbonate phase. The driving force for these membranes is the gradient in electrochemical potential (difference in solute concentration and charge across the membrane) of CO_2 and/or O_2 existing on the opposite surfaces of the membrane.

CO_2 transport through a dense dual-phase membrane can be described with three steps. These are: a) the interface reaction on one side of the membrane, b) the diffusion of charged species and/or electron, electron holes in the bulk phase and c) the interface reaction on the other side of the membrane. The overall rate of carbon dioxide permeation is limited by the slowest process.

A variety of processes can be proposed to describe gas transport through the carbonates without participation of the support. The overall gas transport will be dominated by two major processes: the sorption and the diffusion [34]. Sorption describes the adsorption of gases on the membrane surface and can occur physically or chemically depending on the interaction between the gas molecules and the surface. It is expected that CO_3^{2-} is the main charge carrier; however, it has been recently reported that more carrier charges, such as, oxide ions, hydroxide ions, $C_2O_5^{2-}$, and CO_4^{2-}, can contribute to the overall CO_2 transport, depending on the gas atmosphere and operating conditions [35-38].

The contribution of the chemical and physical dissolution to CO_2 permeation can be calculated using the solubility and diffusivity coefficients of CO_2 in the carbonate mixture. Those coefficients were measured using various techniques in literature and they will be analytically discussed in Section 2.2.2.

The mechanism for CO_2 separation through dual-phase membranes with participation of the support have been suggested from previous studies [39]. Figure 1-2 represents the main CO_2 permeation mechanism proposed through the dual-phase membrane with an oxygen/ionic conductor, such as YSZ, as the oxygen/ionic phase and the molten carbonate mixture (carbonate ions). The oxygen ionic conductor not only serves as a support but also transports

oxygen ions (O^{2-}) and the molten carbonate phase transports the carbonate ions (CO_3^{2-}). As shown in Figure 1-2, oxygen ions within the support react with the CO_2 from one side of the membrane to form carbonate ions. Carbonate ions and oxygen ions diffuse through the molten carbonates and the support respectively, and on the downstream the carbonate ions release CO_2 and return the oxygen ions to the support [39]. The permeation is driven by the partial pressure difference of CO_2 between the two sides of the membrane and the charge neutrality condition is kept by this parallel movement.

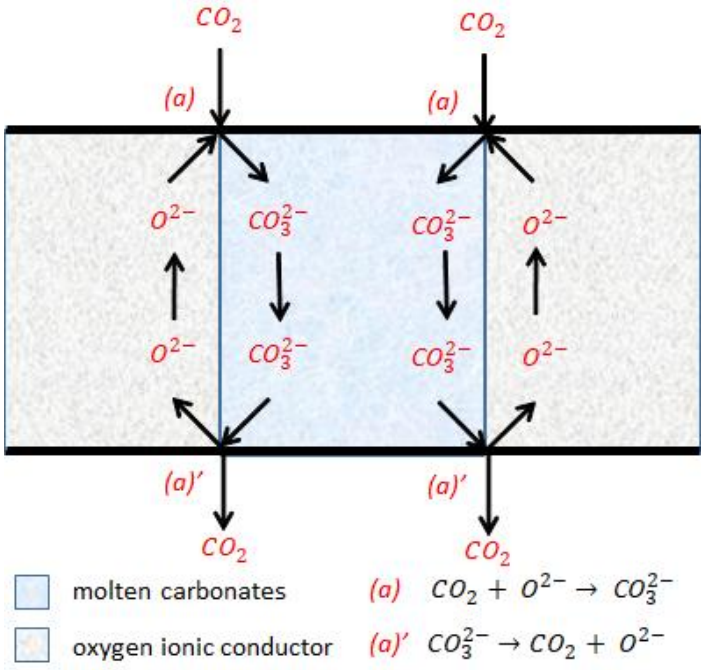

Figure 1-2. Oxygen ionic conducting-molten carbonate membrane transporting CO_2. Reproduced from [39].

Figure 1-3 represents the dual-phase membrane with a mixed ionic and electronic conductor as the support and the molten carbonate mixture phase as the second phase. The support transports oxygen ions (O^{2-}) and electrons (e^-) and the molten carbonate phase transports the carbonate ions. For a mixed ionic electronic conductor such as LSCF, it has been reported that O_2 and CO_2 can permeate through the membrane at high temperatures, usually at 500 °C or higher [39]. O_2 and CO_2 in the feed side react with electrons from the solid oxide phase to form carbonate ions. The permeation is driven by the partial pressure difference of CO_2 or O_2 between the two sides of the membrane. The carbonate ions will transport through the molten carbonate phase reaching the downstream side and the electrons will transport through the ceramic support to the opposite side (to keep charge neutrality). At the permeate side electrons remain in the solid phase and CO_2 and O_2 are released. At the same time, O_2 in the feed side can react with the electrons from the LSCF and produce oxygen ions that diffuse

through the porous oxide. At the permeate side electrons remain in the solid phase and O_2 is released [39]. The mechanism described in Figure 1-2 for ionic conductors, can also take place with the mixed ionic and electronic conductors, however, it is expected that the electronic conductivity contribution will be much higher than the ionic [40].

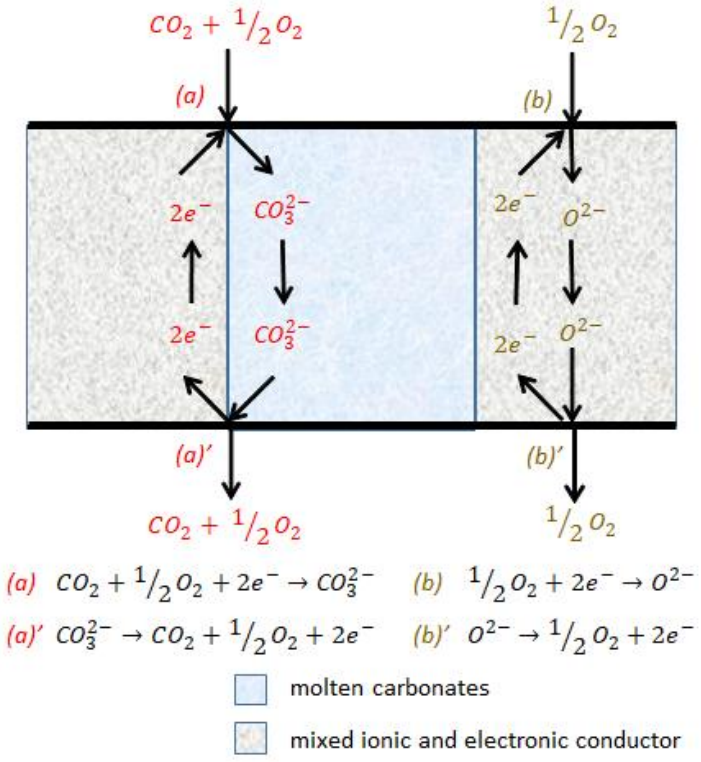

Figure 1-3. Mixed ionic-electronic conducting-molten carbonate membrane transporting CO_2 and O_2. Reproduced from [39].

1.3.2 Factors that affect CO_2 permeation

There are several factors that affect the performance of a dual-phase membrane in terms of CO_2 permeation, including pressure, temperature, partial pressure of gases on either side of the membrane, trans-membrane leaks, and intrinsic factors, such as membrane composition and structure.

Several studies have revealed that the CO_2 permeation rate can be highly affected by the membrane structure. The pore geometry, tortuosity, pore volume, and membrane thickness can all affect CO_2 permeation. It has been seen, experimentally, that the increase in thickness reduces CO_2 permeation rate in an LSCF-carbonate system [41-43]. It was also suggested that there is an optimum solid fraction to tortuosity ratio or carbonate fraction to tortuosity ratio, to

achieve the highest CO_2 permeation rate [44]. These studies will be analytically explained in Section 2.3.1.

The properties of the support material and carbonate phase, such as conductivity, can also affect CO_2 permeation. Carbonate mixtures of different compositions and supports with different ionic conductivities will be analysed in Section 2.3.2.

Operating conditions, such as temperature, pressure, and partial pressure of CO_2 on each side of the membrane, can affect membrane performance as well as the membrane system design. Although the increase in temperature or pressure can increase CO_2 permeation, sealing those membranes can become challenging [45]. Disk-type membranes are usually sealed on an alumina tube support with a high temperature sealant. The choice of sealant is strongly dependent on the operation conditions and application [45] and can cause many problems to the membrane operation; they can reduce the effective surface area and lead to performance degradation [46]. Leaks from failed sealants can also cause lower driving forces, which can lead to lower performance. From a fundamental point of view, leaks limit the quality of mechanistic/kinetic data that one can extract. Seals can also interact with the melt, which will corrode the seal and potentially change the melt composition affecting the performance and durability of the membrane. New membrane system designs are therefore needed to overcome those issues and improve the quality of mechanistic/kinetic data that one can extract. Moreover, CO_2 permeation rate can be highly affected by the partial pressure of CO_2 on each side of the membrane, which provides the driving force for CO_2 permeation. Industrial processes can produce streams containing a wide range of CO_2 partial pressures, greatly depending on the process and the feedstock used. In many cases, those streams contain water, which usually needs to be removed before the separation of the rest of the gases. However, it was found that water promotes CO_2 permeation through ceramic dual-phase membranes [47], indicating that water removal from those streams can be avoided. As water promotes CO_2 permeation, challenging separation processes with dilute CO_2 (such as CO_2 in air), will proceed at rates comparable to processes with higher CO_2 partial pressures. If the driving force of CO_2 could be linked to the driving force of humidity, ‘uphill’ permeation of CO_2 could become feasible because water could drive CO_2 across the membrane even in the absence of a CO_2 driving force (a charge carrier moves in the opposite direction), a concept already proven with O_2 [48]. With these two effects combined, significant separation challenges could be tackled, e.g. separation of CO_2 from the air.

1.4 Aims

This research is based on the importance of understanding and controlling CO_2 transport through dual-phase membranes. The overall aim of this thesis is to improve the quality of mechanistic/kinetic data that can be extracted from the transport of CO_2 through dual-phase membranes by designing leak-free membranes with controlled pore microstructures. In more detail, the aims of this thesis are:

- to control the membrane microstructure and pore geometry by using different fabrication techniques. The complexity of the membranes was the motivation to develop simpler membrane systems whose size, number and geometry of the pores can be tailored with great precision. Membrane systems were simplified down to a single pore system;

- to study the effect of the support material on CO_2 permeation. Oxygen-ionic conducting and inert supports were fabricated and tested for CO_2 permeation;

- to design well-sealed membranes. Systems that require no hot seal were designed to minimise leaks and the interaction between different phases;

- the effect of CO_2 gas composition on both sides of the membrane on CO_2 permeation;

- the effect of the presence of water on both sides of the membrane on CO_2 permeation;

- CO_2 separation from air streams lifted from a low to high partial pressure by using a humidity difference as the driving force.

Chapter 2

Defining the membrane system for CO_2 separation

2.1 Dual-phase membranes for CO_2 separation

As mentioned in the Introduction, membrane diffusion technology includes inorganic-based and polymeric-based membrane processes. Polymeric membranes are limited by the operating conditions -poor thermal and chemical stability- and the permeability-selectivity trade-off [25, 49]. In contrast, inorganic-based membranes exhibit extremely better thermal and chemical stabilities and can operate at high temperatures.

CO_2 permeation mechanism through membranes is based on a solution-diffusion mechanism and the driving force is the gradient in chemical potential of CO_2 existing on the opposite surfaces of the membrane. Molten carbonate dual-phase membranes show great potential for CO_2 separation above 400 °C [41, 50]. Those membranes consist of two phases; the porous support material and the molten carbonate phase infiltrated in the pores of the support.

In the next sections, the properties of the two phases -support material and molten carbonate mixture- will be discussed.

2.1.1 Properties of the support material

The support material is often a high temperature ceramic and can be a material that exhibits structural functionality, or it can also include chemical functionality. The chemical functional materials transport chemical species and participate in reactions at the surface. Those materials include properties such as exclusively ionic or electronic conductivity or mixed ionic and electronic conductivity (MIEC). The conductivity of these materials is attributed to the concentration of mobile defects such us the oxygen vacancies or interstitials, electrons and electron holes [51]. Each of these defects is a chemical specie that migrates from an occupied to a vacant lattice site (or interstitial).

The most widely used MIEC material is perovskite phase oxides (ABO_3) [52]; A is mainly composed of alkaline earth, alkaline and lanthanide ions, lanthanide and B is mainly composed of a transitional metal. The average radii and valence of A-site cations affects the concentration of the oxygen vacancies and the chemical and structural stability of the material. The oxygen ion and electron transition rate are determined by the valence of the B-site cation. The relationship between the A-site and B-site cations has been discussed in recent reviews [53, 54]. Perovskite-type MIEC membrane material composition feature high oxygen

permeability and structural stability and are used for CO_2 separation mainly with the presence of oxygen, due to the high contribution of the electronic conductivity of the support to CO_2 permeation through the reaction $CO_2 + ½ O_2 + 2e^- \rightarrow CO_3^{2-}$.

Researchers have investigated a variety of exclusively ionic conductive materials, which serve as supports on dual-phase membranes, but this work will only focus on YSZ (8 mol% Y_2O_3) because it is the most common solid oxide fuel cell (SOFC) electrolyte and was widely studied experimentally in this lab and in literature [43, 55-58].

Zirconium dioxide (ZrO_2) is an interesting technological material because of its outstanding mechanical and electrical properties [59]. However, the room-temperature monoclinic phase undergoes a first-order phase transition characterized by an important volume variation. Therefore, the phase transformation between the monoclinic and the tetragonal polymorph, due to the large volume change (approximately 2 - 3% [60]), prevents the unique properties of bare zirconia to be used in practice directly [61, 62]. Such phase transition can be suppressed by the substitution of some of the Zr^{4+} ions with slightly larger ions, such as Y^{3+} (addition of yttrium oxide, Y_2O_3). Oxide materials are often doped to generate oxygen vacancies, that become mobile at high temperatures and hence increase the conductivity [63]. Doping zirconia with yttria replaces Zr^{4+} with Y^{3+} and it results to stabilizing the cubic phase of zirconia down to room temperature and to the presence of oxygen vacancies (Figure 2-1) [63]. At low temperatures, the low vacancy mobility limits the O^{2-} mobility, but above 600 °C it can generate high ionic conductivity. YSZ is a solid solution in the cubic fluorite lattice with each cation (yttrium and zirconium) in the centre of a cube of eight anions, oxygen and vacancies in the centre of a cation tetrahedron [63]. YSZ is used as a support for the membranes and the ionic conductivity of it enhances CO_2 permeation.

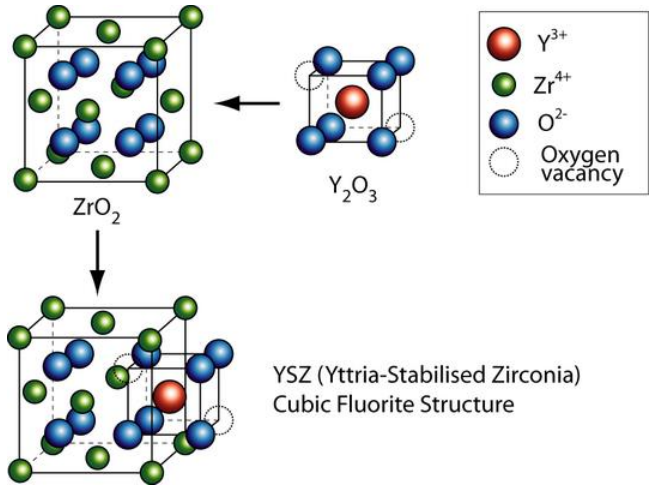

Figure 2-1. Crystal structure of yttria-stabilized zirconia (YSZ) and vacancy transport. Retrieved from [64].

Gorelov [65] studied the region of low-yttria content, and found that in addition to the monoclinic and tetragonal phase, which is stable between 1200 °C and 2300 °C, another tetragonal phase was observed between 2300 °C and 2500 °C, where it transforms to cubic zirconia. This new tetragonal phase is primarily distinguished by differences in lattice parameters. Both tetragonal phases decompose eutectoidically upon cooling, with the high-temperature one forming cubic and the low-temperature tetragonal compound, and the latter yielding monoclinic and cubic YSZ. Due to the limitation on concentrations below 10 mol%, no conclusion can be drawn for 20YSZ or 40YSZ, but 8YSZ should be cubic according to this diagram, and 3YSZ could be either a mixture between monoclinic and cubic YSZ, or one of the tetragonal polymorphs, depending on the ability to keep them metastable at low temperatures.

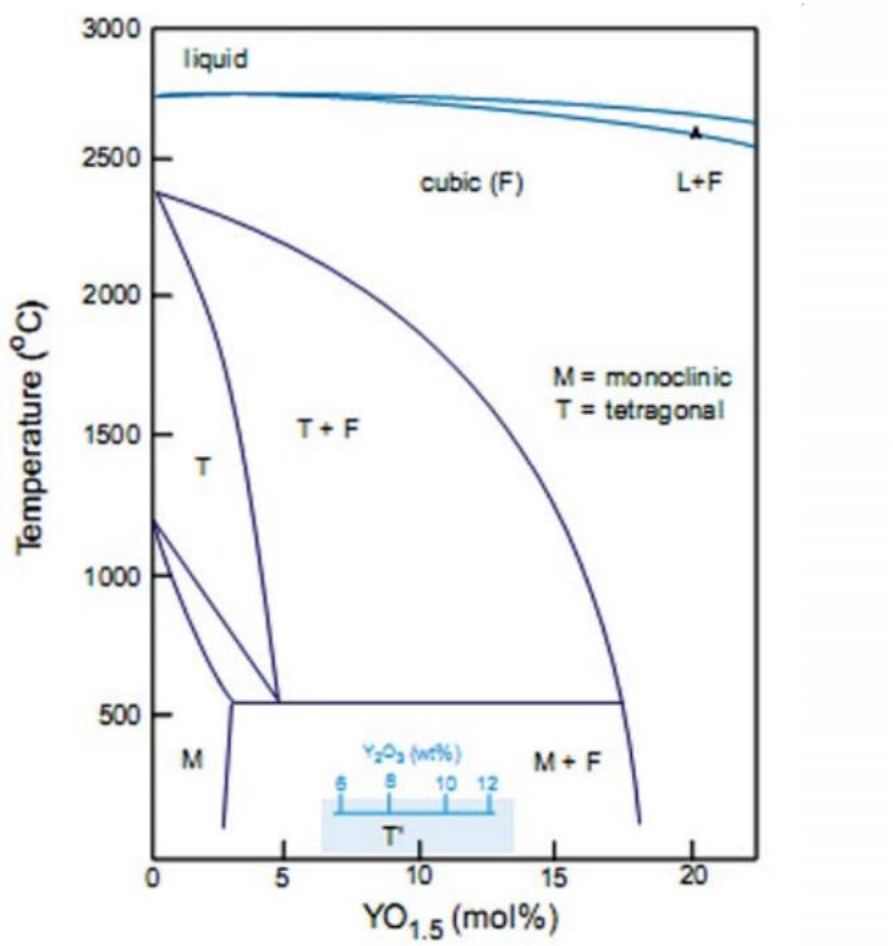

Figure 2-2. Yttria-stabilized zirconia (YSZ) phase diagram. Retrieved from [65, 66].

The ionic and electronic non-conductive supports fabricated and studied in this work are MgO and Al_2O_3 due to their durability and the existing knowledge and experience on fabricating porous supports with several techniques using those materials. Alumina has a very wide range of applications because of its high strength and stiffness, high melting point, chemical stability and low cost [67]. The alumina heated above 1200 °C was named alpha-alumina by Rankin and Merwin in 1916 [68]; the use of Greek letters was an old common practice in Chemistry to differentiate between compounds with the same composition, but with different physical and chemical properties. Alpha phase alumina is the strongest and stiffest of the oxide ceramics. MgO is also used as a support for membranes [69] and it possesses high hardness and a high melting point [70].

MgO supports were fabricated by the powder pressed and freeze-casting method, and Al_2O_3 supports were fabricated by the powder pressed and phase inversion method, and these methods will be analysed in Section 3.1.

2.1.2 Properties of the carbonates

Molten salts are widely used in various fields of science because of their high thermal conductivity, high values of specific heat, low vapor pressure and sufficient stability at high temperatures [71]. They are of importance in pyroprocessing, hot corrosion, electrochemical cells and many other chemical and metallurgical applications [72, 73]. For this reason, many researchers exploit the thermodynamic, electrochemical and transport properties of the molten salts. However, molten salts can pose challenging corrosion issues at high temperatures and this can be a practical limitation for most studies and applications [74]. Among these molten salts, molten alkaline carbonate mixtures have gained special interest as electrolyte materials in fuel cells in dual-phase membranes [75].

Knowledge of the liquid-solid phase equilibrium for the carbonate mixture is essential for this work and the temperature isothermals are shown in Figure 2-3. The composition of the carbonate mixture used in this work is the ternary eutectic mixture of $Li_2CO_3/Na_2CO_3/K_2CO_3$ with composition 43.5/31.5/25.0 mol% respectively and the melting point is at 397 ± 1 °C [76].

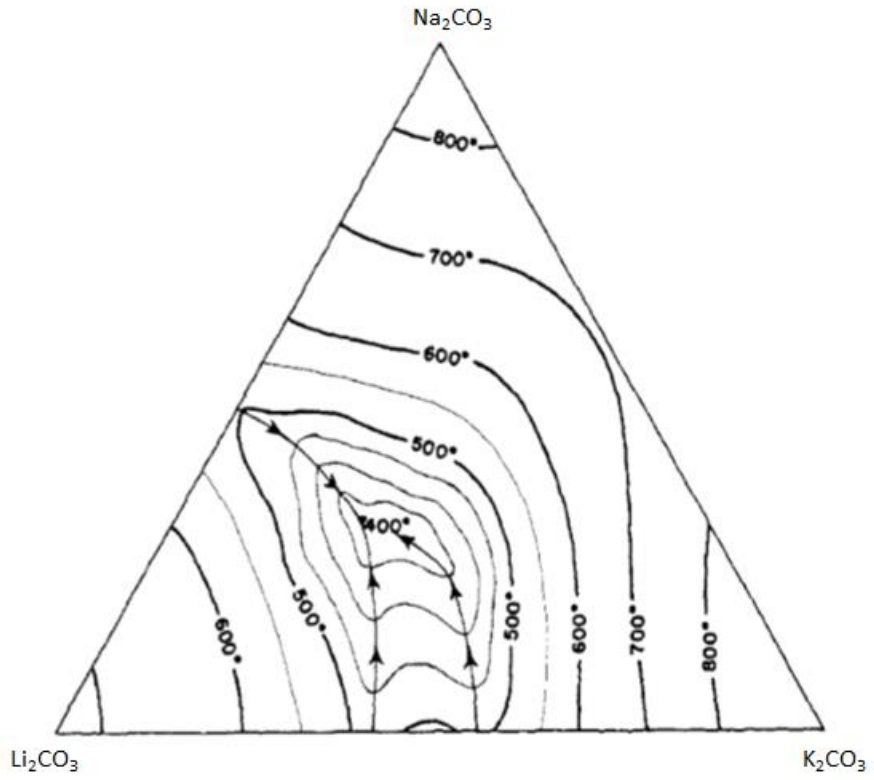

Figure 2-3. Temperature isothermals for liquid-solid equilibrium in the ternary Li_2CO_3, Na_2CO_3, K_2CO_3 system. The composition (in mol%) of the ternary eutectic is 43.5/31.5/25.0 respectively and the melting point is at 397 ± 1 °C. Retrieved from [76].

The density of the carbonate mixture used in this work ($Li_2CO_3/Na_2CO_3/K_2CO_3$ with composition 43.5/31.5/25.0 mol%) varies between 2.05 and 1.87 g cm^{-3} at temperatures between 450 and 900 °C as shown in Figure 2-4 [76].

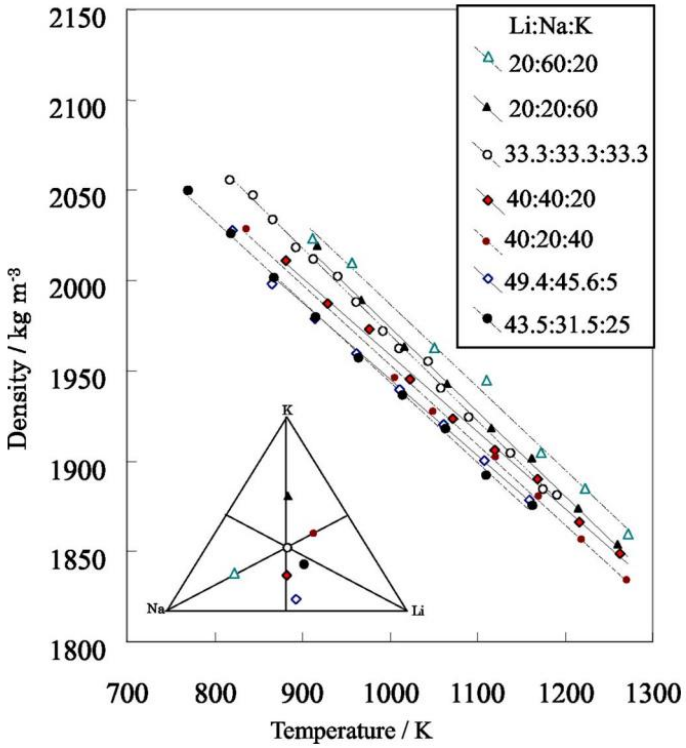

Figure 2-4. Temperature dependence of density of the ternary Li_2CO_3, Na_2CO_3, K_2CO_3 system. Retrieved from [76].

The relationship between temperature and conductivity measured by Kojima et al [77] for several ternary Li_2CO_3, Na_2CO_3, K_2CO_3 systems is shown in Figure 2-5. The conductivity increases with temperature from approximately 0.3 S cm^{-1} at 400 °C to 2.5 S cm^{-1} at 900 °C for the carbonate eutectic mixture. In Figure 2-5, the data points correspond to the experimental results and the lines correspond to the predicted values following an empirical quadratic function [77, 78]. The experimental results were in a good agreement with the predicted equations. For the ternary eutectic mixture of $Li_2CO_3/Na_2CO_3/K_2CO_3$ with composition 43.5/31.5/25.0 mol% the constants of the empirical quadratic function (Eq. 2-4) of temperature were determined experimentally and were equal to:

$$a = -2.797 \text{ S cm}^{-1} \quad \text{Eq. 2-1}$$

$$b = +4.6114 \times 10^{-3} \text{ S cm}^{-1} \text{ K}^{-1} \quad \text{Eq. 2-2}$$

$$c = -0.0291 \times 10^{-6}\ S\ cm^{-1}\ K^{-2} \quad \text{Eq. 2-3}$$

$$\sigma = a + bT + cT^2 \quad \text{Eq. 2-4}$$

The conductivity of the ternary eutectic mixture used in this work is calculated using the above equations and the results are shown in Table 2-1 for different temperatures.

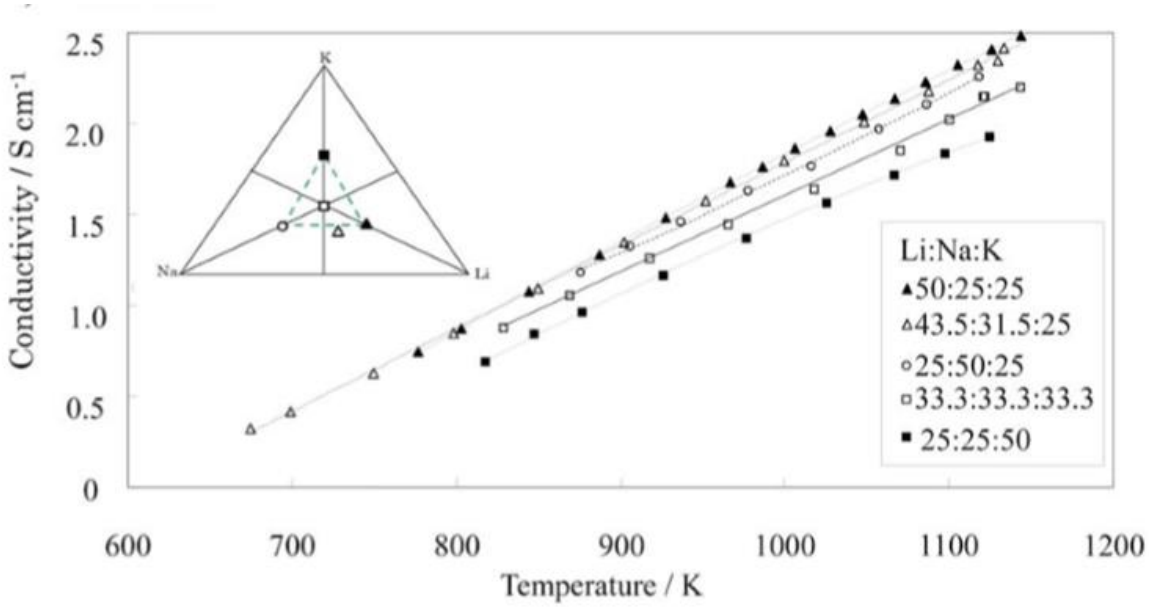

Figure 2-5. **Conductivity against temperature for ternary Li_2CO_3, Na_2CO_3, K_2CO_3 systems of the centre area of the triangular composition diagram.** Retrieved from **[77]**.

Table 2-1. Conductivity of the eutectic mixture $Li_2CO_3/Na_2CO_3/K_2CO_3$ at varying temperatures.

Temperature, K	Ionic conductivity, σ_c, $S\ cm^{-1}$
723	0.522
773	0.750
823	0.978
873	1.207
923	1.435
973	1.662
1023	1.890
1073	2.118
1123	2.345

It is well known that the molten carbonates show high reactivity towards different inorganic species and thermal instability [79]. Olivares at al. [80] studied the thermal stability of the carbonate eutectic mixture under different gas atmospheres, up to a temperature of 1000 °C. The study was conducted using differential scanning calorimetry (DSC)/thermogravimetric–mass spectrometric (TG–MS) analysis in Ar, air, and CO_2. The results of this study show that carbonates were stable under pure CO_2 atmosphere up to at least 1000 °C. Under Ar atmosphere, CO_2 was evolved from the melt soon after melting and above 700 °C the CO_2 evolution rate and weight loss increased. Under air, CO_2 was evolved from the melt at 530 °C, the beginning of decomposition was detected at 601 °C by DSC analysis. The thermodynamics of carbonate decomposition will be studied in detail in Section 2.3.4.

2.2 CO_2 solubility, diffusivity and permeability

CO_2 transport through dual-phase membranes can be described by a multi-ion pathway as discussed in the previous chapter. When an 'inert' support is used, it is expected that the only ionic pathway will be in the carbonate phase through surface ionisation of CO_2 at the CO_2/carbonate interface. CO_2 can dissolve in the melt physically or with chemical interaction between the gas phase and the melt resulting to chemical dissolution. Claes et al. [35] and Zhang et al. [81] proposed the formation of pyrocarbonate ions in molten carbonate via Reaction 2-1. During CO_2 permeation, the flux of CO_3^{2-} is charge-compensated by the flow of $C_2O_5^{2-}$.

$$CO_2 + CO_3^{2-} \rightarrow C_2O_5^{2-} \qquad \text{Reaction 2-1}$$

According to Claes et al. [35] the largest part of dissolution occurs chemically and only 2% of the dissolved CO_2 is due to physical dissolution. However, the first Raman spectroscopic evidence for the formation of pyrocarbonate ions in molten carbonates under CO_2 atmosphere was first reported 14 years later in 2013 [81]. It has been reported that the pyrocarbonate ion, $C_2O_5^{2-}$, has been identified with Raman spectroscopy in a binary carbonate mixture (52 mol% Li_2CO_3, 48 mol% Na_2CO_3) under CO_2 after the melting point (490 °C) of the carbonates. In their work, at least six of the measured characteristic Raman bands of the pyrocarbonate ions where in agreement with the DFT-model calculated from the $Li_2C_2O_5$ and $Na_2C_2O_5$.

In the mid 1870's, Stefan and Exner [82, 83] showed that the permeation rate of a gas through a soap film is proportional to the solubility of the gas and the diffusion coefficient. With the assumption that the ion mobility is independent of the electric field inside the

membrane and based on their findings, the permeability of CO_2 in the carbonate mixture can be calculated from the CO_2 solubility coefficient (k_H) in the molten carbonates and the diffusivity coefficients (D) as shown in Eq. 2-5. For this reason, the following paragraphs will present the CO_2 solubility and diffusivity coefficients measured by different methods.

$$Perm = \quad k_H \times D \; [mol\, m^{-1}\, s^{-1}\, Pa^{-1}] \qquad \text{Eq. 2-5}$$

According to Henry's law, the amount of gas that dissolves in a liquid phase is directly proportional to the partial pressure of the gas in equilibrium with the liquid. The Henry's constant of CO_2 in the molten carbonate salts was measured though different experimental techniques and a summary of the results is shown in Table 2-2. Wilemski [84] presented Henry's constant in the form of an Arrhenius type equation as a function of temperature with Eq. 2-6.

$$k_{H,CO_2} = 1.71 \cdot 10^{-4} exp\left(\frac{-364.6}{T}\right) \quad \left[mol\, m^{-3}\, Pa^{-1}\right] \qquad \text{Eq. 2-6}$$

The above empirical equation gives one order of magnitude lower constants than those measured by Kanai Dubois [85, 86] and Claes [35] but it agrees with the values given by Appleby [87]. The reason for these differences may be explained by the fact that the different estimation methods might be related to different sources of error. The occurrence of the physical and chemical solubility could also explain the differences between solubility data measured by different techniques. Appleby [87] collected his solubility data (quenching method) using the quantity of dissolved gas released during the freezing of the melt. This technique might lead to an underestimation of the chemical solubility of CO_2 if the reaction of the dissolution is very slow. With this method it is important to maintain a slow quenching rate to allow all the gases to escape. The released gases are then flashed with a stream of a carrier gas and the gas is analysed using an appropriate technique, such as mass spectrometry. Moreover, Wilemski [84] gave this empirical equation for describing ternary mixtures with different compositions, however, the solubility of CO_2 is expected to vary vastly in different mixtures. Kanai et al [86] used the elution method for the determination of solubility and this method includes the analysis of the solute gas that is removed from the saturated solution [88]. This technique relies on the negligible solubility of the gas in the solid. The thermogravimetric technique measures the weight increase of the melt during the absorption of the gas using a thermovacuum balance [89, 90]. Potential sources of error can be the effect of the heating rate, the gas flow rate, the geometry of the crucible, inaccuracy in the weight readings etc.

Table 2-2. CO_2 solubility in the eutectic mixture $Li_2CO_3/Na_2CO_3/K_2CO_3$ (43.5/31.5/25.0 mol%) at varying temperatures determined by different methods.

Method	Temperature, K	k_H, $mol\,m^{-3}\,Pa^{-1}$	Reference
Empirical equation	675	$9.96 \cdot 10^{-5}$	[84]
Elution method	675	$1.46 \cdot 10^{-3}$	[86]
Elution method	693	$1.40 \cdot 10^{-3}$	[86]
Elution method	775	$1.65 \cdot 10^{-3}$	[86]
Empirical equation	833	$1.10 \cdot 10^{-4}$	[84]
Thermogravimetric method	833	$8.88 \cdot 10^{-4}$	[85]
Elution method	864	$1.70 \cdot 10^{-3}$	[86]
Empirical equation	973	$1.18 \cdot 10^{-4}$	[84]
Elution method	973	$2.00 \cdot 10^{-3}$	[86]
Titration	973	$9.38 \cdot 10^{-4}$	[35]
Quenching method	973	$3.55 \cdot 10^{-5}$	[87]

CO_2 self-diffusion coefficients in the molten carbonate salts were presented by Janz [91] using the chronopotentiometry method and an empirical equation was produced by Wilemski [84] as shown in Eq. 2-7.

$$D_{CO_2} = 3.38 \cdot 10^{-7} exp\left(\frac{-5432}{T}\right) \quad [m^2\ s^{-1}] \qquad \text{Eq. 2-7}$$

The diffusivity coefficients at different temperatures are shown in There are many advantages in the use of the chronopotentiometry technique for the analysis of molten salts. It requires a simple apparatus and can be performed at high speed, which is particularly important for corrosive solutions, and it has a high sensitivity (<10^{-6} M)) [93]. However, the diffusion data available from electrochemical experiments are frequently affected by the nature of the electrode reactions and by variations of the effective area of the working electrode [93].

The mechanism of carbonate reduction during the chronopotentiometry technique in molten carbonate systems can be a multi-step mechanism involving soluble species and most

probably adsorbed and instable intermediates, that can occur in two one-electron steps or in two-electron unique steps. Based on the recent identification of the pyrocarbonate ions ($C_2O_5^{2-}$), a second path may also occur with rapid recombination of CO_2 and CO_3^{2-} to $C_2O_5^{2-}$ occurring close to the surface of the working electrode. Therefore, the formation of CO_3^{2-} does not describe the entire system for molten carbonate reduction under a CO_2 atmosphere and the CO_2 diffusivity measured with the chronopotentiometry technique could be measuring a combination of the diffusivities of different species ($C_2O_5^{2-}$, CO_3^{2-}).

Table 2-3. The chronopotentiometry method involves the application of a current pulse to the working electrode, which causes the electroactive species to be reduced or oxidised at a constant rate [92]. The potential - time profile of an electrode during an electrochemical reaction under controlled current conditions is then studied. The time at which the concentration of the reactant at the electrode interface is consumed is called the transition time. At the transition time, the potential increases until a new electrode process occurs. The resulting potential is then measured as a function of time against a reference potential.

There are many advantages in the use of the chronopotentiometry technique for the analysis of molten salts. It requires a simple apparatus and can be performed at high speed, which is particularly important for corrosive solutions, and it has a high sensitivity ($<10^{-6}$ M)) [93]. However, the diffusion data available from electrochemical experiments are frequently affected by the nature of the electrode reactions and by variations of the effective area of the working electrode [93].

The mechanism of carbonate reduction during the chronopotentiometry technique in molten carbonate systems can be a multi-step mechanism involving soluble species and most probably adsorbed and instable intermediates, that can occur in two one-electron steps or in two-electron unique steps. Based on the recent identification of the pyrocarbonate ions ($C_2O_5^{2-}$), a second path may also occur with rapid recombination of CO_2 and CO_3^{2-} to $C_2O_5^{2-}$ occurring close to the surface of the working electrode. Therefore, the formation of CO_3^{2-} does not describe the entire system for molten carbonate reduction under a CO_2 atmosphere and the CO_2 diffusivity measured with the chronopotentiometry technique could be measuring a combination of the diffusivities of different species ($C_2O_5^{2-}$, CO_3^{2-}).

Table 2-3. CO_2 diffusivity in the eutectic mixture $Li_2CO_3/Na_2CO_3/K_2CO_3$ [43.5/31.5/25.0 mol%] at varying temperatures.

Method	T, K	D, 10^{-10} m^2 s^{-1}	Reference
Chronopotentiometry method	690	1.02	[91]
Empirical equation	690	1.29	[84]
Chronopotentiometry method	770	2.19	[91]
Chronopotentiometry method	850	4.07	[91]
Chronopotentiometry method	930	6.79	[91]
Chronopotentiometry method	1010	10.46	[91]
Empirical equation	1010	15.60	[84]
Chronopotentiometry method	1080	14.48	[91]
Chronopotentiometry method	1120	17.12	[91]
Empirical equation	1120	26.46	[84]
Chronopotentiometry method	1130	17.82	[91]

As discussed before, permeability can be calculated from both the solubility and diffusivity coefficients. If the diffusivity coefficient of CO_2 in the molten carbonate salts given by Janz [91] (chosen due to the temperature range measured) and the solubility coefficient measured by Kanai [86] (chosen as it was specifically measured for the eutectic mixture $Li_2CO_3/Na_2CO_3/K_2CO_3$ with composition 43.5/31.5/25.0 mol% respectively) is used, the permeability of CO_2 through the melt in the dual-phase membranes would be as shown in Table 2-4.

Table 2-4. CO_2 permeability in the eutectic mixture $Li_2CO_3/Na_2CO_3/K_2CO_3$ (43.5/31.5/25.0 mol%) at varying temperatures.

Temperature, K	CO_2 permeability $10^{-11}\ mol\ m^{-1}\ s^{-1}\ Pa^{-1}$	Reference
~690-693	0.014	[86, 91]
~850-864	0.069	[86, 91]
~930-973	0.136	[86, 91]

The theoretical permeabilities found here will be compared to the experimental values in the following chapters.

2.3 Parameters influencing CO_2 permeation

Dual-phase membranes used in this work consist of a solid phase, which is a porous ceramic support, and a liquid phase, which is a eutectic carbonate mixture undergoing a phase change from solid to liquid at ~400 °C. As described in Section 1.3.1, this type of membrane is permeable towards CO_2 at temperatures above 400 °C.

One of the first studies directed towards synthesizing dual-phase membranes for CO_2 separation was in 2005 by Chung et al, who synthesised a metal-carbonate membrane [94]. CO_2 permeation was measured at temperatures between 450 and 750 °C, with and without the introduction of O_2. However, under an atmosphere that contains O_2, the metal support can be oxidized at temperatures above 650 °C and can form $LiFeO_2$, causing a reduction in the electronic conductivity of the support and thus a reduction in CO_2 permeance. The first study of ceramic-carbonate membrane was reported by Yamaguchi and co-workers [95]. In this work, lithium silicate membranes (Li_4SiO_4) were fabricated on porous alumina supports, and they were infiltrated with a binary molten carbonate mixture consisting of 20%wt K_2CO_3 and 80%wt Li_2CO_3. The CO_2/N_2 selectivity of the membrane was found to be very low of 4–6 at temperatures between 525 and 625 °C. However, permeances reported in this work (1×10^{-8} mol m^{-2} s^{-1} Pa^{-1} at 525 °C), were considered a lot higher than those reported in previous studies (10^{-10}–10^{-11} mol m^{-2} s^{-1} Pa^{-1}) with microporous membranes, where CO_2 can be separated due to the molecular sieving capabilities of the membranes [95-99]. In more recent years, there has been an increasing amount of literature on dual-phase membrane for CO_2 separation using different support materials, membrane geometries, pore structures and operational conditions. Between 2012 to 2014, a number of studies have reported permeances higher than 1×10^{-8} mol m^{-2} s^{-1} Pa^{-1} at temperatures above 650 °C that exceeded all those previous comparable types of membrane [43, 50, 100, 101].

In the last few years, very limited work has been published on ceramic-carbonate dual-phase membranes for CO_2 separation with interesting findings [40, 48, 102], as a lot of the recent published work [103, 104] could have been a lot more original by including some insights on CO_2 permeation mechanism.

Despite the widely existing research on CO_2 permeation in dual-phase membranes, there has been little interest on understanding the parameters influencing CO_2 permeation, thus

comparing the results of different studies can become difficult. Several parameters can affect CO_2 permeation through dual-phase membranes, and these include the membrane structure (thickness and pore geometry), membrane composition (the material of the two phases) and the operating conditions (temperature, pressure, gas phase composition).

2.3.1 Membrane composition

Several supports materials have been studied for CO_2 permeation with carbonates as the second phase. Ionic conducting supports such as, YSZ [43, 55, 57], $Ce_{0.9}Gd_{0.1}O_{1.95}$ (CGO) [55], $Ce_{0.8}Sm_{0.2}O_{1.9}$ (SDC) [50, 57, 99, 105, 106] and CeO_2 [47, 103], and mixed ionic and electronic supports such as LSCF [41, 44, 107] have been widely studied experimentally. Those supports offer different oxygen ionic conductivities as shown in Table 2-5 and therefore it is expected that they will result to different CO_2 permeations.

Wade et al [55] compared the CO_2 permeation through membranes with different support materials, such as YSZ, gadolinia doped ceria (CGO) and Al_2O_3, and the carbonate phase was a tertiary ($Li/Na/K_2CO_3$), or binary (Na/K_2CO_3) carbonate mixture or pure lithium carbonate. They observed that the permeation through the pure lithium carbonate-based membrane was decreasing with time and they explained that this could be due to the formation of a zirconate phase. The Na/K_2CO_3 mixture-based membrane showed similar permeances to the membranes with the $Li/Na/K_2CO_3$ based membranes. CO_2 permeabilities through the YSZ and CGO membranes with the $Li/Na/K_2CO_3$ mixture as the second phase, were similar and were compared to the theoretical transport model derived for the bulk, dual-ionic transport mechanism (transport model will be described in Section 2.3.3). When using the alumina-based membrane, the CO_2 permeability measured was an order of magnitude lower than the permeabilities calculated for the ionic-conductive carbonate membranes at temperatures above 600 °C.

Table 2-5. Oxygen ionic conductivity for different support materials at 600 °C. The carbonate ionic conductivity at 600 °C is 1.25 S cm^{-1} [94].

Material	Abbreviation	Oxygen ionic conductivity at 600 °C, $\sigma_i, S\ cm^{-1}$	Reference
ZrO_2-8mol%Y_2O_3	8YSZ	0.005	[108]
ZrO_2-8mol%Y_2O_3 Single crystal	YSZ single crystal	0.002	[109, 110]
$Ce_{0.9}Gd_{0.1}O_{1.95}$	CGO	0.03	[108]

Material	Abbreviation	Oxygen ionic conductivity at 600 °C, $\sigma_i, S\ cm^{-1}$	Reference
$Ce_{0.8}Sm_{0.2}O_{1.9}$	SDC	0.007	[111]
$La_{0.6}Sr_{0.4}Co_{0.8}Fe_{0.2}O_{3-\delta}$	LSCF6428	0.003	[112]
CeO_2	-	0.00003	[113]
$Bi_{1.5}Y_{0.3}Sm_{0.2}O_3$	BYS	0.08	[57]

Alumina and MgO supports are used in this work due to their very low oxide-ion conductivities. Rondão et al [114] have found that alumina is a highly insulating phase with a very low oxide ion-conductivity and an electrical conductivity of around 5.1 x 10^{-5} S cm^{-1} at 650 °C. However, it has been demonstrated [115] that alumina reacts with molten sodium carbonate to form sodium aluminate and carbon dioxide (Reaction 2-2, where M =Na). The results of this work show that the reaction would be expected to proceed to completion from the thermodynamic considerations, but it will be limited by some kinetic factors. It was also found that sodium aluminate is essentially insoluble in sodium carbonate, thus, a layer of sodium aluminate can be formed on the walls of the alumina support, which can decelerate the reaction. In this case, the rate determining step is expected to be the diffusion of sodium carbonate through the sodium aluminate layer. Similarly, lithium carbonate reacts with alumina to form lithium aluminate and depending on the Li_2O/Al_2O_3 ratio, mixed oxides can be formed, such as $LiAlO_2$, $LiAl_5O_8$ Li_5AlO_4, and $Li_2Al_4O_7$ and Li_3AlO_3 [116-118]. In this work, those reactions will not be considered for simplicity.

$$M_2CO_3(l) + Al_2O_3(s) \leftrightarrow 2MAlO_2(s) + CO_2(g) \quad \text{Reaction 2-2}$$

M = Li, Na, K

This work will also study 8YSZ supports which will be used as oxide-ion conducting supports and the conductivity of this material is reported in Table 2-6 at different temperatures. Carbonates can also react with zirconia oxide to produce zirconates and CO_2 as shown with Reaction 2-3 [119, 120]. In this work, the effect of temperature and gas phase condition on the formation of lithium zirconate will be studied by Raman spectroscopy and the results are discussed in Appendix D. This reaction is expected to occur at very low CO_2 pressures and/or at high temperatures [121]. If the free energy changes of Reaction 2-3 for the different salts are compared, it can be said that the lithium and sodium zirconate formation would occur easier than the formation of potassium zirconate [122, 123].

$$M_2CO_3(l) + ZrO_2(s) \leftrightarrow M_2ZrO_3(s) + CO_2(g)$$

Reaction 2-3

M = Li, Na, K

In recent years, there has been an increasing interest in the reverse reaction (Reaction 2-3) for high temperature CO_2 capture where the lithium zirconate serves as a solid regenerable sorbent that absorbs CO_2 [124-126]. Depending on the aggregate size of Li_2ZrO_3, it was reported that Li_2ZrO_3 can absorb up to 18% of its weight in CO_2 at 650 °C [127, 128].

Table 2-6. The ionic conductivity for 8YSZ at different temperatures [108, 129].

Ionic conductivity, $\sigma_i, S\ cm^{-1}$	**Temperature, °C**
0.001	450
0.001	500
0.003	550
0.005	600
0.008	650
0.016	700
0.020	750
0.032	800
0.040	850

It is also important to emphasize that when the carbonate mixture remains in the solid state (at temperatures below 400 °C for $Li_2CO_3/Na_2CO_3/K_2CO_3$ mixture with composition 43.5/31.5/25.0 mol%), its conductivity is a lot lower than the conductivity of the YSZ support. Therefore, at temperatures below 400 °C the ionic conductivity of the YSZ-phase membrane should be dominated by the oxygen-ion transport through the support. Moreover, the ionic transport within the carbonate mixture is dominated by the cations below melting and by the anions above melting temperature [130, 131]. The activation energy of YSZ was extracted from previous work and it was found to be 93 KJ mol^{-1} (0.96 eV) [130, 131]. For the YSZ single crystal, the activation energy was found to be 102 KJ mol^{-1} in the temperature range of 750 - 850 °C (1.06 eV, Figure 2-6) and 118 KJ mol^{-1} in the temperature range of 400 -750 °C (1.22 eV, Figure 2-6) [109, 110].

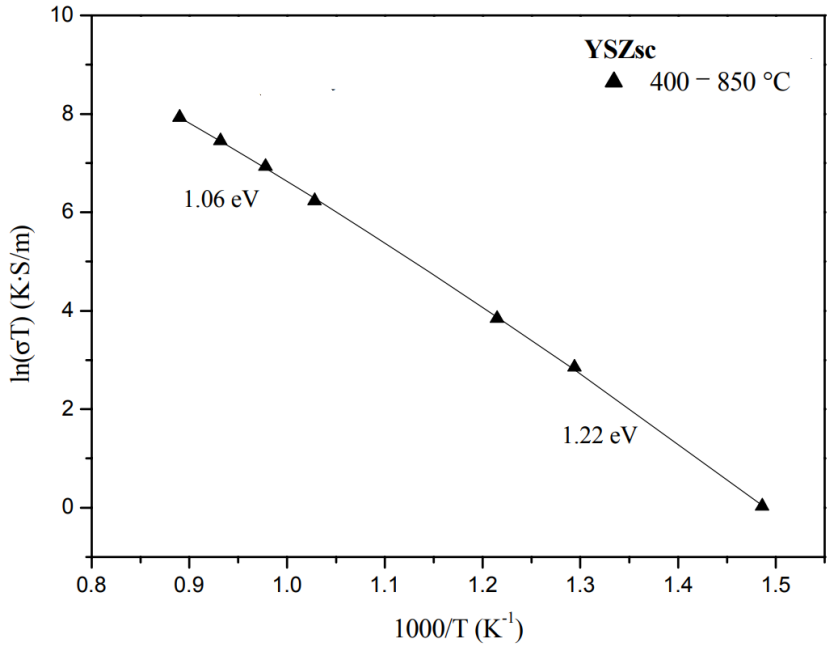

Figure 2-6. Conductivity of the YSZ single crystal (8mol% YSZ) at different temperatures. Retrieved from [109].

2.3.2 Membrane microstructure

Regardless of the chemical composition of the ceramic and carbonate phase, the volume ratio between the two phases and the membrane microstructure can maximise the flux of the carbonate and oxide ions by equalising the conductance of the two phases. The conductivity of both phases has been referenced before and it was found that they have large differences at temperatures above the melting point of the carbonates. Therefore, it is possible to obtain the conductivity of the dual-phase membrane when knowing the partial conductivities of the two phases and the membrane microstructure.

The importance of the membrane microstructure was first discussed by Zhang et al. in 2012 [50] who synthesized a $Ce_{0.8}Sm_{0.2}O_{1.9}$(SDC) porous support with highly interconnected and uniformly distributed pores fabricated by pressing and sintering an SDC-NiO composite powder, where the NiO serves as the sacrificial phase. This was followed by the reduction of the NiO phase and Ni metal particles were etched away. The pores of the support were filled with a binary mixture of Li_2CO_3 and Na_2CO_3 [52/48 mol% respectively]. By assuming a bulk-diffusion controlled charge transport they compared the theoretical CO_2 flux with additional consideration of microstructural factors to their experimental results and their results were in a good agreement. They claimed that they achieved a CO_2 permeance in the order of 10^{-7} mol m^{-2} s^{-1} Pa^{-1} at 650 °C (inlet on feed: 50%CO_2/N_2, inlet on permeate: He), which is significantly

higher than permeances in other similar systems reported in the literature, which are in the order of 10^{-9} to 10^{-11} mol m^{-2} s^{-1} Pa^{-1} [41, 55, 132] at the same temperature and gas composition inlets. The findings of this study suggest that the effective ionic transport pathway length can be larger than the actual support thickness in membranes with a random pore network and the permeance can be decreased by ‘‘inefficient’’ pore microstructure with poorly interconnected pores that can obstruct ionic transport. However, this conclusion would have been more convincing if they have compared their permeances to similar membrane systems (same support material and carbonate mixture) and with some consideration of the microstructural factors of the membranes used in literature.

Another significant work that studied the effect of the pore structure on CO_2 permeation was conducted by Ortiz-Landeros et al. in 2013 [44]. The different pore structures were achieved by preparing disks using the powder pressed method (described in Chapter 3.1.1) with $La_{0.6}Sr_{0.4}Co_{0.8}Fe_{0.2}O_{3-\delta}$ (LSCF) and sintering them at different temperatures (900, 950, 1000, 1050, 1100 and 1200 °C). The average pore radius (d_p), porosity (ε) and tortuosity factor (τ) for all samples were estimated using the Archimedes method and the room temperature helium permeance method. As shown in Figure 2-7, both the average pore size and the porosity to tortuosity factor increase slightly with the sintering temperature until 1050 °C (maximum pore diameter 0.8 μm) and then decreases with further increase. The tortuosity factor was found to decrease with the sintering temperature and the open porosity to increase with the sintering temperature (helium permeance method).

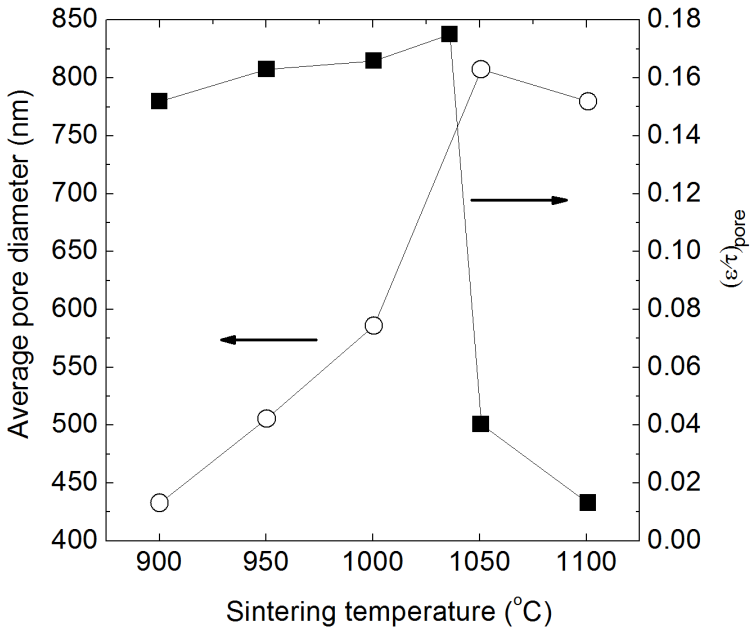

Figure 2-7. The average pore radius (d_p) and the porosity to tortuosity factor (ε/τ) of LSCF supports sintered at different temperatures as a function of the sintering temperature. Reproduced from [44].

The permeation measurements were conducted between 750 and 900 °C for all the supports. The CO_2 permeance showed an increase with the sintering temperature until 1000 °C (highest CO_2 permeance achieved) but decreased for the supports sintered at 1050 and 1100 °C (in the temperature range of 750 - 900 °C). They explained their findings by suggesting that there is an optimum solid fraction to tortuosity ratio and carbonate fraction to tortuosity factor to achieve the highest CO_2 permeance.

Assuming distinct dominant ionic species and transport mechanisms involved in both phases (both phases provide parallel ionic pathways), the ambipolar conductivity can be described as a function of the partial conductivities of the two phases (σ_{amb}, Eq. 2-8). The ambipolar conductivity is considered a key property in dual-phase membranes for CO_2 separation [40, 102, 132, 133]. To obtain the conductivity of a dual-phase membrane a simple mixing rule can be assumed; the partial conductivity of each phase will be proportional to the corresponding phase content. Therefore, Eq. 2-8 can be further expressed as a function of the conductivities of the pure phases (Eq. 2-9). However, this model can be considered crude as it assumes that there is no disturbance on the conductivity of an individual phase in the dual-phase membrane, which can be difficult to achieve if a film of carbonates covers the ceramic particles. Moreover, this model neglects microstructural constrains, such as tortuosity, and ion blocking grain boundaries.

In the previous work described [44], the theoretical ambipolar conductivity was calculated using Eq. 2-10, where tortuosity is taken into account , and the oxygen ionic conductivities for LSCF and carbonate mixture at 900 °C given by Anderson and Lin in 2010 [41]. The predicted values, did not match the experimental values, but they showed a similar trend with the highest ambipolar conductivity calculated at 1050 °C. However, these results do not take into consideration any possible contributions of oxygen ions through grain boundaries that can evolve by the sintering temperature and are known for their oxide-ion blocking characteristics.

$$\sigma_{amb} = \frac{\sigma_{c,p}\,\sigma_{s,p}}{\sigma_{c,p} + \sigma_{s,p}} \qquad \text{Eq. 2-8}$$

$$\sigma_{amb} = \frac{\varphi_C \sigma_C \varphi_s \sigma_s}{(\varphi_c \sigma_c) + (\varphi_s \sigma_s)} \qquad \text{Eq. 2-9}$$

$$\sigma_{amb} = \frac{[(\varphi/\tau)_c \sigma_c][(\varphi/\tau)_s \sigma_s]}{[(\varphi/\tau)_c \sigma_c] + [(\varphi/\tau)_s \sigma_s]} \qquad \text{Eq. 2-10}$$

Where,

σ_C and σ_s are the ionic conductivies of the carbonate phase and the support respectively, with the subscript p used to distinguish between the partial conductivities of each phase in the composite and the conductivities of the same phases as fully dense materials,

τ is the tortuosity,

φ is the volume fraction of each phase,

with the subscripts c and s used to distinguish between the carbonates and the support.

The ambipolar conductivity can be considered an important parameter for the CO_2 flux through those membranes. The transport models will be further discussed in the following pages (Section 2.3.4).

Recent research by Marques' group in collaboration with Metcalfe's group gave some insight into the performance, kinetics and stability of composite CO_2 separation membranes. In particular, Patrício et al. in 2017 [134] calculated the ideal performance values using the ambipolar conductivity, which can be expressed as a function of the partial conductivities of the two phases. They found that the ideal performances calculated from the ambipolar conductivity were much higher than the actual membrane performances (30-40% higher), which highlights the importance of the contribution of the porous microstructure and features such as tortuosity and grain boundaries that were not taken into account in the ideal

performance calculations. The same groups in 2016 [102] have also used a new illustrative diagram inspired by corrosion (Evans-type) plots which consists of net thermodynamic voltages (V) versus the effective cell current density (J) and includes information on ideal and real membrane performance. Surface/interface processes (non-ohmic) and ambipolar transports (ohmic) are the source of an overvoltage and the sum of the contributions must match the net thermodynamic voltage. The ohmic contribution is estimated with impedance spectroscopy data, partial pressure difference of CO_2 in the feed and permeate side are determining and CO_2 permeation data show the current density. They suggested that this plot can be used to obtain some insight on the ideal phase compositions and working temperatures for CO_2 separation membranes. However, this model neglects the dependence between the conductivity of the membrane and the gas phase composition. In the case of ceria-based membranes studied in this work [102], it was shown that the performance in terms of CO_2 permeance might be improved by decreasing tortuosity factors (eg. by using fully aligned pore microstructures) or by decreasing the membrane thickness. Both factors would decrease the ion transport pathway and they suggested that the most effective design parameter would be the decrease of the membrane thickness as the tortuosity values are already small. Moreover, in this work [102] they estimated a temperature range (650 - 800 °C) where the membrane CO_2 permeation regime changes from oxide-ion to carbonate-ion controlled.

Although a thin membrane would result to higher permeances as suggested in literature, from a practical point of view, there is a limit on the thickness of the membrane for an adequate mechanical strength. It has been reported that the thickness of the membrane to produce a membrane with adequate mechanical strength is dependent on the size of the largest pore diameter of the support [135]. It was suggested that the thickness needs to be at least three times higher than the size of the largest pore diameter in the case of a stainless-steel membrane, however, this was only tested at 350 °C.

Dual-phase membranes with an oxide-ion conducting support are particularly important for CO_2 separation application as the net flow of CO_2 through those membrane is the result of counter transport of carbonate ions and oxide ion through the carbonate phase and the support respectively. A few attempts have been made to study the role of each ion using classical dc techniques [136, 137]. Zuo et al. [136] has studied the transport properties and electrical conductivity of samarium-doped ceria (SDC) supports infiltrated with a potassium-lithium carbonate mixture at temperatures between 450 and 550 °C. The effect of the carbonate content on the total conductivity of the dual-phase membranes was measured in air with impedance analysis and the results are shown in Figure 2-8. As shown in this figure, when the

carbonate volume fraction is above 30% the conductivity increases to several times higher values. Below 30 vol% the conductivity of the dual-phase membrane is close to the intrinsic conductivity of the support (SDC) and this could be due the fact that the carbonate particles are separated by the particles of the support, hence the transportation of the carbonate ions is blocked.

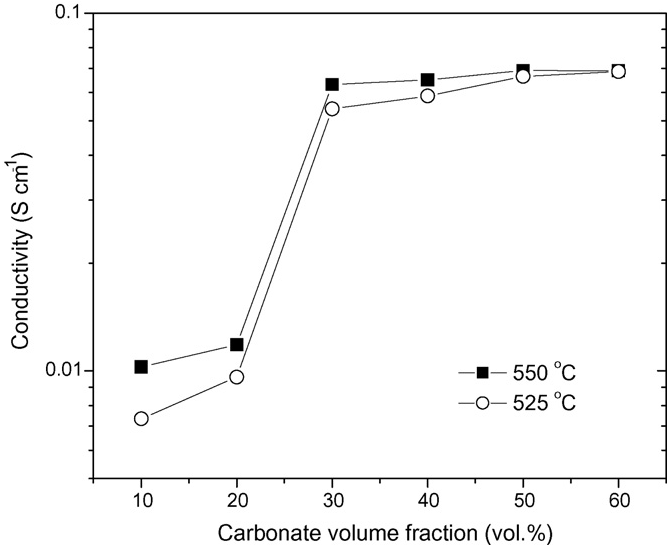

Figure 2-8. Conductivity of SDC- carbonate membrane as a function of carbonate content at 525 and 550 °C. Retrieved from [136].

Similarly, Zhao et al. [137] studied the effect of the carbonate content on the ionic conductivities of SDC-carbonate membranes as shown in Figure 2-9. This figure shows that the conductivity of the dual-phase membrane increases with the increase of the carbonate content with both cathodic gases. The total conductivity increases with the addition of CO_2 as expected due to the formation of CO_3^{2-}.

Both studies described above [136, 137] use mixed working conditions to measure the average transport properties of the ions. It is expected that the behaviour of the extreme cell regions will be different at different conditions because there is significant interaction between the gas phase composition and the ionic transport [138].

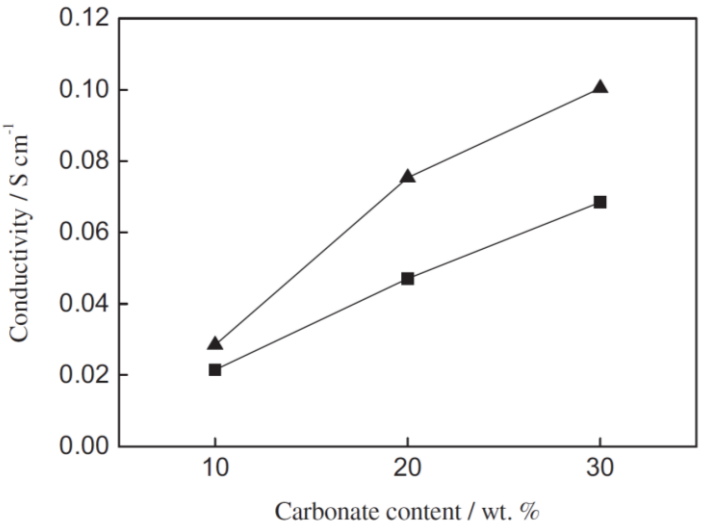

Figure 2-9. Conductivity of SDC- carbonate membrane as a function of carbonate content at 650 °C with (■) O_2 and (▲) O_2/CO_2 as the cathodic gas. Retrieved from [137].

The relevance of the porous support functionality on the performance of these dual-phase membranes but also the compositional range where the transport through the oxide and carbonate phase are balanced, were inspected by impedance spectroscopy [101, 139, 140]. Studies were performed using a ceria-based ceramic support, prepared using pure CeO_2 as a modest conductor or Gd-doped ceria, which are considered modest and excellent oxide-ion conductors respectively. The supports were infiltrated with a carbonate mixture of Li and Na carbonates in a 1:1 molar ratio.

Low temperature impedance spectra (below the melting point of the carbonates, Figure 2-10 A) allow the access to transport data, where the individual characteristics of each phase can be considered. At this temperature, the electrical properties of the support were preserved after the carbonate infiltration and this confirms that the conductivity of the support, which is the most conductive phase at this temperature, determines the conductivity of the dual-phase membrane. The high temperature spectra (Figure 2-10 B) of the support and the dual-phase membrane (above the melting point of the carbonates) have shown pronounced differences in magnitude and shape. At this temperature, both phases contribute with district charge carriers, and it is known that the carbonate mixture has much higher conductivity than the ceramic support. From the high frequency intercept with the Z´ axis, the total conductivity of the support and dual-phase membrane can be measured directly, and therefore an estimate of the actual transport properties of each phase within the membrane can be provided.

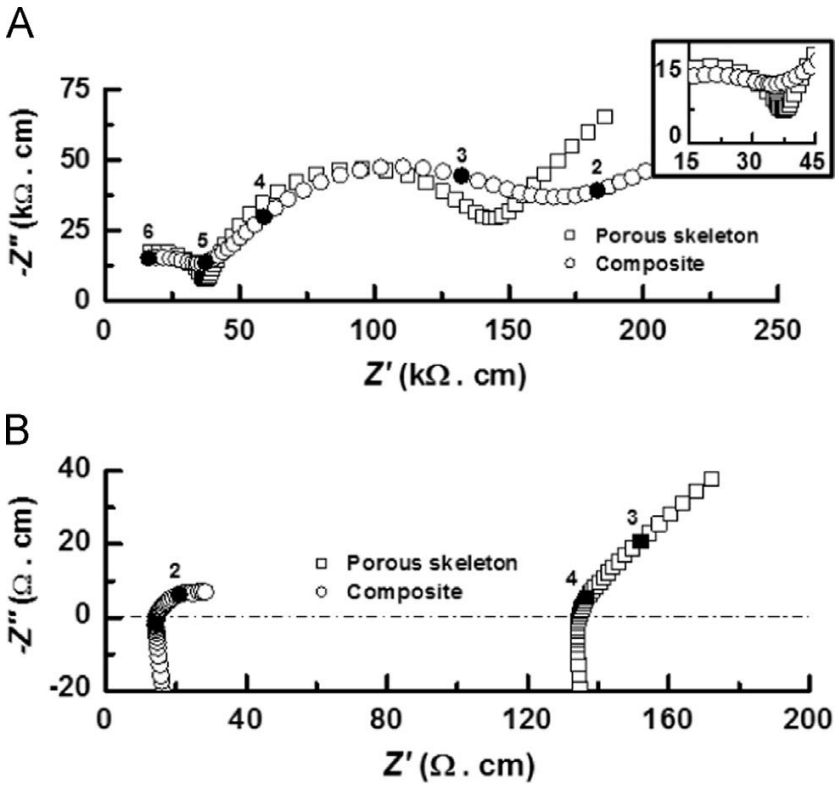

Figure 2-10. Impedance spectra of CGO-carbonate membrane (composite) and of the support (porous skeleton) at A) 250 and B) 600 °C in air. An exploited view of the high frequency data is shown in the A) inset. Retrieved from [101].

Based on Eq. 2-9 that was given before for the ambipolar conductivity and some published data on the conductivity of individual phases [141-143], a model dependence between the ambipolar conductivity and the phase compositions is shown in Figure 2-11. The conductivity is the intrinsic property and conductance is the extrinsic property. The conductance changes with the cross-sectional area and length of the material as shown with the below equation:

$$G = \sigma A/l \qquad \text{Eq. 2-11}$$

Where G is the conductance,

σ is the conductivity,

A is the cross-sectional area and

l is the length.

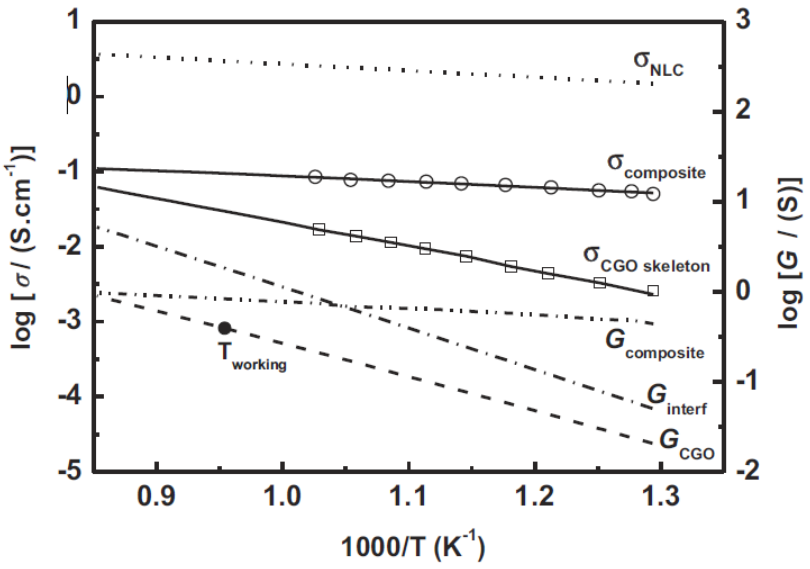

Figure 2-11. Logarithmic electrical conductivity and conductance of the CGO support (skeleton), carbonates (NLC) and dual-phase membrane (composite) versus temperature. Retrieved from [101].

Although recent literature identifies the microstructure complexity of the membranes and the importance of the pore characteristics on the membrane separation performance in terms of CO_2 permeation [50, 147], most of the studies have very little control on the membrane microstructure and its effect on CO_2 permeation remains a complex factor. For this reason, this work will focus on designing membranes with well controlled pore microstructures.

2.3.3 Membrane geometry

Almost all commercial membrane systems are either flat disks, tubular or hollow fibres [144, 145], as shown in Figure 2-12. The geometry of the membranes used for most of the studies are disks because the temperature, thickness and surface area can be easily controlled, and they are easy to fabricate and at very low cost. However, disk membranes suffer from limited surface area and their sealing is challenging at high temperatures. Tubular membranes have been developed using an extrusion process to increase the surface area to volume ratio (approximately 250 m^2 m^{-3} [146]). They can be packed together or form a multi-channel tube and the sealing can be achieved outside the high temperature zone using a cold seal. To further increase the surface area to volume ratio, hollow fibre membranes were fabricated by phase inversion method, with surface area to volume ratio up to 3000 m^2 m^{-3} [146].

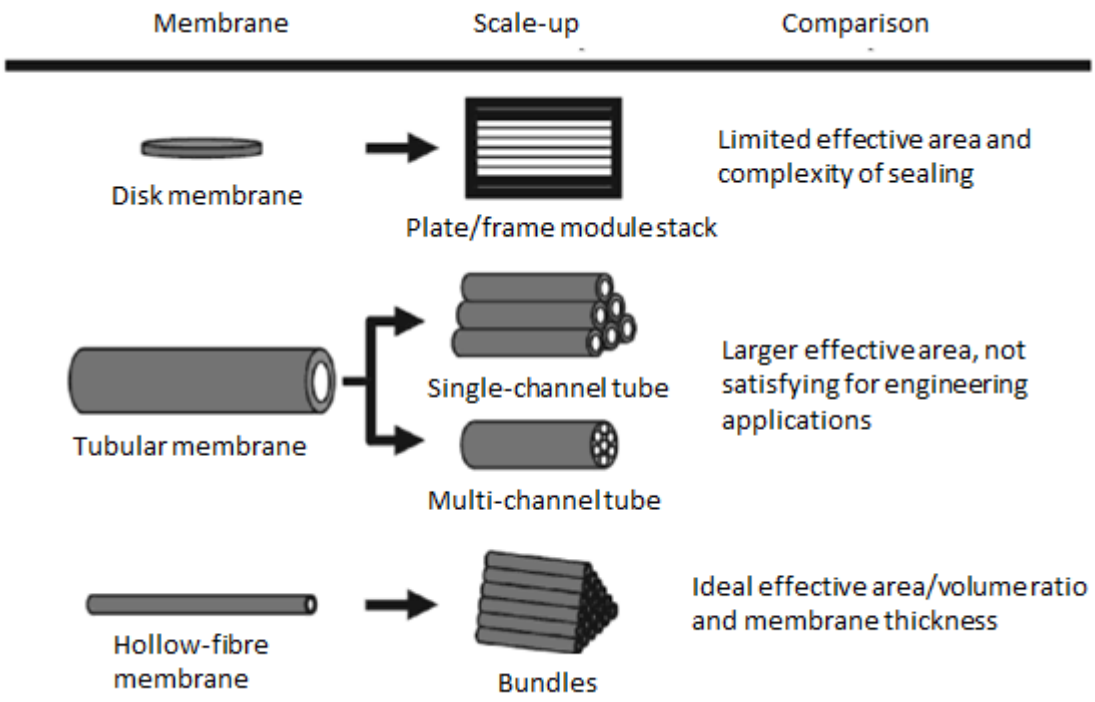

Figure 2-12. Ceramic membrane support classification in view of geometrical configuration. Retrieved from [146].

2.3.4 Operational conditions

Permeation through dual-phase membranes is a thermally activated process, yielding a positive activation energy that follows an Arrhenius behaviour. The temperature dependence of CO_2 permeation in various dual-phase membranes reported in the literature are shown in Table 2-7. The activation energies through those membranes are between 63 and 106 kJ mol^{-1}. The highest activation energy was observed with the very thin (~10 μm) YSZ-carbonate membrane and this could be due to surface limitations. The differences between the activation energies of the different membranes could suggest that the CO_2 transport is mostly controlled by the oxygen ion diffusion through the support of the dual-phase membrane, which is expected because the conductivity of the carbonates is much higher than the ionic conductivity of the support at these temperatures. Patrício et al. [101] published a paper with a molten carbonate-Gd-doped ceria (CGO) membrane, which exhibited permeances of about 4.4×10^{-8} mol m^{-2} s^{-1} Pa^{-1} at 650 °C and 9.2×10^{-8} mol m^{-2} s^{-1} Pa^{-1} at 850 °C (0.92 mm thickness). In their work, they have also investigated the effectiveness of the membrane microstructure using impedance spectroscopy. At temperatures below the melting point of the carbonates (in this work at 250 °C) the membrane performance will be governed by the

ceramic phase that shows the highest conductivity. However, at temperatures above the melting point of the carbonates the situation is reversed and the spectra of the ceramic support alone and the composite dual-phase membrane are very distinct in magnitude and shape. This strong relationship between the ceramic support alone and the composite dual-phase membrane was used to predict the temperature at which the conductivity of the two phases is roughly balanced and can correspond to the ideal temperature operating condition for the membrane. The conductivity of the ceramic support shows higher activation energy than the composite dual-phase membrane and therefore, with the increase of temperature, a point is reached where the ionic transport through both phases is matched. This prediction was confirmed with the permeation data reported through the analysis of the activation energies of this membrane.

Table 2-7. Activation energies for different dual-phase membranes with an oxygen ionic conducting support at temperatures above 600 °C. The CO_2 partial pressure at the feed side is between 20% and 50%.

Ceramic support	Thickness, μm	Activation energy, $kJ\ mol^{-1}$	Reference
8YSZ	~10	106	[43]
CGO	200 - 400	84	[55]
CGO	9200	70-80	[101]
SDC	300 - 400	80	[147]
SDC	1200	63	[50]
CeO_2	1000	95	[47]

As mentioned in the introduction of this thesis, CO_2 permeation through dual-phase membranes involves three steps: (i) the surface-exchange reaction on one interface; (ii) the bulk diffusion of charged species or molecular species in the bulk phase and (iii) the surface exchange reaction of the other interface. The slowest process is expected to limit the overall CO_2 permeation rate. A different step can become the controlling process depending on temperature, membrane composition, thickness etc.

If the slowest process is bulk diffusion, a modified Wagner equation can be used to describe CO_2 flux. Wagner theory [148] is based on the assumption that permeation proceeds mainly via the diffusion of charged species through a linear diffusion equation and that the potential acting is the electrochemical potential:

$$J_i = -\frac{\sigma_i}{(z_i F)^2}(\nabla\mu_i + z_i F \nabla\varphi) \quad \text{Eq. 2-12}$$

Where σ_i and z_i are the conductivity and charge of species i, respectively; μ_i and $\nabla\varphi$ are the chemical potentials of species i and the electric field gradient respectively; R, T and F are the gas constant, the temperature and the Faraday constant. Because of the fast movement of the ions inside the membrane, a steady-state electric field gradient does not exist:

$$\nabla\varphi = 0 \quad \text{Eq. 2-13}$$

Assuming that the main moving species are the carbonate ions and oxygen ions and that the charge neutrality is kept ($J_{CO_3^{2-}} z_{CO_3^{2-}} + J_{O^{2-}} z_{O^{2-}} = 0$), Eq. 2-12 becomes:

$$J_{CO_3^{2-}} = -\frac{\sigma_{CO_3^{2-}}\sigma_{O^{2-}}}{\left(z_{CO_3^{2-}} F\right)^2 L}\left(\frac{\nabla\mu_{CO_3^{2-}} + {}^{z_{CO_3^{2-}}}/_{z_{O^{2-}}}\nabla\mu_{O^{2-}}}{\sigma_{CO_3^{2-}} + \sigma_{O^{2-}}}\right) \quad \text{Eq. 2-14}$$

Considering Reaction 2-4, and assuming ideal behaviour (no intermolecular interaction between species) and that the ionic conductivities are independent of the CO_2 partial pressure, the CO_2 flux can be obtained by integrating Eq. 2-14:

$$M_2CO_{3(molten)} \rightarrow M_2O_{(molten)} + CO_{2(g)} \quad \text{Reaction 2-4}$$

$$J_{CO_2} = J_{CO_3^{2-}} = -\frac{RT}{4F^2 L}\frac{\sigma_{CO_3^{2-}}\sigma_{O^{2-}}}{\sigma_{CO_3^{2-}} + \sigma_{O^{2-}}}\ln\frac{P''_{CO_2}}{P'_{CO_2}} \quad \text{Eq. 2-15}$$

Where P'_{CO_2} and P''_{CO_2} are the CO_2 partial pressures in the feed and permeate side of the membrane respectively.

If microstructural effects are considered, the effective diffusivity and concentration in Eq. 2-12 will be:

$$D_i^{eff} = \frac{\varepsilon}{\tau} D_i \quad \text{Eq. 2-16}$$

$$C_i^{eff} = \varphi_i C_i \quad \text{Eq. 2-17}$$

Where ε, τ and φ_i are the porosity, tortuosity and phase volume ratio respectively. If we assume that the pores of the membrane support are filled with carbonates, we can assume that φ_c/τ (volume ratio of carbonates) is the same as ε/τ.

Eq. 2-15 will then become:

$$J_{CO_2} = -\frac{RT}{4F^2L}\frac{\varepsilon}{\tau}\left(\frac{\varphi_c\sigma_{CO_3^{2-}}(1-\varphi_c)\sigma_{O^{2-}}}{\varphi_c\sigma_{CO_3^{2-}}+(1-\varphi_c)\sigma_{O^{2-}}}\right)\ln\frac{P_{CO_2}^{"}}{P_{CO_2}^{'}} \quad \text{Eq. 2-18}$$

Transport models on CO_2 and O_2 permeation through membranes composed of a mixed ionic and electronic conductive phase and molten carbonate phase were also studied [132, 133, 149]. However, this work will only focus on ionic conducting supports and therefore those models will not be discussed here.

The effect of varying CO_2 partial pressure experimentally through dual-phase membranes was first studied by Norton et al [107] in 2014 who studied CO_2 flux through an LSCF-carbonate membrane. In this work, the CO_2 partial pressure on the feed side was varied from 25% to 90% at 900 °C and the CO_2 permeation flux was plotted against the logarithmic CO_2 partial pressure difference between the two sides of the membrane. Their work confirmed the prediction that the CO_2 permeation is proportional to the logarithmic CO_2 partial pressure difference and therefore limited by bulk diffusion. However, the author overlooks the fact that their conclusions are based on a small range of logarithmic CO_2 differences since they have only varied the CO_2 partial pressure on the feed side of the membrane and not on both sides.

As mentioned in the introduction, many industrial processes can produce streams containing CO_2 and water. Water dissolution in molten carbonates has been observed from 1965 [150], however, its effect on CO_2 permeation was first studied by Xing *et al.* in 2015 [47], and was found to increase permeation flux by 250-300% when 2.5% water was fed to the permeate stream and by 30% when water was fed to the feed side. In their analysis, Xing *et al.* proposed a transport mechanism (Figure 2-13) and a theoretical model (Eq. 2-19) for CO_2 flux under the presence of H_2O. Under humidified conditions, water will be involved in CO_2 permeation forming $[OH]^-$ inside the melt as shown in Figure 2-13. The reactions on both sides of the membrane are illustrated in this figure. The membrane will then function with three main charged carriers, the oxide ions, carbonate ions and hydroxide ions. Carbonate ions and hydroxide ions transport in opposite directions in the molten salt phase and if the support is an oxide-ion conductor, the CO_2 flux will benefit from the oxide ion transport. In their work [47], the CO_2 flux was given for a dual-phase membrane with an oxygen ionic conducting support where the O^{2-} is transported through the support (Eq. 2-19).

$$J_{CO_2} = \frac{RT}{2F^2L}\int_{,,}^{'}\sigma_{CO_3^{2-}}\left[(t_{O^{2-}}+t_{OH^-})d\ln P_{CO_2} - t_{OH^-}d\ln P_{H_2O}\right] \quad \text{Eq. 2-19}$$

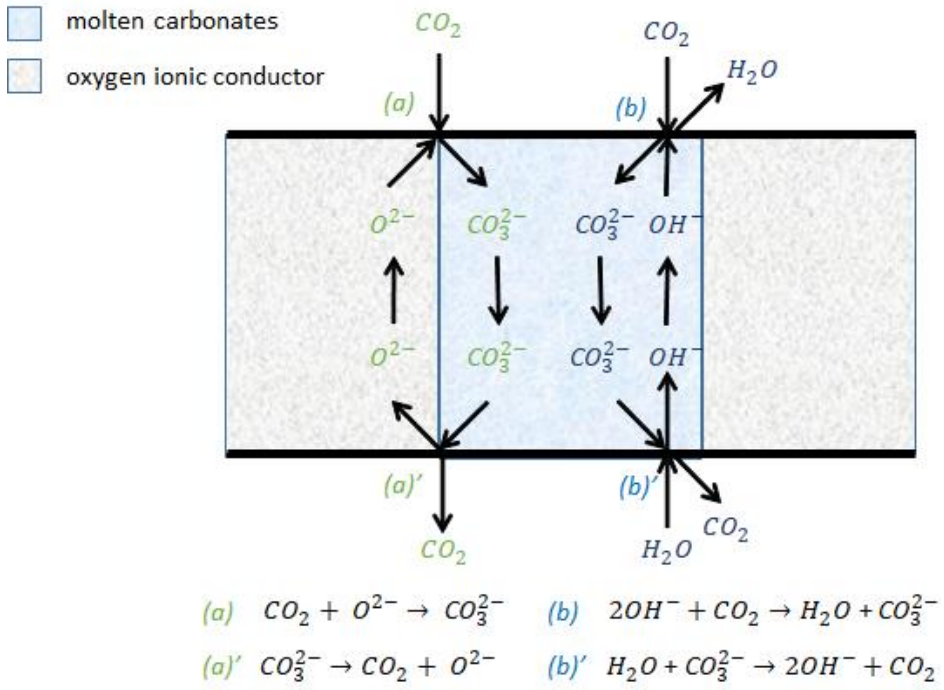

Figure 2-13. Transporting CO_2 through the molten salt phase under the presence of water.

Xing's paper [47] would have been more interested if the author had linked the theoretical equation to their experimental findings. Moreover, no attempt was made to measure water permeation or to explain the increase in CO_2 permeation when water was fed to the feed side which cannot be explained by the suggested transporting model, as H_2O and CO_2 travel to the opposite directions. A likely explanation for the latter is that leaks might have contributed to CO_2 permeation as sealants are more likely to fail under humidified conditions. The authors fail to fully describe the contribution of leaks or the reproducibility of their data.

According to the transport model described in Figure 2-13, when certain amount of water is introduced to the permeate side, and since CO_2 and H_2O transports are linked, CO_2 could be transported against its own chemical gradient difference. This concept was already proven with oxygen [48] in a membrane consisting of a mixed ionic and electronic conducting phase and a carbonate phase. In this study, this link between CO_2 and H_2O transport will be studied in a leak-free membrane system with controlled pore microstructure.

The CO_2 flux through a dual-phase membrane has been discussed here under dry conditions. However, in the presence of steam, the membrane performance will be affected as the water is involved by reacting with the carbonates and forming hydroxide ions. The flux of CO_2 under "wet" conditions with an oxygen ionic conducting support was previously given [47] as shown in Eq. 2-19. Eq. 2-19 was derived from the Wagner transport theory with the assumption that

there is local equilibrium between the charged species and hypothetical neutral species, such as molecular CO_2 and H_2O and the rate-limiting step is the bulk diffusion.

$$J_{CO_2} = \frac{RT}{2F^2L}\int_{''}^{'}\sigma_{CO_3^{2-}}\left[(t_{O^{2-}} + t_{OH^-})d\ln P_{CO_2} - t_{OH^-}d\ln P_{H_2O}\right] \quad \text{Eq. 2-20}$$

Where L is the membrane thickness, P_{CO_2} and P_{H_2O} are the partial pressures of CO_2 and H_2O and $t_{O^{2-}}$ and t_{OH^-} are the transport numbers of CO_2 and H_2O respectively; R, T and F are the gas constant, the temperature and the Faraday constant respectively.

In this work, wet conditions will be studied with dual-phase membrane that consist of an "inert" support and therefore the permeation will be related to the transport properties of only the molten carbonate phase. As mentioned previously the surface reaction converts water to hydroxides and if M = Li, Na, K for the molten carbonate mixture, then:

$$M_2CO_{3(molten)} + H_2O_{(g)} \rightarrow 2\ MOH_{(molten)} + CO_{2(g)} \quad \text{Reaction 2-5}$$

If the transport number, t_{OH^-}, is assumed to be constant, Eq. 2-20 will become:

$$J_{CO_2} = \frac{RT}{2F^2L}\int_{''}^{'}\sigma_{CO_3^{2-}}t_{OH^-}\left[d\ln P_{CO_2} - d\ln P_{H_2O}\right] \quad \text{Eq. 2-21}$$

The transport number, t_{OH^-}, can be described in terms of conductivity:

$$t_{OH^-} = \frac{\sigma_{OH^-}}{\sigma_{OH^-} + \sigma_{CO_3^{2-}}} \quad \text{Eq. 2-22}$$

Since $d\ln x$ is equal to $\frac{dx}{x}$ then Eq. 2-21 after integration will become:

$$J_{CO_2} = -\frac{RT}{2F^2L}\frac{\sigma_{CO_3^{2-}}\sigma_{OH^-}}{\sigma_{OH^-} + \sigma_{CO_3^{2-}}} ln\left(\frac{P'_{CO_2}P''_{H_2O}}{P''_{CO_2}P'_{H_2O}}\right) \quad \text{Eq. 2-23}$$

Because the reaction on the surfaces was considered fast compared to the bulk ionic diffusion and thus pseudo-steady state approximation is considered, from the stoichiometry of the surface reactions given above:

$$J_{CO_2} = J_{H_2O} = 2J_{OH^-} = J_{CO_3^{2-}} \quad \text{Eq. 2-24}$$

Ionic solutions generally require a complex mathematical modelling of the accurate movement of multiple mobile ionic and non-ionic species. For this reason, a binary dilute solution will be

assumed, and therefore, the diffusivity and ionic conductivity relationship can be calculated by the Nernst-Einstein relationship [151]:

$$\sigma_i = \frac{cF^2 z_i^2 D_i}{RT} \quad \text{Eq. 2-25}$$

Where D_i is the self-diffusivity, z_i is the charge number and c is the bulk molar concentration; R, T and F are the gas constant, the temperature and the Faraday constant respectively.
The diffusion coefficient, D_{OH^-}, in the melt could not be found in literature and therefore it will be calculated using a correction term to allow for masses. The self-diffusion coefficient of components differing only in their particle masses in a binary fluid mixture were studied [152, 153] and it was found that:

$$\frac{D_{m_1}}{D_{m_2}} \sim \left(\frac{m_{m_2}}{m_{m_1}}\right)^k \quad \text{Eq. 2-26}$$

Where,
D_{m_1} and D_{m_2} are the self-diffusion coefficients of component 1 and 2 respectively with m_1 and m_2 particle mass. The coefficient k was evaluated in various approaches and varied between different studies.
A number of researchers conducted more extensive molecular dynamics (MD) simulations [154-156] and provided this relation (Eq. 2-27), assuming that the particles of the system interact through the same interaction potential for an isotopic liquid.

$$\frac{D_{m_1}}{D_{m_2}} = \sqrt{1/2}\left(1 + \frac{m_{m_2}}{m_{m_1}}\right)^{1/2} \quad \text{Eq. 2-27}$$

And for this work:

$$\frac{D_{CO_3^{2-}}}{D_{OH^-}} = \sqrt{1/2}\left(1 + \frac{m_{OH^-}}{m_{CO_3^{2-}}}\right)^{1/2} \quad \text{Eq. 2-28}$$

Where,
m_{OH^-} and $m_{CO_3^{2-}}$ are the molar masses of OH^-(17 g mol^{-1}) and CO_3^{2-} (60 g mol^{-1}) respectively.

With the diffusivity coefficient of CO_2 in the molten carbonate salts given by Janz et al. [91] (2.19 x 10^{-10} m^2 s^{-1} at 770 K), and Eq. 2-28 the diffusion coefficient of the hydroxide ions, D_{OH^-}, can be calculated and it will be equal to 5.1 x 10^{-10} m^2 s^{-1} at 500 °C.

2.3.5 Thermodynamics of the oxide and hydroxide formation

As mentioned in the introduction of this thesis, it is expected that CO_3^{2-} is the main charge carrier, however, it has been recently reported that more carrier charges, such as, oxide ions, hydroxide ions, $C_2O_5^{2-}$ and CO_4^{2-}, can contribute to the overall CO_2 transport, depending on the gas atmosphere and the operating conditions [35-38]. In this section, the thermodynamics of the oxides and hydroxides will be studied.

Most metal carbonates of group 1, M_2CO_3 (M = Li, Na, K), undergo thermal decomposition at high temperatures (below Bunsen temperatures) and can form dissolved oxides with the release of carbon dioxide. The decomposition of the carbonates, and the reverse reaction can also participate on CO_2 transport with the release of CO_2 on one side of the membrane (Reaction 2-6) and the reverse reaction on the other side of the membrane.

$$\mathrm{M_2CO_{3(molten)}} \rightarrow \mathrm{M_2O_{(molten)}} + \mathrm{CO_{2(g)}} \qquad \text{Reaction 2-6}$$

The Gibbs free energy, ΔG_1, of Reaction 2-6, when the oxides are molten, assuming ideal mixture with no thermal effects associated with mixing, is given by:

$$\Delta G_1 = \overbrace{\Delta G_{M_2O(s)} + \Delta G_{CO_2(g)} - \Delta G_{M_2CO_3(s)}}^{\Delta G_{R1}} + \\ - \overbrace{(\Delta H_{fus,M_2CO_3} - T\,\Delta S_{fus,M_2CO_3})}^{\Delta G_{fus,\,M_2CO_3}} \qquad \text{Eq. 2-29}$$

Where,

ΔG_{R1} is calculated from the standard Gibbs free energies of formation of the compounds, for the solid carbonates ($\mathrm{M_2CO_{3(s)}}$)

$\Delta G_{M_2O(s)}$, $\Delta G_{CO_2(g)}$ and $\Delta G_{M_2CO_3(s)}$, is the Gibbs free energy of formation ($\Delta_f G^o$) of the $\mathrm{M_2O}$, $\mathrm{CO_2}$ and $\mathrm{M_2CO_3}$ respectively.

$\Delta G_{fus,\,M_2CO_3}$, is the Gibbs energy required to melt carbonates, calculated from the heats and entropies of fusion.

Under humidified conditions, water will be involved in CO_2 permeation forming new ionic species inside the melt. With the assumption that hydroxide ions (OH^-) are formed inside the melt (proposed by Xing *et al.* [47]), the membrane will then function with three charged carriers, the oxide ions, carbonate ions and hydroxide ions.

Under humidified conditions:

$$M_2CO_{3(molten)} + H_2O_{(g)} \rightarrow 2\ MOH_{(molten)} + CO_{2(g)}$$ Reaction 2-7

The Gibbs free energy, ΔG_2, of Reaction 2-7, when the carbonates and corresponding hydroxides are molten, is given by:

$$\Delta G_2 = \overbrace{2\ \Delta G_{MOH(s)} + \Delta G_{CO_2(g)} - \Delta G_{H_2O(g)} - \Delta G_{M_2CO_3(s)}}^{\Delta G_{R2}} + \\ + 2\ \overbrace{(\Delta H_{fus,MOH} - T\ \Delta S_{fus,MOH})}^{\Delta G_{fus,MOH}} \\ - \overbrace{(\Delta H_{fus,M_2CO_3} - T\ \Delta S_{fus,M_2CO_3})}^{\Delta G_{fus,\ M_2CO_3}}$$ Eq. 2-30

Where,

ΔG_{R2} is calculated from the standard Gibbs free energies of formation of the compounds, for the solid carbonates and hydroxides

$\Delta G_{fus,MOH}$ is the Gibbs energy required to melt hydroxides, calculated from the heats and entropies of fusion.

In both Eq. 2-29 and Eq. 2-30, it is assumed ideal mixture with no thermal effects associated with mixing. Reaction 2-6 and Reaction 2-7 will occur on the hydration side of the membrane, and the reverse reactions will occur on the other side of the membrane (carbonation side).

Figure 2-14 shows the free energy change of Reaction 2-6 and Reaction 2-7 versus temperature at the interface between the membrane and the humidified gas. The comparison between the two groups of curves (formation of hydroxides and oxides) shows that Reaction 2-7 occurs easier than Reaction 2-6. Moreover, in both reactions, the compounds of lithium react easier than the corresponding compounds of sodium and potassium.

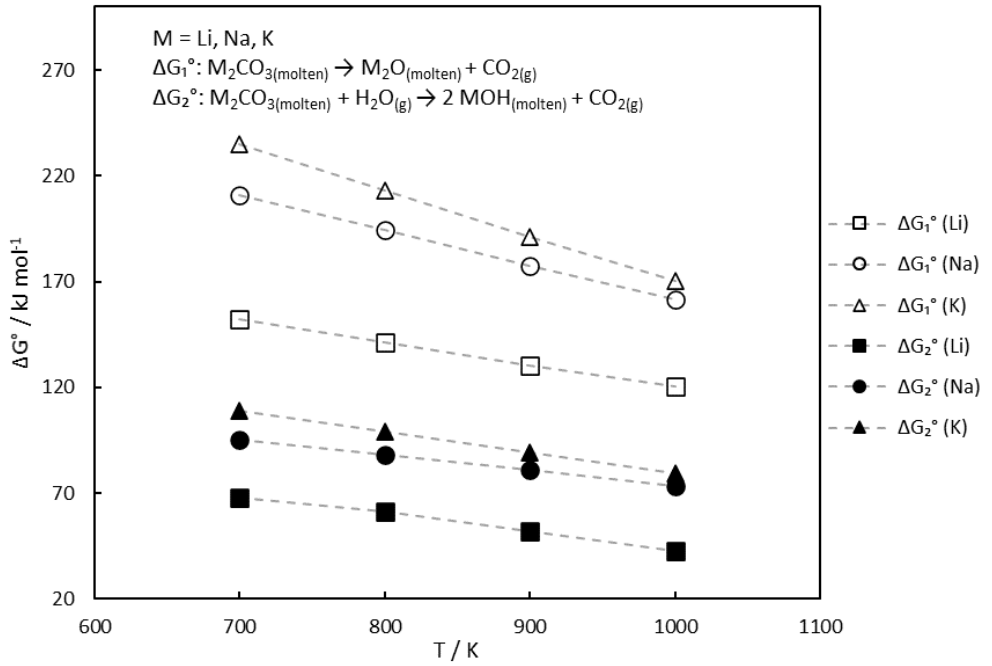

Figure 2-14. The standard Gibbs free energy change of the reactions at the interface of the membrane versus temperature, under humidified conditions. $\Delta \boldsymbol{G_1^o}$ and $\Delta \boldsymbol{G_2^o}$ represent the standard Gibbs free energy of Reaction 2-6 and Reaction 2-7 respectively, when the carbonates and corresponding oxides or hydroxides are molten. $\Delta \boldsymbol{G_1^o}$ and $\Delta \boldsymbol{G_2^o}$ have been calculated using Eq. 2-29 and Eq. 2-30 respectively. The data used for these calculations are given in Appendix A.

The free energy of a reaction is given by the following equation:

$$\Delta G_r = \Delta G_r^o + RTlnQ \qquad \text{Eq. 2-31}$$

Where,

ΔG_r^o is the standard free energy of the reaction

And Q is the reaction quotient, which shows the relative amount of the products and the reactants when the reaction is not at equilibrium.

At equilibrium $\Delta G_r = 0$ and $Q = K$, therefore Eq. 2-31 will become:

$$\Delta G_r^o = -RTlnK \qquad \text{Eq. 2-32}$$

Substituting Eq. 2-32 to Eq. 2-31:

$$\Delta G_r = -RTlnK + RTlnQ \qquad \text{Eq. 2-33}$$

Figure 2-15 shows the equilibrium constants, K, of Reaction 2-6 and Reaction 2-7 calculated using Eq. 2-32 and the free energy change from Figure 2-14.

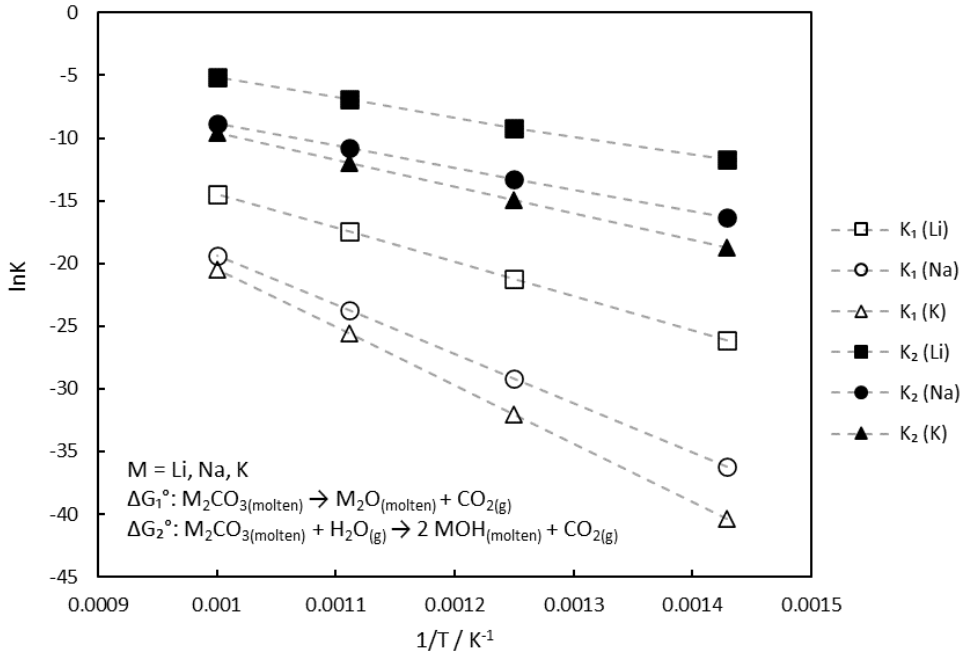

Figure 2-15. The lnK of Reaction 2-6 and Reaction 2-7 versus 1/T. $\boldsymbol{K_1}$ and $\boldsymbol{K_2}$ represent the equilibrium constant of Reaction 2-6 and Reaction 2-7 respectively, when the carbonates and corresponding oxides or hydroxides are molten. $\boldsymbol{K_1}$ and $\boldsymbol{K_2}$ have been calculated using Eq. 2-32 and the $\boldsymbol{\Delta G_1^o}$ and $\boldsymbol{\Delta G_2^o}$ from Figure 2-14.

The equilibrium constants according to Reaction 2-6 and Reaction 2-7 are defined as:

$$K_1 = \frac{a_{M_2O}}{a_{M_2CO_3}} P_{CO_2} \qquad \text{Eq. 2-34}$$

$$K_2 = \frac{{a_{MOH}}^2}{a_{M_2CO_3}} \frac{P_{CO_2}}{P_{H_2O}} \qquad \text{Eq. 2-35}$$

Where,

P_{CO_2}, and P_{H_2O} is the partial pressure of CO_2 and H_2O respectively

a_{M_2O}, $a_{M_2CO_3}$ and a_{MOH} are the activities (dimensionless quantity) of the oxides, carbonates, and hydroxides respectively. Activity is the effective concentration of solutions like ionic solutions, under non-ideal conditions. The activity is being related to the mole fraction of the substance and the activity coefficient γ. Assuming ideal solution, the activity coefficient (account for deviations from ideal behaviour in a mixture) equals to 1.

Assuming equilibrium at the two interfaces of the membrane, the mole faction of O^{2-} and OH^- within the melt can be calculated from Eq. 2-34 and Eq. 2-35 respectively. Knowing that K_1 is four orders of magnitude smaller than K_2, the mole faction of O^{2-} can be neglected and if the mole faction of OH^- at equilibrium is $[OH^-]$, then Eq. 2-35 will become:

$$K_2 = \frac{[OH^-]^2}{[CO_3^{2-}]}\frac{P_{CO_2}}{P_{H_2O}}$$ Eq. 2-36

2.4 Summary and thesis outline

Although recent literature identifies the microstructure complexity of the membranes and the importance of the pore characteristics on the membrane separation performance in terms of CO_2 permeance [50, 157], most of the studies have very little control on the membrane microstructure and the effect of it on CO_2 permeation remains a complex factor. Moreover, an unresolved engineering issue is sealing those membranes at high temperatures or pressures [45]. From a fundamental point of view, trans-membrane leaks can limit the quality of mechanistic/kinetic data that one can extract and can cause lower driving forces which can lead to lower performance. Seals can also interact with the melt which will corrode the seal and potentially change melt composition and therefore the membrane performance and durability. This was the motivation behind the present study.

Therefore, the overall objective of this thesis is to design leak-free membrane systems with controlled pore microstructures to improve the quality of mechanistic/kinetic data that can be extracted from the transport of CO_2 through dual-phase membranes. More specifically, this work focused on designing well sealed membrane systems that do not require any hot seal, which is the main reason for trans-membrane leaks and can often interact with the membrane and the gas phase. The present work attempts to study a wide variety of membrane microstructures and membrane materials. Ceramic membranes with different microstructures were fabricated using several manufacturing techniques, and simple membrane microstructures with controlled size, number and geometry of pores were developed. To show the importance of designing leak-free membrane systems with controlled pore microstructures on the quality of the mechanistic/kinetic data that can be extracted, the effect of CO_2 gas composition and presence of water on both sides of the membrane was studied.

More analytically, membranes in this work ranged from randomly orientated porous structures to well-defined model structures, with multiple interim stages (Figure 2-16). The most complex pore network geometry can be seen in dry-pressed pellets that consist of a random pore network with poorly interconnected pores (discussed in Chapter 4). Membranes fabricated by a phase inversion and freeze-casted method (fabrication methods are analysed in Section 3.1) are highly porous with hierarchically organized ceramic structures and show parallel pore channels with different shapes; pores in freeze-casted membranes show more irregular geometries (honeycomb-like structures or oval-cylindrical structure) than those

produced by phase inversion (cylindrical pores). The complexity of the porous structures of this membranes and lack of mechanistic understanding, was the motivation to develop single-pore membranes with well-defined geometry. The transparent nature of the single crystals used allows the use of microscopy techniques and observation of the infiltration of molten carbonate. Chapter 5 moves on to describe permeation rates in single-pore and multiple-pore single crystal membranes. Model-porous structures can be used to investigate whether CO_2 permeation is controlled by the reaction at the surface of the melt, at the periphery of the holes (triple phase boundary length), or by the diffusion of chemical species, by comparison of permeation rates.

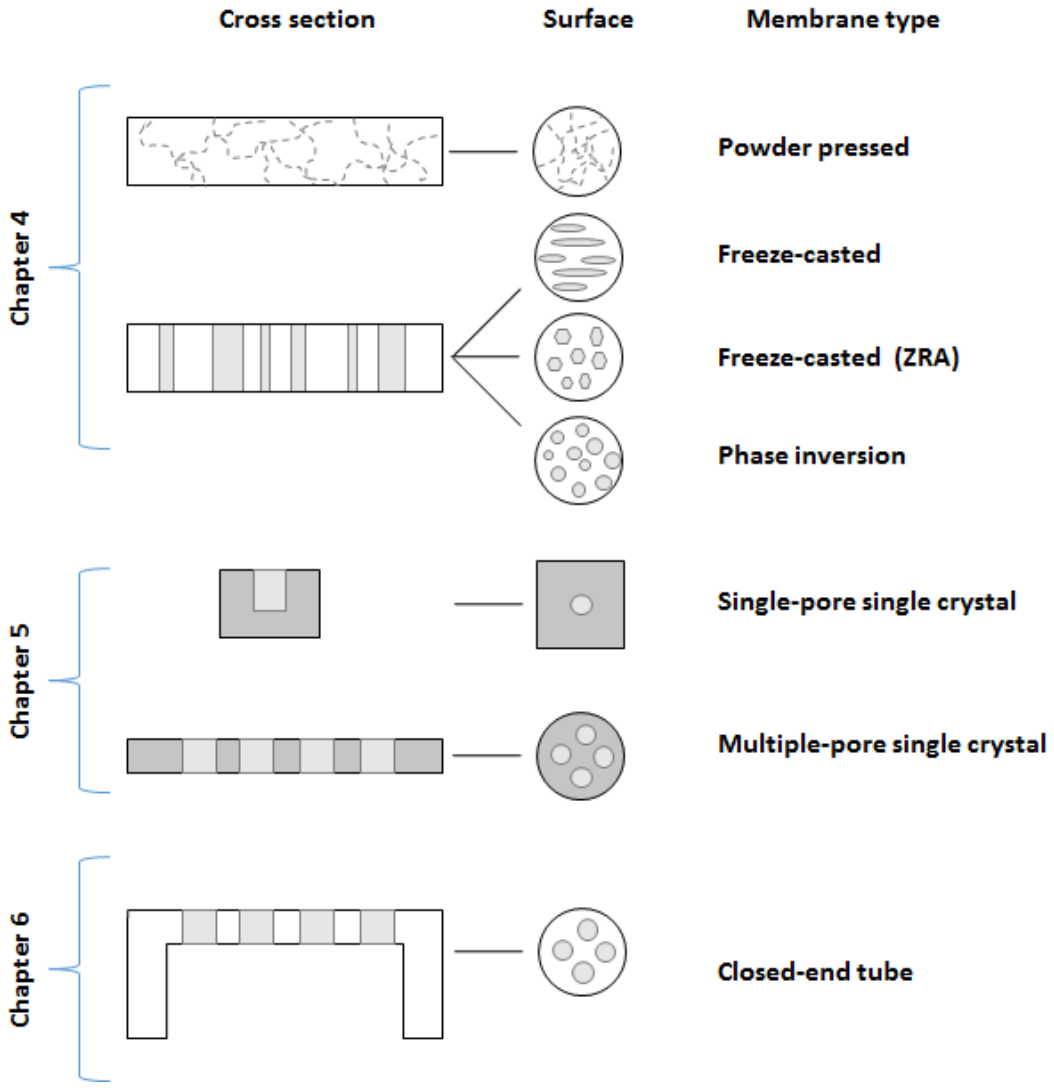

Figure 2-16. Schematics of the different membrane pore microstructures studied at each chapter. Chapter 4 studies membranes with random and parallel pore microstructure fabricated by powder pressed, freeze-casted and phase inversion method. Chapter 5 studies single-pore and multiple-pore single crystal membranes. Chapter 6 studies closed-end tube membranes.

The pores can be tailored with high precision using laser drilling and the geometry, size and number of pores can be controlled. The simplest model membrane would be a support with a single well-defined pore and with the absence of grain boundaries (Figure 2-16). Grain boundaries and grain size can affect the properties of the material, thus, in this work, a single pore has been drilled with a laser to a specified depth on a single crystal. Furthermore, it allows the study of permeation in a highly controlled manner. Chapter 6 moves on to study permeation through multiple-pore polycrystalline membranes with the geometry of a closed-end tube, a unique design that offers a leak-free system.

CO_2 permeation was investigated in dual-phase systems that consist of all the above ceramic supports with an infiltrated ternary eutectic carbonate mixture (32 wt% Li_2CO_3, 33 wt% Na_2CO_3 and 35 wt% K_2CO_3). The preparation of the membranes and the testing procedure can be found in Chapter 3 (Experimental) and the description of the pore geometry of the membranes can be found within the respective chapters.

Chapter 3
Experimental

3.1 Preparation of the membrane supports

3.1.1 Powder-pressed method

Porous YSZ and MgO supports were prepared by mixing approximately 80 wt% of the ceramic powder (YSZ, Pi-kem, 8 mol % yttrium, 5 μm, MgO, Alfa Aesar, 90% <44 μm) with 20 wt% pore former (Starch from corn, Sigma Aldrich, practical grade). Around 1.2 g of the mixtures or Al_2O_3 powder (Aluminium oxide, alpha phase, 99.9% <1 μm) were placed in a 30 mm diameter stainless steel die and pressed to 3 tons for 2 min (model: Atlas™ Series Hydraulic Presses T28, Specac). The YSZ, MgO and Al_2O_3 disks were sintered at 1250, 1400 and 1450 °C respectively for 4 h with heating and cooling ramping rates of 1 °C min^{-1}, and the cornstarch was burnt out at 200 °C for 2 h. These conditions result in disks with approximately 15 mm, 19 mm and 18 mm diameter respectively. The thickness was controlled to 1 mm by polishing the ceramic disks with SiC polishing paper (Screwfix, Titan Wet & Dry Sanding Paper, 600 grit) after sintering. Considering the measured dimensions of the disks and the theoretical densities of the support materials, the total porosity of the samples can be calculated. The total porosity for each supports is given in Chapter 4.2.2 using the theoretical densities of 5.9 g cm^{-3} [158], 3.58 g cm^{-3} [159] and 3.95 g cm^{-3} for the YSZ (8 mol% Y_2O_3), MgO and Al_2O_3 respectively.

The powder-pressed technique is simple to implement; however, the organisation of the porosity is random. The mathematical representation of the tortuosity of those microstructures have been recently given [160], however, the porosity of those supports remains random and difficult to control.

3.1.2 Freeze-casted method

Freeze-casted or ice-templating technique, is an emerging method for the fabrication of hierarchically organized ceramic structures with high porosity [161]. Samples in this work were prepared by Serra and co-workers at the University of Valencia. Details of the fabrication steps were not given and therefore, only some basic principles of this method will be covered here. The basic principle of this method is the freezing of a ceramic slurry and the sublimation of the solvent by freeze-drying at low pressure and temperature. A ceramic slurry

formulation usually comprises of at least 3 components: the ceramic powder, the solvent, and the additives. The ceramic powder is usually in the range 10–50 vol% to maintain a balance between the mechanical stability of the final structure and the formation of connected porosity. Characteristics such as, the grain size, the distribution size, the specific area, or the acidity/basicity of the powder can influence the slurry stability. Up to now, several ceramics and metals were used and shaped with this method [162-165]. The second component is the solvent, which is usually water and results into a vertical ice growing velocity. The last component is the additives which generally consist of a powder dispersant, for controlling the stability and viscosity of the slurry, and a binder which role is to provide sufficient mechanical strength during the freeze-drying step. Additives can also be present in the slurry as structuring agent. The temperature is reduced on one side of the slurry, until the formation of ice crystals. The crystals will grow towards the less cold side as shown in Figure 3-1.

In this work, a zirconium acetate complex (ZRA) was used as a structuring agent in one of the YSZ slurries and resulted to pores with hexagonal shape and a honeycomb-like microstructure.

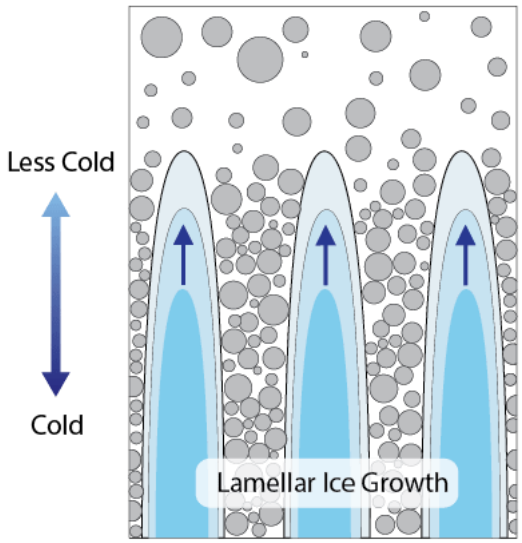

Figure 3-1. Freeze-casted technique; ice crystals (light blue) growing vertically through the suspension, trapping the particles (grey) in the spaces between the crystals. Retrieved from [166].

3.1.3 Phase inversion method

Phase inversion method for membrane fabrication was invented in 1963 by Loeb et al, to fabricate anisotropic cellulose acetate membranes for sea water demineralization [167]. The

formation of the finger-like voids via this method, is originated due to the difference in viscosity between the ceramic suspension and the non-solvent which intrudes into the ceramic suspension [168]. The first ceramic composite membranes were fabricated in 1993 [169] spin-coated poly(phenylene oxide)-ceramic composite membranes and solution-deposited polyimide-ceramic composite membranes. Carbonate-ceramic membranes fabricated by phase inversion were first used for CO_2 separation in 2016 [170].

In this work, YSZ and Al_2O_3 supports were fabricated by phase-inversion method, and the process can be divided into three stages: preparation of the suspension, the immersion and the sintering process [171]. Figure 3-3 shows a schematic of the steps followed to fabricate phase inversion membranes. To prepare the suspension, 39.3 wt% solvent Dimethyl sulphoxide (DMSO, HPLC grade, VWR) was mixed for 30 min with 0.4 wt% dispersant inside a closed container (CITHROL DPHS-50- (MV)) with the use of an ultrasonic bath at 50 °C. The dispersant was used to prevent the formation of ceramic agglomerates. 54.8 wt% aluminium oxide or YSZ powder were then added to the mixture which was milled with 10 mm diameter grinding balls for 48 h (Retsch, PM 100 Ball mills). 5.5 wt% polymer Polyethersulfone (PESf) (Radal A300, Ameco Performance, USA) was then added in the suspension and the suspension was milled for a further 48 h. The speed of the ball mill was set to 250 rpm.

In ceramic membrane fabrication, the polymer acts as a binder, instead of a membrane material, and is only present in small quantities in the suspension. The suspension was then transferred to a gas tight reservoir and degassed under vacuum with stirring until bubbles were no longer visible. The degassed suspension was then poured into a steel mould with the desired shapes (shapes of disks with 1 mm thickness and 30 mm diameter) as shown in Figure 3-2.

Figure 3-2. Steel mould for phase inversion membranes.

The mould was placed horizontally in a bowl filled with deionised water (immersion stage) and was left in water for more than 2 h. A continuous flow of water was maintained across the water bath to ensure that there is a constant supply of fresh water, as it is expected that DMSO will be released during phase inversion. The disks were then removed and dried in air for 24 h (the lab temperature and humidity were not monitored). The dried disks were sintered in air using the following profile: the temperature was increased from room temperature to 600 °C with 2 °C min^{-1} (polymer burnout stage) and held for 2 h, and then to 1250 and 1400 °C for the YSZ and Al_2O_3 support respectively, with 2 °C min^{-1} and held for 4 h. The temperature was then reduced to room temperature with 2 °C min^{-1}. Two morphologies are observed in those membranes; the finger-like voids (channels) and a sponge-like structure which is less than 10 μm in thickness. The sponge-like structure is observed near the top and bottom surface of the membranes. The microstructure of the phase inversion supports is retained during sintering, however, at elevated sintering temperature the sponge-like regions will densify.

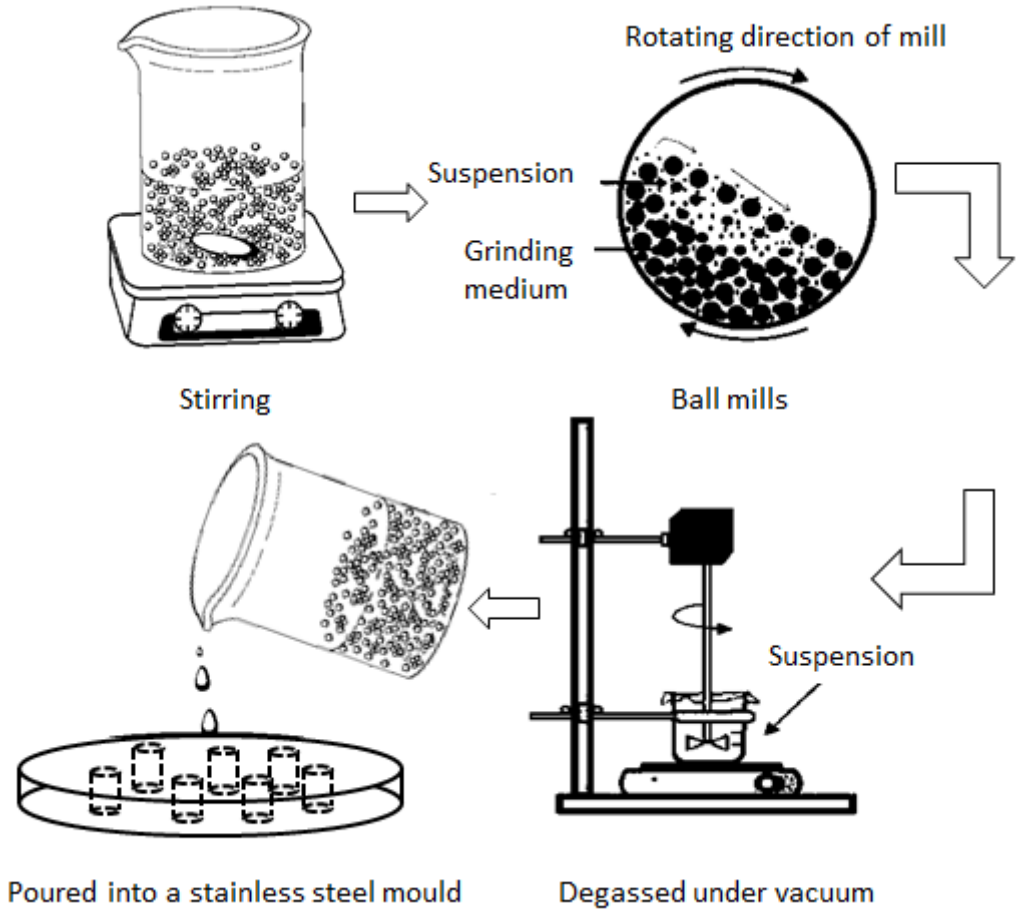

Figure 3-3. Schematic of the multi-stages process to fabricate phase inversion membranes.

Strathmann et al [172] explained the thermodynamic aspect of this type of membrane structure using the ternary phase diagrams (Figure 3-4) for delayed and instantaneous demixing processes. In Figure 3-4, the corners of the triangles represent the three components involved, the polymer, the solvent, and the nonsolvent (water in this case) and any point within this triangle represents a mixture of those components. According to this figure, there is two regions within this system: the region where all components are miscible (one-phase region) and the region where there is a separation between polymer-rich and polymer-poor phases (two-phase region). The tie line connects a pair of equilibrium compositions and the binodal curve represents the liquid-liquid phase boundary.

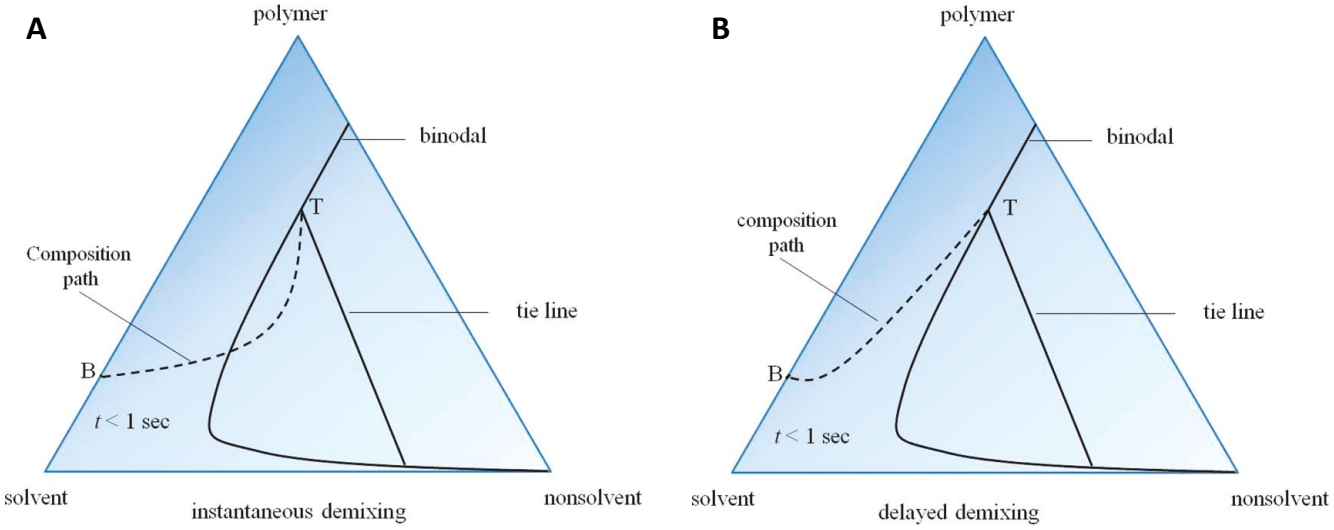

Figure 3-4. Ternary phase diagrams for (A) instantaneous and (B) delayed demixing immediately after the membrane immersion (t < 1 s) inside the water. The instantaneous demixing is achieved on the top surface of the membrane and the delayed demixing is achieved on the bulk of the membrane; T and B represent the top and bottom surface of the membrane layer respectively. Retrieved from [173].

Compositions inside the binodal curve will demix into two liquid phases which are in equilibrium with each other. During the instantaneous demixing and at t < 1 sec (Figure 3-4A), liquid-liquid demixing starts immediately after immersion as the composition path crosses the binodal line. Figure 3-4B represents the compositions directly beneath the top layer of the membrane and it shows that no demixing occurs immediately after immersion and the compositions remain in the one-phase region. After a longer time interval, compositions beneath the top layer will cross the binodal curve and demixing will start. The two different demixing processes described above can result to two different types of phase separation and thus membrane morphology. The formation of the finger-like voids (channels) can be

described in two steps: the initiation and the finger propagation [174]. The points at which the "skin" has been fractured from the initiation points for the growth of the fingers. Once a finger has been initiated (for example through a "skin" fracture due to shrinkage stress in the polymer skin), a fast exchange of solvent and precipitant occurs and the precipitation front moves (finger propagation) by draining the freshly precipitated polymer, at the bottom of the finger, to the side [172]. A bottom skin (<200 μm in thickness) is also observed with those membranes. This can be cause by the adhesion of the suspension to the mould, preventing the polymer at the bottom from moving to the sides of the finger.

The morphology of the membranes as well as the success of the phase-inversion process, can be affected by the viscosity of the suspension and the precipitation rate of the polymer.

3.1.4 Laser drilling

Pores in ceramic supports were tailored with high precision using laser drilling. The geometry, size and number of pores can be controlled. Dense ceramic supports (MgO, Al_2O_3 and YSZ) were initially drilled with laser by Dr Daniel Sola at the University of Zaragoza (preliminary drilling) and then the laser drilling was completed at Laser Micromachining Limited (LML, referred as final drilling in this work) by using a pulsed laser radiation at 532nm (green laser, Nd-YAG) in ambient atmosphere conditions. The laser parameters for the drilling were not given by the user. Due to the Gaussian beam shape (the intensity of the beam drops to $1/e^2$ (≈ 13.5%) of the maximum value with the distance along the beam axis), the drilled holes have a conical shape resulting in holes with larger diameter at the laser incident surface and smaller diameter at the opposite surface. Figure 3-5 shows the 2D Gaussian profile of the laser beam and the intensity distribution at different positions, responsible for the conical shape of the pores produced in the samples of this work.

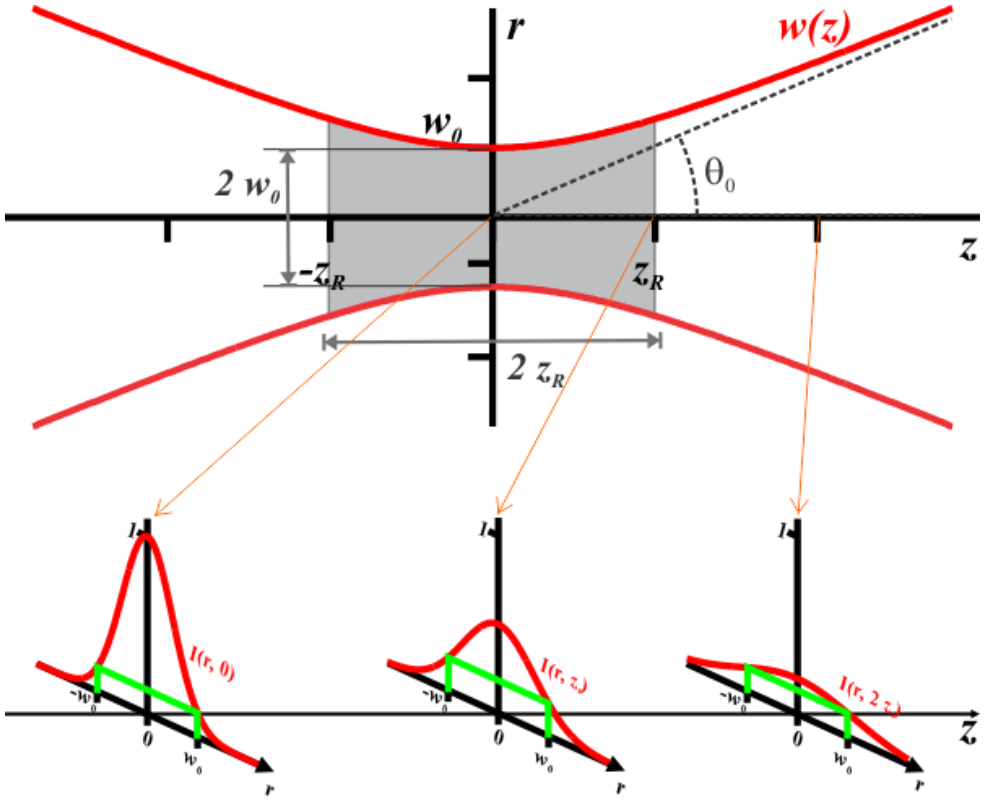

Figure 3-5. A 2D Gaussian profile of the laser beam and the intensity distribution at different positions. *z* is the position along the direction of propagation, *r* is the distance from the beam centre, and *I* is the laser intensity. Retrieved from [175].

3.2 Preparation and infiltration of the carbonate eutectic into the support

A carbonate mixture (eutectic mixture) was chosen as the ionic conducting phase, because of its low melting point and high ionic conductivity. The carbonate mixture contains 32 wt % Li_2CO_3, 33 wt % Na_2CO_3 and 35 wt % K_2CO_3 and each powder was dried at 300 °C for 24 h and grind with a mortar and pestle to reduce the particle size. The mixture was mixed in a mixing container with 3 - 4 balls for at least 30 min. Around 0.6 g of the mixture were placed in a 12 mm in diameter stainless steel die and pressed to 5 tons for 1 min (model: Atlas™ Series Hydraulic Presses T28, Specac).

Synthesis of the disks dual-phase membranes was achieved by placing the carbonate disk on the top of the ceramic supports and infiltrated it into the pores of the support by heating to 450 °C -above the melting point of the carbonates- with heating rate of 1 °C min^{-1} in air. Excess carbonate on the membrane surface was removed using SiC polishing paper (Screwfix, Titan Wet & Dry Sanding Paper, 1200 grit). Many trials were performed on the membranes by infiltrating more than once and measuring the weight of the membrane after each infiltration. Approximately 0.3 - 0.5 g can be infiltrated in the porous disks fabricated by

powder-pressed, freeze-casted and phase inversion method depending on the porosity of each support.

The laser-drilled closed-end tube and multiple-pore single crystal membranes were infiltrated *in situ* under 50%CO_2/N_2 using 0.045 g of pelletised carbonates. Infiltration of the single-pore single crystals will be described in Chapter 5 as it is more complicated, and directly related to the results.

3.3 Analytical techniques

3.3.1 SEM

SEM operates by shooting an electron beam on to the surface of the sample from a powerful electron gun located at the top of the machine. The beam systematically scans across a specified area of the sample and the electrons that reflect off the surface (secondary electrons, Figure 3-6) are captured by a detector, which collects the data to form the SEM image [176, 177].

SEM analysis has been used in this investigation to compare the surface morphology and the cross section of the porous ceramic supports before and after infiltration and to optically compare the surface of YSZ and Al_2O_3 polycrystalline and single crystals before and after drilling. The SEM used in this work was a simple bench-top SEM (Hitachi TM3030) that could offer up to 30,000x magnification.

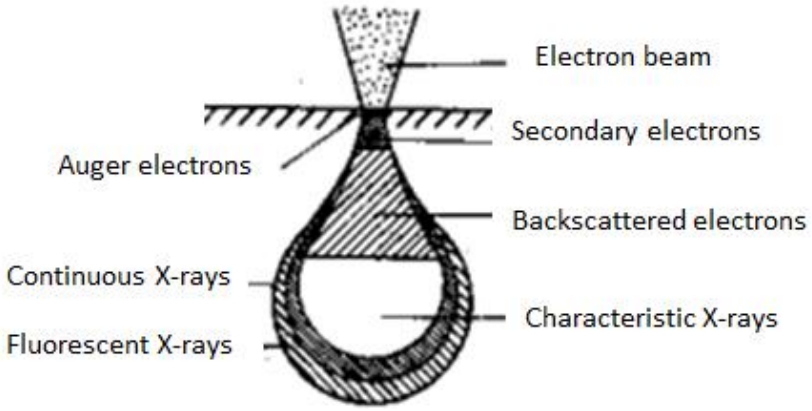

Figure 3-6. The interaction between the electron beam and the atoms in the sample and the different regions from where the various types of signals are produced. Secondary electron detectors are standard equipment in SEM equipment (retrieved from [178]).

3.3.2 Micro-CT

Micro computed tomography (micro-CT) represents a 3D microscopy, where a micro-focus x-ray source illuminates an object and the magnified projection images are collected by a planar x-ray detector which measures the intensity of x-rays transmitted [179, 180]. By rotating the sample, a whole set of such two-dimensional projections can be acquired, and the computer synthesizes virtual cross section slices to a 3D reconstruction.

In this work, micro-CT was used to characterise the geometry of the pores drilled in the Al_2O_3 closed-end tube membrane. The surface area of the pores on both surfaces (laser incident surface and opposite surface) and the total pore volume were extracted from the micro-CT image analysis. The micro-CT analysis was conducted at Manchester University at the Henry Moseley X-ray Imaging Facility.

3.3.3 Wettability studies

Wettability studies involve the measurement of contact angles, which shows the degree of wetting when a liquid and solid interact. Wetting phenomena studies give information on the surface and interfacial energies of the materials or materials systems used. Each system (gas-liquid-solid phase) has a unique equilibrium contact angle [181, 182].

Figure 3-7 shows the different degrees of wetting of a liquid drop on a surface. The contact angle decreases with the increase of the wettability.

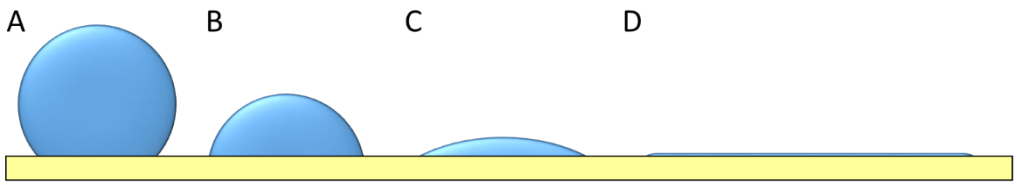

Figure 3-7. Different degrees of wetting. (A) Low wettability (contact angle $90° \leq \theta < 180°$), **(B)** and **(C)** show high wettability (contact angle $0° \leq \theta < 90°$) and **(D)** shows complete wetting (contact angle $\theta = 0°$).

Young's equation and work of adhesion

As first described by Thomas Young [183], the equilibrium contact angle of a liquid drop on an ideal solid surface is defined by Young's equation (Eq. 3-1):

$$\gamma_{SV} - \gamma_{SL} = \gamma_{LV} \cdot cos\theta \qquad \text{Eq. 3-1}$$

Where γ_{SV} , γ_{SL}, and γ_{LV} is the solid-vapor, solid-liquid and liquid-vapor, interfacial energies, respectively, and θ is the contact angle.

In 1869, Athanase Dupre [184] defined the work of adhesion for two immiscible liquids in contact as the free energy difference between two phases a and b in contact in equilibrium and two phases separate in equilibrium in vacuo with Eq. 3-2:

$$W_{ab} = \gamma_a + \gamma_b - \gamma_{ab} \quad \text{Eq. 3-2}$$

where the subscripts a and b describe the two condensed phases.

By substituting Eq. 3-1 into Eq. 3-2 and when a or b is a solid, the work of adhesion can be calculated by Eq. 3-3:

$$W_{ab} = \gamma_{LV}(1 + cos\theta) \quad \text{Eq. 3-3}$$

This indicates that the contact angle is directly related to the strength of the adhesion between liquid and solid in the same gas atmosphere and suggests that contact angle measurements can be used to estimate adhesion energies. The larger the value of W_{ab}, the more easily the liquid wets the solid and the stronger the bonding at the interface of the liquid and the solid.
The surface energy of a substrate can be quantitatively determined from the interactions between the surface and a series of probe liquids of different (and known) interfacial properties. As reported in literature (Table 3-1), the surface energy of Al_2O_3 is higher that the surface energy of YSZ. Knowing that a liquid will wet a solid when its surface energy is lower than the surface energy of the solid, it can be said that the substrates with low surface energy are more easily wet out than substrates with high surface energy.

Table 3-1. The temperature dependence of the surface energy of the ceramic oxides.

Oxides	**Surface energy, γ_{SV} J m^{-2}**	**References**
Al_2O_3	2.559 - 0.784 x 10^{-3} T	[185]
YSZ-8 mol%	1.927 – 0.428 x 10^{-3} T	[186]

Contact angle measurements with ImageJ

The contact angles of the carbonates with the supports were measured with LB-ADSA plugin for ImageJ. The LB-ADSA is a manual technique of drawing an ellipse onto a cross-sectional image of a drop to estimate the circularity. This technique is based on fitting the shape of the experimental drop to a theoretical drop profile according to the Young-Laplace equation of

capillarity, using surface / interfacial tension as an adjustable parameter. The best fit identifies the correct surface / interfacial tension from which the contact angle can be determined by a numerical integration of the Young-Laplace equation based on the analysis of the geometric characteristics of a liquid drop. The drop is usually not spherical resulting in two or more different radii of curvature. The Young-Laplace equation for this case is given by:

$$\Delta P = \sigma \left(\frac{1}{R_1} + \frac{1}{R_2}\right) \quad \text{Eq. 3-4}$$

Where, ΔP is the hydrostatic pressure difference across the air–liquid interface, σ is the surface tension and R_1 and R_2 are the two principal radii of curvature of the drop.
In this study, the contact angles of the carbonate eutectic mixture on YSZ and Al_2O_3 single crystals under different gas atmospheres were measured and the results are given in Chapter 5.

3.3.4 Hg porosimetry

Mercury porosimetry is used to measure pore size, volume, distribution, density, and other porosity-related characteristics of a material [187-189]. Mercury is a non-wetting liquid for most substances, and it must be forced to penetrate pores by the application of external pressure. The pressure required to intrude mercury into the pores of the sample is inversely proportional to the size of the pores and the size distributions can be generated using the Washburn equation (Eq. 3-5):

$$D = \frac{1}{P} 4\gamma \cos\varphi \quad \text{Eq. 3-5}$$

Where, D is the pore diameter, P is the applied pressure, γ is the surface tension of mercury and φ is the contact angle between the mercury and the sample.

This equation assumes that the pores are cylindrical and the volume of mercury penetrating the pores is measured directly as a function of the applied pressure. The real shape of the pore is however quite different, and this assumption can lead to significant errors.

As shown in Figure 3-8, the sample is loaded into the penetrometer, which is sealed and evacuated to remove air and moisture. The penetrometers cup is then backfilled with mercury and pressure is applied to force the mercury to penetrate the pores of the sample.

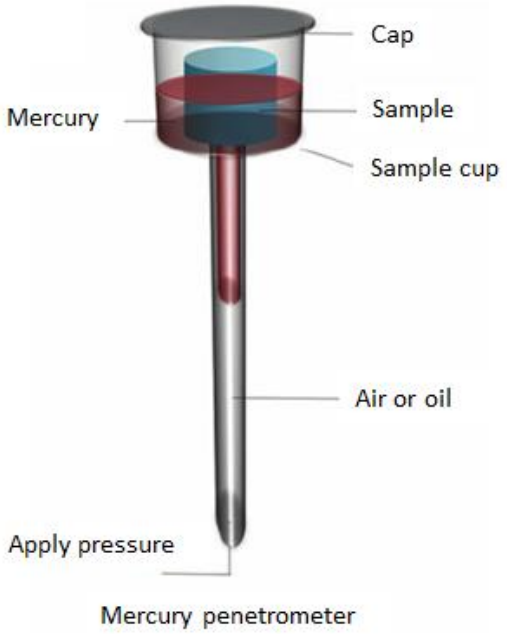

Figure 3-8. Schematic of the mercury penetrometer. External pressure is needed to force the liquid into the pores of the sample. Retrieved from [190].

3.3.5 Raman spectroscopy

Raman spectroscopy is a spectroscopic technique which uses a monochromatic light, usually from a laser, which interacts with molecular vibrations and due to this interaction, the scattered light changes frequency [191]. The frequency changes can give information about the vibrational, rotational, and other low-frequency modes in the system [192]. For a quantitative analysis of Raman spectra, the concentration of species is related to the Raman intensities and areas of the corresponding peaks. The quantitative analysis of Raman spectroscopy is based on Placzek's polarizability theory [193, 194] as given by Eq. 3-6

$$A_i = I_0 \sigma_i N_i \eta_i \qquad \text{Eq. 3-6}$$

Where, A_i, is the integrated peak area of the Raman peak for the active specie i, I_0, is the irradiance of the sample, σ_i, is the cross section of the Raman scattering of a specie i at a certain wavelength of the exciting source, N_i, is the number of molecules of i present in the scattering volume and η_i, is the instrumental efficiency.

In situ Raman measurements in this work, were conducted in a thermostat set-up (high temperature cell described in Chapter 5.2) with a large focal length microscope objective 50x. The Raman was excited using the 514.5 nm line of an Ar^+ laser and CCD detection. This was only a preliminary work and therefore the results of this study will be presented in Appendix D and some findings will be discussed in Chapter 5.

3.4 Gas analysis

3.4.1 Quadrupole Mass Spectrometer (QMS)

A mass spectrometer is a gas analysis technique that ionises the atom or molecule by knocking one or more electrons off to give a positive ion [195, 196]. The ion signal is then plotted as a function of the mass-to-charge ratio (m/z). In a quadrupole mass spectrometer, ions are introduced with a small velocity component in the axial direction into the set of four conducting rods arranged in parallel, creating the quadrupole field. The electromagnetic field deviates the ions depending on their m/z value. The specifications of the mass spectrometer used in this work are shown in Table 3-2.

Table 3-2. Technical specifications of Mass Spectrometer.

RC Quadrupole Mass Spectrometer	
Type	HIDEN, HALO 100-RC
Mass range	1-200 amu
Detector type	Faraday/Secondary electron multiplier (SEM)
Filament	Oxide Coated Iridium
Ion source	Direct inlet high pressure source
Minimum detectable limit	1 ppm

3.4.2 IR CO_2/H_2O analyser

The IR CO_2/H_2O analyser is an infrared gas analyser measuring the absorption of the IR energy as the gas travels through the optical path. The concentration measurements are based on the difference ratio in the IR absorption between the sample and the reference signal. The infrared gas absorption in the reference and sample channels are measured in a single path using narrow band optical filters. The CO_2 and H_2O signal are corrected for the temperature and pressure using a ratiometric computation and the signal is converted to a mole fraction in air given in μmol CO_2 per mole of air (ppm), and mmol H_2O per mole of air (mmol/mol).

Figure 3-9 shows the schematic of the IR CO_2/H_2O analyser used in this work (LI-COR, LI-840A). The broad band IR source is mounted in a parabolic reflector to collimate the light and concentrates the energy reaching the detector. To further increase energy transmission, the reflector and optical path are gold plated. The pyroelectric detector operates based on thermal energy received and is illuminated only by the wavebands of interest due to the narrow band

optical filters. This allows the determination of CO_2 and H_2O concentrations in the presence of other infrared absorbing gases. The calculation of the CO_2 and H_2O concentration depends on both pressure and temperature in the optical path, and therefore, the pressure is measured with an in-line pressure transducer and the temperature is maintained by a thermostat at approximately 50 °C. Two heating elements are used as thermal sources in both the source and detector housing. It is important to mention, that it is assumed that temperature of the gas will equilibrate to the optical bench temperature by the time it enters the optical path.

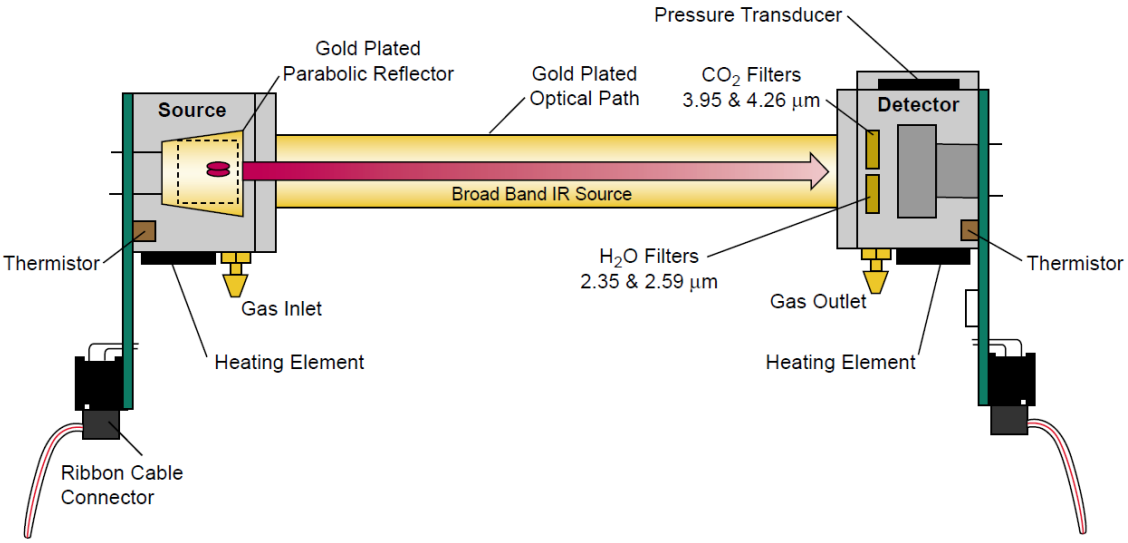

Figure 3-9. Schematic of the IR CO_2/H_2O analyser (LI-840A optical bench). Retrieved from [197].

The specifications of IR CO_2/H_2O analyser used in this work are shown in Table 3-3.

Table 3-3. Technical specifications of IR CO_2/H_2O analyser (LI-840A optical bench).

IR CO_2/H_2O analyser		
Type	Non-Dispersive Infrared	
Maximum Gas Flow Rate:	1000 mL min^{-1}	
Internal Optical Cell Volume:	14.5 mL	
	CO_2	H_2O
Measurement Range	0-20,000 ppm	0-60 mmol mol^{-1}
Sensitivity	To water vapour: < 0.1 ppm CO_2/mmol mol^{-1} H_2O	To CO_2: <0.0001 mmol mol^{-1} H_2O /ppm CO_2
Accuracy	>1.5% of reading	>1.5% of reading

Total Drift	at 370 ppm: <0.4 ppm $°C^{-1}$	at 10 mmol mol^{-1}: <0.009 mmol mol^{-1} $°C^{-1}$

3.4.3 Gas Chromatograph

A gas chromatograph (GC) contains a narrow column, and the different chemical constituents of the gas stream pass through this column with a carrier gas at different rates, depending on their various chemical and physical properties and their interaction with the specific column filling [198-200]. The chemical constituents of the gas steam exit the column at different times (*retention time*) and they are detected and identified electronically. The order or retention time can be adjusted by changing the carrier gas flow rate, column length and the temperature. A "make-up" gas is also used to sweep components through a detector to minimize band broadening. In this work, the carrier and make-up gas were argon and the detector was a thermal conductivity detector (TCD), which contains a heated filament with an applied current. As the gas stream passes through the cell, a change in the filament current occurs and this change is compared against the current in a reference cell. The column used in this work was a ShinCarbon ST material (Restek) with dimensions 2 m x 1 mm ID micropacked, which could separate CO_2 from N_2 at different temperatures and the GC was a 3800 GC model from Varian.

3.5 Permeation experiments

3.5.1 Testing setup

All disk samples from Chapter 4, were sealed on an alumina tube with 12 mm OD and 8 mm ID. The ID of the tube is restricting the permeation area of the pellet and therefore, the active permeation area will be 0.5×10^{-4} m^2 with the assumption that the sealant does not reduce this area. The first step of the sealing process was to apply a high temperature commercial silver sealant (FuelCellMaterials, silver ink AG-1, 73.8 wt%) on the ring of the alumina tube, to place the sample on the top of the tube (preferable centred) and press firmly. The second step of the sealing process was to apply a high temperature alumina based ceramic sealant (Resbond 940 LE) with 2 drops of thinner between the membrane and the alumina tube. The last step was to apply a very thin layer of thinner around the alumina paste with a brush. For each step, the sealant was allowed to dry in air for 24 h at room temperature. The alumina tube is then sealed to the base of the reactor with the use of high-vacuum silicone grease (Dow Corning, Sigma-Aldrich). For the closed-end tube membranes, only one seal is required

at the open end of the tube. The tube is sealed with the high-vacuum silicone grease in a stainless-steel holder which is screwed into the stainless-steel base of the reactor. The difference in sealing between the closed-end tube membranes and disk membranes are shown in Figure 3-10.

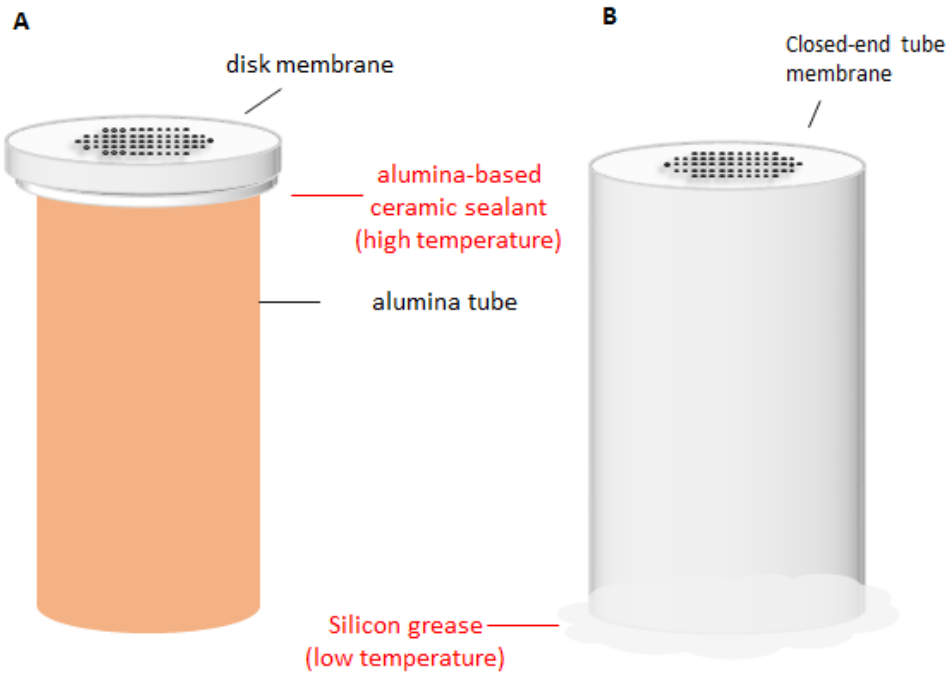

Figure 3-10. Sealing disk membranes and closed end tube membranes. (A) Disk membranes with the use of a high temperature sealant and **(B)** closed-end tube membranes with the use of a low temperature sealant.

Figure 3-11 shows the membrane reactor used for CO_2 permeation experiments with pellets and closed-end tube membranes operated at atmospheric pressure. Three alumina tubes of 3 mm diameter are used for the feed and permeate-side inlet gas streams and the thermocouple (RS Components, Pro K Type Thermocouple, RS 787-7793). The system (3 mm alumina tubes and membrane) is enclosed in a quartz tube which is sealed with an O-ring on the stainless-steel base of the reactor. The reactor comprises of two chambers: the feed-side and permeate-side chamber, which are enclosed by the dual-phase membrane tube and quartz tube respectively. The volumes of the two chambers are around 12 cm^3 and 250 cm^3 respectively. The residence time distribution (Figure 3-12) for the two chambers was determined experimentally by switching between N_2 and Ar on both chambers. Before each switch, it is considered that the inlet and outlet partial pressures have become equal. If there are no dead or stagnant zones within the reactor, then the residence time distribution determined in Figure 3-12 should be equal to the theoretical residence time which can be

calculated from the volumetric flowrate and chamber volume. The mole fraction of the molecules leaving the system can be characterised by an exponential relationship with time [201]. By considering the theoretical and experimental residence time distribution, it can be reasonably concluded that the membrane is exposed to the outlet conditions from each chamber. The reactor designed for the closed-end tube membranes is larger resulting in volumes of 29 cm^3 and 200 cm^3 for the feed-side and permeate-side chamber respectively. The residence time distribution of both chambers was similar to the one shown in Figure 3-12 and therefore, it is not shown here.

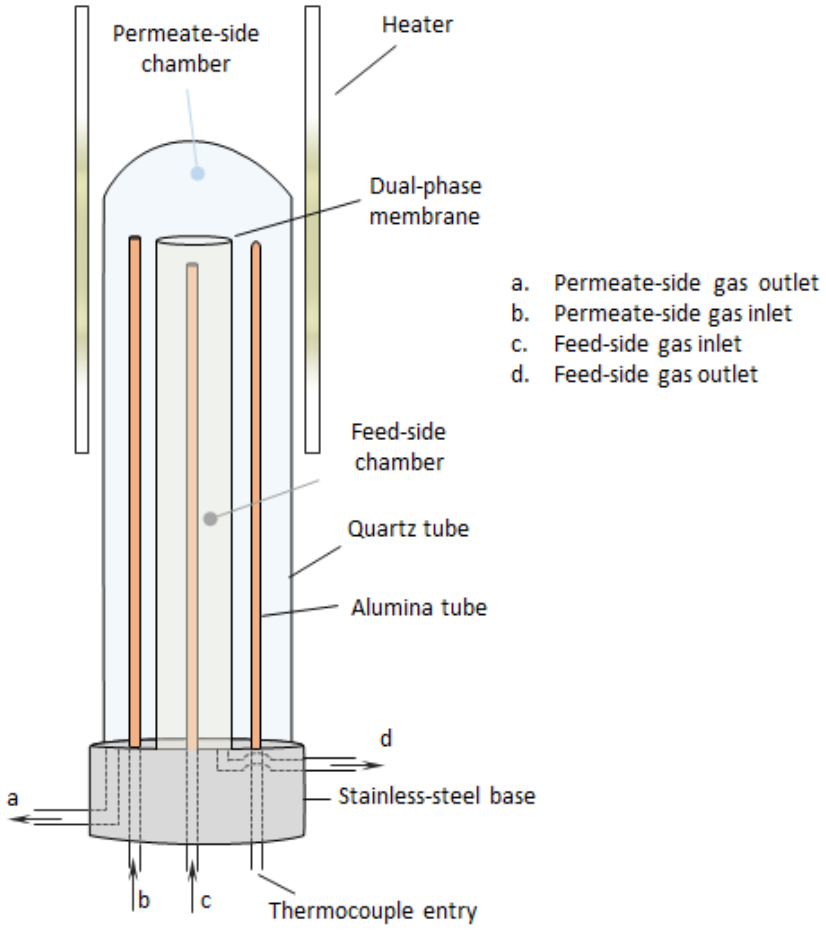

Figure 3-11. Membrane reactor for permeation experiments. Two chambers: feed-side and permeate-side chamber enclosed by the dual-phase membrane tube and quartz tube respectively.

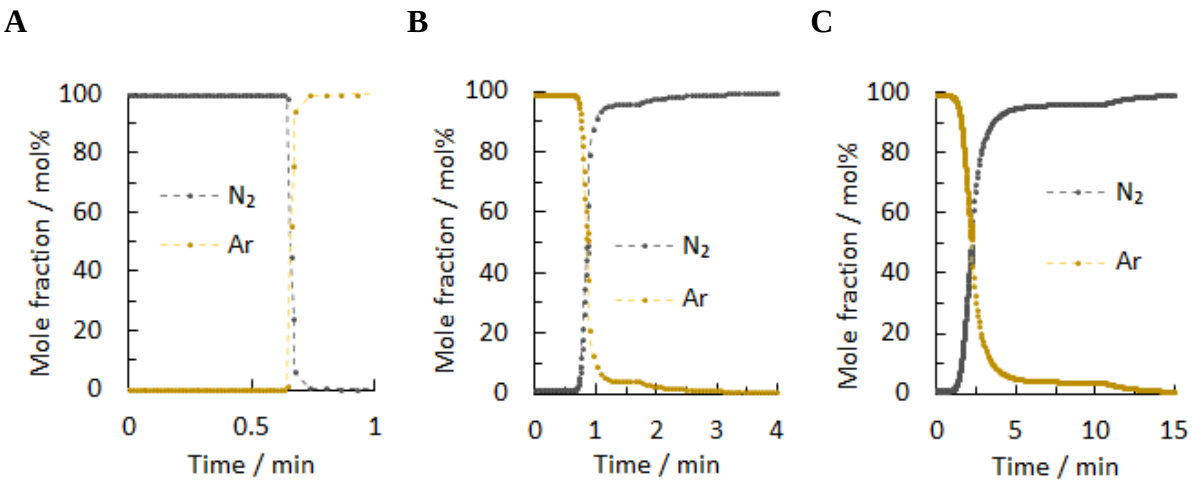

Figure 3-12. Residence time distribution of N_2 and Ar in the membrane reactor. The residence time **(A)** when bypassing the reactor (only tubing), **(B)** in the feed-side and **(C)** the permeate-side chamber. The flows were maintained at 30 ml min^{-1}.

The flow system was adjusted depending on the experimental conditions needed. A simplified flow system used for most of the experiments is shown in

Figure 3-13. Mass flow controllers were used to deliver the gas. It was observed that they may drift over time from their calibration point and therefore regular calibrations were carried out and most of the gases were ordered as mixtures. For the downhill experiments in dry gas streams 50% CO_2/N_2 (cylinder 1) and Ar (cylinder 3) were fed to the feed-side and permeate-side chamber respectively. For the downhill experiments in humidified gas streams, the streams 50% CO_2/N_2 or Ar, (cylinder 5) respectively are humidified by passing through a water bath before being delivered to the reactor. For the uphill experiments, 409 ppmCO_2/20%O_2/N_2 (on a dry basis, cylinder 2 and 4) were fed to both feed-side and permeate-side chamber as a dry and humidified gas stream respectively. For the humidified gas streams, the compositions on a dry basis are going to be used for the description. Finally, for the uphill experiment with humidified gas streams on both sides of the membrane, 409 ppmCO_2 / 20%O_2 / N_2 with different water content (0.6% H_2O and 3.5% H_2O) were fed to feed-side and permeate-side chamber respectively.

The water content in the humidified gas streams were controlled using water baths (Grant, R2, GD100). 0.6% H_2O in the gas stream was achieved using ice in the water bath (maintaining the temperature at 0 °C) and 3.5% H_2O was achieved by adjusting the temperature of the water bath to 30 °C. A hygrometer (Vaisala, F2520137) was connected to the water bath outlet to monitor the water-vapour mole fraction (e.g. 3.5% H_2O) in the gas stream. The outlet gases of the feed-side and permeate-side chamber were analysed with two CO_2/H_2O IR

analysers and a GC or a mass spectrometer (depending on the availability in the lab and the type of experiment) usually connected in series. Closed-end tube experiments were always conducted with an IR CO_2/H_2O analyser connected in series with the mass spectrometer (HIDEN, HALO 100-RC) to record N_2 (used to indicate any trans-membrane leaks, described later in Chapter 3.5.3). To prevent condensation of water in the humidified gas streams, silicone rubber heating tapes (Watlow Ltd., series EHG) were used. The heating tapes were connected to a temperature controller with a thermocouple sensor, and the temperature was maintained at 60 °C.

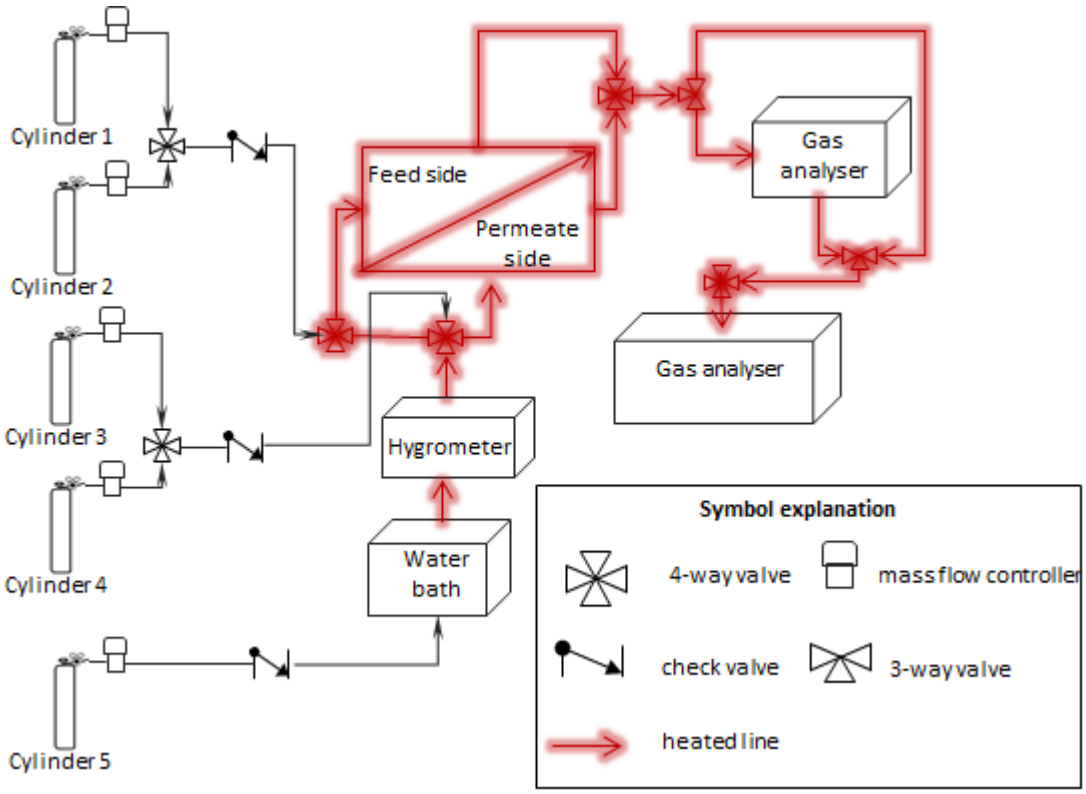

Figure 3-13. Schematic of the flow system used for the membranes. A generic schematic that was adjusted according to the requirements of the specific experiment conducted.

3.5.2 Testing procedure

For the permeation experiments, a flow rate of 30 mL(STP) min^{-1} was used for both feed-side and permeate-side gas streams. Both chambers were operated at atmospheric pressure and all gases were provided by BOC (certified gases, compositions on a molar basis). The heating of the membrane was performed under symmetrical gas conditions in 50% CO_2 /N_2 (apart of the visualisation experiments in Chapter 5, heating procedure is described within the chapter). The system was heated in a temperature programmable split tube furnace (Vecstar,

VST/1150). The temperature of the membrane was varied from 400 to 850 °C with 50 °C increments and a heating rate of 1 - 2 °C min^{-1}. Gas flow rates were regulated using mass flow controllers (Brooks SLA5850).

The mass spectrometer and GC were calibrated using pure Ar or 400 ppm N_2/400 ppm O_2/Ar. The calibration was performed every 12 h to account for the drift of the detector. The IR analysers and GC were calibrated prior to the experiment using a 3-point calibration at 0 ppm CO_2, 400 ppm CO_2 and 1% CO_2. The calibration of H_2O was conducted by the manufacturer using a 3-point calibration at 0, 0.1 and 3.5% H_2O.

During downhill experiments, N_2 was introduced to the feed-side chamber to indicate any trans-membrane leaks and to estimate any CO_2 leak rates, if present. The leak contribution will be described in the next section.

During uphill permeation experiments, switches were conducted between symmetrical (sym) and asymmetrical (asym) operating conditions for a more accurate determination of permeation rates. Under symmetrical conditions dry streams of 409 ppmCO_2 / 20%O_2 / N_2 were fed to both feed-side and permeate-side chamber and under asymmetrical conditions one of the streams or both streams were switched to humidified streams of 409 ppm CO_2 / 20%O_2 / N_2 (concentrations on a dry basis).

There are multiple points in the assembly where air leaks are possible, as there are several connections present in this setup. The leak detection was conducted in two ways: (1) with an electronic leak detector which can detect leaks of any gas with a different thermal conductivity to air and (2) by creating a positive pressure in the setup and observing the pressure of it with time by using a pressure gauge. If leaks are present, the electronic leak detector will be activated, and the pressure displayed on the pressure gauges will decrease.

3.5.3 Data analysis and interpretation

For the downhill experiments, the permeation rates were calculated using the flow rate (Q) of the permeate-side gas and the average increase of CO_2 mole fraction (or H_2O under humidified conditions) in the permeate-side outlet stream at steady state. The mole fractions were taken once steady carbon dioxide levels are reached and do not change more than 1% within 0.2 h (sampling rate 10 s). N_2 was present on the feed-side gas and was used as a leak indicator to extract leak contributions to CO_2 permeation rates. If the mole fraction of N_2 was more than 10% of the mole fraction of CO_2 the experiments were terminated and the CO_2 permeation rate was not taken into account for further calculations. N_2 was selected because it

is an inert gas and due to its similar kinetic diameter to CO_2 (3.64 Å N_2 and 3.3 Å CO_2 [202], related to the mean free path of molecules in a gas). The corrected CO_2 permeation rate (PR), assuming that the diffusion through the leaks is determined by the Knudsen diffusion mechanism, was determined as:

$$PR = \left(x''_{CO_2} - x''_{N_2} \frac{x^{feed}_{CO_2}}{x^{feed}_{N_2}} \right) \cdot Q \qquad \text{Eq. 3-7}$$

Where the superscripts ^{feed} and $''$ refer to the feed-side inlet and permeate-side outlet respectively.

Trans-membrane leaks can be developed due to several reasons, such as, a failed sealant, a cracked membrane or an empty pore. If 50%CO_2 /N_2 was fed to the feed-side chamber (most of experiments in this thesis), then $\frac{x^{feed}_{CO_2}}{x^{feed}_{N_2}}$ would be equal to 1 and therefore the CO_2 permeation rates would be:

$$PR(downhill) = \left(x''_{CO_2} - x''_{N_2} \right) \cdot Q \qquad \text{Eq. 3-8}$$

CO_2 permeation rates for uphill experiments in Chapter 6, were calculated from the difference in CO_2 mole fraction at steady state in the feed-side outlet between a symmetrical condition (sym) and an asymmetrical condition (asym) and the flow rate (Q) as shown in Eq. 3-9, where $'$ refers to feed-side outlet. Under symmetrical conditions, both sides of the membranes are exposed to the same gas phase and under asymmetrical conditions one of the streams is switched to a humidified stream. The permeated CO_2 mole fraction can be calculated from the difference between the symmetrical and asymmetrical CO_2 mole fraction on the opposite side of where the switch was made.

It is also important to mention that uphill experiments presented in Chapter 6 were conducted with the closed-end tube membranes because they were leak-free systems. Therefore, Eq. 3-9 does not include the extraction of the leak contribution.

$$PR(uphill) = \left(x'_{CO_2(sym)} - x'_{CO_2(asym)} \right) \cdot Q \qquad \text{Eq. 3-9}$$

CO_2 mole fractions during asymmetrical conditions are measured on a wet basis (IR analyser readings of the humidified streams in the outlet of the reactor). CO_2 material balance was performed by measuring the outlets of the feed-side and permeate-side gas streams during

uphill experiments. The closure of the CO_2 material balance could be confirmed at steady state and the rate of consumption of carbon dioxide on the feed side was equal to the rate of carbon dioxide evolution on the permeate side at steady state (Eq. 3-10, $'$ refers to feed-side outlet and $''$ to the permeate-side outlet).

$$\overbrace{\left(x'_{CO_2(\,sym)} - x'_{CO_2(asym)}\right)\cdot Q}^{rate\ of\ consumption} = \overbrace{\left(x''_{CO_2(\,asym)} - x''_{CO_2(sym)}\right)\cdot Q}^{rate\ of\ evolution} \qquad \text{Eq. 3-10}$$

Fluxes are calculated by dividing permeation rates with the membrane permeation area, which in this work, is assumed to be the area of the membrane exposed to the feed-side gas (smallest compared to the area exposed to the permeate-side gas). This was determined by the ID of the alumina tube used to seal the membrane and it is approximately 0.5 x 10^{-4} m^2.

Permeances are calculated by dividing the flux with the respective driving force. In this work, permeances were calculated in two ways, by dividing the flux with: (1) the CO_2 partial pressure difference as shown in Eq. 3-11 or (2) with the logarithmic CO_2 partial pressure difference between the two sides of the membranes as shown in Eq.3-12. Approach (1) is the most common reported in literature and it was used to compare membranes exposed to similar CO_2 partial pressures on each side of the membrane (usually for inlets of 50% CO_2/N_2 on the feed side and Ar on the permeate side) and approach (2) has been proposed by other studies [132, 133, 149] assuming that the slowest process is bulk diffusion and was used to compare membranes with significantly different driving forces (mainly in Chapter 5). The latter approach is also used when modified Wagner equation is applied to predict the phase volume ratio that participates to CO_2 permeation.

$$Permeance\ I\ (downhill) = \frac{x''_{CO_2}}{P'_{CO_2} - P''_{CO_2}}\frac{Q}{A} \qquad \text{Eq. 3-11}$$

$$Permeance\ II(downhill) = \frac{x''_{CO_2}}{\ln\left(P'_{CO_2}/P''_{CO_2}\right)}\frac{Q}{A} \qquad \text{Eq. 3-12}$$

For uphill experiments in Chapter 6, the driving force would be negative if only the driving force of CO_2 is considered. Therefore, the driving force is calculated by adding the negative driving force of CO_2 to the driving force of water as shown in Eq. 3-13.

$$Permeance\ I(uphill) = \frac{x'_{CO_2(asym)} - x'_{CO_2(\ sym)}}{\left(P''_{H_2O,asym} - P'_{H_2O,asym}\right) - \left(P''_{CO_2,asym} - P'_{CO_2,asym}\right)} \frac{Q}{A}$$ Eq. 3-13

Chapter 4
Membranes with random and parallel pore network

4.1 Introduction

Dual-phase membranes used in this work consist of a solid phase, which is a porous ceramic support, and a liquid phase, which is a eutectic carbonate mixture undergoing a phase change from solid to liquid at ~400 °C. As described in the introduction of this thesis, this type of membrane is permeable towards CO_2 at temperatures above 400 °C. Despite the widely existing research on CO_2 permeation in dual-phase membranes, there has been little interest in understanding the parameters and mechanisms influencing CO_2 permeation, thus comparing the results of different studies can become difficult.

Recent literature identifies the membrane complexity and the importance of the pore characteristics on the membrane separation performance in terms of CO_2 permeation [50, 157]. In this chapter, the effect of the ceramic porous structures, which serve as supports on dual-phase membranes, for CO_2 permeation will be investigated. Oxygen ionic conductors and non-ionic conductors are fabricated by several fabrication techniques which can affect the porous structure, the geometrical characteristics and tortuosities of those supports. The fabrication techniques chosen in this work, are methods that have been reported in literature [161, 171] and result to porous structures that range from randomly orientated pores to parallel pore networks with different geometries. The membrane separation performance in terms of CO_2 permeance has been studied and compared to the literature data.

4.2 Membrane characterisation

4.2.1 Membrane microstructure

A set of digital and SEM images presenting the surface morphology and the cross section of the YSZ porous supports, obtained by different fabrication techniques, is given in Figure 4-1. The supports were fabricated by four different techniques: powder pressed, freeze-casted, freeze-casted with a zirconium acetate complex structuring agent (ZRA) and phase inversion (all techniques are described in Chapter 3). The pore sizes, porous organization and thickness of the ceramic walls strongly vary between samples. The most complex pore network geometry can be seen in powder pressed pellets (Figure 4-1A and A') that consist of a random pore network with poorly interconnected pores and high tortuosity. Pore diameters are smaller

than 5 μm. Hierarchically ordered and vertically aligned pores (channels) can be obtained by the freeze-casting technique (Figure 4-1B, B', C and C'). Freeze-casted supports show channels with a rectangular shape (Figure 4-1B and B') and the presence of a structuring agent (ZRA) in the initial slurry results to supports with honeycomb-like structure (Figure 4-1C and C'). Finally, phase inversion supports (Figure 4-1D and D') contain of two layers with different pore characteristics; a layer of cylindrical channels and a thin layer (~5 μm thickness) of random pores. Al_2O_3 and MgO supports fabricated by the above techniques showed similar porous structures with the YSZ supports for the respective fabrication techniques, and therefore the SEM images of those supports are not shown here.

Figure 4-2 shows the cross-section SEM images of the freeze-casted supports before and after infiltration. After infiltration, carbonates (shown in dark grey) have filled most of the channels and the pores of the ceramic walls. Some dead-end channels are present in the freeze-casted supports.

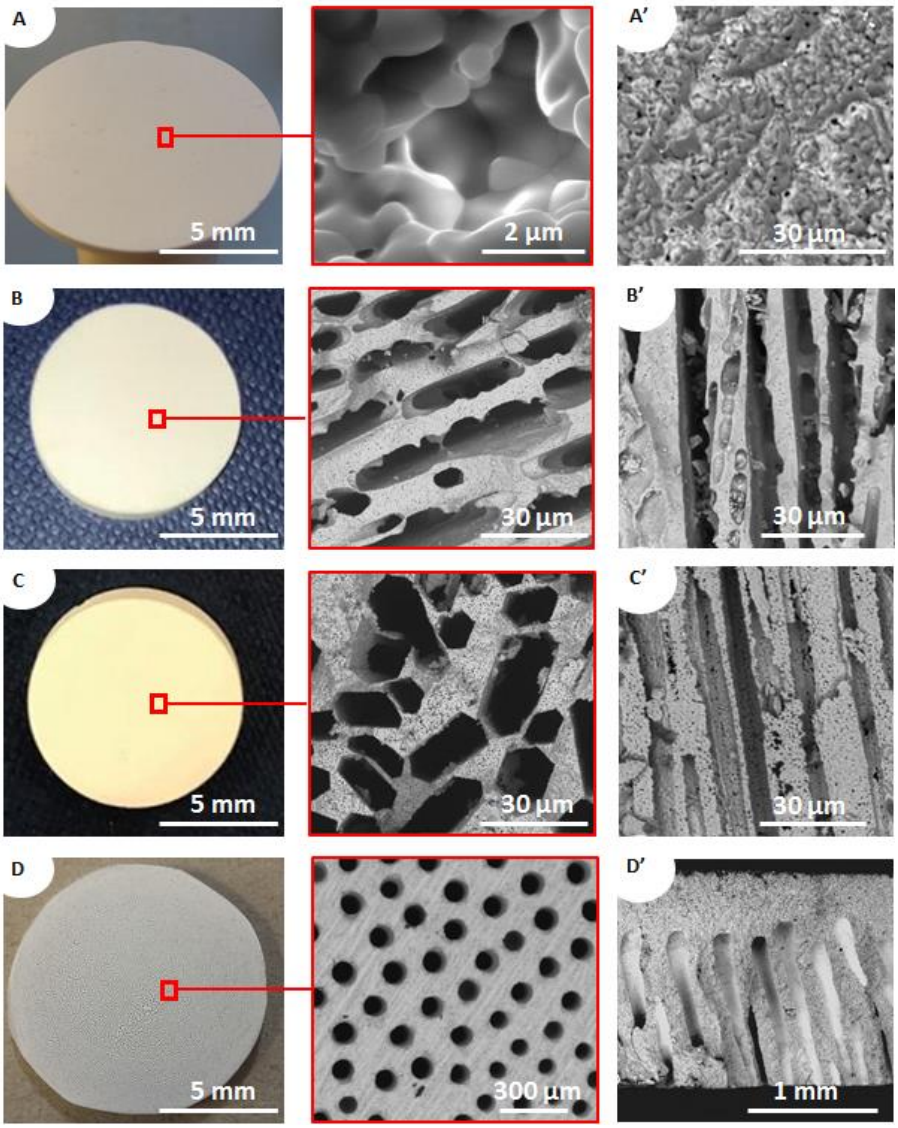

Figure 4-1. Digital and SEM images of the surface and cross section of YSZ porous supports. Supports were fabricated by **(A)** powder pressed, **(B)** freeze-casted, **(C)** freeze-casted with a zirconium acetate complex (ZRA) structuring agent and **(D)** phase inversion method. **(A')**, **(B')**, **(C')** and **(D')** refer to the cross section of those membranes respectively.

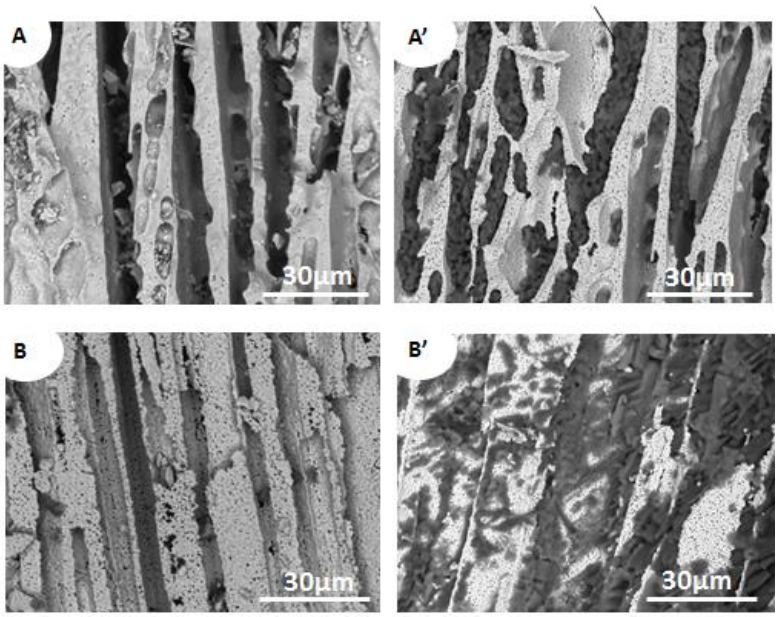

Figure 4-2. SEM images of the cross section of YSZ freeze-casted porous supports before and after infiltration. (A) and **(B)** are the YSZ freeze-casted and YSZ freeze-casted (ZRA) supports respectively and **(A')** and **(B')** refer to the same supports after infiltration.

4.2.2 Membrane porosity characteristics

The characteristics of the membrane pore structures (pore size, pore size distribution, pore density) are important to be measured, since such characteristics govern the permeation performance of membranes. High porosities are associated with low mechanical strength but can also have an impact on CO_2 permeation rates.

Figure 4-3 shows the mercury intrusion curves of the YSZ porous samples. The powder pressed support (Figure 4-3A) shows a very narrow pore-size distribution at the diameter of 3 μm. The freeze-casted support (Figure 4-3B) shows pore sizes from 5 to 15 μm (with an average pore size of around 9 μm) and the freeze-casted support with the structuring agent (Figure 4-3C) shows a wider range of pore sizes from 1 to 80 μm (with an average pore size of around 10 μm). Most of the channels in the phase inversion supports (Figure 4-3D), range from 60 to 100 μm diameter and the random pores are smaller than 1 μm. At this point, it should be mentioned that the pore diameters measured by mercury porosimetry are not truly indicative of the true pore diameter because of the different pore geometries discussed in Chapter 4.2.1 (rectangular shapes, honeycomb-like structure, irregular shapes). Moreover, the porosity of the samples can be changed by a variety of processes due to the applied pressure during mercury porosimetry such as deformation or fracture porosity.

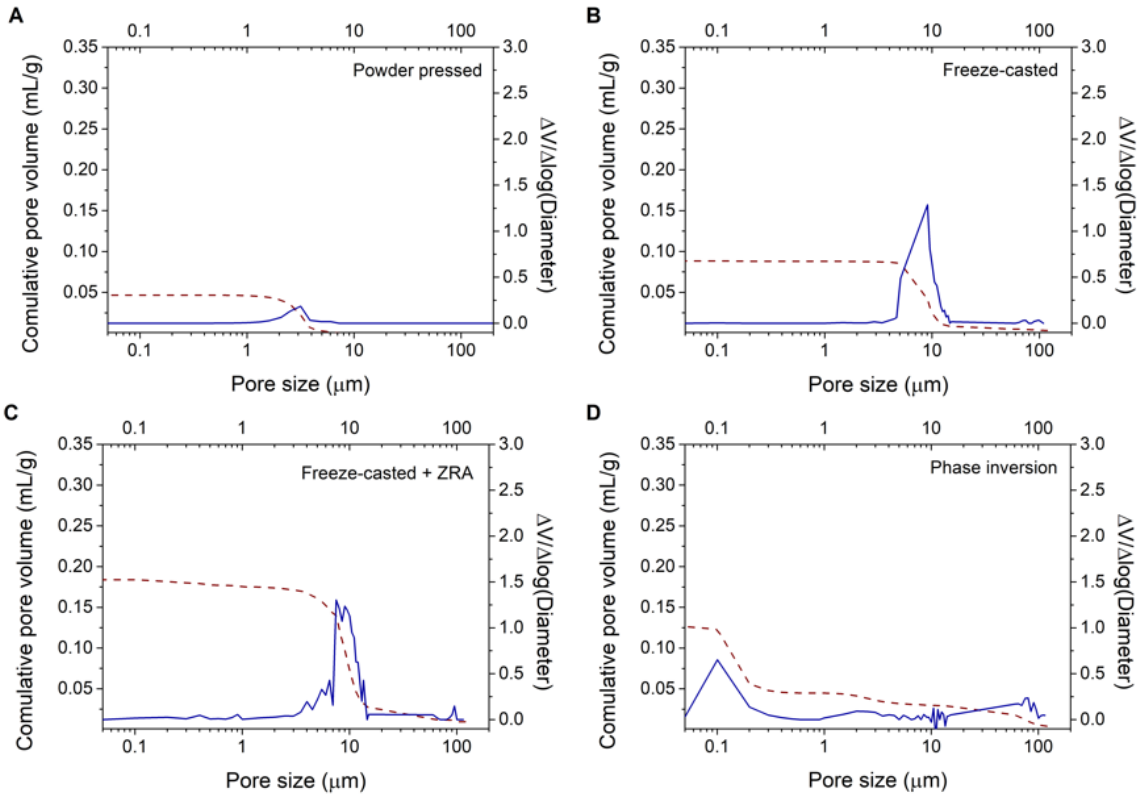

Figure 4-3. Cumulative pore size distributions and pore volume distributions for YSZ porous supports, as measured by mercury intrusion porosimetry. Supports were fabricated by **(A)** powder pressed, **(B)** freeze-casted, **(C)** freeze-casted with a zirconium acetate complex (ZRA) structuring agent and **(D)** phase inversion method.

The total and open porosity of all membrane supports calculated from the measured dimensions and mercury intrusion method respectively are shown in Table 4-1. The total porosity was calculated as the difference between bulk volume and "skeletal" volume. The bulk volume of the material was determined from consideration of the measured dimensions and the skeletal volume was calculated by dividing the dry weight of the membrane support with the density of the support material. The open porosity is the volume of the interconnected and non-interconnected open pores, into which a liquid can penetrate, as a percentage of the total volume. Approximately 65% of the total porosity is open for most of the supports and only 44% of the total porosity is open for the YSZ freeze-casted support. The open porosities of the non-ionic conducting supports (Al_2O_3 and MgO) are comparable and between the YSZ supports, the freeze-casted (ZRA) membrane is the most porous support.

Table 4-1. Total and open porosity of all the membrane supports calculated from measured dimensions and mercury intrusion method.

Fabrication technique	Sintering temperature, °C	Total porosity (calculated from measured dimensions)	Open porosity (mercury intrusion method)
YSZ support			
Powder pressed	1250	35%	26%
Freeze-casted	1250	54%	24%
Freeze-casted (ZRA)	1250	63%	41%
Phase inversion	1250	52%	37%
Al_2O_3 support			
Powder pressed	1400	55%	30%
Phase inversion	1400	53%	35%
MgO support			
Powder pressed	1350	51%	30%
Freeze-casted	1350	54%	31%

4.2.3 Membrane tortuosity characteristics

The tortuosity is another parameter that can affect the permeability as mentioned in previous chapters. The tortuosity can be defined as the ratio of the mean path or pore length to the membrane thickness. There are no experimental methods to directly evaluate the tortuosity, and, in consequence, it is usually estimated by theoretical equations or empirical models.

As seen by the SEM images, the phase inversion and freeze-casted membranes show aligned channels that run linearly straight through the thickness of the membrane. Therefore, the tortuosity of those channels is expected to be close to 1. However, the existence of some cross-linking pores may exist through the lamellae walls, and this was identified in previous study on vacuum-induced surface directional freezing [203]. In this work, the membrane walls of the phase inversion and freeze-casted may be assumed to be impermeable and the tortuosity to be equal to 1.

In previous work on powder pressed membranes, tortuosity was calculated by correlating the helium permeance data to the following viscous flow and Knudsen equations as shown with the below equations:

$$\frac{Perm}{L} = \alpha + \beta P_{avg} \quad \text{Eq. 4-1}$$

$$\alpha = 1.06 \frac{\varepsilon}{\tau} \frac{r_p}{L\sqrt{RTM_w}} \quad \text{Eq. 4-2}$$

$$\beta = 0.125 \frac{\varepsilon}{\tau} \frac{{r_p}^2}{L\mu RT} \quad \text{Eq. 4-3}$$

Where, $Perm$ is the permeance, L is the support thickness, P_{avg} is the average pressure across the support, ε is the tortuosity, τ is the porosity, r_p is the average pore radius, R is the gas constant, T is the temperature, M_w is the molecular weight of helium and μ is the viscosity of helium.

The tortuosity of different powder pressed substrates in literature was then calculated from the $\frac{\varepsilon}{\tau}$ and was found to be between 2 and 3 [44, 105, 133, 204]. Those values will be used in the below discussion to compare permeances between different membranes.

4.3 Permeation experiments through dual-phase membranes

An example of an experiment conducted to determine permeation rates through dual-phase membranes is shown in Figure 4-4. This figure shows the CO_2 and N_2 mole fraction in the permeate-side outlet of the YSZ-carbonate membrane at temperatures of 700, 750 and 800 °C. In this experiment, the membrane was heated with 0.5 °C min^{-1} and a mixture of 50%CO_2/N_2 was used on the feed side and Ar was used as a sweep gas on the permeate side of the membrane. Membranes used in this work are selective to CO_2 and therefore, any trans-membrane leaks can be a result of a membrane crack, sealant failure or unfilled pores of the support. The gas analysis for this experiment was conducted with a gas chromatographer (Varian 3800 GC). At each temperature, the membrane was given ample time to reach equilibrium, in which mole fractions do not change more than ±10% over a period of 30 min. During heating from room temperature (t = 0 h), CO_2 and N_2 evolution was observed at around 250 °C (t = 8 h), which can be due to the release of the trapped air within the carbonates (infiltration was conducted in air) and the sealant, or due to the burning of the organic compounds within the sealants (Figure 4-4). At the melting point of the carbonates (~400 °C), CO_2 is again evolved from the melt (t = 15 h) until the temperature plateau is reached, which suggests that the composition of the melt is changing during temperature change and may be due to the formation of O^{2-} in the melt through the reaction $CO_3^{2-} \rightleftharpoons CO_2 + O^{2-}$. At steady state the CO_2 mole fraction in the feed-side outlet is measured to be 0.08% at 700 °C and 0.12% at 750 °C, while N_2 mole fraction is below the detectable limit of the

instrument which is 0.01%. At 800 °C, CO_2 and N_2 mole fractions are gradually increasing for more than 10 h, indicating the development of trans-membrane leaks. After the development of the leaks, the N_2 and CO_2 mole fractions did not reach a steady value and N_2 mole fraction exceeded the value of 0.02% (more than 10% of the CO_2 mole fraction, criteria for terminating permeation experiments), and therefore the experiment was terminated (Figure 4-4).

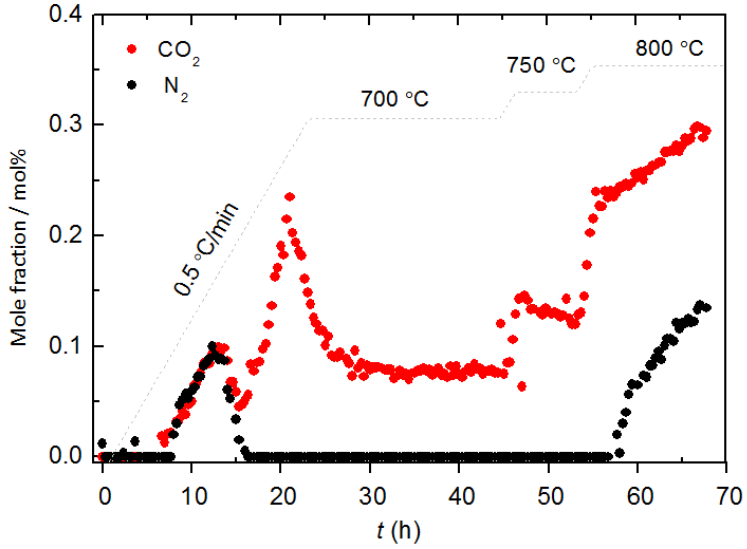

Figure 4-4. Mole fraction of CO_2 and N_2 in the permeate-side outlet against time through a YSZ-carbonate membrane with increasing temperature. The mole fractions of CO_2 and N_2 were measured with a GC and the membrane was fabricated by powder pressed method. Time zero represents the moment the heating starts from room temperature. The feed-side inlet is 50% CO_2/ N_2 and permeate side inlet is Ar.

Permeation experiments were conducted in the same manner as described above for the rest of the membranes and temperatures. After the development of leaks, if the N_2 and CO_2 mole fractions reach a steady value and N_2 mole fraction was below 10% of the CO_2 mole fraction, the permeated CO_2 was calculated by subtracting the measured N_2 mole fraction from the measured CO_2 mole fraction.

4.4 CO_2 permeances through molten carbonate dual phase membranes

It has been seen that the geometrical/physical properties and the chemical structure of the membrane can influence CO_2 permeance and selectivity of a gas through the membrane. Researchers have investigated a variety of oxygen ionic conductive materials, which serve as supports on dual-phase membranes, but this work will only focus on YSZ (8 mol% Y_2O_3) because it is the most common solid oxide fuel cell (SOFC) electrolyte and has been widely studied experimentally in this lab and in literature [43, 55-58]. Non-ionic conductors have

also been studied for comparison, in similar dual-phase membrane systems. With the use of an "inert" support, all mobile species involved in CO_2 permeation, are expected to go through the molten phase and a small amount of oxide may dissolve in the membrane. The non-ionic conductive supports fabricated and studied in this work are MgO and Al_2O_3 due to their durability and the existing knowledge and experience on fabricating porous supports with several techniques using those materials. A variety of fabrication techniques has been developed, such as powder pressing, freeze-casted and phase inversion, resulting in porous supports with several pore characteristics. The fabrication techniques are described in Chapter 3 and the pore characteristics of all supports are described in Section 4.2.

Figure 4-5 shows the CO_2 permeance in logarithmic scale as a function of temperature through (A) YSZ-carbonate membranes and (B) MgO-carbonate and Al_2O_3-carbonate membranes studied in this project (unfilled symbols) and for references: [43, 55, 57] (to the best of found knowledge these are the only references in literature on YSZ-carbonate and Al_2O_3-carbonate membranes using a ternary carbonate mixture). Some porosity fluctuations between the samples fabricated by the same fabrication technique can cause some uncertainty to the results and therefore the experiments were repeated 2-3 times with a fresh sample. Error bars, that correspond to the associated standard deviations over the average of the permeances calculated in 2 - 3 separate experiments, are smaller than the symbols and therefore, they are not shown here. As the membrane thickness can affect the diffusional path length, supports of 1 mm thickness are used in this work, which is significantly higher than the thickness used in references [43, 55, 57], where they use supports with thicknesses of 10 μm, 200 - 400 μm and 200 - 500 μm respectively. The inlet gas on the feed side of the membrane was a mixture of CO_2 with an inert gas in a 1:1 volume for all membranes. The inlet gas on the permeate side was an inert gas for all membranes excluding Wade's work [55], where they used 1%CO_2/Ar.

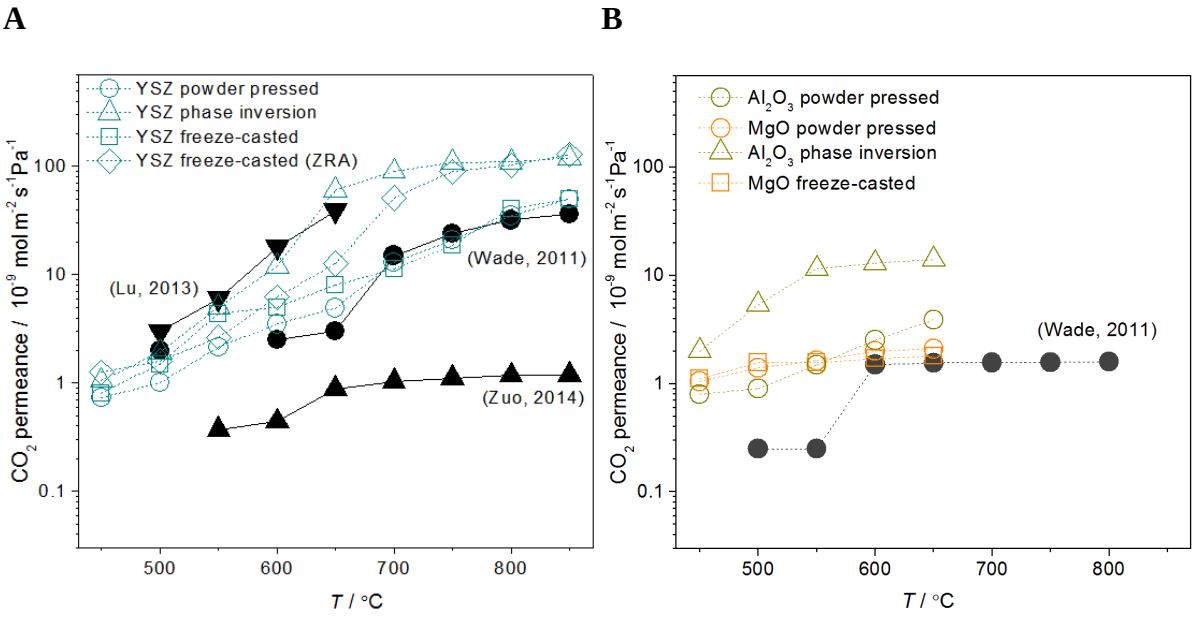

Figure 4-5. Carbon dioxide permeances (logarithmic scale) through dual-phase membranes as a function of temperature for this work (open symbols) and for references (filled symbols). (A) for YSZ supports (ionic conductors) fabricated by powder pressed, freeze-casted, freeze-casted with ZRA and phase inversion method, and **(B)** for Al_2O_3 and MgO supports (non-ionic conductors) fabricated by powder pressed, freeze-casted and phase inversion method. Data for references in **(A)** correspond to YSZ-carbonate membranes and in **(B)** to Al_2O_3-carbonate membrane. Data are connected with lines to aid the eye and correspond to the average of the permeances calculated in 2–3 separate experiments. Error bars are smaller than the symbols.

In Figure 4-5A, at temperatures below 600 °C the CO_2 permeances of all membranes are comparable; no differences greater than 2 x 10^{-9} mol m^{-2} s^{-1} Pa^{-1} were observed. However, above 600 °C, there are significant differences, e.g. YSZ phase inversion membrane shows permeances in the order of 10^{-7} mol m^{-2} s^{-1} Pa^{-1}, and YSZ powder pressed membrane, in the order of 10^{-8} mol m^{-2} s^{-1} Pa^{-1} at 650 and 700 °C. This probably indicates that either the CO_2 permeation mechanism or the rate determining step, changes above 600 °C, thus, the role of the porous structure characteristics (such as the solid fraction and carbonate fraction to tortuosity factor) becomes more significant. This has been identified before by Ortiz-Landeros et al. in 2013 [44] as described in Chapter 2, for LSCF-carbonate membrane operating above 750 °C. Phase inversion and freeze-casted (ZRA) membranes exhibit the highest CO_2 permeances above 650 °C. The hierarchically and vertically aligned internal porosity of those membranes, which can result to a shorter effective ionic transport pathway length can explain the high permeances observed compared to the rest of the membranes. As mentioned before, typical values of tortuosity in literature for powder pressed supports range between 2 and 3

and for freeze-casted and phase inversion membranes they are expected to be close to 1. From Eq. 2-18, it can be said that decreasing the tortuosity by a factor of 3 the flux can increase by the same factor. This evidences that the tortuosity plays an important role to the permeation, and could explain the differences observed between the powder pressed and phase inversion or freeze-casted (ZRA) membranes at temperatures above 750 °C. However, at temperatures between 600 and 650 °C, differences are a lot higher and cannot only be explained by differences in tortuosity. Therefore, a combination with some other microstructural characteristics could explain those differences. From the mercury porosimetry data, it was found that the phase inversion membrane and the freeze-casted (ZRA) show the highest open porosity (37 and 41% respectively) compared to the powder pressed and freeze-casted membranes (26% and 24% respectively). Such an increase in porosity according to Eq. 2-18, could improve the flux at most by a factor of 1.7. Moreover, differences in the size of the pores were observed between substrates. Phase inversion membranes have the largest pore sizes and the mercury porosimetry data showed an average pore size of 60 μm, freeze-casted (ZRA) membranes showed an average pore size of 10 μm, freeze-casted showed an average pore size of 9 μm and powder pressed showed the smallest pore sizes of around 3 μm. As seen from the SEM images, pores have different shapes (rectangular, honeycomb-like etc). The size and shape of the pores can also affect the permeation, as the triple phase boundary and surface phase fraction can change significantly. Those differences are difficult to be quantified in such complex microstructures but can affect could affect permeances but much higher factors, considering that pores range from 3 to 60 μm. Other factors that could also affect the permeation can be attributed to the contribution of leaks (CO_2 leak rate might not be equal to N_2 leak rate) and the permeation area that could have been limited by the sealant (the sealant was applied on the inlet side of the alumina tube before placing the membrane). Due to challenges on sealing those membranes, experiments we repeated only 2 - 3 times for all temperatures. Results in literature [43, 55, 57] presented in Figure 4-5A, show up to two orders of magnitude differences on the CO_2 permeance in the temperature range 500 - 850 °C. Lu et al. [43] suggested that the reduction of the thickness of the support reduced the effective ionic transport pathway length, resulting to an increase on CO_2 permeance. However, this cannot explain that membranes with 500 μm thickness, studied by Zuo in 2014 [57], showed two orders of magnitude lower permeances than the membranes studied in this work (1 mm thickness). These low permeances can possibly be attributed to the microstructural characteristics of the support and the total porosity of the support that were not given.

As shown in Figure 4-5A the slope changes at around 650 °C and since the skeleton shows higher activation energy than the dual-phase membrane, on increasing temperature the membrane CO_2 permeation regime changes from carbonate-ion controlled to oxide-ion. Therefore, a comparison of the activation energies (E_a) seems tempting and the relevant Arrhenius-type plots and E_a values are shown in Figure 4-6 (YSZ membranes). The activation energies decrease with the increase of temperature for the phase inversion and freeze-casted (ZRA) membranes, starting from 64 - 69 kJ mol^{-1} below 600 °C and moving to 28 and 44 kJ mol^{-1} respectively at temperatures above 650 °C. The values of 64 - 86 kJ mol^{-1} are typically found for kinetics governed by oxide-ions transport and the activation energy of the support (activation energy of YSZ is equal to 106 kJ mol^{-1} [43]) is expected to be higher than the activation energy of the dual-phase membranes [101]. Values between 28 and 44 kJ mol^{-1} are closer to the values expected for carbonate-ion controlled kinetics (around 20 kJ mol^{-1} [78, 205]), however, they are still higher, and this could be because permeation is controlled by mixed kinetics. This means that permeation can become carbonate-ion controlled at even higher temperatures (or lower 1000/T values). The activation energies of the powder-pressed and freeze-casted (Non-ZRA) membranes are in the order of 62 - 69 kJ mol^{-1} at temperatures between 450 and 850 °C which comes in contradictory with the phase inversion and freeze-casted (ZRA) membranes. This could be explained but the difference in carbonate volume fraction which can affect the actual breaking point in the activation energies. The actual shift can be probably found at higher temperatures for those membranes.

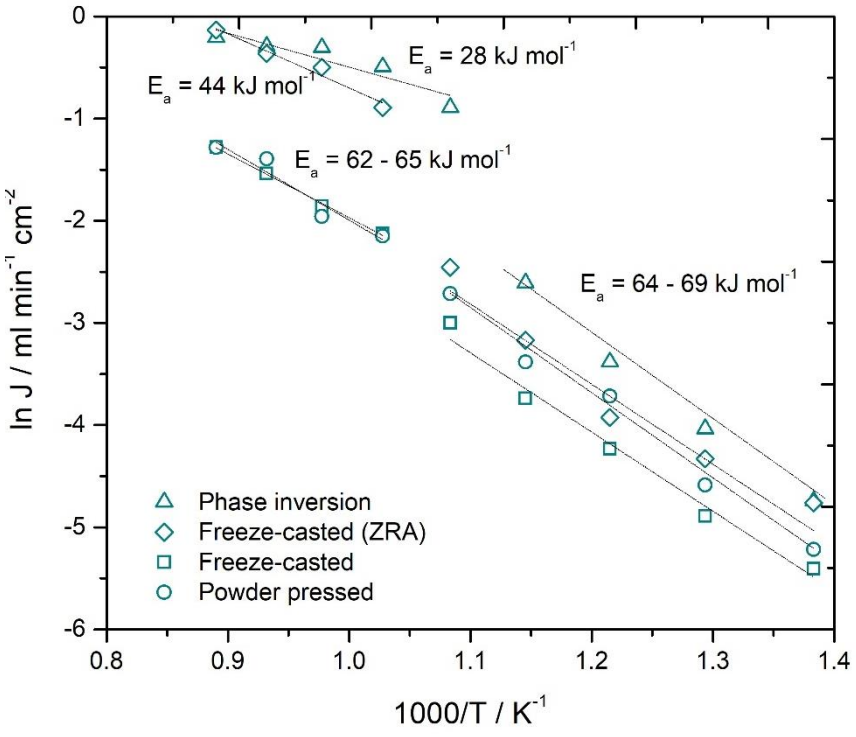

Figure 4-6. The Arrhenius plot for CO_2 flux through the YSZ membranes. The feed-side inlet used was 50%CO_2/N_2 and the permeate side inlet was Ar.

As discussed in Chapter 2, previous microstructural analysis along with high and low impedance measurements [101], were used to characterise ceramic supports and dual-phase membranes, and the membrane performance was predicted based on the membrane conductivity. It is expected that both phases participate to the CO_2 transport through parallel electrical pathways for separate charge carriers. If then the membranes shown in Figure 4-5A are compared in terms of conductivity, it is expected that the conductivity of the dual-phase membranes studied here, will be lower than the conductivity of the carbonates because the support is dominant in volume fraction (volume of the open porosity) and has a lower conductivity. The ambipolar conductivity calculated with Eq. 4-1 (discussed in Section 2.3.2), can be used to obtain the conductivity of the dual-phase membrane, and the results of the YSZ – carbonate membranes are shown in Figure 4-7. There is a continuous increase of the ambipolar conductivity with temperature as expected from the increase of the partial conductivities of both phases. This is also expected to be the tendency of the CO_2 permeation. According to Figure 4-7, YSZ – carbonate membranes show similar conductivities at temperatures below 600 °C, however, at temperatures above 600 °C the powder pressed and freeze casted membranes show higher conductivities than the rest of the membranes. If the conductivities are then compared to the CO_2 permeances in Figure 4-5A, it can be said that at low temperatures, below 600 °C, the performances show similar values as predicted by the calculated ambipolar conductivities. However, at temperatures higher than 600 °C, the conductivity and CO_2 permeances show opposite trends for the different membranes; powder pressed and freeze casted membranes show the highest conductivities and the lowest CO_2 permeances when compared to the rest of the membranes. A possible explanation for these results may be that any microstructural constrains, such as closed pores, high tortuosity and ion blocking grain boundaries, play an important at higher temperatures (above 600 °C), which are neglected with this ideal performance. Moreover, another possible explanation can be that the transport mechanisms where both phases provide parallel ionic pathways, is not the only mechanism involved in CO_2 permeation and this can be supported by the permeances observed with non-ionic (Figure 4-5B) conductive supports.

$$\sigma_{amb} = \frac{\varphi_C \sigma_C \varphi_s \sigma_i}{(\varphi_C \sigma_C) + (\varphi_S \sigma_i)} \qquad \text{Eq. 4-1}$$

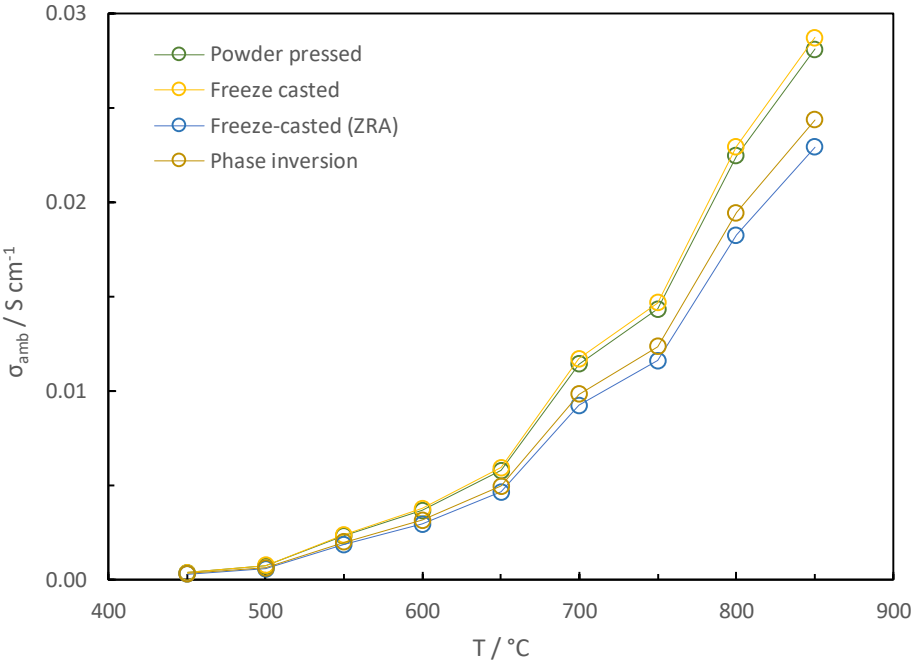

Figure 4-7. Ambipolar conductivity as a function of temperature for YSZ membranes fabricated by powder pressed, freeze-casted, freeze-casted with ZRA and phase inversion method.

As observed in Figure 4-5A, permeation is favoured for the highest carbonate content (phase inversion and freeze casted with ZRA membranes) at temperatures above 600 °C. If the conductivity of the dual-phase membrane is calculated with the assumption of a simple mixing rule; the partial conductivity of each phase will be proportional to the corresponding phase content (Eq.4-2) and the total conductivity of the membranes will be as shown in Figure 4-8. This simple mixing rule can better describe the CO_2 permeance tendencies at temperatures above 600 °C. However, microstructural constrains are again neglected due to their complexity.

$$\sigma_{total} = (\varphi_C \sigma_C) + (\varphi_S \sigma_i) \qquad \text{Eq. 4-2}$$

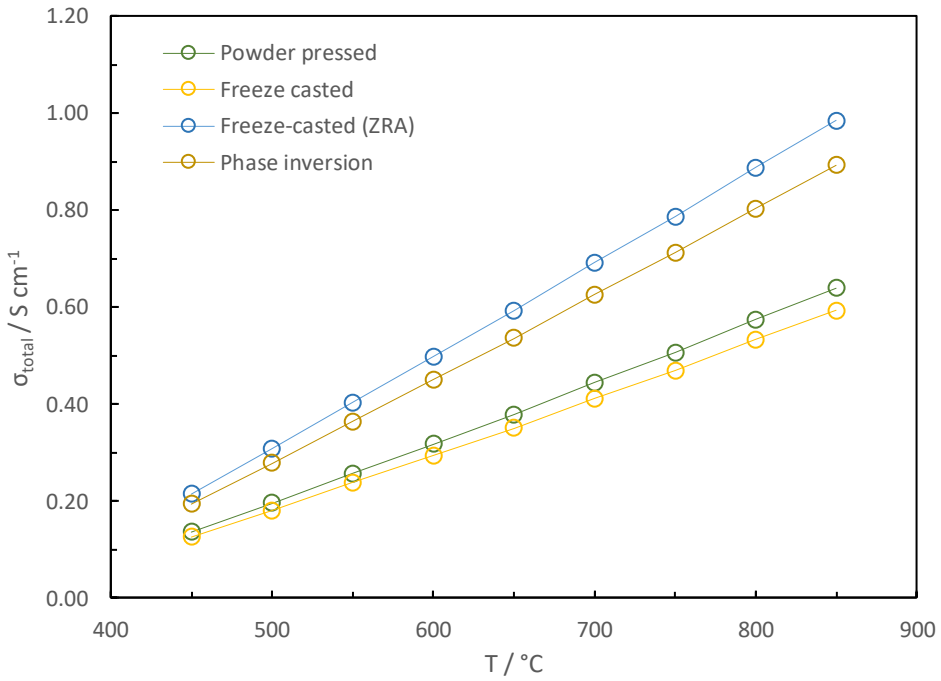

Figure 4-8. Total conductivity as a function of temperature for YSZ membranes fabricated by powder pressed, freeze-casted, freeze-casted with ZRA and phase inversion method.

In Figure 4-5B, data above 650 °C could not be collected, because N_2 trans-membrane leaks were observed at rates similar to the CO_2 rates for all experiments attempted. The Al_2O_3 phase inversion membrane exhibits the highest CO_2 permeance in the order of 10^{-8} mol m^{-2} s^{-1} Pa^{-1} above 500 °C compared to 10^{-9} mol m^{-2} s^{-1} Pa^{-1} that was calculated for the rest of the non-ionic conducting membranes. This support has the largest pore diameter (~100 μm) and the most hierarchically and vertically aligned porosity. As mentioned above, it is expected that the tortuosity can increase the flux at most by a factor of 3 and the porosity by a factor of 1.2. However, the surface area of the carbonates in both the feed and permeate side are around 2 times higher for the Al_2O_3 phase inversion membrane (calculated from the SEM images of the membrane surface) which could affect the permeation. The combination of all the above parameters could explain the differences found between the phase inversion and the rest of the supports. Wade in 2014 [55] was to the best of found knowledge the only reference presenting an experiment with a non-ionic conducting membrane (Al_2O_3 – carbonate membrane) and the results of this study are shown in Figure 4-5B. The activation energy of the Al_2O_3 and MgO membranes are shown in Figure 4-9. There is no clear shift in activation energies at this temperature range (450 - 650 °C), however, there is a significant difference on values between the Al_2O_3 and MgO membranes. For the MgO membranes the activation energies are in the order of 14 - 23 kJ/mol (typical values for carbonate-ion controlled kinetics [78, 205]),

however, the activation energies for the Al_2O_3 membranes are in the order of 55 - 65 kJ mol^{-1}, which could be due to the formation of other ions, such as aluminates that could be formed on the permeate side of the membrane, where CO_2 concentration is very low.

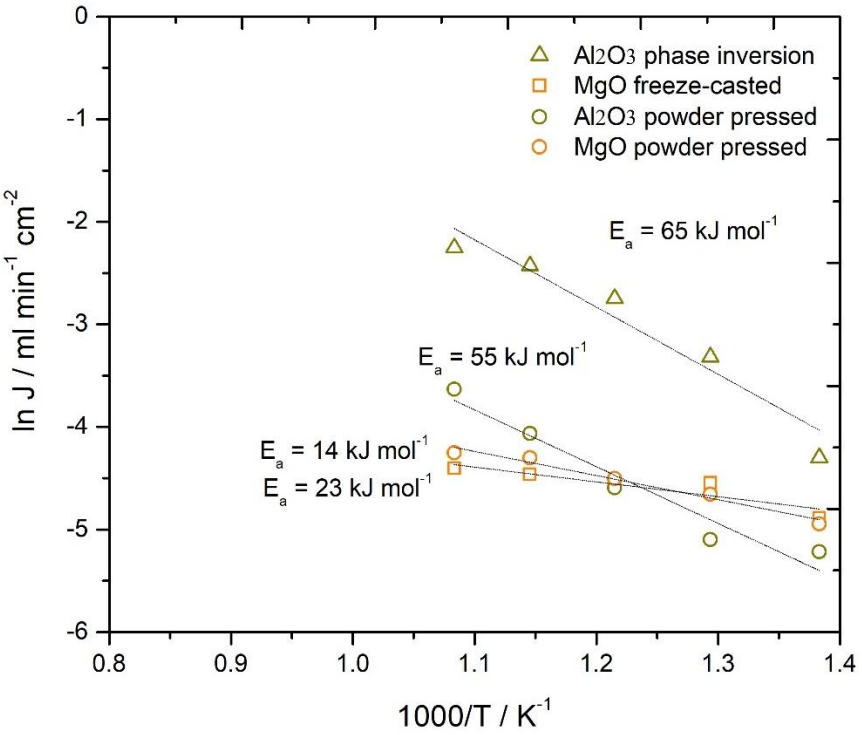

Figure 4-9. The Arrhenius plot for CO_2 flux through the Al_2O_3 and MgO membranes. The feed-side inlet used was 50%CO_2/N_2 and the permeate side inlet was Ar.

What follows is a comparison between ionic (Figure 4-5A) and non-ionic (Figure 4-5B) conductive supports that are fabricated with the same technique. CO_2 permeance through ionic conducting-carbonate membranes is accomplished by the dual-ionic transport mechanism as described in the introduction of this thesis. However, non-ionic conducting membrane supports are considered "inert" with no participation on CO_2 permeation. When comparing permeances between the YSZ and Al_2O_3 phase inversion supports, we find that CO_2 permeances are higher with the inert support (Al_2O_3) until 550 °C. This shows a non-significant contribution of the oxygen-ionic conductivity of the YSZ support on the CO_2 permeance in the temperature range 450 to 600 °C, suggesting that the pore microstructure plays an important role at these temperatures. CO_2 permeances through the membranes consisting of supports fabricated by freeze-casted method are similar between the two materials (YSZ and MgO) below 500 °C. However, at 650 °C we observe that both YSZ supports (freeze-casted and phase inversion) show higher CO_2 permeances compared to their

respective inert supports fabricated by the same technique. This can be because the oxygen ion conductivity of YSZ (8 mol% Y_2O_3) becomes significant above 600 °C and according to literature values is approximately 2 x 10^{-4} S cm^{-1} at 450 °C and 4 x 10^{-3} S cm^{-1} at 600 °C [206, 207]. According to Eq. 2-18 described in Section 2.3.3, the flux and consequently the permeance is directly proportional to the ionic conductivity since the conductivity of the carbonates is much higher than the oxygen ionic conductivity. Therefore, if the oxygen ionic conductivity increases by an order of magnitude from 450 to 600 °C, the permeance is also expected to increase by an order of magnitude as observed in Figure 4-5A.

If the theoretical permeabilities calculated in Section 2.2, are then compared to the membranes with the non-ionic conductive supports (Table 4-2), it can be observed that the working membranes show slightly higher values than the theoretical values. The theoretical values are based on solubility and diffusivity results found in literature and with the assumption that the carbonate phase is the only ionic pathway through surface ionisation of CO_2 at the CO_2/carbonate interface. The experimental values in Table 4-2 correspond to the permeances of the Al_2O_3 and MgO membranes multiplied by the membrane thickness (1 mm = 0.0001 m). MgO membranes show the best agreement to the theoretical values, however, it is expected that microstructural limitations would also influence the permeability value.

Table 4-2. Theoretical and experimental CO_2 permeability at varying temperatures.

Temperature, °C	**Theoretical permeability, 10^{-11} mol m^{-1} s^{-1} Pa^{-1}**	**Experimental permeability for Al_2O_3, 10^{-11} mol m^{-1} s^{-1} Pa^{-1}**	**Experimental permeability for MgO, 10^{-11} mol m^{-1} s^{-1} Pa^{-1}**
~550	0.069	0.28 – 2.16	0.29 – 0.31
~650	0.136	0.73 – 2.63	0.34 – 0.39

4.5 Conclusions

In this chapter, the effect of the ceramic porous structures, which serve as supports on dual-phase membranes, for CO_2 permeation were investigated at temperatures between 450 and 850 °C. Oxygen ionic conductors and electronic and ionic non-conductors were fabricated by several manufacturing techniques which can affect the porous structure, the geometrical characteristics and tortuosities of those supports. To the best of found knowledge there are no references in literature on ceramic-carbonate membranes for CO_2 permeation at temperatures

as low as 450 °C, and most of the references focus on temperatures higher than 600 °C. Moreover, freeze-casted membranes were tested for the first time as dual-phase membranes for CO_2 separation in this work.

The results of this study suggest that the shift in activation energy and thus the change in the rate determining regime can be found at temperatures between 600 and 650 °C for the YSZ-carbonate membranes (oxygen ionic conductors) with carbonate content above 37%. At temperatures below 600 °C, the activation energies indicated that the kinetics are governed by oxide-ions transport and above this temperature (from 600 to 850 °C), they suggested that the regime can be a mixed kinetic control as the values were slightly higher than the values expected for carbonate-controlled transport. The actual shift in rate determining regime can be probably found at temperatures higher than 850 °C. For the Al_2O_3-carbonate and MgO-carbonate membranes (electronic and ionic non-conductors), the activation energies showed no apparent shift in the rate determining regime at temperatures between 450 and 650 °C. MgO-carbonate membranes showed activation energies very close to the values expected for carbonate-controlled transport, however, the Al_2O_3-carbonate membranes showed slightly higher activation energies than those expected for carbonate-controlled transport, which indicates that the regime can be a mixed kinetic control due to the formation of other ions inside the melt (e.g. aluminates).

The assumption of a simple mixing rule for the partial conductivity of each phase accords with the earlier observations at temperatures above 600 °C, which showed that membranes with high porosities and thus carbonate context exhibit the highest permeations.

This study has also shown that microstructural constrains can strongly influence CO_2 permeances; the performance of the membranes studied in this work, in terms of CO_2 permeation, showed that the geometrical properties of the membrane have a stronger impact on the membrane performance compared to the nature of the support material. Generally, membranes with low tortuosities, high porosities and parallel pore channels exhibited the highest permeations compared to membranes with random pore networks. However, the membrane microstructural parameters, such as, pore geometry, tortuosity, total porosity, thickness and carbonate and solid fraction to tortuosity ratio, are difficult to control in membranes fabricated with the above techniques and thus, render it complicated to study those parameters and improve the membrane performance in terms of CO_2 permeance. This case demonstrates the need for membranes with better controlled porous structure in order to understand its effects and provide mechanistic insights that can improve membrane

performance. Moreover, N_2 trans-membrane leaks have limited the results that could be collected at high temperatures and they can highly affect the quality of data that one can extract. The following chapters, Chapter 5 with the creation of single-pore single crystals and Chapter 6 with closed-end tube systems, address those problems at once.

Chapter 5
Single crystal membranes

5.1 The concept of using single-pore systems for calculating permeances

The complexity of the membrane microstructure was the motivation of this research to work with simple physical models in order to generate mechanistic insight for CO_2 permeation. As seen in Chapter 4, the geometry of the pores has a significant effect on the performance of the membrane. The grain boundaries and grain sizes of the ceramic supports can also change with the fabrication technique and sintering temperature, thus effecting the properties of the material (such as the oxygen ion diffusion) [208, 209]. The simplest model for a dual-phase membrane system would be a support with a single well-defined pore and with the absence of grain boundaries.

To obtain the simplest model, a single pore was laser drilled on a single crystal support (laser drilling is briefly described in Chapter 3.1.4). The transparent nature of the YSZ and Al_2O_3 crystals allows the use of microscopy technique for the observation of the molten carbonate infiltration and the visualisation of an effect of CO_2 permeation (explained in detail below).

One concept that could be used to measure permeation rates in a single pore, would be to infiltrate a blind pore, and once the internal gas phase (gas phase behind the meniscus or inside a gas bubble) is equilibrated in a known gas, to make a change to the external gas phase and observe the displacement of the molten salt meniscus (Figure 5-1) or the growth/shrinkage of a gas bubble trapped inside the melt (internal gas phase). If permeation is selective to CO_2 and the mole fraction of CO_2 at t_0 is equal to the known gas at equilibrium, the internal gas phase volume can be used to calculate CO_2 mole fraction at any time due to CO_2 partial pressure changes to the external gas phase. If N_2 is the balance gas and with the assumption that the number of moles in the internal gas phase does not change with time, then:

$$n_t = n_{CO_2,t} + n_{N_2,t} \text{ or } n_t = n_{CO_2,t} + n_{N_2,t_0} \qquad \text{Eq. 5-1}$$

Where,

n_t, is the total number of moles of the gas mixture in the internal gas phase at time t

$n_{CO_2,t}$ and $n_{N_2,t}$ is the number of CO_2 and N_2 moles in the internal gas phase respectively at time t

n_{N_2,t_0} is the initial number of N_2 moles in the internal gas phase, before changes are introduced to the external gas phase, at time t_0 (time the gas switch is made on the external gas phase)

And from the ideal gas equation, Eq. 5-1 will give:

$$P_t V_t = P_{CO_2,t} V_t + P_{N_2,t_0} V_{t_0} \qquad \text{Eq. 5-2}$$

Where,

P_t, it the total pressure in the internal gas phase at time t (the total pressure of the gas mixture in the internal gas phase is calculated in Appendix C)

$P_{CO_2,t}$, is the CO_2 partial pressure in the internal gas phase at time t

V_{t_0}, is the volume of the internal gas phase at time t_0

P_{N_2,t_0} is the partial pressure of N_2 in the internal gas phase at time t_0

If Eq. 5-2 is rearranged to make $P_{CO_2,t}$ the subject:

$$P_{CO_2,t} = P_t - \frac{P_{N_2,t_0} \cdot V_{t_0}}{V_t} \qquad \text{Eq. 5-3}$$

The thermodynamic limit for the V_t / V_{t_0} after introducing a change on the CO_2 partial pressure (balance is N_2) of external gas phase can be found from Eq. 5-3 and by substituting $(P_t - P_{CO_2,t})$ with $P_{N_2,t}$:

$$V_t / V_{t_0} = \frac{P_{N_2,t_0}}{P_{N_2,t}} \qquad \text{Eq. 5-4}$$

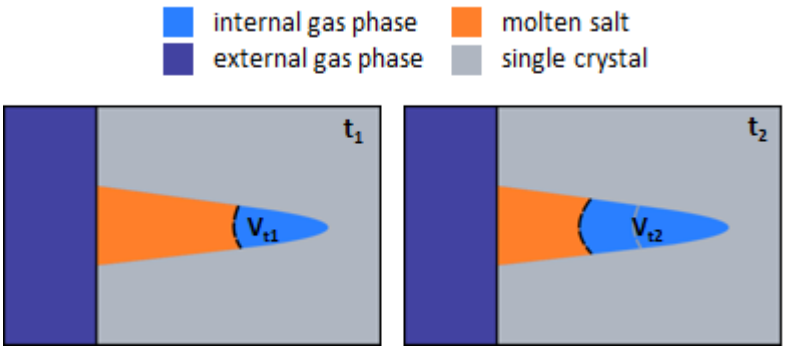

Figure 5-1. Concept schematic of the meniscus displacement when CO_2 partial pressure increases on the external gas phase resulting in CO_2 permeation towards the internal gas phase and subsequently to the displacement of the meniscus. At t_1 the volume of the internal gas phase is V_{t1} and due to the increase of CO_2 partial pressure in the external

environment, at t_2 the volume of the internal gas phase increases to V_{t2} as a result of CO_2 permeation.

If permeation is selective to CO_2 and the volume change of the internal gas phase is a result of CO_2 permeation, then the permeation rate can be calculated using Eq. 5-5.

$$Permeation = \frac{P_t \cdot |V_{t_2} - V_{t_1}|}{RT(t_2 - t_1)} \quad \text{Eq. 5-5}$$

Where,

V_{t_1}, V_{t_2} is the volume of the internal gas phase at times t_1 and t_2 respectively.

Moreover, microscopy with *in situ* Raman spectroscopy can also be facilitated due to the transparent nature of the single crystal. For this reason, spectroscopic measurements were carried out in order to identify chemicals species inside the melt that could be involved in CO_2 permeation mechanism. The existence of $C_2O_5^{2-}$ and Li_2ZrO_3 in a eutectic carbonate mixture infiltrated in a single crystal was investigated under CO_2 and Ar atmosphere with *in situ* Raman spectroscopy and the results are shown in Appendix D. Moreover, it was attempted to quantify the concentration of CO_2 in the internal gas phase through the analysis of the intensity and area differences of Raman corresponding peaks for CO_2 attributed to concentration changes. However, the results of this study will not be shown here as the corresponding peaks for CO_2 were very weak to be studied.

5.2 Experimental setup for single-pore system

Figure 5-2 shows the schematic set-up used for the visualisation experiments. The single crystal was placed on a quartz disk support and was subsequently loaded into the high temperature cell (Linkam TS1500 stage), with the pore placed horizontally to the stage holder. Carbonate infiltration took place under 0.1% CO_2 /N_2 or 1.1% CO_2 /N_2 (depending on the experiment) at 400 °C with 20 °C min^{-1}. The temperature was controlled by using the system controller provided by Linkam and the gas flow rate was controlled with mass flow controllers. A fixed camera was used to observe the sample through the quartz lid window. The melting point of the ternary eutectic mixture was observed at 430 °C, but it is possible that some temperature gradient can appear across the sample, causing the melting to appear at higher temperature than the expected. The meniscus displacement or bubble growth/shrinkage inside the single hole was achieved with gas switches between 0.1% CO_2 /N_2 or 1.1% CO_2 /N_2 and 50% CO_2 /N_2 with a 4-way valve (Figure 5-2) and this was recorded with the camera. The volume of the internal gas phase was determined by the image analysis.

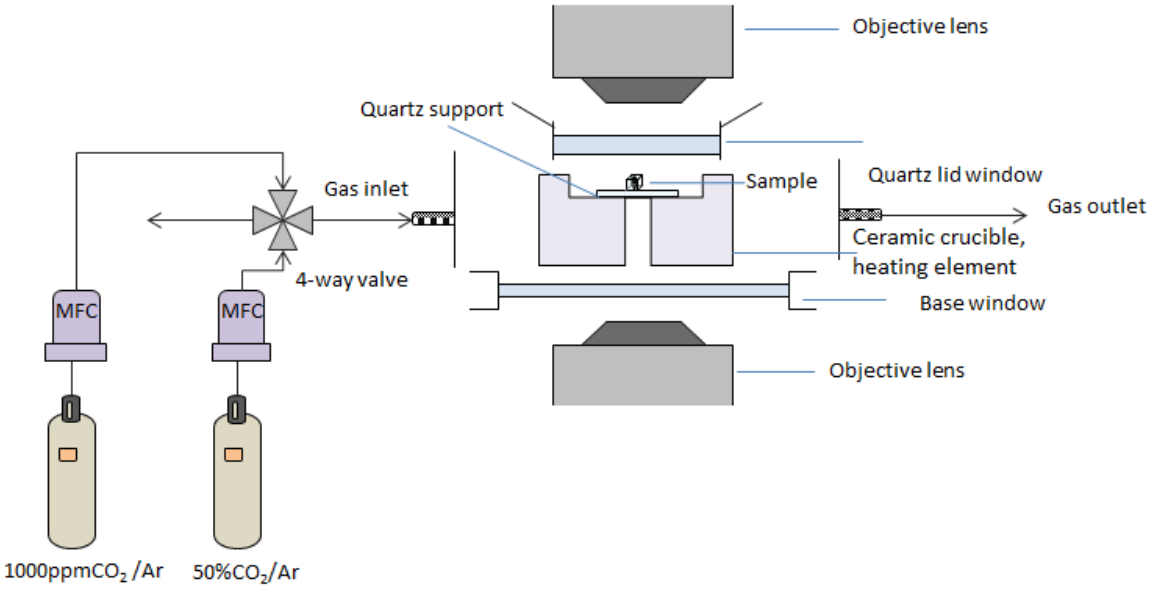

Figure 5-2. Schematic of the visualisation set-up. The high temperature cell (Linkam TS1500 stage) and the flow system used for visualisation experiments.

The volume of the high temperature cell is difficult to be measured accurately due to its complex geometry, however, it was calculated to be between 80 - 100 cm^3. The residence time distribution of the cell was measured as shown in Figure 5-3. The flow rates were maintained at 30 ml min^{-1} and before each switch, the inlet and outlet partial pressures of the cell are considered to be equal. The switches were conducted between N_2 and Ar, and the residence time distribution was found to be around 8 min. This results to a nominal volume of 240 cm^3 which is almost 2.5 times higher than the real volume of the cell (80 -100 cm^3). This indicates that the gases are not well mixed inside the cell, and thus there will be significant errors associated with the calculation of the external gas phase concentration during the first 8 min of permeation. To reduce the dead volume inside the cell, a Macor insert was designed and added into the cell. The volume of the high temperature cell, with the addition of the Macor insert, was significantly reduced and it was estimated to be between 20 and 40 cm^3.

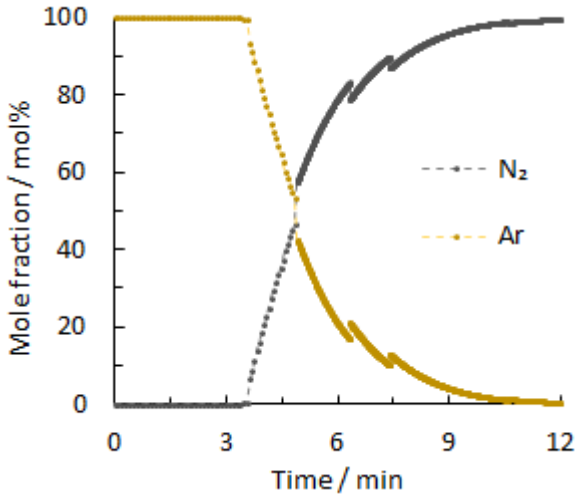

Figure 5-3. Residence time distribution of N_2 and Ar in the visualisation cell. The flows were maintained at 30 ml min^{-1} for switches between N_2 and Ar at room temperature.

The residence time distribution of the cell with the added Macor insert was then determined experimentally with switches between 50% CO_2/N_2 and 1.1% CO_2/N_2 and the flow rate was maintained at 50 ml min^{-1}. Before each switch, it is considered that the inlet and outlet partial pressures of the cell have become equal. If there are no dead or stagnant zones within the cell, the residence time distribution determined in Figure 5-4A and B should be equal to the theoretical residence time which can be calculated from the volumetric flowrate and chamber volume. The mole fraction of the molecules entering and leaving the system can be characterised by an exponential decay function ($y = y_0 + A_1 e^{-t/\lambda}$) with time as shown in Figure 5-4C and D. Where y_0 is the mol% CO_2 at time equal 0 min, A1 represents the mol% CO_2 difference at time equal 0 min (y_0) and time equal infinity (y_{inf}) and λ is the decay constant. By considering the theoretical residence time distribution (calculated above to be between 0.4 and 0.8 min) and experimental residence time distribution (decay constant was approximately 0.4 for the CO_2 removal and 0.7 min for CO_2 introduction), it can be said that there are no significant stagnant zones within the reactor, and thus, the external gas phase composition can be calculated over time. The R^2 was equal to 0.998 for changes between 50% CO_2/N_2 to 1.1% CO_2/N_2 and 0.989 for changes between1.1% CO_2/N_2 to 50% CO_2/ N_2.

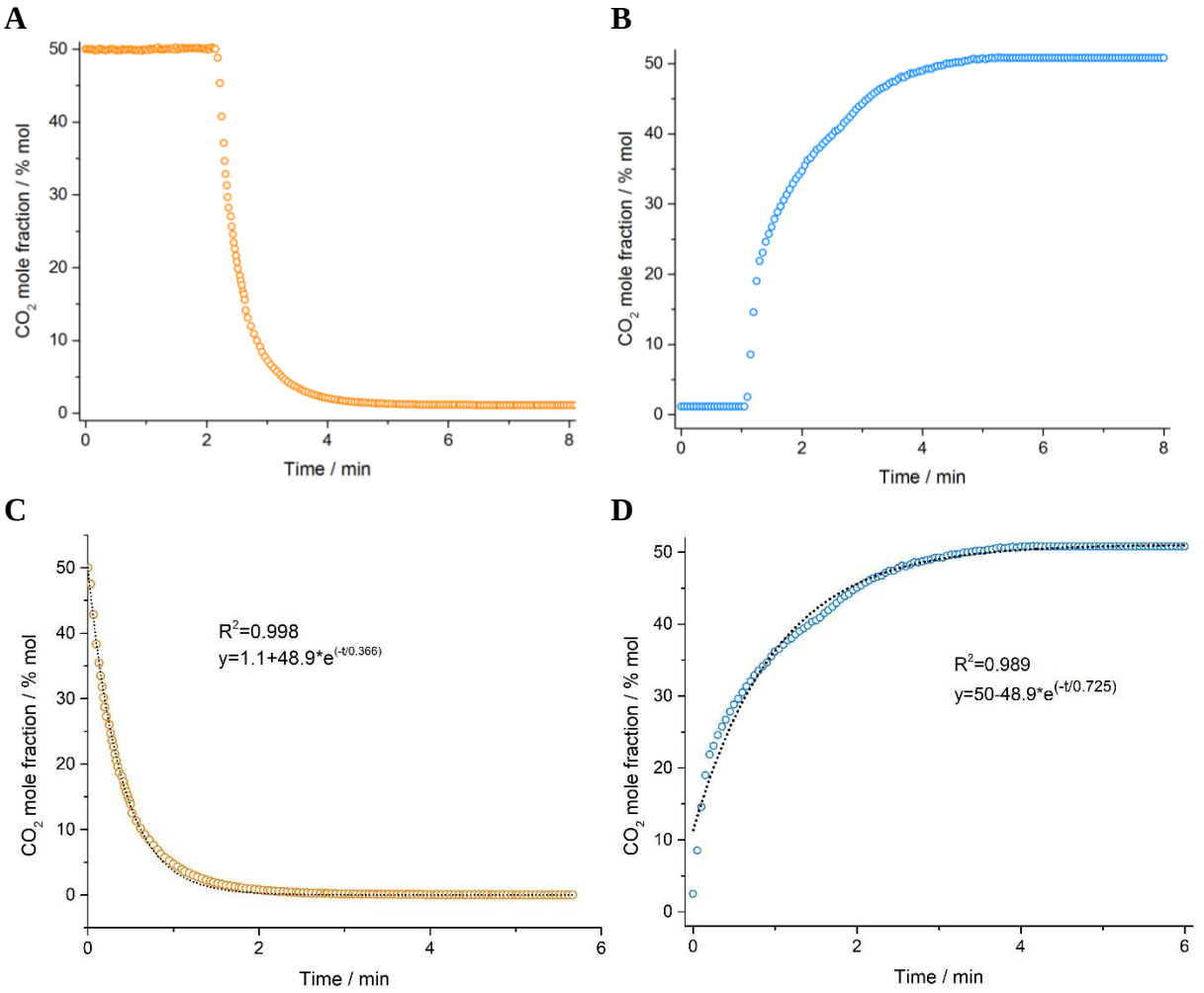

Figure 5-4. Residence time distribution of the visualisation cell with the Macor insert. The flows were maintained at 50 ml min^{-1} for switches between 50% CO_2/N_2 and 1.1% CO_2/N_2 at room temperature and the curves represent the averaged curve of three repeats. **(A)** At t = 2.2 min the flow is switched from 50% CO_2/N_2 to 1.1% CO_2/N_2 and **(B)** at t = 1 min the flow is switched from 1.1% CO_2/N_2 to 50% CO_2/N. **(C)** and **(D)** represent the **(A)** and **(B)** switches fitted to an exponential function respectively. The model used to characterise the mole fractions with time is a decay exponential function $\boldsymbol{y = y_0 + A_1 e^{-t/\lambda}}$ and the decay constant, $\boldsymbol{\lambda}$, is 0.366 ± 0.005 min and 0.725 ± 0.019 min for **(C)** and **(D)** respectively.

5.3 Morphology of single-pore systems

Pores were drilled in YSZ, MgO and Al_2O_3 single crystals (Figure 5-5 and Figure 5-6) as described in Chapter 3.1.4. The preliminary drilling was conducted at the University of Zaragoza and three different geometries were achieved (Figure 5-5); a blind pore in the YSZ single crystal with 80 µm diameter at the laser incident surface and 100 µm depth (Figure 5-5A), blind pores in the YSZ and MgO single crystals with 300 µm diameter at the laser incident surface and 800 µm depth (Figure 5-5B,C) and slits in the YSZ and Al_2O_3 single crystals of 45 µm width, 1000 µm length and 500 µm depth. The 300 µm diameter pores

showed a more cylindrical geometry with smaller reduction of the diameter with depth compared to the 80 µm diameter pores, which have a more conical shape. The drilling was then completed at LML, to make use of the newest femtosecond laser (final drilling). As shown in Figure 5-6, two different sizes were achieved for each material with the diameter reducing with depth. The pore tapering was larger in the Al_2O_3 single crystal with rough and uneven walls. The minimum achievable diameter with low implication on the wall transparency was 100 µm.

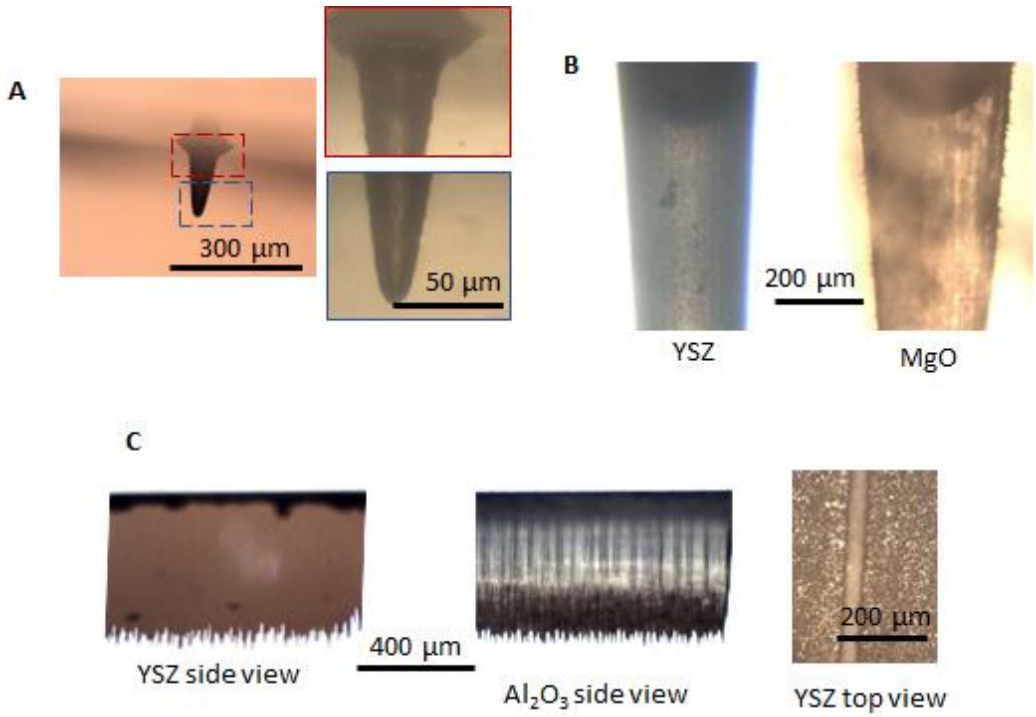

Figure 5-5. Digital microscope images of the preliminary drilling in single crystals. (A) Blind pores with high conical degrees in YSZ single crystal, **(B)** blind pores with a more cylindrical geometry in YSZ and MgO single crystals and **(C)** side and top view of slits drilled in a YSZ and Al_2O_3 single crystal.

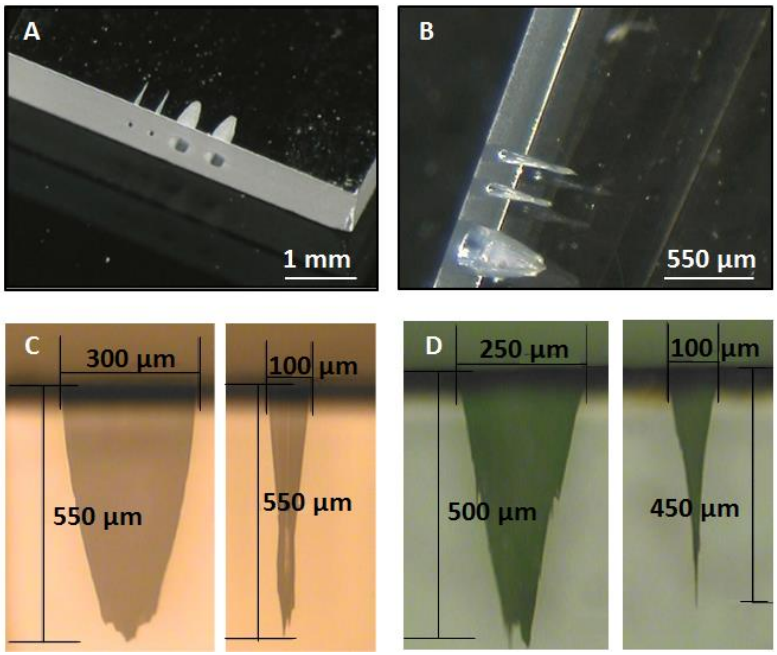

Figure 5-6. Digital microscope images of the final drilling in single crystals. (A) and **(B)** show the edge views of the pores drilled on the YSZ single crystal, **(C)** the dimensions and geometry of the YSZ laser drilled pores and **(D)** of the Al_2O_3 laser drilled pores.

5.4 The effect of pore size and geometry on carbonate wetting

The infiltration of the blind pores was achieved by placing < 0.01 g of the carbonate mixture on the mouth of the pores and heating up to 400 °C -above the melting point of the carbonates- with a heating rate of 20 °C min^{-1} under 0.1% or 1.1%CO_2/N_2.

The infiltration of the 80 µm diameter blind pore in the YSZ single crystal of the preliminary drilling, will not be shown here, as it was difficult to visualise inside the pore and the quality of the images was very poor. Blind pores of 300 µm diameter (from preliminary and final drilling) in the YSZ and Al_2O_3 single crystal were always fully filled with carbonates during the infiltration and bubbles were formed inside the melt (Figure 5-7A, B). The formation of bubbles in the YSZ single crystal cannot be considered satisfying, as the contact area or the triple phase boundary between the support, the melt and the gas atmosphere inside the bubble remains unknow and it can be particularly important due to the participation of the support in CO_2 permeation. In the case of the MgO and Al_2O_3 single crystals, the support is considered "inert", as it is not expected to participate in the mechanism of CO_2 permeation, and therefore, the formation of bubbles can be considered satisfying. Slits were drilled as an effort to overcome the issue with the unknown triple phase boundary in the YSZ support as it was expected that bubbles will be "squeezed" between the walls of the slit and create a clearer contact area with the walls. As shown in Figure 5-7**C**, many bubbles were formed inside the

melt of the slit. The most unexpected observation with the multiple bubbles formed inside the slits, was that bubbles with same initial apparent areas (areas of bubbles shown in the 2D image), formed inside the same melt and in positions with the same distance from the meniscus, showed different growth/shrinkage rates under the same permeation conditions. This may be due to any kind of interaction between the bubbles or the lack of accuracy of the slits visualization on the prediction of the bubble shape and therefore, the results will not be shown here, and the study moved on to the pores of the final drilling.

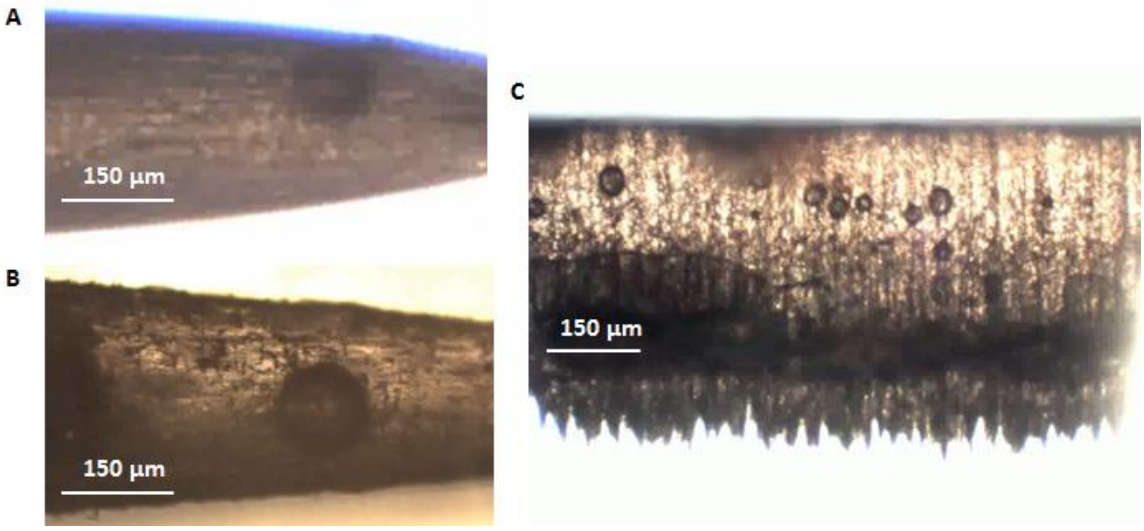

Figure 5-7. Digital microscope images of the infiltrated pores in single crystals drilled as part of the preliminary work. (A) and **(B)** show the formation of a single gas bubbles in the melt infiltrated in the 300 µm diameter pore of the YSZ and MgO single crystal respectively and C the formation of multiple gas bubbles in the melt infiltrated in the 45 µm width slit of the YSZ single crystal.

The study from now on will only focus on the 100 µm diameter pores of the final drilling. Two types of infiltration were achieved with the blind pores: the formation of bubble(s) in the fully filled pore (Figure 5-8A) and the formation of a meniscus of carbonates, with the gas phase trapped at the bottom of the pore (Figure 5-8B).

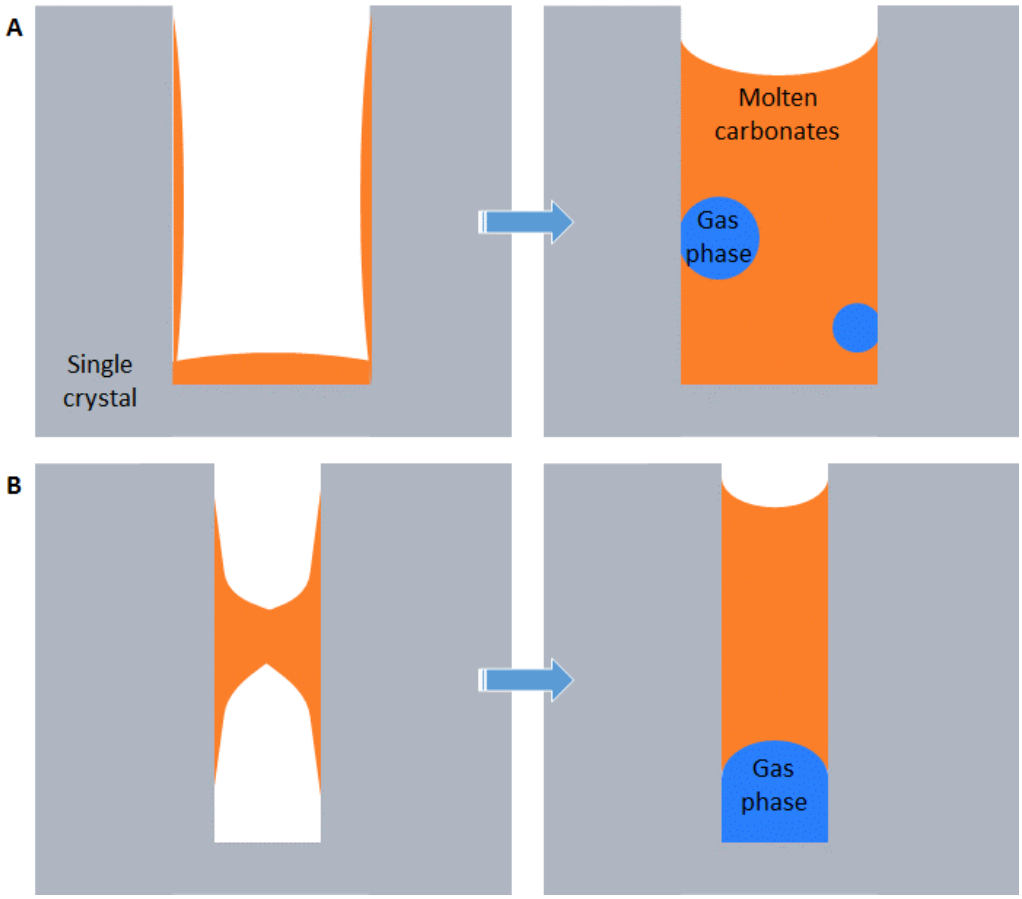

Figure 5-8. Simple schematics of the two types of infiltrations achieved with the single-pore single crystals. An internal gas phase (blue) is separated from the external environment by a carbonate ion conducting molten carbonates (orange), confined within a laser drilled single crystal (grey); **(A)** the molten carbonates fill the pore and some gas gets trapped in a form of a bubble (multiple bubbles can also be formed) and **(B)** the molten carbonates form a meniscus and the gas phase is trapped in the closed-end of the blind hole.

The wettability of the carbonates (wettability is discussed in Chapter 3.3.4) on the YSZ single crystal was studied, and it was found that when the carbonates are fully melted, above 400 °C, a complete wetting occurs (Figure 5-9). This shows that the adhesive forces between the carbonates and the walls are very strong and the carbonates will prefer to wet the walls and subsequently fill the pore (Figure 5-8A). However, if the diameter of the pore is sufficiently small (in this work, it was observed in the 100 µm diameter pore in the YSZ single crystal), the carbonates will form a meniscus due to the increase of the cohesion force within the liquids of the opposite walls (Figure 5-8B). The gas phase that is trapped at the closed end of the pore creates a pressure that is just balanced by the surface tension of the carbonate. Because the system YSZ/molten carbonate is a wetting system, the shape of the meniscus is curved as shown in Figure 5-8. However, in the 100 µm diameter pore in the Al_2O_3 single crystal this phenomenon was not observed, possibly because the walls show higher tapering,

which propels the molten carbonates to fill the pore. The flow of the liquid to fill the pore, can be expressed in terms of the pressure gradient in the liquid and the gravity, where the pressure gradient is determined by the curvature of the gas-liquid interface and the surface tension.

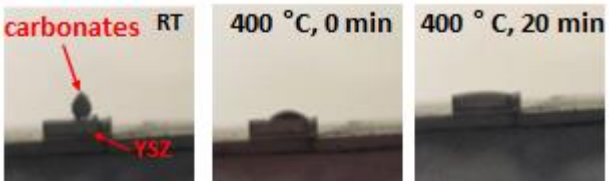

Figure 5-9. Wetting experiment with the YSZ single crystal/molten carbonate system. Heating was conducted under pure Ar in a controlled atmosphere furnace.

Experiments presented in the next sections, will only include the results collected with the 100 μm pore diameter of the final drilling.

5.5 Visualisation in the Al_2O_3 single-pore single-crystal system

As discussed above, blind pores in the Al_2O_3 single crystal were always fully filled during infiltration and bubbles were formed inside the melt. The volume of the bubbles was calculated assuming a perfect sphere using the diameter of the bubble that can be seen in the two-dimensional image of the camera. The bubble volume in the Al_2O_3 single crystal was calculated by Eq. 5-6, using the x dimension of the bubble as shown in Figure 5-10:

$$V = 4/3 \cdot \pi \cdot (\frac{x}{2})^3 \qquad \text{Eq. 5-6}$$

Figure 5-10. The determination of the size of the bubble formed inside the melt of the single pore in the Al_2O_3 single crystal using the two-dimensional image of the camera.

In this work, only bubbles that lack of mobility and show the highest contrast in the images were studied. However, several sources of error can affect the results of this study; observational errors when estimating the diameter of the bubbles and the non-spherical shape of the bubbles that cannot be observed in a two-dimensional image. The shape and size of the bubble will have a direct impact on the bubble volume and consequently to the permeation rate. For instance, by considering the blurry boundaries of the bubbles (approximately an area

of 1 μm width around the periphery of the bubble), the fractional uncertainty of the bubble volume will be less than 10% (assuming a perfect sphere, calculations are analytically shown in Appendix E). The uncertainties in bubble volume will certainly decrease with the increase of the initial bubble volume and are expected to be higher for bubble growth compared to bubble shrinkage as the initial bubble volume is approximately 15 x 10^3 μm^3 and 300 x 10^3 μm^3 respectively as shown in Appendix E. Bubble volume uncertainties range from 2% to above 5% depending on the bubble size as shown in Appendix E.

Figure 5-11 shows the relative bubble volumes (normalised to the initial bubble volume at t = 0 s) formed inside the melt of the Al_2O_3 single crystal as a function of time. The images in Figure 5-11A are taken at 550 °C, at the two thermodynamic limits, which are considered to be when the concentration of CO_2 in the bubble gas phase is in equilibrium with the external gas phase (0.1% CO_2 /N_2 and 50% CO_2 /N_2) and can be calculated using Eq. 5-2 and assuming $P_t \approx 1$ atm. Figure 5-11B shows the growth of the bubble at 450 °C and 550 °C during the first 30 min of growth and t = 0 s is the time the switch from 0.1% CO_2 /N_2 to 50% CO_2 /N_2 is made. The final bubble volume at 550 °C, is in a good agreement with the thermodynamic limit (shown in dash lines in Figure 5-11B), indicating that permeation is selective to CO_2. However, this was not observed at 450 °C, and this may be because more than 30 min were needed for the gas bubble to reach the thermodynamic limit. Similar behaviour was observed with the bubble shrinkage (Figure 5-11C).

If permeation is selective to CO_2 and the volume change of the internal gas phase is a result of CO_2 permeation, through the carbonate phase, then the permeation area can be considered the bubble surface area or the surface area of the pore mouth. As described before, permeation rates can be extracted from the volume changes with time, however, due to the high uncertainty of the results (up to 50% on the calculations of the permeation rate as shown in Appendix E), those results will only be used as a proof of the visualisation concept.

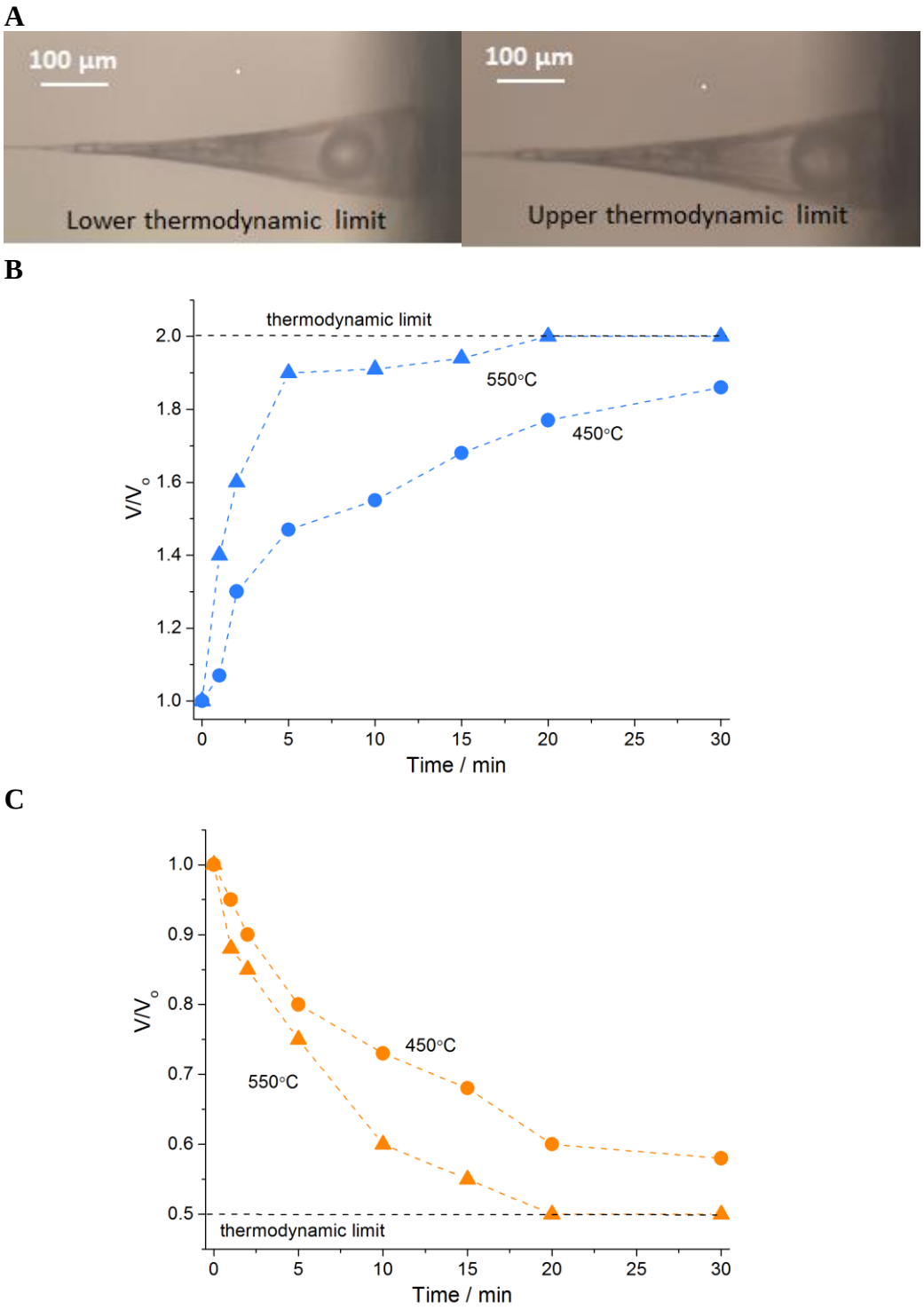

Figure 5-11. Concept of the bubble growth/shrinkage to visualise an effect of permeation in an Al_2O_3 single pore. (A) shows the microscopic images of the bubble formed inside the melt at the theoretical thermodynamic limits (0.1 and 50% CO_2) achieved at 550 °C. As the external CO_2 concentration changes between 0.1 and 50 %, the concentration of CO_2 within the bubble adapts to achieve equilibrium, resulting in **(B)** bubble growth when the external CO_2 concentration increases and **(C)** bubble shrinkage when the external CO_2 concentration decreases; bubble volume normalised to the volume at t = 0 s and monitored with time during, **(B)** external CO_2 concentration increase from 0.1 to 50 % and **(C)** external CO_2 concentration

decrease from 50 to 0.1 %. The experiment was performed at 450 and 550 °C inside a single pore of a laser drilled Al_2O_3 single crystal. Dashed coloured lines are shown to aid the eye.

5.6 Visualisation in YSZ single-pore single-crystal systems

As discussed in Chapter 5.4, in the blind pores of the YSZ single crystal, a meniscus of carbonates could be formed, with the gas phase trapped at the bottom of the pore. The volume of the internal gas phase (gas phase trapped behind the meniscus) was calculated from the geometry of the blind pore, assuming a perfect cone (volume of a frustum of a cone) and half an ellipsoid (accounting for the meniscus curve). The uncertainty in the determination of internal gas phase volume and permeation rate during the first 60 s of meniscus displacement, considering 1 μm width for the blurry meniscus curve, will be smaller than 0.3% and 1% respectively as shown in Appendix E.

The internal gas phase volume is calculated by Eq. 5-7 and Eq. 5-8, and the dimensions used for these equations are shown in the two-dimensional image of the microscope camera marked in Figure 5-12. The uncertainties in the internal gas phase volume are shown in Appendix E (Table E- 2) and are below 1% as gas phase volumes are above 600 x 10^3 μm^3, significantly higher than those observed with the Al_2O_3 single crystal.

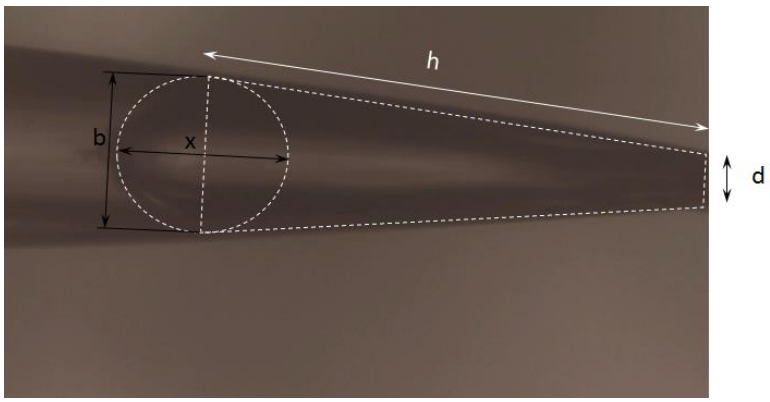

Figure 5-12. Digital microscope image of the YSZ single-pore single crystal for the determination of the x, b, d and h dimensions of the internal gas phase.

$$V_{cone} = \frac{\pi h}{12}(d^2 + db + b^2)$$ Eq. 5-7

$$V_{ellipsoid} = \frac{4\pi}{3}\left(\frac{x^2}{4}\frac{b}{2}\right)$$ Eq. 5-8

Figure 5-13A shows the displacement of the meniscus in the YSZ single crystal. The images are taken at 550 °C, at the two thermodynamic limits (the internal gas phase is in equilibrium with the external gas phase). In Figure 5-13B, at t = 0 s , the switch is made from 0.1% CO_2 / N_2 to 50% CO_2 / N_2 and in Figure 5-13C from 50% CO_2 / N_2 to 0.1% CO_2 / N_2. The final volume of the internal gas phase at 550 °C corresponds to the thermodynamic limit (shown in grey dashed line), suggesting that permeation is selective to CO_2. However, at 450 °C, this was not observed because the displacement was slower and did not reach equilibrium within the first 30 min. Similar behaviour was observed with the bubble shrinkage (Figure 5-13**C**).

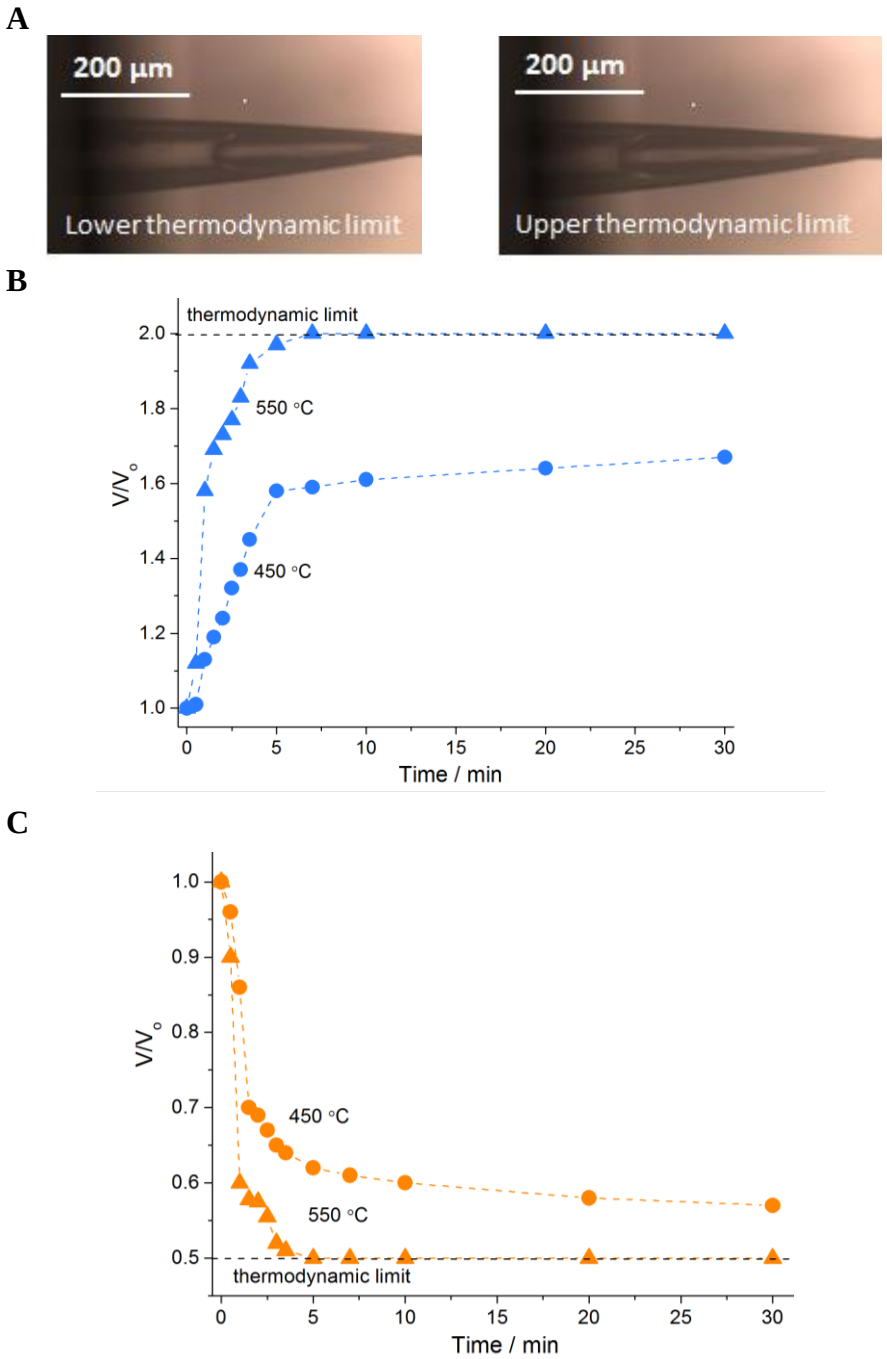

Figure 5-13. Concept of the moving meniscus to visualise an effect of permeation in a YSZ single pore. (A) shows the microscopic images of the meniscus formed at the theoretical thermodynamic limits achieved at 550 °C. As the external CO_2 concentration changes between 0.1 and 50 %, the concentration of CO_2 within the internal gas phase adapts to achieve equilibrium, resulting in a meniscus displacement **(B)** towards the mouth of the pore and **(C)** towards the closed end; the volume of the internal gas phase was monitored with time during, **(B)** external CO_2 concentration increase from 0.1 to 50 % and **(C)** external CO_2 concentration decrease from 50 to 0.1 %. The experiment was performed at 450 and 550 °C inside a single pore of a laser drilled YSZ single crystal. Dashed coloured lines are shown to aid the eye.

5.7 Calculation of permeation rates and driving forces from single-pore systems

The videos recorded with the meniscus displacement in the YSZ single crystal, were also analysed computationally by my colleague Dr Dragos Neagu with the use of Mathetica. The principle of the computational analysis is to convert the video into its constituent frames (videos recorded have 3.9 fps). The frames are then cropped around the area of interest (internal gas phase) and segmented based on pixel contrast. The cross-section of the area of interest resembles an elongated capsule. The cross-section area and corresponding capsule volume were then computed for an average of every 4 frames.

Figure 5-14 shows the variation of the normalised internal gas phase volume (V/V_o) calculated manually and computationally and the permeation rate versus time for the first 150 s of the meniscus displacement. At t = 0 s, as the external CO_2 concentration changes between 50 and 1.1%, the concentration of CO_2 in the internal gas phase adapts to achieve equilibrium, resulting in a volume decrease. The experiment was performed at 550 °C inside a single pore of the 100 μm laser drilled pore in the YSZ single crystal. The computational results compare reasonably well with the manual measurements and are lower than ±1%. The manual measurements were repeated at least 3 times. The most significant volume change occurs during the first 30 s of a change in the external gas phase composition. The permeation rate was calculated considering the internal gas phase volume change in a discrete time element (in this case 0.26 s). During this time increment, it is assumed that the permeation rate is constant even though it is a dynamic region where both the internal and external gas phase composition undergo changes. Due to very small volume changes the internal gas phase is undergoing (uncertainty increases), beyond 30 s the scatter in the permeation rates increases in this region, but there is still measurable decrease occurring. This region will not be considered for further calculations. A sensitivity analysis on the permeation rate, considering ±1% and ±20% errors on the determination of the internal gas phase volume are shown in Appendix E. It is shown that even up to ±20% errors have negligible impact on the permeation rates determined (the relative range has not changed significantly). Here, it is assumed that permeation is selective to CO_2, considering the high selectivity of molten carbonate membranes for CO_2 over N_2 [210]. This has also been confirmed by the thermodynamic limits studied in the previous section.

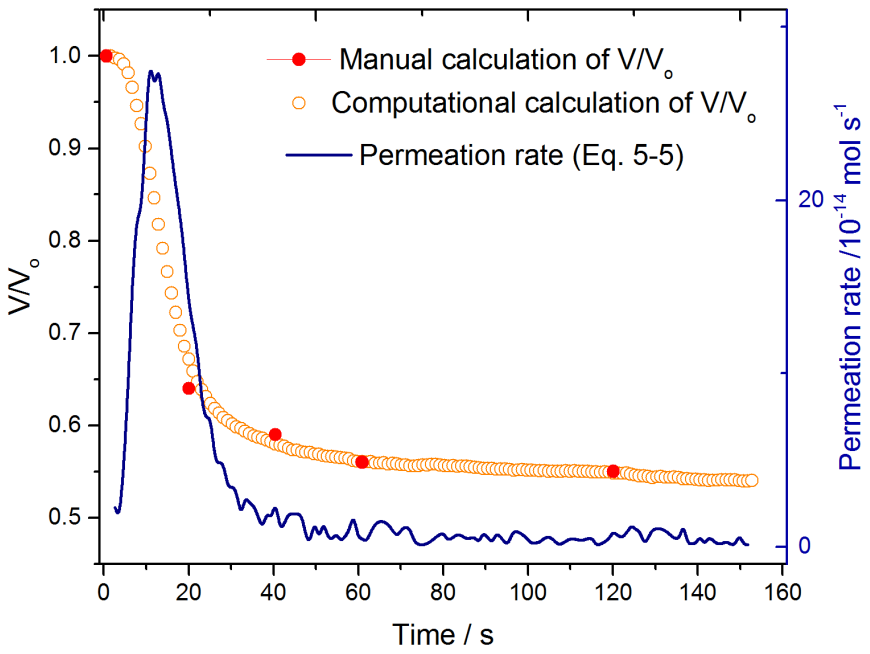

Figure 5-14. The variation of the normalised internal gas phase volume (V/V_0) calculated manually and computationally and the permeation rate versus time for the first 150 s of the meniscus displacement. At t = 0 s, as the external CO_2 concentration changes between 50 and 1.1 %, the concentration of CO_2 in the internal gas phase adapts to achieve equilibrium, resulting in a volume decrease. The experiment was performed at 550 °C inside a single pore of a laser drilled YSZ single crystal. Permeation rates were calculated with Eq. 5-5 and are based on the computational calculations for the volume changes of the internal gas phase.

The external gas phase (gas phase introduced to the cell) is changing along with the meniscus displacement as a function of time as calculated from the residence time distribution in Section 5.2. As mentioned in this chapter, the residence-time distribution of a reactor is a characteristic of the mixing that occurs, and it was found that the mole fraction of the external gas phase can be characterised by an exponential decay function ($y = y_0 + A_1 e^{-t/\lambda}$), where λ was found to be 0.366 when CO_2 concentration reduces and 0.725 when CO_2 concentration increases. The uncertainty on the decay constant is shown in Appendix E.

Figure 5-15 shows the CO_2 mole fraction in the internal and external gas phase and the resulting driving force ($\ln(p_{CO_2,\text{ external}}/p_{CO_2,\text{ internal}})$) as a function of time at 550 °C for switches between 1.1 % and 50% CO_2. The $p_{CO_2,\text{ external}}$ was calculated from the exponential decay equation for λ = 0.366, assuming that the gases are well mixed inside the cell. The $p_{CO_2,\text{ internal}}$ was calculated using Eq. 5-3 and the data from the computational analysis. The uncertainty of the CO_2 mole fraction in both the internal and external gas phase and a sensitivity analysis on the driving force assuming a 3 sec time lag between the internal and external gas phase

composition is presented in Appendix E. As shown in Appendix E, a time lag of 3 s, that could be caused due to relaxation phenomenon, would have a significant impact on the driving forces determined.

Interestingly, the driving forces shown in Figure 5-15 and permeation rates in Figure 5-14, show similar tendencies during the first 30 s of permeation, however, after the first 30 s surface limitations may be in control; driving forces increase and permeation rates decrease after the first 30 s.

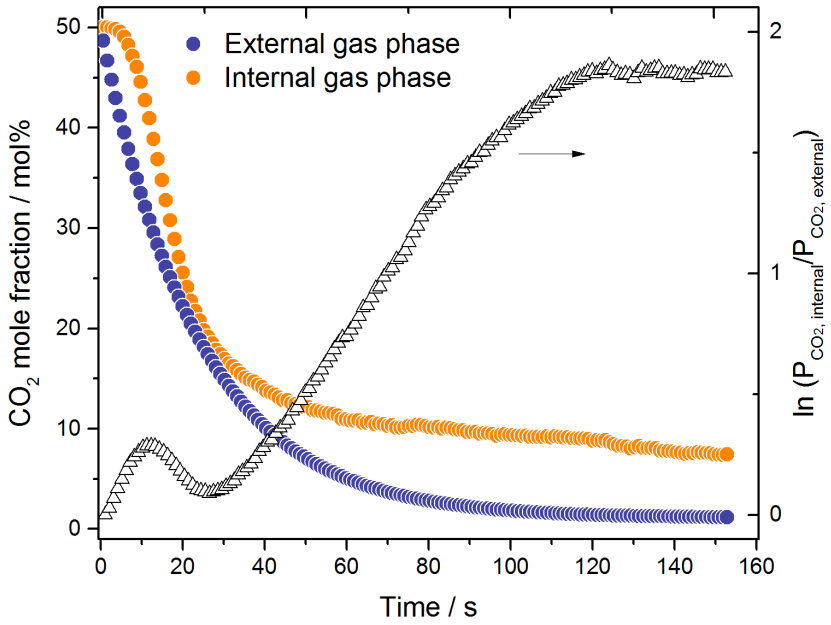

Figure 5-15. Driving force changes for the first 150 s of the meniscus displacement. $p_{CO_2,\ external}$ was extracted from the residence time distribution study, assuming that the gases are well mixed inside the cell. $p_{CO_2,\ internal}$ was calculated using Eq. 5-3 and the computational analysis for the volume variation.

Figure 5-16 shows the CO_2 flux in YSZ single crystal single pore and dual-phase ceramic membranes in literature [43, 50, 55, 57, 94, 100, 103, 106, 211] versus driving forces. Literature data are shown in black and dark blue, and they cover any kind of CO_2 membrane for CO_2 separation in the temperature range 500 - 900 °C. Single crystal permeation fluxes shown in this figure represent the transient concentration changes during the first 30 s of the meniscus displacement (computational analysis for the volume variation) with changes in the external phase gas between 1.1 and 50% CO_2 at 550 °C. The error bars in Figure 5-16 correspond to the uncertainties in driving forces estimated by the limits of the ranges on both internal and external gas phase compositions and a 3 s time lag between those gas phase compositions as discussed in Appendix E. The CO_2 flux was calculated using the average

permeation rate for the first 30 s with 5 sec intervals divided by the surface area of the single-pore mouth. The surface area of the mouth of the pore is the area assumed to be available for the sorption and desorption of CO_2. However, as CO_2 permeation at 550 °C is expected to be determined by the oxygen transport through the support, the permeation area would be the interfacial area between the carbonates and the YSZ support; the interfacial surface area is expected to be larger during shrinkage as the meniscus is closer to the mouth of the pore, which is the largest part of the conical shape. The interfacial surface area is estimated below using the Wagner transport theory. The differences between the fluxes extracted from the volume decrease of the internal gas phase (orange) and the volume increase of the internal gas phase (blue) can also be attributed to the different effective ionic transport pathway lengths. With the assumption that the bulk diffusion is the control mechanism, for the same driving forces, CO_2 flux would be inversely proportional to the effective ionic transport pathway length. For the results on single-pore systems presented, the thickness of the effective ionic transport pathway length can be considered to be the thickness of the molten carbonate meniscus. The thickness of the molten carbonate meniscus varied from 100 to 150 μm during shrinkage and from 200 to 300 μm during growth. Therefore, changes in the position of the meniscus can influence permeation by up to a factor of 3. Therefore, variations in both the CO_2 transport pathlength or meniscus position and the permeation area could account for the differences observed between shrinkage and growth.

One of the limitations here, is that the largest internal gas phase volume changes and hence the highest permeances with the lowest uncertainties, occur before the external gas phase composition reaches steady state. A further reduction of the size of the chamber could improve this. Another limitation is that one of the sides of the molten salt meniscus (the one closer to the mouth of the single pore) cannot be seen in the 2D images and therefore the ionic transport pathlength was assumed to be the distance between the single-pore mouth and the centre of the meniscus.

Single-pore single crystal experiments permit calculation of CO_2 flux at low driving forces ($\ln(p_{CO_2,\text{ external}}/p_{CO_2,\text{ internal}} < 2$) unobtainable in membrane permeation experiments. This is important because common membrane processes in a variety of applications, deal with low CO_2 driving forces. Moreover, kinetic studies can be conducted in a wider range of driving forces. By controlling the thermodynamic limits of the gas phases in a single-pore system, CO_2 flux can be extracted in a range of driving forces.

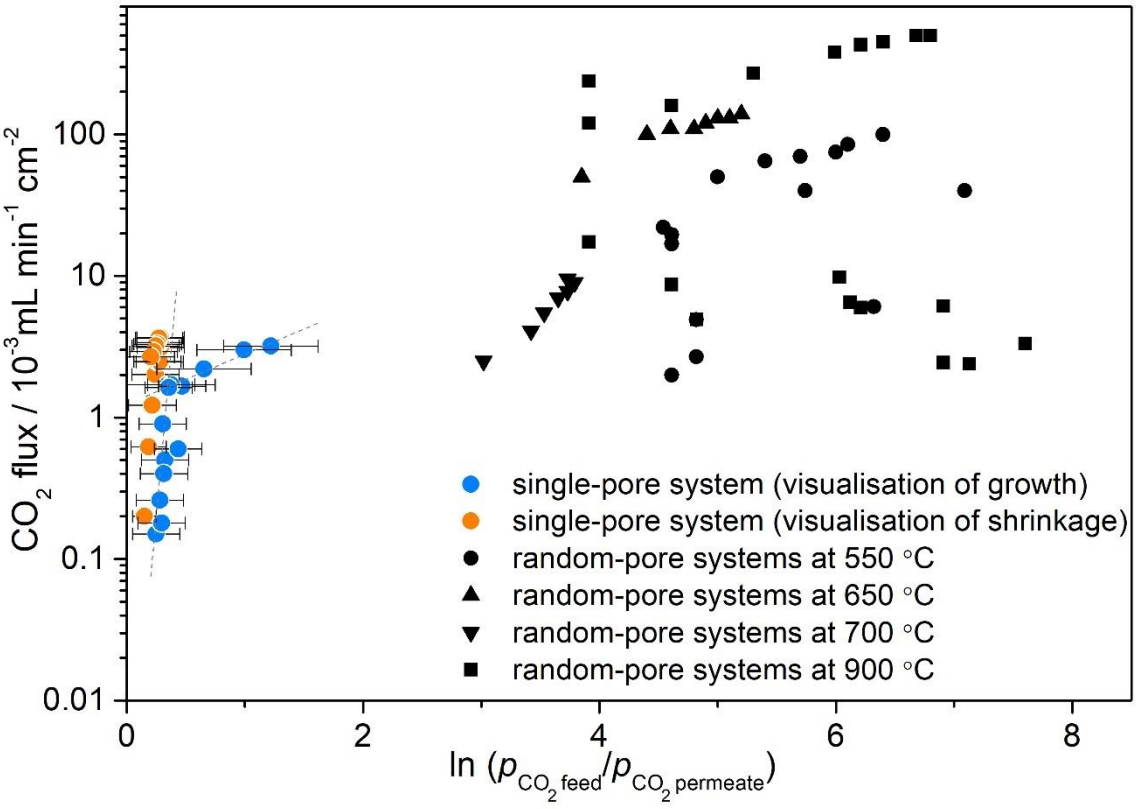

Figure 5-16. CO_2 flux in YSZ single crystal single pore and membranes in literature versus $\ln(P_{CO_2,feed}/P_{CO_2,permate})$. CO_2 flux with single-pore single crystal experiments (blue for growth and orange for shrinkage) at low driving forces and in literature (black). Literature data [41, 43, 55, 57, 94, 204, 212, 213] cover any kind of dual-phase membrane used for CO_2 separation in the temperature range 500 - 900 °C. Single crystal permeation fluxes were calculated during transient concentration changes in the external phase gas between 1.1 and 50% CO_2 at 550 °C.

As was found in Chapter 4, at temperatures below 600 °C the permeation is governed by oxide-ions transport. Therefore, it is likely that the permeation data shown for the single crystal and the random-pore systems at 550 °C in Figure 5-16, are in a regime of oxide-ion kinetic control. As shown in Figure 5-16 there is a shift in the rate determining regime at driving forces, $\ln(p_{CO_2,\,feed}/p_{CO_2,\,permeate})$, of 0.4. The slope of the fitted lines decreases with the increase of the driving force for the single-pore system. At low driving forces ($\ln(p_{CO_2,\,feed}/p_{CO_2,\,permeate}) < 0.4$) surface reaction limitations may be in control and therefore, the mechanism model (Eq. 2-18) that was based on Wagner transport theory (discussed in Section 2.3.4), does not apply here. When surface reaction limitations are in control, it is expected that the gas phase will have a steep gradient or discontinuity in the chemical potential of carbon dioxide between the gas phase and the initial layer at the membrane surface. The overall driving force of the membrane system will be controlled by the interfacial layer between the

gas phase and membrane surface and can be expressed in terms of concentration of carbon dioxide between the start and end of this interface.

At driving forces, $\ln(p_{CO_2,\,feed}/p_{CO_2,\,permeate})$, higher than 0.4, the mechanism model (Eq. 2-18) discussed in Section 2.3.4 could be applied. If Eq. 2-18 is considered and rearranged for $J_{CO_2}/ln\left(P''_{CO_2}/P'_{CO_2}\right)$ and $\frac{\varepsilon}{\tau} = 1$, the phase volume ratio that participates to CO_2 permeation can be calculated from the slope of the fitted line (0.0042 mL min^{-1} cm^{-2}, Eq. 5-9). The conductivity of the YSZ single crystal and carbonates is equal to 0.0012 S cm^{-1} and 0.978 S cm^{-1} at 550 °C respectively (conductivity values can be found in Chapter 2, Figure 2-6). The volume ratio, φ_c, was found to be 0.025 and the detailed calculations are shown in Eq. 5-10. With the assumption that the single pore can be described by a circular cone with a radius of 50 μm and a height of 550 μm, the pore volume will be equal to 1.44 x 10^{-6} cm^3. From the volume ratio calculated above and with the assumption that the carbonates have fully filled the pore, it is expected that a volume of 5.76 x 10^{-5} cm^3 of the YSZ single crystal participates to CO_2 permeation, which can be described by a ring with a thickness of 270 μm around the conical pore (assumption of an outer cone with the same height as the inner cone of the pore). Therefore, the total permeation area can be considered to be 0.003 cm^2 (area of the carbonate meniscus and the YSZ single crystal area around the pore). If the same calculations are then repeated using the simple mixing rule of the partial conductivities, $(\varphi_c\sigma_{CO_3^{2-}} + (1-\varphi_c)\sigma_{O^{2-}})$, then φ_c, will be equal to 0.01, which can be described by a ring with a thickness of 480 μm around the conical pore and the total permeation area can be considered to be 0.009 cm^2. As discussed in Chapter 4, the total conductivity of the dual-phase membrane is better described by the ambipolar conductivity at temperatures below 600 °C and therefore, the total permeation area will be considered to be 0.003 cm^2 for further calculations.

$$J_{CO_2}\Big/\ln\frac{P''_{CO_2}}{P'_{CO_2}} = -\frac{RT}{4F^2L}\left(\frac{\varphi_c\sigma_{CO_3^{2-}}(1-\varphi_c)\sigma_{O^{2-}}}{\varphi_c\sigma_{CO_3^{2-}} + (1-\varphi_c)\sigma_{O^{2-}}}\right) \qquad \text{Eq. 5-9}$$

$$\left. J_{CO_2} \middle/ \ln\frac{P''_{CO_2}}{P'_{CO_2}} \right. = 0.0042\ mL\ min^{-1}cm^{-2} =$$

$$= -\frac{RT}{4F^2L}\left(\frac{\varphi_c\sigma_{CO_3^{2-}}(1-\varphi_c)\sigma_{O^{2-}}}{\varphi_c\sigma_{CO_3^{2-}}+(1-\varphi_c)\sigma_{O^{2-}}}\right) =$$

$$= -\frac{8.314\frac{\mathrm{J}}{(\mathrm{K\,mol})}(550+273)\mathrm{K}}{4\left(9.6485\cdot\frac{10^4\ \mathrm{Coulomb}}{\mathrm{mol}}\right)^2 0.055\ cm}\cdot 22400\ \mathrm{ml\ mol^{-1}} \qquad \text{Eq. 5-10}$$

$$\cdot 60\ \mathrm{s}\,min^{-1}\left(\frac{\varphi_c\cdot 0.978\frac{S}{cm}\cdot(1-\varphi_c)\cdot 0.0005\frac{S}{cm}}{\varphi_c\cdot 0.978\frac{S}{cm}+(1-\varphi_c)\cdot 0.0005\frac{S}{cm}}\right)$$

$$\Leftrightarrow \varphi_c = 0.025$$

With the single-pore single crystal experiments, both the feed and permeate side are exposed to relatively high CO_2 partial pressures (1.1 and 50% CO_2) compared to the multiple-pore systems where pure argon is fed to the permeate side. Therefore, it is important to bear in mind that solid/gas interactions can change under different CO_2 partial pressures and the formation of other ions, such as lithium zirconate, might not be occurring here, as it is more likely to be formed on the side of the membrane that is exposed to very low CO_2 partial pressures during permeation experiments.

5.8 Multiple-pore single crystal

5.8.1 Morphology of multiple-pore single crystals and sealing method

CO_2 permeation study was extended to single crystals with multiple parallel pores to be compared to the single-pore single crystal experiments. In this work, dense YSZ single crystal-disks of 150 μm thickness were drilled with laser. Six disks were drilled with two different patterns and the specifications of the drilled samples are shown in

Table 5-1.

Table 5-1. Patterns drilled in YSZ single crystal disks.

Pattern	Number of pores	Pore diameter, μm	Thickness, μm	Surface area of pores*, 10^{-3} cm^2
1	100	45	150	1.6
2	100	75	150	4.4

* Surface area of pores is defined as the projected area of the pores on the membrane plane.

SEM images presenting the pore geometry of the multiple-pore single crystal support (pattern 1), obtained by laser drilling, are given in Figure 5-17. The pore diameter and centre-to-centre pitch are approximately 45 and 500 μm respectively.

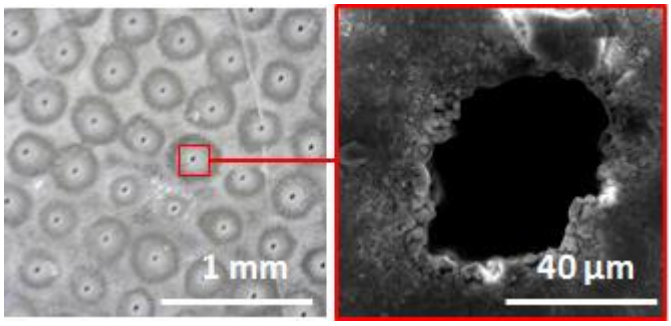

Figure 5-17. SEM images of the multiple-pore YSZ single crystal. The pore diameter and centre-to-centre pitch are approximately 45 and 500 μm respectively.

Permeation through multiple-pore single crystal samples can be tested using the conventional permeation experiments. The configuration of the reactor used is the same as the pellet reactor described in Chapter 3.5.1, however, due to the fragility of the samples, the sealing method has been slightly modified. The single crystal was mounted on a YSZ ceramic sleeve (short tube) with a silica-based water sealant (Ceys Masilla Refractaria) which was then mounted on the alumina tube used for the disk membranes as shown in Figure 5-18. The sleeve was added to reduce tensions coming from the thermal expansion of the sealant. More analytically, the silica-based water sealant that was used between the single crystal and the YSZ sleeve was cured by increasing the temperature to 80 °C for 30 min with 1 °C min^{-1} and then to 370 °C for 3 h with 3 °C min^{-1} (this was suggested by the manufacturer, no investigation of the appropriate conditions was conducted). The single crystal with the sleeve was then mounted on the alumina tube with an alumina based ceramic sealant from Aremco and it was allowed to dry in air for 24 h. A silicate thinner was then brushed around the ceramic sealant and allowed to dry for more than 24 h.

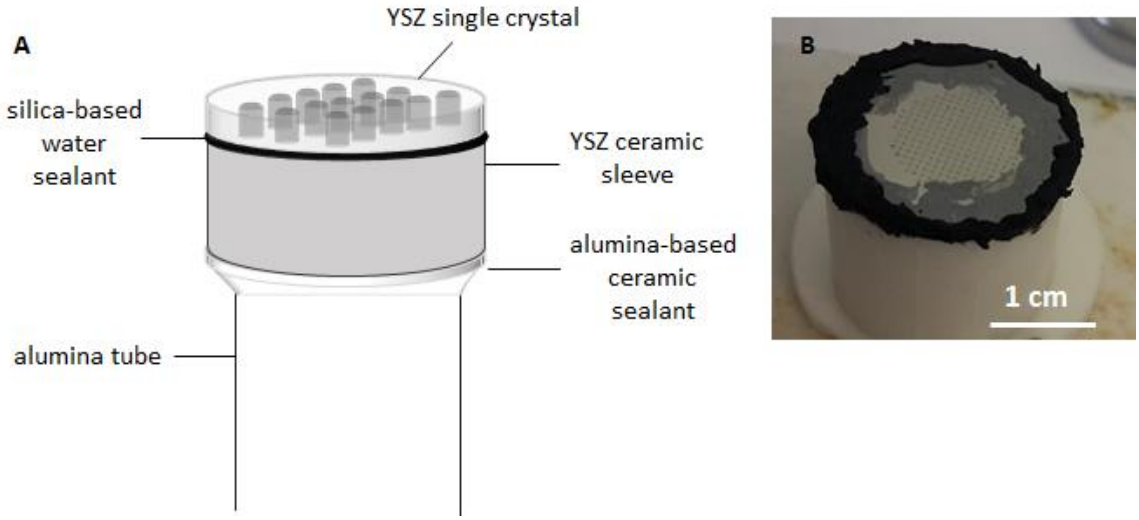

Figure 5-18. The single crystal-membrane configuration. (A) schematic of the multiple-pore YSZ single crystal membrane mounted on the alumina tube using a YSZ ceramic sleeve and two types of sealants and **(B)** the image of the sample mounted on the sleeve.

5.8.2 CO_2 permeances and comparison with single-pore systems

Difficulty has been encountered in the testing of the multiple-pore single crystals due to their high cost and low mechanical stability. Due to laser drilling limitations, the thickness of the single crystals was kept to 150 μm, however, at those thicknesses the samples were very fragile. Only two samples (samples with pattern 2 from

Table 5-1) survived during permeation experiments, from which one was tested at 550 °C and the other one at 600 °C. The conditions used, were the same as for the membranes in Chapter 4 (the inlet gas on the feed side of the membrane was a mixture of CO_2 and N_2 in a 1:1 volume and pure Ar on the permeate side, 30 mL (STP)/min flow rate).

Figure 5-19 shows logarithmic permeances against temperature, calculated for the YSZ single-pore system, multiple-pore system and literature. Logarithmic permeances are used here in order to investigate the applicability of the modified Wagner equation. In this figure, the data for the single-pore single crystal represent the mean permeances extracted from the computational volume calculations during the first 30 s of the meniscus. The error bars for the single-pore single crystal system correspond to the associated standard deviations over the average of the permeances calculated during the first 30 s of the meniscus displacement. The deviation on the permeances includes the driving force and diffusional path length changes during the first 30 s of the meniscus displacement, but also uncertainties on the surface area involved in permeation. The permeances are calculated using both the surface area of the single-pore mouth (dark-shade blue and orange symbols, 7.9 x 10^{-5} cm^2) and the theoretical surface area calculated in section 5.7, (semi-transparent symbols, 0.003 cm^2) as predicted by the ambipolar conductivity. Permeances through single-pore single crystals calculated using the pore mouth as the permeation area, compare well with those reported in literature by Lu et al [43] with thin supported membranes (10 μm thickness). However, those permeances are calculated for a lot higher driving forces ($\ln(P_{CO_2,feed}/P_{CO_2,permate})$>3) compared to those studied for the single-pore systems ($\ln(P_{CO_2,feed}/P_{CO_2,permate})$<1). The error bars indicate the errors in the determination of the permeances due to permeation rate and driving force uncertainties, analytically explained in Appendix E.

Similarly, permeances for the multiple-pore system are calculated using both the surface area of the pores (dark-shade red symbols, defined as the projected area of the pores on the membrane plane ≈ 4.4 x 10^{-3} cm^2) and the total permeation area using the phase volume ratio predicted by the conductivities (0.22 cm^2). However, the surface area of the carbonates is very likely to be higher than the surface area of the drilled pores because cracks were observed at the end of the experiments and, any crack propagation between the pores during permeation could have been self-healed by carbonates. Cracks were estimated to have a surface area in the same order of magnitude as the hole surface area. Even though, the first N_2 trans-membrane leaks were observed during the first hour of plateau at 550 and 600 °C for each sample and therefore, the calculations will not consider those cracks. Permeances corrected to

the predicted permeation area for the multiple-pore single crystal, were in a good agreement with the those reported in literature by Lu et al [43]. In this work [43], supported thin membranes (10 μm) were used with same inlet CO_2 partial pressures on both sides of the membrane. Therefore, comparison of the two systems seems more reasonable. The single-pore system is the simplest system in terms of geometry; however, it is a very complex system in terms of permeance as it is calculated for a range of driving forces with a shift in the rate determining regime.

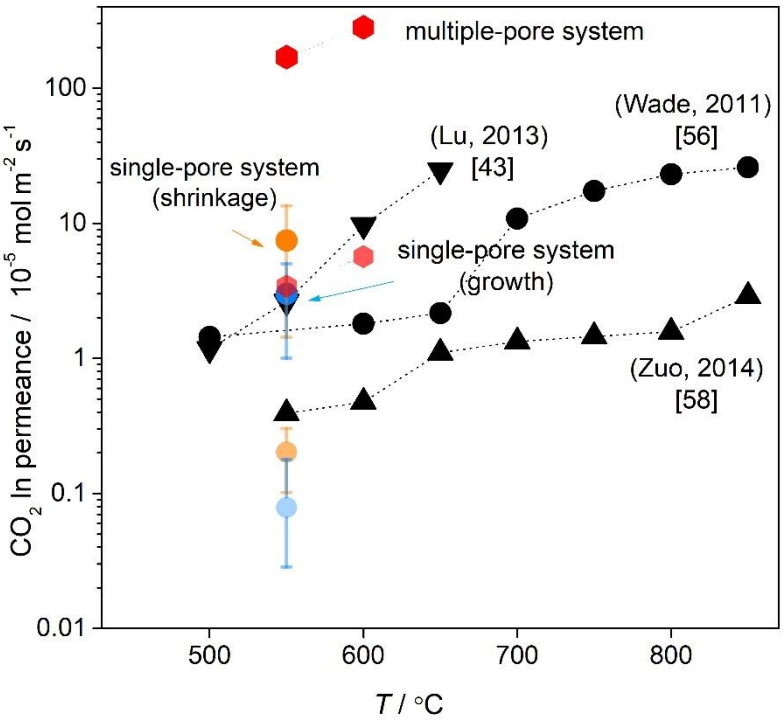

Figure 5-19. CO_2 logarithmic permeance versus temperature for YSZ single crystal membranes with multi- and single-pore microstructures and for membranes in literature. The logarithmic permeance is normalised to the $\mathbf{ln(P_{CO_2,feed}/P_{CO_2,permate})}$. Error bars for the single-pore single crystal system correspond to the associated standard deviations over the average of the permeances calculated during the first 30 s of the meniscus displacement. The logarithmic permeances for the multiple pore system have been calculated using the carbonate surface (4.4 x 10^{-3} cm^2).

5.9 Conclusions

The transparent nature of the crystal allows the use of microscopy techniques, and this is the first visualisation technique used to *in situ* observe an effect of CO_2 permeation. The single

crystal single pore experiments permit calculation of CO_2 flux at low driving forces ($\ln(p_{CO_2,\,feed}/p_{CO_2,\,permeate}) < 2$) unobtainable in conventional membrane permeation experiments. This is the first study reporting CO_2 fluxes at such low driving forces, which can only be obtained with this setup. In a real membrane system, those driving forces are more likely to be found in a practical application.

The findings of this study provide a new understanding on the effect of CO_2 partial pressure on CO_2 permeation. This study suggests that there is a shift in the rate determining regime at driving forces, $\ln(p_{CO_2,\,feed}/p_{CO_2,\,permeate})$, of 0.4 at 550 °C. At driving forces below 0.4, the flux and the logarithmic CO_2 partial pressure difference across the membrane showed a non-proportional linear relationship. At those driving forces, the surface reaction limitations may be in control. At driving forces higher than 0.4, flux is proportional to the natural logarithmic CO_2 partial pressure difference across the membrane. This is in a good agreement with previous studies for driving forces, $\ln(p_{CO_2,\,feed}/p_{CO_2,\,permeate})$, between 3 and 8, however, this range was extended to lower values of driving forces. The modified Wagner equation was then used to calculate the volume ratio of the YSZ support that participates to CO_2 permeation, and hence the permeation area was extracted. This theory emerged as a reliable predictor of the permeation area, because it showed that permeances corrected to this predicted permeation area, were in a good agreement with those reported in literature for similar systems (thin membranes with same CO_2 partial pressures on the inlet streams of both sides of the membrane). Returning to the findings of the previous chapter, it is now possible to suggest that at 550 °C, the kinetics are governed by oxide-ions transport and permeation proceeds via the diffusion of charged species at driving forces, $\ln(p_{CO_2,\,feed}/p_{CO_2,\,permeate})$, higher than 0.4, however, surface limitations are in control below those driving forces.

Due to the optically transparent nature of the single crystals used, Raman spectroscopy was also employed *in situ* to identify and quantify the chemical compounds that may be formed in the liquid phase and to quantify the moles of CO_2 in the internal gas phase (gas phase behind the meniscus or inside a gas bubble). Preliminary work is shown in Appendix D, mainly as a suggestion for a route to gain mechanistic insight into the mechanism of CO_2 permeation through dual-phase membranes and to highlight the possibility of using the visualisation principle as a new tool to study gas permeation. Further investigation and experimentation into *in situ* Raman spectroscopy are required.

Chapter 6
Closed-end tubes with parallel pore network

6.1 Introduction

One of the main advantages of laser drilling is the possibility of controlling the pore microstructure. As discussed in the previous chapter, multiple-pore single crystals were very fragile, and the effect of different pore sizes could not be studied. Therefore, the next step would be to work with polycrystalline supports and avoid the use of a hot seal. For this reason, polycrystalline closed-end tubes were drilled with laser, which is a major design change that does not require a hot seal. From a fundamental point of view, the absence of leaks can increase the quality of mechanistic/kinetic data that one can extract.

6.2 Tubes with different pore patterns

6.2.1 Characterisation of the closed-end tubes

Parallel pores were laser drilled perpendicularly to the polished closed-end alumina and YSZ tubes at Laser Micromachining Limited (LML). Figure 6-1A and B show images of the Al_2O_3 closed-end tube before and after drilling, respectively. Figure 6-1C shows the schematic of the closed-end tube. The terms "top surface" and "bottom surface" have been used to refer to the laser-incident surface and the opposite surface, respectively. Due to the inherent Gaussian shape of the laser beam, the pores exhibit a truncated conical shape, with a diameter of 220 μm (Figure 6-1D) on the top surface and an average diameter of 75 μm on the bottom surface for the Al_2O_3 closed-end tube. Due to the corner radius of 1 mm, as seen in the cross-section image (Figure 6-1E), only approximately 900 pores are through channels. Additionally, due to the variation in thickness (400 - 700 μm) of the drilled end of the tube, as seen in the cross-section image (Figure 6-1E), the diameter of the through pores on the bottom surface was varied from 25 μm to 105μm. The pore-pattern specifications of the Al_2O_3 and YSZ closed-end tubes, calculated from the micro-CT image analysis and the digital image analysis respectively, are summarised in Table 6-1. The effective volume of the tube is considered to be the base of the tube, assuming the shape of a disk with a thickness of 0.68 mm and a diameter of 12 mm.

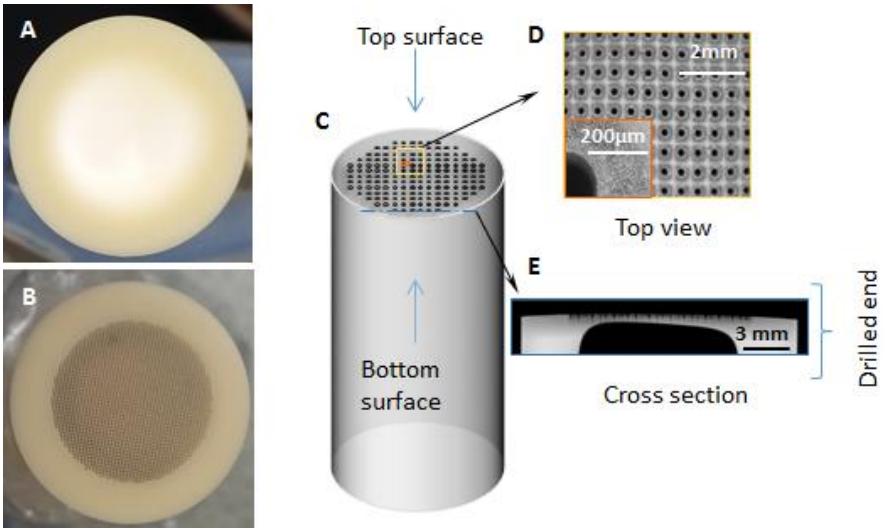

Figure 6-1. Al_2O_3 closed-end tube images and schematic. Images of the closed end of the tube **(A)** after polishing and **(B)** after drilling. **(C)** Schematic of the closed-end tube indicating the top and bottom surface of the closed-end tube. **(D)** SEM images of the surface of the top surface. **(E)** Micro-CT image of the cross section of the drilled end of the tube.

Table 6-1. Pore-patterns of the closed-end tube supports. The values have been calculated from the micro-CT and digital image analysis.

Al_2O_3 (micro-CT image analysis)	
Total number of pores	2022
Number of through pores	900 ± 50
Average diameter of pores on the bottom surface of the membrane, mm	0.075 ± 0.03
Average diameter of pores on top surface of the membrane, mm	0.220 ± 0.02
Centre-to-centre pitch of pores, mm	0.25
Average base thickness, mm	0.68 ± 0.12
Total volume of pores, mm^3	18
Surface area of the pores on the bottom surface, mm^2	3.9 ± 0.2
Surface area of the open pores on the top surface, mm^2	34.2 ± 1.9
Carbonate volume fraction, φ_C (considering only the effective volume of the tube)	0.53
YSZ_1 (digital image analysis)	
Total number of pores	1000
Average diameter of pores on top surface of the membrane, mm	0.15
Centre-to-centre pitch of pores, mm	0.35

Surface area of the pores on the top surface, mm^2	18
Carbonate volume fraction, φ_C (considering only the effective volume of the tube and assuming cylindrical pores)	0.35
YSZ_2 (digital image analysis)	
Total number of pores	500
Average diameter of pores on top surface of the membrane, mm	0.30
Centre-to-centre pitch of pores, mm	0.50
Surface area of the pores on the top surface, mm^2	35
Carbonate volume fraction, φ_C (considering only the effective volume of the tube and assuming cylindrical pores)	0.71

Although this chapter will only demonstrate part of the experimental work that was performed with the closed-end tube membranes, it is important to emphasize that the Al_2O_3 closed-end tube membrane is a very robust membrane that was operated for more than 50 days. The conditions under which the membrane was operated are shown in Appendix F.

6.2.2 Permeation rates from Al_2O_3 and YSZ closed-end tube

The CO_2 permeation rates measured through the Al_2O_3 and YSZ closed-end tubes are shown in **Figure 6-2A** as a function of temperature. With the assumption that YSZ_1 and YSZ_2 closed-end tubes are fully infiltrated, and no excess of carbonates covers the top or bottom surface of the drilled end, it can be said that the triple phase boundary of the pores is the same for both tubes (on the top surface only, specifications of the bottom surface are not known) and the total surface area of the carbonates within the pores of the YSZ_2 is two times higher than that of the YSZ_1. By comparing the permeation rates between YSZ_1 and YSZ_2 membranes, it could be suggested that permeation rate is controlled by the surface area of the carbonates and not by the triple phase boundary. However, there is high uncertainty associated with these results for many possible reasons. One possible reason that contributes to this uncertainty, is that carbonates may have covered part of the top or bottom surface and consequently the triple phase boundary and surface area of the pores cannot be defined by the pore geometry. Moreover, the specifications of the bottom surface are not known, and some pores are likely to be blind as was shown from the micro-CT of the Al_2O_3 closed-end tube. The measurement repeatability could not be verified, because both tubes appeared with cracks after cooling, adding even more uncertainty to the results obtained.

Al_2O_3 and YSZ_2 closed-end tube closed-end tube have comparable carbonate volume fractions and same surface area of carbonates on the top surface. However, as shown in Figure 6-2A, Al_2O_3 showed much lower permeation rates than the YSZ membranes at all temperatures. This finding is contrary to the results found in Chapter 4, where no significant differences were observed between YSZ-carbonate and Al_2O_3-carbonate membranes at temperatures below 600 °C. This highlights even more the importance of the microstructural characteristics of the membrane, which could not be controlled in Chapter 4 and had a very strong impact on the membrane performance. The results shown in **Figure 6-2A**, suggest that the ionic conductivity of the YSZ supports clearly promotes CO_2 permeation from temperatures above 450 °C.

Figure 6-2B shows the Arrhenius plot used to calculate the activation energy for CO_2 permeation. The activation energies for CO_2 permeation through both YSZ tubes were very similar with an average of 57 kJ mol^{-1} below 600 °C, and for the Al_2O_3 tube it was around 35 kJ mol^{-1} at temperatures between 400 and 700 °C. In Chapter 4, the shift in activation energy for the YSZ supports was observed at temperatures above 600 °C, which supports the results found here (Figure 6-2B) for steady activation energies below 600 °C. The activation energies in Chapter 4 were found to be in the range of 64 - 86 kJ mol^{-1} which is approximately 25% higher than the values found here (53 - 60 kJ mol^{-1}). However, if only the lower activation energy values are considered from Chapter 4 (for freeze casted and powder pressed membranes), then it can be said that the results compare well to those found here. For example, differences of 13% in the activation energies could be explained by the differences in carbonate volume fractions, φ_C, (approximately 0.35 and 0.71 for the YSZ_1 and YSZ_2 respectively) between membranes. The activation energy was higher for the lower carbonate volume fraction as expected, knowing that the activation energy of the support is a lot higher than that of the carbonates. As discussed before, those values are typically found for kinetics governed by oxide-ions transport. For the Al_2O_3 - carbonate membrane, the activation energy value of 35 kJ mol^{-1} indicates that permeation is controlled by mixed kinetics as the values are a bit higher than those expected for carbonate-ion controlled kinetics (around 20 kJ mol^{-1} [78, 205]). If those energies are then compared to those found in Chapter 4, it can be said that they are approximately 40% lower than those found in Chapter 4 (55 - 65 kJ mol^{-1}). This discrepancy could be attributed to the formation of carbonate film on the base of the tubes which could cover part of the support; infiltration was challenging with the closed-end tubes, because they require a very small amount of carbonates (< 0.04 g) and some excess was used to ensure that all the pores were covered.

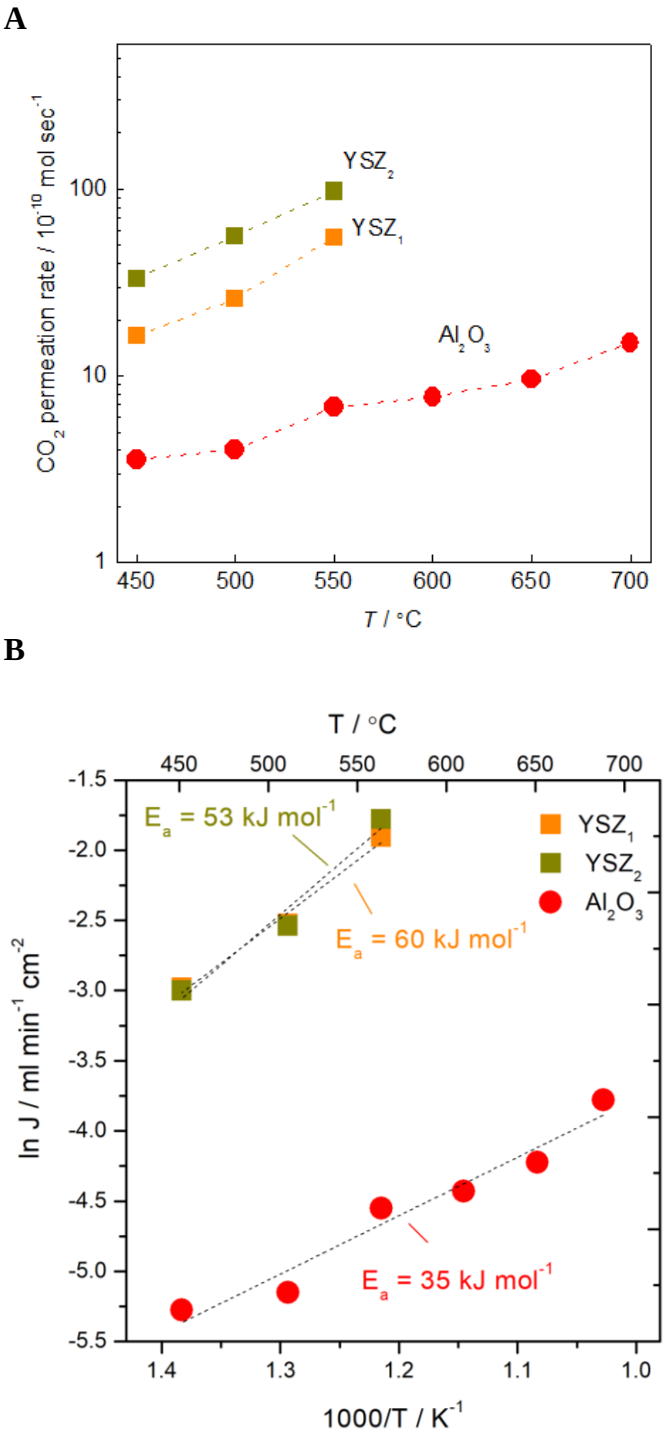

Figure 6-2. (A) CO_2 permeation rates (logarithmic scale) against temperature and (B) the Arrhenius plot for CO_2 flux through the YSZ and Al_2O_3 closed-end tube membranes. The feed-side inlet used was 50%CO_2/N_2 and the permeate side inlet was Ar. All membranes were infiltrated with the same amount of carbonates (approximately 0.045 g).

The CO_2 permeability through those membranes was also calculated and compared to the theoretical permeability for the solution diffusion process (discussed in Section 2.2), where the permeation is a result of the diffusivity and solubility of CO_2 inside the melt. The results our shown in Figure 6-3 and it is found that the theoretical permeability for the solution

diffusion process is comparable to the experimental CO_2 permeability calculated for the Al_2O_3 – carbonate membrane. This could suggest that permeation occurred through surface ionisation of CO_2 at the CO_2/carbonate interface and diffusion through the melt. The formation of other ions that was suggested in Chapter 4, seems to be minor with the closed-end tubes, which could be due to the formation of a thin film of carbonates on the top surface of the base of the tube as explained above.

It can be argued that permeation measured through dual-phase membranes is a result of the molar hold up of the carbonates, releasing CO_2 through the decomposition reaction. For this reason, the permeation of the membrane was tested continuously over a period of 250 h as shown in Appendix G. Over this period, the temperature, gas phase compositions and water content were varied, and the average permeation rate measured was approximately 1×10^{-9} mol s^{-1}. Therefore, the molar amount of CO_2 permeated during the 250 h will be 8.3×10^{-4} mol. By comparing this to the molar hold up of the carbonates (0.045 g or 4.5×10^{-4} mol since the average molecular weight of carbonates is 100 g mol^{-1}), it can be proved that the carbonate decomposition cannot account for the CO_2 permeation.

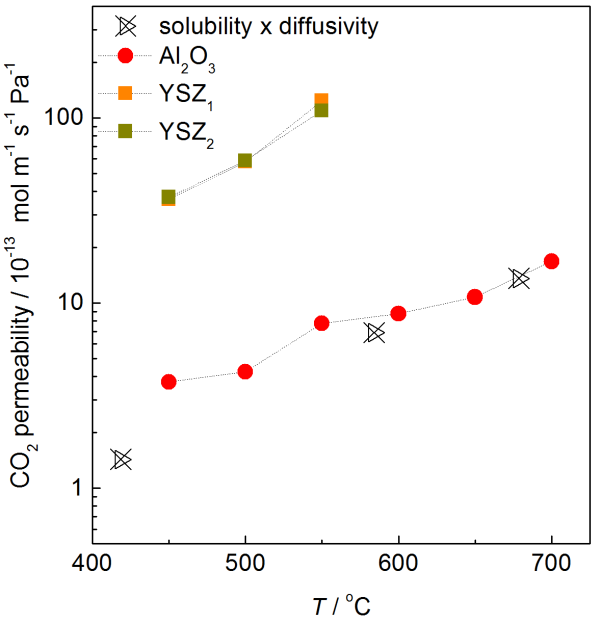

Figure 6-3. CO_2 permeability through the YSZ and Al_2O_3 closed-end tube membranes. The theoretical permeability is calculated through the solubility and diffusivity of CO_2 in the melt that has been measured in literature by the elution [86] and chronopotentiometry method [91] respectively (more details in Chapter 2.2.2).

To improve upon understanding on CO_2 permeation through the Al_2O_3 closed-end tube membrane, the direction of CO_2 permeation was reversed by feeding the feed-side gas ($50\%CO_2/N_2$) to the permeate-side chamber and the permeate-side gas (Ar) to the feed-side chamber. Due to the conical shape of the pores, the total surface area of the pores on the top surface is larger than the surface area of the pores on the bottom surface of the membrane (assuming that only the pores were filled with carbonates), and by reversing the two inlets, an indication on whether CO_2 permeation is limited by CO_2 consumption or CO_2 evolution through the melt could be extracted. Those two reactions can be kinetically distinct as they have different controlling transition states and reaction orders. As suggested above, permeation is expected to be controlled by mixed kinetics at these temperatures, and therefore, it is expected that the direction of the flow could have some impact on permeation. The concentration of different ions formed in the liquid could depend on the carbonate/ceramic volume ratio. Figure 6-4 shows that at temperatures above 600 °C, CO_2 permeation increases when CO_2 is evolved from the greater channel area (top surface), indicating that CO_2 permeation is limited by the CO_2 evolution from the melt above 600 °C. Experiments were repeated 2-3 times, however, the error bars are not shown here as they are smaller than the symbols.

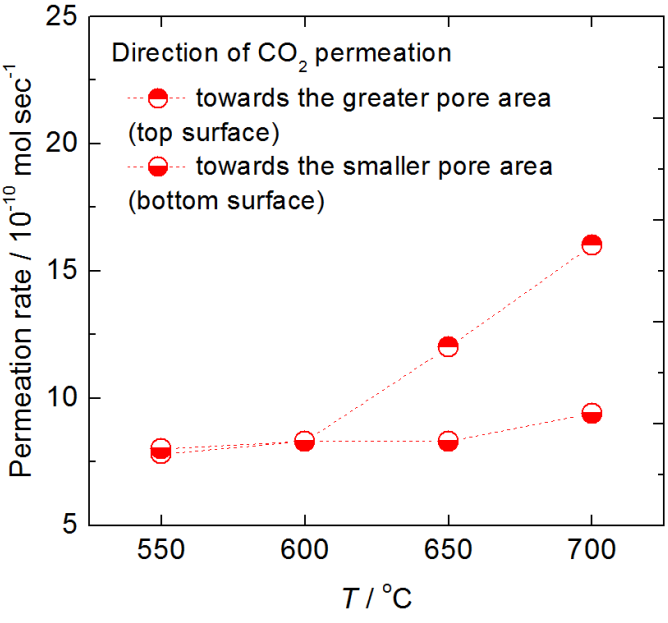

Figure 6-4. CO_2 permeation rate against temperature through the Al_2O_3 closed-end tube for both directions of permeation. The inlets on the two sides of the membrane were $50\%CO_2/N_2$ and Ar. The total area of the pores on the top surface is 34.2 mm^2 and on the bottom surface is 3.9 mm^2. Experiments were repeated 2-3 times and the error bars that correspond to the standard deviation of the repeats are smaller than the symbols.

6.3 Effect of CO_2 partial pressure on the permeation rate

6.3.1 Al_2O_3 closed-end tube

CO_2 partial pressure gradient across the membrane provides the driving force for the CO_2 transport across dual-phase membranes. Therefore, if the CO_2 partial pressure on each side of the membrane is varied, information about the effect of driving force on permeation can be obtained. Figure 6-5 shows the effect of the CO_2 partial pressure difference across the Al_2O_3 - carbonate membrane on the CO_2 permeation rate at 550 and 700 °C. The $p_{CO_2,feed}$ and $p_{CO_2,permeate}$ represent the CO_2 partial pressure in the outlet of the feed and permeate side respectively. The feed-side inlet gas composition was varied from 25 to 90%CO_2 / N_2 and the permeate side inlet compositions used were Ar, 440 ppm CO_2 / Ar, and 1%CO_2 / Ar. At both temperatures, the increase of the CO_2 partial pressure in the inlet of the feed or permeate stream results in a larger driving force, and therefore, an increase in CO_2 permeation flux. However, the prediction that CO_2 permeation is proportional to the natural logarithmic CO_2 partial pressure difference across the membrane can only be applied at 700 °C for the driving forces studied here. Even though there was no apparent change on the activation energy of alumina-carbonate membrane at temperatures between 550 and 700 °C, it can be said that from the below data, CO_2 permeation is generally limited by the diffusion in the melt at 700 °C and reaction limited at the gas-melt interface at 550 °C.

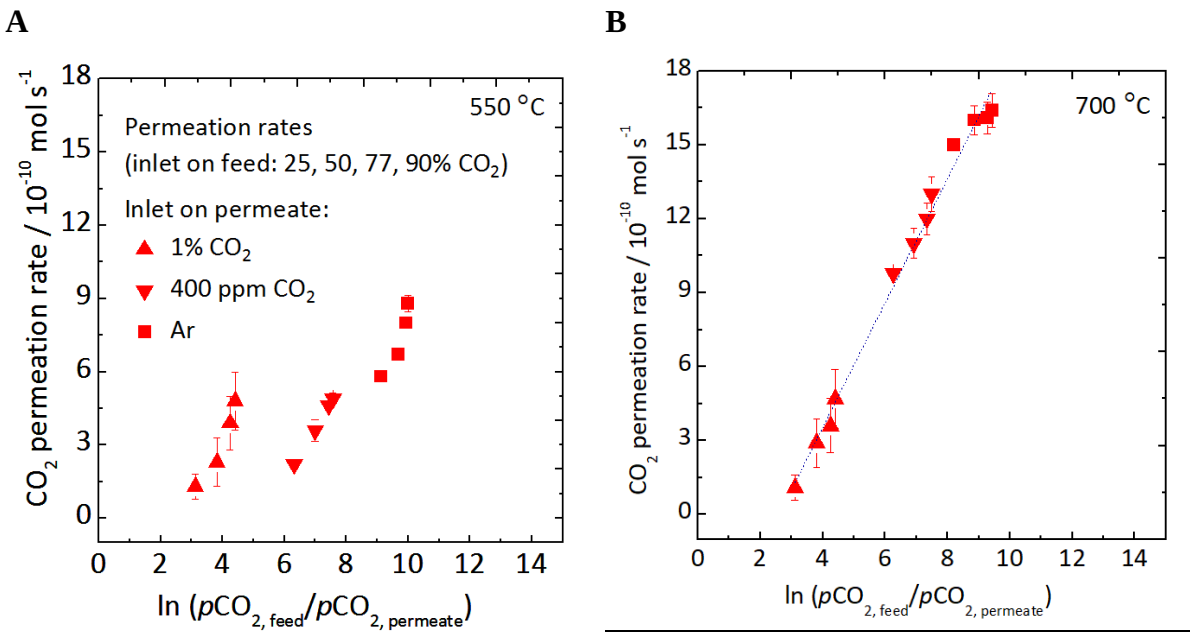

Figure 6-5. CO_2 permeation rate calculated from the CO_2 mole fraction increase in the permeate-side outlet at 550 and 700 °C against the logarithmic partial pressure difference of CO_2 between the feed and permeate side outlet through the Al_2O_3 closed-end tube. Symbols show the composition of the permeate-side inlet and the feed side inlet was varied from 25 to 90% CO_2 / N_2. The increase of the permeation rate for the same permeate side inlet compositions corresponds to the increase of CO_2 mole fraction on the feed side inlet. Experiments were repeated 4-5 times and the error bars correspond to the standard deviation of the repeats.

6.3.2 YSZ closed-end tube

Figure 6-6 shows the effect of the CO_2 partial pressure difference across the YSZ_2-carbonate membrane on the CO_2 permeation rate at 550 °C. The feed side inlet gas composition was varied from 25 to 90% CO_2 / N_2 and the permeate side inlet compositions used were Ar, and 1%CO_2 /Ar. Figure 6-6 gives a straight line, showing some agreement with Eq. 2-10, which was used to describe a bulk diffusion control mechanism, and this could indicate that CO_2 permeation is generally limited by the diffusion in the melt across the YSZ_1-carbonate membrane at 550 °C. As discussed before, from the activation energy data, permeation is controlled by oxide-ions transport at 550 °C. If Eq. 2-18 (equation based on Wagner transport theory) is applied here, the volume fraction of YSZ participating to CO_2 permeation can be calculated. The theoretical carbonate volume fraction, φ_c, of the YSZ_2-carbonate membrane calculated with Eq. 2-18, was found to be 0.8 which is very close to carbonate volume fraction that was calculated considering only the effective volume of the tube and assuming cylindrical pores (φ_c= 0.71).

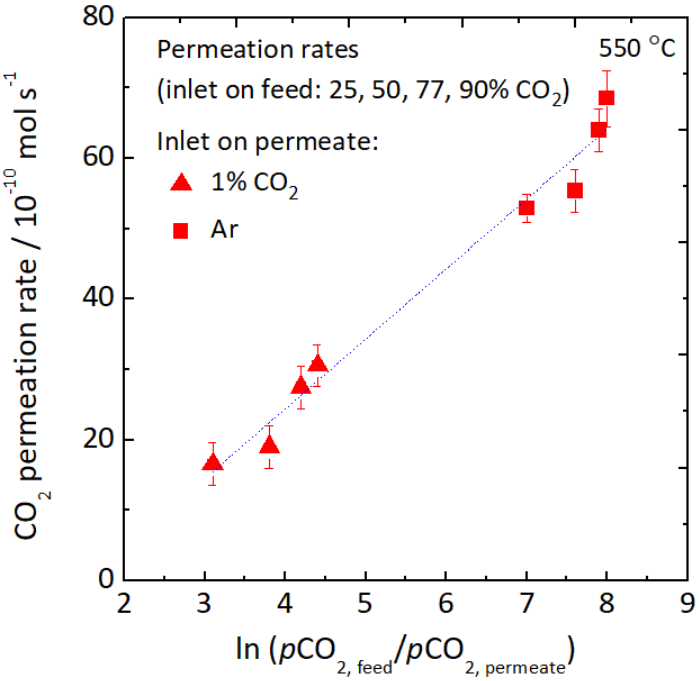

Figure 6-6. CO_2 permeation rate calculated from the CO_2 mole fraction increase in the permeate-side outlet at 550 °C against the logarithmic partial pressure difference of CO_2 between the feed and permeate side outlet through the YSZ closed-end tube. Symbols show the composition of the permeate-side inlet and the feed side inlet was varied from 25 to 90%CO_2 /N_2. The increase of the permeation rate for the same permeate side inlet compositions corresponds to the increase of CO_2 mole fraction on the feed side inlet. Experiments could not be repeated as the membranes cracked during this experiment.

6.4 Effect of water on the permeation rate

The presence of water in CO_2 streams was found that it is promoting CO_2 permeation through ceramic dual-phase membranes [47] as described in the Introduction and in Chapter 2. It was suggested that this is a result of the formation of a counter ion, OH^-, transported though the molten salt. It has been shown that water increases permeation flux through a CeO_2 - carbonate membrane by 250 - 300% when 2.5% water was fed to the permeate stream and by 30% when fed to feed stream. In this work, the influence of water on CO_2 permeation was studied through a dual-phase membrane consisting of an inert support (Al_2O_3) by comparing CO_2 permeation rate under dry streams (Figure 6-7A) and under humidified streams. 3.5% water was introduced with the feed-side gas (Figure 6-7B) or with the permeate-side gas

(Figure 6-7C). Water permeation was also measured at the opposite side. The schematics in Figure 6-7D, E and F represent the dual-phase membranes and the conditions used for the plots shown in Figure 6-7A, B and C respectively. The presence of water on the feed side of the membrane gives a negligible influence on CO_2 permeation and no water permeation was observed, which contrasts with what was observed by Xing et al [47]. However, when water is introduced to the permeate side, CO_2 permeation increases significantly, up to about 750%. Moreover, the corresponding amount of the permeated CO_2 is equal to the amount of the permeated H_2O (Figure 6-7C). The inconsistency between the findings of this work with the reference [47] could be a result of the poorly sealed membrane system they used, where leaks can limit the quality of mechanistic data that one can extract. The main advantage of the new membrane system design used in this work is that the data can be a lot more reliable due to the absence of leaks.

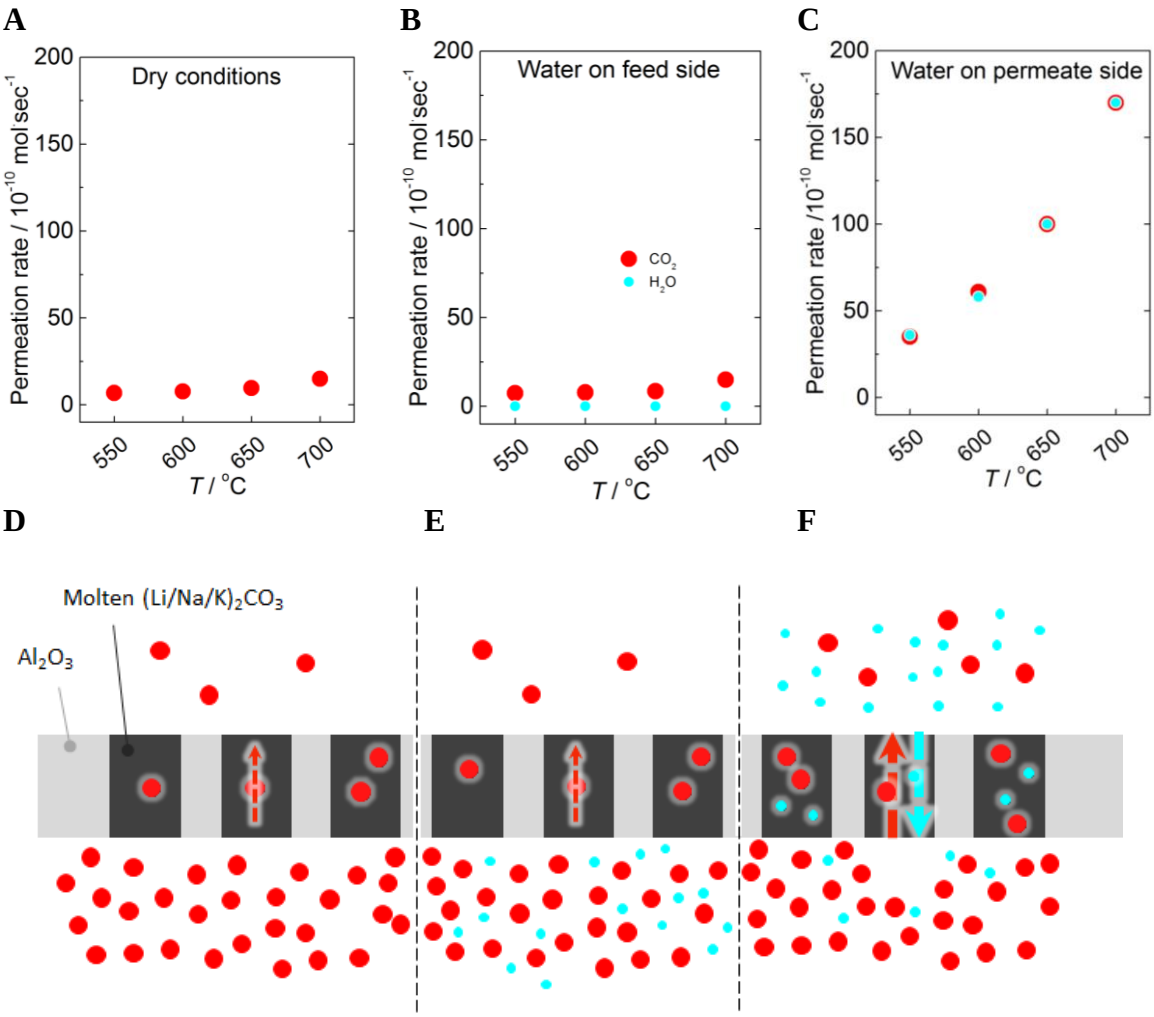

Figure 6-7. CO_2 and H_2O permeation rate as a function of temperature under dry and humidified conditions and the schematic of the Al_2O_3 closed-end tube support and molten carbonate mixture membrane. (A) the feed-side inlet was argon and the permeate-

side inlet was 50%CO_2/N_2. Dry conditions represent the condition when the water content is less than 100 ppm on both sides of the membrane (water content within the cylinders). **(B)** the feed-side inlet was 50%CO_2/N_2 with 3.5% and the permeate-side inlet was argon. **(C)** the feed-side inlet was 50%CO_2/N_2 and the permeate-side inlet was argon with 3.5% H_2O. CO_2 permeation is promoted by the presence of water on the permeate side. **(D)**, **(E)** and **(F)** are the schematics of the Al_2O_3 closed-end tube support and molten carbonate mixture membrane for **(A)**, **(B)** and **(C)** respectively. Experiments were repeated 3-4 times and the error bars that correspond to the standard deviation of the repeats are smaller than the symbols.

The activation energies of CO_2 permeation under dry and humidified streams through the Al_2O_3-carbonate membrane were calculated using the Arrhenius plot in Figure 6-8. The activation energy for CO_2 permeation calculated when the feed-side inlet is 50%CO_2/N_2 and the permeate side inlet is Ar with 3.5% H_2O was double the activation energy calculated under the same testing conditions but with the absence of water. This means that the mechanism for CO_2 permeation changes when water is introduced, and permeation has a stronger dependency on temperature. This contrast with that of Xing et al. [47] who reported lower activation energy under humidified conditions 49 kJ mol^{-1} and higher under dry conditions 79 kJ mol^{-1}.

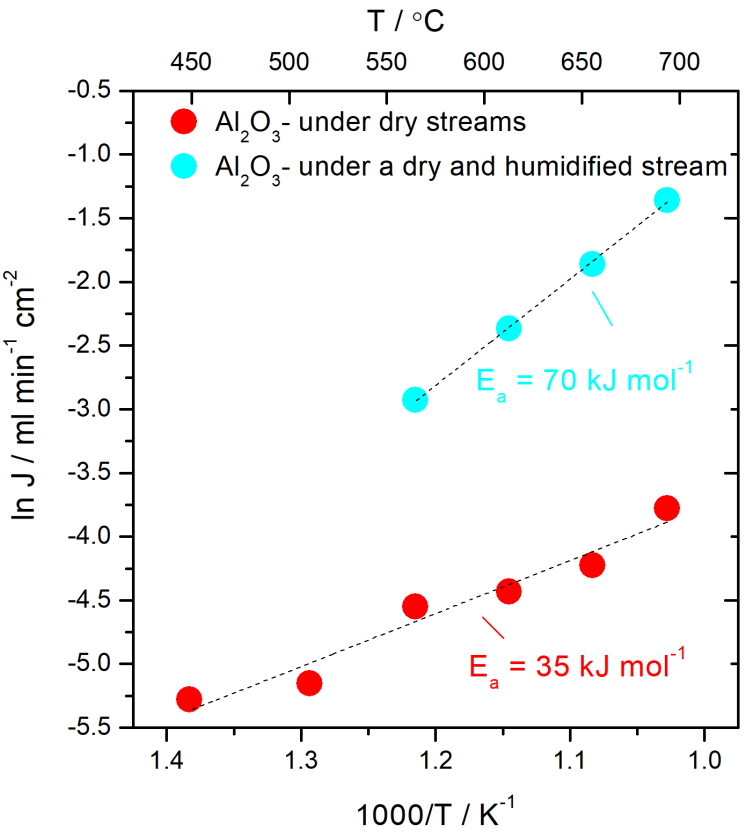

Figure 6-8. Arrhenius plot for CO_2 permeation through the Al_2O_3 closed-end tube membrane under dry and humidified conditions. Dry streams: the feed-side inlet is

50%CO_2/N_2 and the permeate side inlet is Ar. Dry and humidified stream: the feed-side inlet is 50%CO_2/N_2 and the permeate side inlet is Ar with 3.5% H_2O.

The equilibrium constants according to the reaction $H_2O + CO_3^{2-} \rightleftharpoons CO_2 + 2OH^-$ can be defined as:

$$K_2 = \frac{[OH^-]^2}{[CO_3^{2-}]}\frac{P_{CO_2}}{P_{H_2O}} \quad \text{Eq. 6-1}$$

By using Eq. 6-1 and setting $[CO_3^{2-}]$ equal to 1 (the molten carbonates mainly consist of CO_3^{2-}), the mole faction of OH^- can be calculated on the two interfaces of the membrane; on the hydration side at equilibrium (where $\frac{P_{CO_2}}{P_{H_2O}}$ is approximately 0.0029) , the mole faction of OH^- will be 15%, and on the carbonation side (where $\frac{P_{CO_2}}{P_{H_2O}}$ is approximately 5000), the mole faction of OH^- will be around 0.009%.

As discussed in Chapter 2, the permeation flux of water through a membrane, can be calculated using the below equations:

$$J_{H_2O} = -\frac{RT}{2F^2L}\frac{\sigma_{CO_3^{2-}}\sigma_{OH^-}}{\sigma_{OH^-} + \sigma_{CO_3^{2-}}} ln\left(\frac{P'_{CO_2}P''_{H_2O}}{P''_{CO_2}P'_{H_2O}}\right) \quad \text{Eq. 6-2}$$

$$\sigma_i = \frac{cF^2z_i^2\,D_i}{RT} \quad \text{Eq. 6-3}$$

$$J_{CO_2} = J_{H_2O} \quad \text{Eq. 6-4}$$

The conductivity of the carbonate ions can be found in Figure 2-5 and knowing that the density and the average molecular weight of the carbonates is 2.3 g cm^{-3} and 100 g mol^{-1} respectively, from Eq. 6-3 the H_2O conductivity can be calculated. It is expected that there is a concentration gradient of hydroxides within the melt and the theoretical values can be calculated using the mole fraction of hydroxide ions on both the hydration and carbonation side at equilibrium.

Assuming that the bulk concentration is equal to the mole fraction of hydroxide ions on the hydration side (equal to 15%), the conductivity of the hydroxide ions will be:

$$\sigma_{OH^-} = \frac{0.15 \cdot 2.3g\ c\mathrm{m}^{-3}}{100\ g\ \mathrm{mol}^{-1}}\frac{\left(9.6485 \cdot \frac{10^4\ \mathrm{Coulomb}}{\mathrm{mol}}\right)^2 (-1)^2\ \cdot 5.1 \cdot \frac{10^{-10}m^2}{s}}{8.31446\frac{\mathrm{J}}{(\mathrm{K\ mol})(550+273)\mathrm{K}}} =$$

$= 0.00345 \frac{mol}{cm^3} 1.36 \cdot 10^6 \, s \frac{S}{mol} \, 5.1 \cdot 10^{-10} \frac{m^2}{s} \cdot 10^4 cm^2 m^{-2} = 2.4 \cdot 10^{-2} S/cm$ at 550 °C on the hydration side.

Similarly, the conductivity of the hydroxide ions on the carbonation side (approximately 0.009%) will be equal to 1.4 x 10^{-3} S cm^{-1} at 550 °C.

The flux of water at 550 °C can then be calculated using the hydroxide conductivity values, Eq. 6-2 and Eq. 6-4, for example, for the hydration side the flux will be:

$$J_{H_2O} = J_{CO_2} = -\frac{RT}{2F^2L} \frac{\sigma_{CO_3^{2-}} \sigma_{OH^-}}{\sigma_{OH^-} + \sigma_{CO_3^{2-}}} ln\left(\frac{P'_{CO_2} P''_{H_2O}}{P''_{CO_2} P'_{H_2O}}\right) =$$

$$= -\frac{8.31446 \frac{\text{J}}{(\text{K mol})} (550 + 273)\text{K}}{2 \left(9.6485 \cdot \frac{10^4 \text{ Coulomb}}{\text{mol}}\right)^2 0.05 \, cm} \cdot \frac{0.978 \frac{S}{cm} \cdot 2.4 \cdot \frac{10^{-2} S}{cm}}{2.4 \cdot \frac{10^{-2} S}{cm} + 0.978 \frac{S}{cm}}$$

$$\cdot ln\left(\frac{50 \cdot 3.5}{0.01 \cdot 0.01}\right) \cdot 22400 \text{ ml mol}^{-1} \cdot 60 \text{ s } min^{-1} = 3.3 \text{ ml } min^{-1} cm^{-2}$$

If the flux of water is approximately 3.3 ml min^{-1} cm^{-2} at 550 °C, the permeation rate (for a surface area of carbonates equal to 34 mm^2) will be 3.0 x 10^{-3} mol s^{-1} at 550 °C.

If we then use the mole faction of hydroxide ions on the carbonation side) and repeat the above calculations:

$$J_{H_2O} = J_{CO_2} = 2.4 \text{ x } 10^{-1} \text{ ml } min^{-1} cm^{-2}$$

The permeation rate will then be 1.8 x 10^{-4} mol s^{-1} at 550 °C.

The theoretical values are significantly higher than the experimental values (in the order of 10^{-9} mol s^{-1}), which suggests that the reactions on the surfaces are slow compared to the bulk ionic diffusion (reaction kinetic limitations). The theoretical values would be comparable to the experimental values if the bulk concentration of the hydroxide ions is extremely small (<0.1 ppm).

6.5 Water driven uphill permeation experiment in air

6.5.1 Uphill permeation mechanism

As previously seen, by imposing a water chemical potential driving force to the system, high rates of CO_2 permeation are achieved. This is achieved by forcing a counter ion to also be transported though the molten salt and by linking the transport of CO_2 permeation with that of water permeation. This means that if the chemical gradient of OH^- is sufficient, CO_3^{2-}

transport can be dragged against its chemical gradient, and the overall CO_2 flux is determined by the two effects (more details on thermodynamics can be found in Chapter 2.3.4). Figure 6-9 shows a schematic of the concept of uphill CO_2 permeation with the assumption that OH^- and CO_3^{2-} are the only significant mobile species and therefore, two OH^- species will need to cross the membrane in the opposite direction of one CO_3^{2-}.

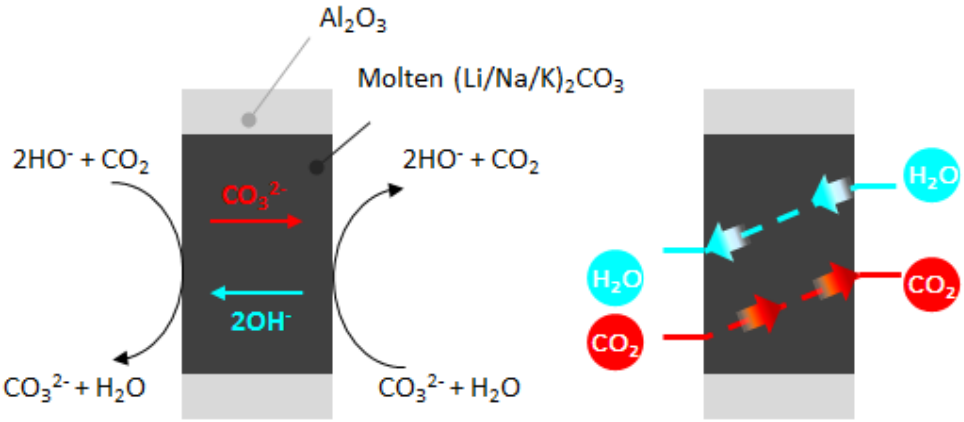

Figure 6-9. Uphill CO_2 permeation mechanism through the Al_2O_3 - molten carbonate membrane under humidified conditions. The dashed lines indicate the chemical potential of CO_2 and H_2O and the arrows indicate the direction of permeation.

This mechanism suggests that the composition of the melt is changing upon water introduction due to the formation of OH^- in the melt through the reaction $H_2O + CO_3^{2-} \rightleftharpoons CO_2 + 2OH^-$. The mole fraction of OH^- under equilibrium can be estimated from the thermodynamics, assuming equilibrium at both sides of the membrane or measuring it experimentally. In Appendix H, the chemical response of the membrane upon subsequent introduction and removal of water (3.5% H_2O) in the gas phase under non-permeating conditions (water was introduced on both sides) is presented. The moles of CO_2 evolved from the melt were obtained through peak integration.

6.5.2 Dry and humidified air stream

By combining the CO_2 uphill mechanism and the high rates that can be achieved by using a water chemical potential driving force, CO_2 separation can be studied in streams with low CO_2 partial pressure as in air by using a humidity difference as the driving force. Therefore, in this work, a dry air stream and a humidified air stream were used. As shown in Figure 6-10, the membrane was initially held under symmetrical conditions for approximately two hours and at time t_1, the inlet of the permeate side was switched from dry gas stream of 409 ppm CO_2 / 20% O_2/ N_2 to humidified gas stream of 409 ppm CO_2 / 20% O_2/ N_2 with 3.5% H_2O.

The flow rate on the feed-side was maintained at 30 cm^3 (STP)/min in both sides of the membrane. CO_2 material balance was performed by measuring the outlets of the feed and permeate-side gas streams during uphill experiments. The closure of the CO_2 material balance was confirmed at steady state and the rate of consumption of carbon dioxide on the feed side was equal to the rate of carbon dioxide evolution on the permeate side (Eq. 6-5, ‘ refers to feed-side outlet and " to the permeate-side outlet).

$$\overbrace{\left(x'_{CO_2(\,sym)} - x'_{CO_2(asym)}\right)\cdot Q}^{rate\ of\ consumption} = \overbrace{\left(x''_{CO_2(\,asym)} - x''_{CO_2(sym)}\right)\cdot Q}^{rate\ of\ evolution} \qquad \text{Eq. 6-5}$$

And the link between the OH^- and CO_3^{2-} species gives:

$$(x'_{CO_2(sym)} - x'_{CO_2(asym)})Q = x'_{H_2O(\,asym)}Q \qquad \text{Eq. 6-6}$$

Under the conditions shown in Figure 6-10, $x'_{CO_2(sym)} = x''_{CO_2(\,sym)} = 409\ ppm$, $x'_{CO_2(asym)} = 170\ ppm$, $x''_{CO_2(asym)} = 650\ ppm$ and $x'_{H_2O(\,asym)} = 230\ ppm$. Those values are in a good agreement with the material balance equation (Eq. 6-5) and the link between the OH^- and CO_3^{2-} species (Eq. 6-6). It was also observed that the outlet CO_2 mole fraction on the permeate side overshoots upon subsequent introduction of water in the gas phase and undershoots upon water removal while the mole fraction of CO_2 on the feed side does not show the same behaviour.

With the assumption that the CO_2 evolution upon water introduction is due to the formation of OH^- in the melt, the mole fraction of OH^- inside the melt can be calculated through the peak integration of the CO_2 mole fraction, which is a result of the chemical response of the membrane upon subsequent introduction and removal of water, as shown in Appendix H. The mole fraction of OH^- was calculated to be approximately 9%. Moreover, the mole faction of OH^- within the melt can be also calculated thermodynamically, assuming equilibrium at the two interfaces of the membrane. As shown in Appendix H, the mole faction of OH^- on the hydration side at equilibrium (where $\frac{P_{CO_2}}{P_{H_2O}}$ is approximately 0.01 during uphill experiments) will be 6%, and on the carbonation side (where $\frac{P_{CO_2}}{P_{H_2O}}$ is approximately 1 during uphill experiments) it will be around 0.6%. The concentration of the OH^- and the below equations that were derived in 2.3.4 were then used to calculate fluxes and was compared to the values obtained experimentally as shown in Appendix H.

This experiment shows that by using an Al_2O_3 - carbonate membrane with a relatively small active area (0.0016 cm^2), as much as 60% of CO_2 may be captured from a humidified-air stream (3.5% H_2O) when using dry air at the opposite side.

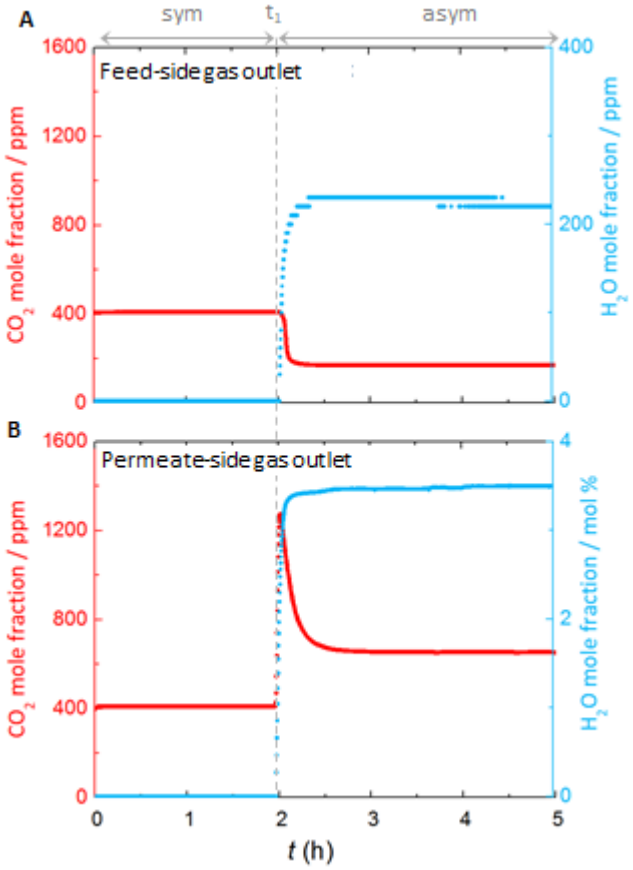

Figure 6-10. Mole fraction of gases in both (A) feed- and (B) permeate-side outlets at 550 °C. Symmetrical operation (sym): feed and permeate side inlet 409ppm CO_2/20%O_2/N_2. Asymmetrical operation (asym): feed-side inlet 409ppm CO_2/20%O_2/N_2, permeate side inlet 409ppm CO_2/20%O_2/N_2 with 3.5% H_2O

The experiment discussed in Figure 6-10, was repeated at different temperatures and the CO_2 and H_2O permeation rates achieved at different temperatures are shown in Figure 6-11B along with the schematic that shows the separation process (Figure 6-11A). The corresponding CO_2 permeation rate is equal to the H_2O permeation rate at all temperatures and there is a weak temperature dependence compared to downhill permeation with water (Figure 6-7C).

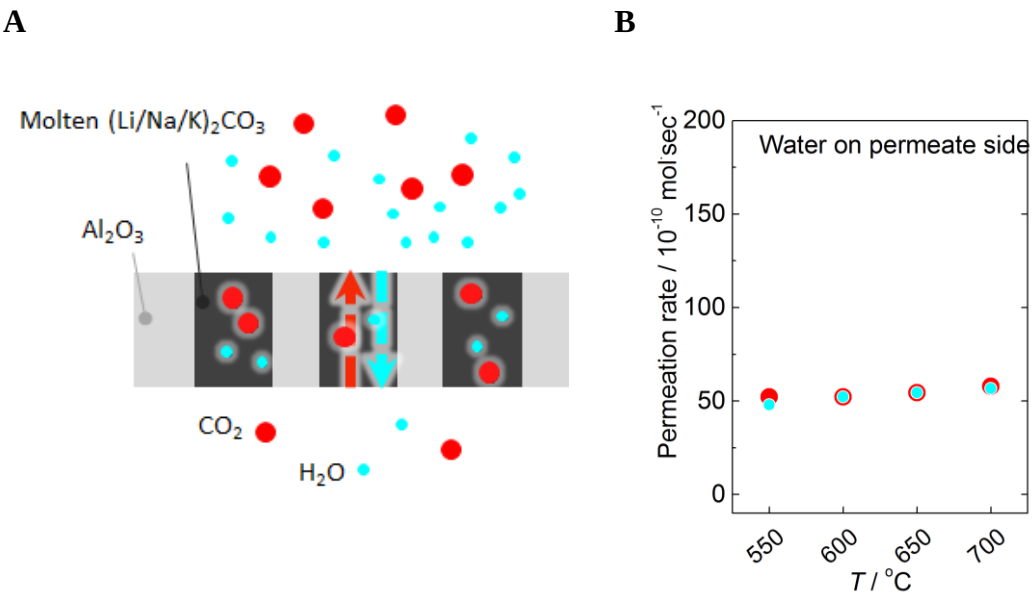

Figure 6-11. CO_2 and H_2O permeation rate as a function of temperature under a dry and humidified air stream and the schematic of the membrane under those conditions. A is the schematic of the Al_2O_3 closed-end tube support and molten carbonate mixture membrane under uphill conditions. B the permeation rates against temperature under uphill conditions: the feed-side inlet is 409ppm CO_2/20%O_2/N_2 and the permeate-side inlet is 409ppm CO_2/20%O_2/N_2 with 3.5% H_2O. Experiments were repeated 3-4 times and the error bars that correspond to the standard deviation of the repeats are smaller than the symbols.

To investigate the effect of external mass transfer resistance with flow rate on CO_2 permeation rate, the permeation of CO_2 was measured under the uphill conditions used in Figure 6-10, and by changing the flow rate of the permeate side. Initially the membrane was held under symmetrical conditions for approximately an hour and at time t_1, the external-chamber gas inlet was switched to 409 ppm CO_2 / 20% O_2/ N_2 with 3.5% H_2O. The flow rate of the feed-side gas inlet was maintained at 30 cm^3 (STP)/min and of the permeate-side gas inlet at 6 cm^3 (STP)/min. The H_2O and CO_2 mole fractions at the feed-side gas outlet were measured to be 210 and 190 ppm, respectively, while at the permeate-side gas outlet, the CO_2 mole fraction raised to 1380 ppm. Note that the increase in CO_2 mole fraction at the permeate-side gas outlet is five times higher than the decrease in the internal-chamber gas outlet, consistent with the ratio of the corresponding flow rates.

At time t_2, the membrane was again held under symmetrical conditions for approximately two hours and at time t_3, the external-chamber gas inlet was again exposed to 409ppm CO_2 / 20% O_2/ N_2 with 3.5% H_2O, and the flow rates were maintained at 30cm^3 (STP)/min on both sides. The H_2O and CO_2 mole fraction of the internal-chamber gas outlet were measured to be 220 ppm and 160 ppm respectively and on the external-chamber gas outlet the CO_2 mole fraction

was raised to 640 ppm. The absence of external mass transfer limitations with flow rate is proved with this experiment.

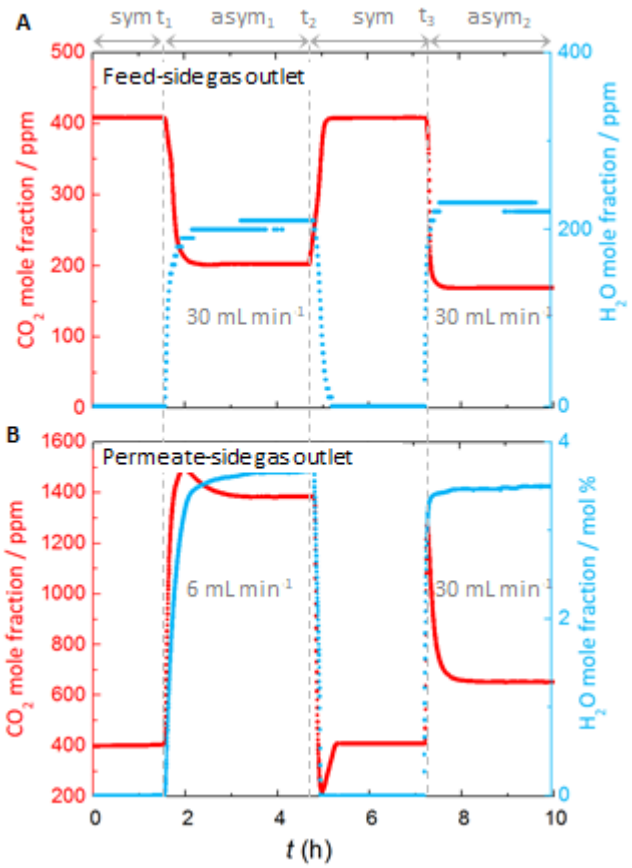

Figure 6-12. Mole fraction of gases in both (A) feed- and (B) permeate-side outlets at 550 °C. Symmetrical operation (sym): feed and permeate side inlet 409ppm CO_2/20%O_2/N_2. Asymmetrical operation: feed-side inlet 409ppm CO_2/20%O_2/N_2, permeate side inlet 409ppm CO_2/20%O_2/N_2 with 3.5% H_2O, $asym_1$: 30cm^3/min on feed-side chamber and 6 cm^3/min on permeate-side chamber, $asym_2$: 30 cm^3/min on both chambers.

6.5.3 Humidified air steams on both sides with different humidity levels

Figure 6-13 shows the result from CO_2 uphill permeation when both streams contain water. The membrane was initially under symmetrical conditions (sym) with 409 ppmCO_2/ 20%O_2/ N_2 as the feed to both feed and permeate side at 550 °C. At time t_1, the inlet of the feed and permeate side was switched to 409 ppm CO_2 / 20% O_2/ N_2 (composition on a dry basis) with 3.5% H_2O and with 0.6% H_2O respectively. The flow rate on both sides was maintained at 30 cm^3 (STP)/min. The CO_2 mole fraction of the feed-side reduced to 330 ppm and on the permeate-side, it raised to 485 ppm. The rate of consumption of CO_2 on the feed side equals

the rate of evolution of CO_2 on the permeate-side, indicating the CO_2 mass balance. At time t_2, the membrane was held again under symmetrical conditions.

This experiment shows that CO_2 capture from a wet-air stream with 3.5% H_2O, using a membrane with an air stream of 0.6% H_2O on the other side and an active area of 0.0016 cm^2 is 20%.

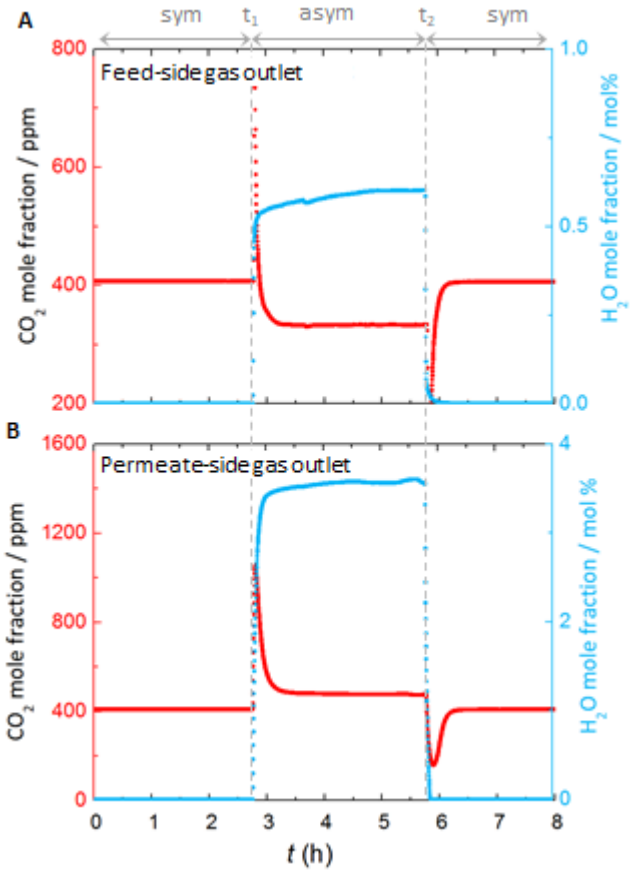

Figure 6-13. Mole fraction of gases in both (A) feed- and (B) permeate-side outlets at 550 °C. Symmetrical operation (sym): feed and permeate side inlet 409ppm CO_2/20%O_2/N_2. Asymmetrical operation(asym$_1$): feed-side inlet 409ppm CO_2/20%O_2/N_2 with 0.6% H_2O, permeate-side inlet 409ppm CO_2/20%O_2/N_2 with 3.5% H_2O.

6.6 Conclusions

The present study was undertaken to design leak-free membranes systems and evaluate the effect of temperature, CO_2 gas composition and presence of water on CO_2 permeation. YSZ and Al_2O_3 leak-free membrane systems which consist of a close-end tube with a tailored multi-pore microstructure were successfully designed. The unique design of the closed-end tube membranes, which only requires a low temperature sealant on the open end of the tube allowed the long duration of operation of those membranes with no detectable leaks, where

multiple conditions were used (Appendix F). The long-term stability and the absence of sealing failures with those membrane systems, proved that those membranes are ideal candidates for studying CO_2 kinetics and permeation under the presence of humidity. The effect of temperature on the performance of the YSZ-carbonate systems, showed that the activation energy increases with the decrease of the carbonate volume fraction and the kinetics are governed by oxide-ions transport at temperatures below 600 °C. This confirms previous findings discussed in Chapter 4. For the Al_2O_3 - carbonate membrane, the activation energy values indicate that permeation is controlled by mixed kinetics. The CO_2 kinetic studies showed that CO_2 permeation is generally limited by the diffusion in the melt at 700 ℃ and reaction limited at the gas-melt interface at 550 ℃ through an Al_2O_3 - carbonate membrane.

Moreover, as water promotes CO_2 permeation, challenging separation processes with dilute CO_2 were studied. It was found that the driving force of CO_2 can be linked to the driving force of humidity. One of the most important findings to emerge of this study is that "uphill" permeation of CO_2 is feasible as water can drive CO_2 across the membrane even in the absence of a CO_2 driving force (a charge carrier moves in the opposite direction). An apparent direct link between CO_2 and H_2O permeation was successfully demonstrated as there was a clear 1:1 ratio in the permeation ratio of H_2O:CO_2. This is the first study that shows a clear stoichiometric relationship between H_2O and CO_2 permeation rates.
Moreover, 60% of CO_2 capture was achieved from a humidified-air stream (3.5% H_2O) when using Al_2O_3 - carbonate membrane with a relatively small active area (0.0016 cm^2) and dry air on the opposite side of the membrane.

A summary of the permeances calculated with the closed-end tubes, together with some relevant literature data, is provided in Figure 6-14. CO_2 permeances are calculated by using the most common approach reported in literature, which is by dividing the CO_2 rate with the membrane permeation area and the CO_2 partial pressure difference between the two sides of the membranes. For the uphill experiment, the driving force would be negative if only the driving force of CO_2 is considered. Therefore, the driving force was calculated by adding the negative driving force of CO_2 to the driving force of water. This was calculated by using Eq. 6-7:

$$CO_2\ permeance\ (uphill) = \frac{x'_{CO_2(asym)} - x'_{CO_2(sym)}}{\left(P''_{H_2O,asym} - P'_{H_2O,asym}\right) - \left(P''_{CO_2,asym} - P'_{CO_2,asym}\right)} \frac{Q}{A} \quad \text{Eq. 6-7}$$

Where,

Q is the flow rate,

A is the membrane permeation area

$'$ refers to feed-side outlet and $''$ to the permeate-side outlet

In Figure 6-14, YSZ closed-end tubes show the highest CO_2 permeances under dry conditions than any reported dual-phase membrane. Lu et al [43] shows the closest comparable data to the YSZ closed-end tube membranes. Both works demonstrate that CO_2 permeation can increase significantly when thin membranes with low tortuosities are used. The results under humidified conditions (Figure 6-14) suggest that by imposing a water chemical potential driving force, permeances can increase up to two orders of magnitude which led to CO_2 permeances of 2 x 10^{-7} mol m^{-2} s^{-1} Pa.

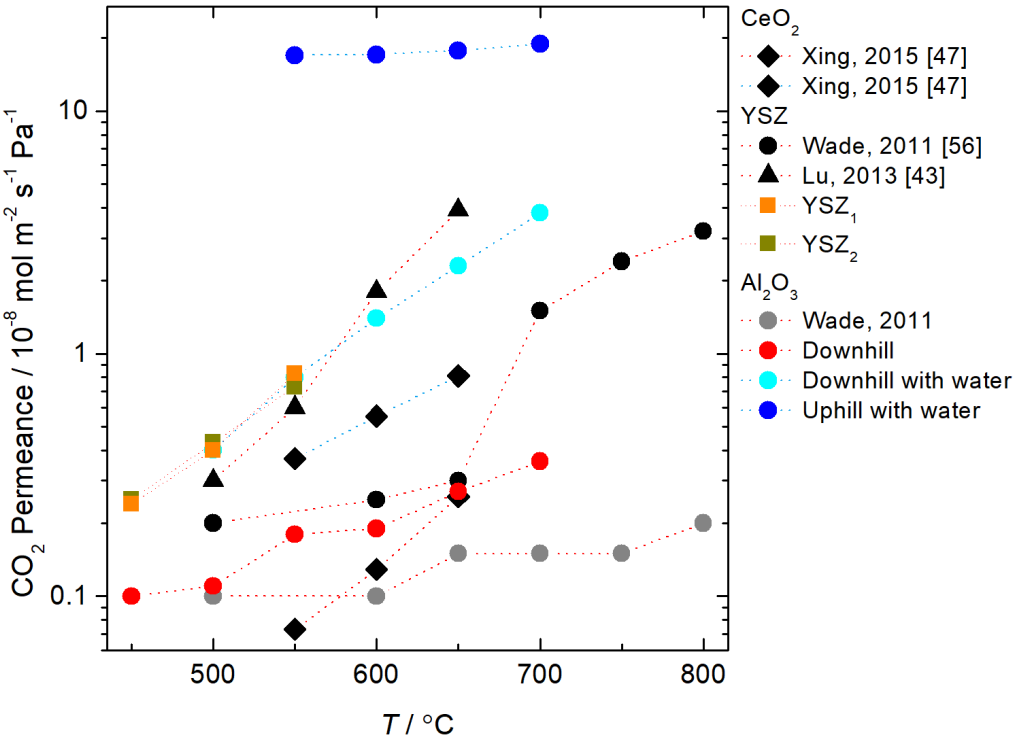

Figure 6-14. CO_2 permeance (logarithmic scale) against temperature through the YSZ and Al_2O_3 closed-end tube membranes and CeO_2, YSZ and Al_2O_3 -carbonate membranes from literature. Red dotted lines correspond to experiments under dry conditions and blue dotted lines correspond to experiments under humidified conditions. Permeances for closed-end tubes have been calculated using the area of the pores. Downhill

experiment: feed-side inlet is 50%CO_2/N_2 and permeate side inlet is Ar. Downhill with water: feed-side inlet is 50%CO_2/N_2 and permeate side inlet is Ar with 3.5% H_2O. Uphill with water: feed-side inlet is 409ppm $CO_2/20\%O_2/N_2$, permeate-side inlet is 409ppm $CO_2/20\%O_2/N_2$ with 3.5% H_2O.

Chapter 7
Conclusions and future work

7.1 Conclusions

This research aimed to design leak-free membrane systems with tailored pore microstructures in order to improve the quality of mechanistic/kinetic data that can be extracted from CO_2 transport through dual-phase membranes.

Initial observations of membranes systems fabricated with several manufacturing techniques, such as powder pressed, freeze-casted and phase inversion method, and with different membrane materials, has shown that microstructural constrains can have a stronger impact on the membrane performance compared to the nature of the support material. However, parameters, such as pore microstructure, pore geometry, tortuosity, total porosity, thickness and carbonate/solid fraction, are difficult to control in membranes fabricated with the above techniques.

This study has designed, for the first time, leak-free membrane systems with well-defined and controlled physical microstructures. The absence of sealing failure and long-term stability of those membranes (more than 50 days of operation) proved that those membranes are ideal candidates for challenging permeation experiments, such as mechanistic/kinetic studies and permeation under humidified conditions.

Additionally, to the development of simple membrane systems, a new approach was presented to optically investigate the role of CO_2 transport mechanism in a single-pore membrane system, by employing a host solid phase in the form of an optically transparent single crystal. This unique approach for the visualisation of an effect of the CO_2 transport was validated against thermodynamic expectations. The analysis of permeation through single-pore single crystal systems undertaken here, has extended the existing knowledge on the effect of the CO_2 partial pressure on CO_2 permeation, as it allows to report data at very low driving forces ($\ln(p_{CO_2,\,feed}/p_{CO_2,\,permeate}) < 2$), which are more likely to be found in a practical application. This region of driving forces was entirely unexplored by the literature and up to three orders of magnitudes lower than relevant membrane literature. The results suggest that there is a shift in the rate determining regime at driving forces of 0.4 at 550 °C, as below this value, the surface reaction limitations may be in control. The modified Wagner equation emerged as a

reliable predictor of the permeation area for those membrane systems, and permeances were in a good agreement with those reported in literature for similar systems.

The present study confirms previous findings on steam-promoted CO_2 flux in dual-phase membranes and contributes additional evidence that clearly support the direct link between CO_2 and H_2O, as they show a clear stoichiometric relationship between H_2O and CO_2 permeation rates (1:1). Data obtained from the Al_2O_3 closed-end tube system revealed that a membrane with a relatively small active area (0.0016 cm^2), can capture as much as 60% of CO_2 from a humidified-air stream (3.5% H_2O) when using dry air stream at the opposite side.

Moreover, this is the first study to prove that "uphill" permeation of CO_2 is feasible under humidified conditions, as water can drive CO_2 across the membrane even in the absence of a CO_2 driving force. The water driving force across the membrane could pump CO_2 from an air stream to a more concentrated product stream.

A brief summary of the main data obtained in this work seems tempting as it can provide an overview of the results of this work and highlight the contribution to the field of CO_2 permeation through the dual-phase membranes. Figure 7-1 shows the CO_2 permeance in logarithmic scale against temperature through the dual-phase membranes studied in this work and relevant systems in literature. The pore microstructure of the membranes studied, ranged from random to tailored multi- or single pore microstructures. CO_2 permeances were normalised to the membrane permeation area and to the CO_2 partial pressure difference between the two sides of the membrane. The differences in permeances observed in Figure 7-1 are up to three orders of magnitude. This can be explained by the contribution of several parameters mainly due to microstructural characteristics such as, pore size and alignment, pore density and shape, tortuosity, thickness, and surface area of carbonates on both the feed and permeate side of the membranes. Tortuosities ranged at most by a factor of 3, pore sizes were varied from few microns (eg. powder pressed membranes in Chapter 4) up to 150 μm (eg. YSZ_1 closed-end tube in Chapter 6), porosity was ranged from 21% (eg. YSZ freeze-casted in Chapter 4) to 71% (eg. YSZ_2 closed-end tube in Chapter 6) and membrane thicknesses ranged from 0.5 to 1 mm. Finally, multiple pore shapes were investigated such as irregular, round, honeycomb-like and rectangular. All those characteristics combined can affect CO_2 permeances through dual-phase membranes, as the interfacial surfaces, triple-phase boundaries and ionic path lengths can be significantly different between those substrates. Generally, the YSZ-carbonate membranes with parallel pore channels (phase inversion, closed-end tubes, multiple-pore single crystals) exhibited the highest permeances

compared to the rest of the membranes. Previous transport models [132] on CO_2 separation membranes predicted that at the best case scenario, where all parameters (microstructural and driving forces) are realistically optimized, fluxes greater than three orders of magnitude can be achieved. The 'uphill with water' and 'downhill with water' experiments prove that the presence of water in CO_2 streams has a very stronger impact on CO_2 permeation and can offer permeances above 10^{-7} mol m^{-2} s^{-1} Pa^{-1} at temperatures higher than 500 °C with an Al_2O_3-carbonate membrane. The presence of water could accelerate the CO_2 permeability by three orders of magnitude. This may open new opportunities for dilute chemical separations by tackling both the thermodynamic and kinetic limitations. Finally, fundamental limitations of routine supported molten-carbonate membranes experiments such as, sealant failure and leakage, were tackled with the new systems presented in this work.

Overall, this thesis highlights the benefit of new leak-free membrane systems (closed end tubes and single-pore systems), and their applications on mechanistic studies for dilute chemical separation under humidified conditions. The benefits of the new membrane systems described in this thesis have been proven due to their long-term stability (more than 50 days of operation), the mechanistic data extracted under humidified conditions (clear stoichiometric relationship between H_2O and CO_2 permeation rates), and the study of permeations at very low driving forces that were previously unexplored.

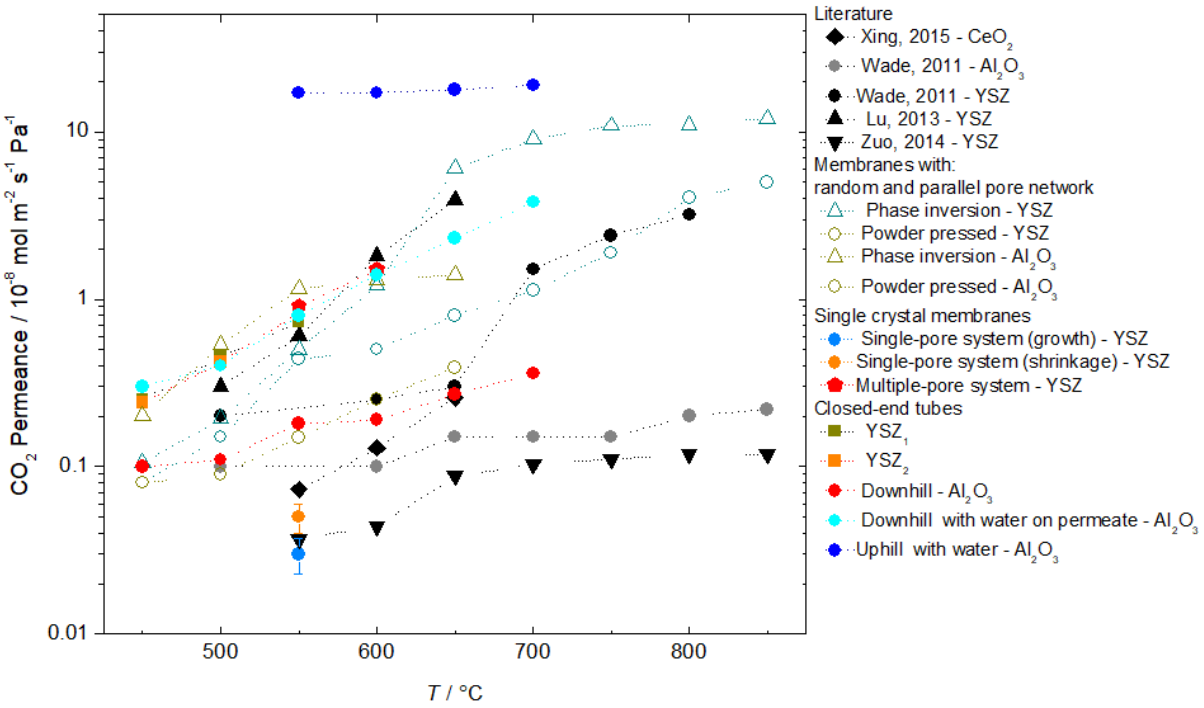

Figure 7-1. CO_2 permeance (logarithmic scale) against temperature through dual-phase membranes with random or tailored, multi- or single pore microstructures and membranes from literature. Powder pressed and phase inversion membranes are described in Chapter 4, single crystal membranes are described in Chapter 5 and closed-end tube membranes are described in Chapter 6. CO_2 permeances have been normalised to the CO_2 partial pressure difference between the two sides of the membrane.

7.2 Future work

Dual-phase membranes show promise for carbon dioxide separation, with high selectivities and permeabilities, at temperatures where other gas separation processes show limitations. However, there is lack of information on fundamental properties of the molten salts and complex pore microstructures that are poorly characterised.

Molten salt speciation and gas solubility in molten salts, could be studied both computationally and experimentally, as they can provide valuable information in designing new separation processes and determining permeation mechanisms. For example, a greater focus on *in situ* Raman spectroscopy could produce interesting findings that account more for the formation of ions in the melt. This would help to establish a greater degree of understanding on the mechanism for CO_2 permeation through dual-phase membranes. Moreover, the wettability of the molten salts on various supports and under a variety of conditions, would help the design of membrane systems with long term stability.

Although a number of studies to improve CO_2 permeation through dual-phase membranes have been published, it seems particularly important to investigate the effect of H_2O partial pressure on CO_2 permeation through dual-phase membranes - including "uphill" permeation - consisting of oxide-ion conducting materials, as it would probably shift the permeances to even higher values than those observed in this work.

In terms of direction for future research, instead of aiming for supports with increasingly higher conductivity, a focus on leak-free membrane systems with good performance over a long period of time may be very useful. Any further work could concentrate on employing those leak-free membrane systems designed in this work, to improve the quality of mechanistic/kinetic data that one can extract with any other membrane system used in a wide range of high-temperature gas separation applications, after a long period of operation. An interfacial solid phase may form during operation that can change in composition and volumes after long periods of operation. Furthermore, the molten carbonate composition may also be influenced by the temperature and gas phase composition and may form other active species, particularly under SO_2 and steam atmospheres. In literature, an equimolar nitrogen and carbon dioxide mixture has primarily been used to study carbon dioxide, however, in most applications, carbon dioxide needs to be separated from gas phase compositions that contain several impurities.

A deeper mechanistic understanding of gas separation processes, such as hydrogen, oxygen, nitrogen, CO_2, H_2S and CO separation, will allow the development and improvement of those technologies.

Last, one of the limitations of the single-pore systems designed in this work was the determination of the active permeation area that was quantified by geometrical approximation. X-ray micro-CT analysis, and in particular high temperature *in-situ* X-ray micro-CT, could be very useful to further understand the effect of the ionic pathlength and carbonate area on permeation.

References

1. Aye, G.C. and P.E. Edoja, Effect of economic growth on CO_2 emission in developing countries: Evidence from a dynamic panel threshold model. Cogent Economics & Finance, 2017. **5**(1): p. 1379239.

2. Global Carbon Capture and Storage Institute Limited. What happens when CO_2 is stored underground? CO_2 Monitoring and Storage Project. 2014 [cited 2018 January 2018]; Available from: https://hub.globalccsinstitute.com/sites/default/files/publications/151303/co2-stored-underground-ieaghg-weyburn-midale-co2-monitoring-storage-project.pdf.

3. Bui, M., et al., Carbon capture and storage (CCS): the way forward. Energy & Environmental Science, 2018.

4. Earth's CO_2 Home Page. Historical CO_2 Datasets Global CO_2 Yearly 2017; Available from: https://www.co2.earth/historical-co2-datasets.

5. IPCC, Special report on emissions scenarios: a special report of working group III of the Intergovernmental Panel on Climate Change. Cambridge University Press, 2000.

6. Rockström, J., et al., A roadmap for rapid decarbonization. Science, 2017. **355**(6331): p. 1269-1271.

7. United Nations Climate change. Intended Nationally Determined Contributions (INDCs) [cited March 2018; Available from: http://unfccc.int/focus/indc_portal/items/8766.php.

8. Leung, D.Y.C., G. Caramanna, and M.M. Maroto-Valer, An overview of current status of carbon dioxide capture and storage technologies. Renewable and Sustainable Energy Reviews, 2014. **39**(Supplement C): p. 426-443.

9. Damen, K., et al., A comparison of electricity and hydrogen production systems with CO_2 capture and storage. Part A: Review and selection of promising conversion and capture technologies. Progress in Energy and Combustion Science, 2006. **32**(2): p. 215-246.

10. Muradov, N.Z. and T.N. Veziroğlu, "Green" path from fossil-based to hydrogen economy: An overview of carbon-neutral technologies. International Journal of Hydrogen Energy, 2008. **33**(23): p. 6804-6839.

11. De Visser, E., et al., Dynamis CO_2 quality recommendations. International Journal of Greenhouse Gas Control, 2008. **2**(4): p. 478-484.

12. Olajire, A.A., CO_2 capture and separation technologies for end of pipe applications – A review. Energy, 2010. **35**(6): p. 2610-2628.

13. Jansen, D., et al., Pre-combustion CO_2 capture. International Journal of Greenhouse Gas Control, 2015. **40**: p. 167-187.

14. Stanger, R., et al., Oxyfuel combustion for CO_2 capture in power plants. International Journal of Greenhouse Gas Control, 2015. **40**: p. 55-125.

15. Gibbins, J. and H. Chalmers, Carbon capture and storage. Energy Policy, 2008. **36**(12): p. 4317-4322.

16. Figueroa, J.D., et al., Advances in CO_2 capture technology—The U.S. Department of Energy's Carbon Sequestration Program. International Journal of Greenhouse Gas Control, 2008. **2**(1): p. 9-20.

17. Rodney, J.A., B. Rune, and D. Enrico, Carbon Dioxide Separation Technologies. Vol. 2. 2003: Knuwer academic publisher.

18. Simmonds, M., et al., A Study of Very Large Scale Post Combustion CO_2 Capture at A refining & Petrochemical Complex, in Greenhouse Gas Control Technologies - 6th International Conference. 2003, Pergamon: Oxford. p. 39-44.

19. Drioli, E. and M. Romano, Progress and New Perspectives on Integrated Membrane Operations for Sustainable Industrial Growth. Industrial & Engineering Chemistry Research, 2001. **40**(5): p. 1277-1300.

20. Favre, E., Carbon dioxide recovery from post-combustion processes: Can gas permeation membranes compete with absorption? Journal of Membrane Science, 2007. **294**(1–2): p. 50-59.

21. D'Alessandro, D.M., B. Smit, and J.R. Long, Carbon Dioxide Capture: Prospects for New Materials. Angewandte Chemie International Edition, 2010. **49**(35): p. 6058-6082.

22. Mobius, A., D. Henriques, and T. Markus, Sintering behaviour of $La_{1-x}Sr_xCo_{0.2}Fe_{0.8}O_{3-\delta}$ ($0.3<x<0.8$) mixed conducting materials. Journal of the European Ceramic Society, 2009. **29**: p. 2831-2839.

23. Li, J., et al., Carbon dioxide capture-related gas adsorption and separation in metal-organic frameworks. Coordination Chemistry Reviews, 2011. **255**(15): p. 1791-1823.

24. MTR. CO_2 Removal from Syngas-Polaris solution. [cited March 2018; Available from: http://www.mtrinc.com/co2_removal_from_syngas.html.

25. Kim, S. and Y.M. Lee, High performance polymer membranes for CO_2 separation. Current Opinion in Chemical Engineering, 2013. **2**(2): p. 238-244.

26. Wijmans, J.G. and R.W. Baker, The solution-diffusion model: a review. Journal of Membrane Science, 1995. **107**(1): p. 1-21.

27. Ho, M.T., et al., Economics of CO_2 and Mixed Gas Geosequestration of Flue Gas Using Gas Separation Membranes. Industrial & Engineering Chemistry Research, 2006. **45**(8): p. 2546-2552.

28. Yang, H., et al., Progress in carbon dioxide separation and capture: A review. Journal of Environmental Sciences, 2008. **20**: p. 14-27.

29. Yang, H., et al., Progress in carbon dioxide separation and capture: A review. Journal of Environmental Sciences, 2008. **20**(1): p. 14-27.

30. Kovvali, A.S., H. Chen, and K.K. Sirkar, Dendrimer Membranes: A CO_2-Selective Molecular Gate. Journal of the American Chemical Society, 2000. **122**(31): p. 7594-7595.

31. Hussain, A. and M.B. Hägg, A feasibility study of CO_2 capture from flue gas by a facilitated transport membrane. Journal of Membrane Science, 2010. **359**(1): p. 140-148.

32. Zhu, X., et al., Novel dual-phase membranes for CO_2 capture via an oxyfuel route. Chemical Communications, 2012. **48**(2): p. 251-253.

33. Atkinson, A. and A. Selçuk, Mechanical behaviour of ceramic oxygen ion-conducting membranes. Solid State Ionics, 2000. **134**(1–2): p. 59-66.

34. Langmuir, I., Chemical reactions at low pressures. Journal of the American Chemical Society, 1915. **37**(5): p. 1139-1167.

35. Claes, P., D. Moyaux, and D. Peeters, Solubility and Solvation of Carbon Dioxide in the Molten $Li_2CO_3/Na_2CO_3/K_2CO_3$ (43.5:31.5:25.0 mol-%) Eutectic Mixture at 973 K I. Experimental Part. European Journal of Inorganic Chemistry, 1999. **1999**(4): p. 583-588.

36. Evans, A., W. Xing, and T. Norby, Electromotive Force (emf) Determination of Transport Numbers for Native and Foreign Ions in Molten Alkali Metal Carbonates. Journal of The Electrochemical Society, 2015. **162**(10): p. F1135-F1143.

37. Fang, J., J. Tong, and K. Huang, A superior mixed electron and carbonate-ion conducting metal-carbonate composite membrane for advanced flue-gas carbon capture. Journal of Membrane Science, 2016. **505**: p. 225-230.

38. Anantharaman, R., et al., Dual phase high-temperature membranes for CO_2 separation - performance assessment in post- and pre-combustion processes. Faraday Discussions, 2016. **192**(0): p. 251-269.

39. Thursfield, A. and I.S. Metcalfe, High temperature gas separation through dual ion-conducting membranes. Current Opinion in Chemical Engineering, 2013. **2**: p. 217-222.

40. Patrício, S.G. and F.M.B. Marques, Benchmarking the ambipolar conductivity of composite electrolytes for gas separation membranes. International Journal of Energy Research, 2016. **40**(15): p. 2150-2161.

41. Anderson, M. and Y.S. Lin, Carbonate-ceramic dual-phase membrane for carbon dioxide separation. Journal of Membrane Science, 2010. **357**(1-2): p. 122-129.

42. Matthew, A., Carbonate-Ceramic Dual-Phase Membranes for High Temperature Carbon Dioxide Separation in Chemical Engineering. 2011, Arizona State University

43. Lu, B. and Y.S. Lin, Synthesis and characterization of thin ceramic-carbonate dual-phase membranes for carbon dioxide separation. Journal of Membrane Science, 2013. **444**: p. 402-411.

44. Ortiz-Landeros, J., T. Norton, and Y.S. Lin, Effects of support pore structure on carbon dioxide permeation of ceramic-carbonate dual-phase membranes. Chemical Engineering Science, 2013. **104**: p. 891-898.

45. Basile, A. and S.P. Nunes, Advanced Membrane Science and Technology for Sustainable Energy and Environmental Applications. 2011: Elsevier Science.

46. Qi, X., F.T. Akin, and Y.S. Lin, Ceramic–glass composite high temperature seals for dense ionic-conducting ceramic membranes. Journal of Membrane Science, 2001. **193**(2): p. 185-193.

47. Xing, W., et al., Steam-promoted CO_2 flux in dual-phase CO_2 separation membranes. Journal of Membrane Science, 2015. **482**(Supplement C): p. 115-119.

48. Papaioannou, E.I., H. Qi, and I.S. Metcalfe, 'Uphill' permeation of carbon dioxide across a composite molten salt-ceramic membrane. Journal of Membrane Science, 2015. **485**(Supplement C): p. 87-93.

49. Sun, J., et al., CO_2 separation membranes with high permeability and CO_2/N_2 selectivity prepared by electrostatic self-assembly of polyethylenimine on reverse osmosis membranes. RSC Advances, 2017. **7**(24): p. 14678-14687.

50. Zhang, L., et al., High CO_2 permeation flux enabled by highly interconnected three-dimensional ionic channels in selective CO_2 separation membranes. Energy & Environmental Science, 2012. **5**(8): p. 8310-8317.

51. Ramanarayanan, T., S.C. Singhal, and E.D. Wachsman, High Temperature Ion Conducting Ceramics. Vol. 10. 2001. 22-27.

52. Dong, X. and W. Jin, Mixed conducting ceramic membranes for high efficiency power generation with CO_2 capture. Current Opinion in Chemical Engineering, 2012. **1**(2): p. 163-170.

53. Zhang, K., et al., Research progress and materials selection guidelines on mixed conducting perovskite-type ceramic membranes for oxygen production. RSC Advances, 2011. **1**(9): p. 1661-1676.

54. Sunarso, J., et al., Mixed ionic–electronic conducting (MIEC) ceramic-based membranes for oxygen separation. Journal of Membrane Science, 2008. **320**: p. 13-41.

55. Wade, J.L., et al., Composite electrolyte membranes for high temperature CO_2 separation. Journal of Membrane Science, 2011. **369**(1–2): p. 20-29.

56. Rojana, P., et al., Predicting ionic conductivity of solid oxide fuel cell electrolyte from first principles. Journal of Applied Physics, 2005. **98**(10): p. 103513.

57. Zuo, M., et al., Ionic conducting ceramic–carbonate dual phase hollow fibre membranes for high temperature carbon dioxide separation. Journal of Membrane Science, 2014. **458**: p. 58-65.

58. Xin, X., et al., Solid oxide fuel cells with dense yttria-stabilized zirconia electrolyte membranes fabricated by a dry pressing process. Journal of Power Sources, 2006. **160**(2): p. 1221-1224.

59. Xia, X., Computational Modelling Study of Yttria-stabilized Zirconia. 2010: University College London (University of London).

60. Hannink, R.H.J., P.M. Kelly, and B.C. Muddle, Transformation Toughening in Zirconia-Containing Ceramics. Journal of the American Ceramic Society, 2000. **83**(3): p. 461-487.

61. Torardi, C., Mesoporous metal oxide. 2007: Google Patents.

62. Chevalier, J., et al., The Tetragonal-Monoclinic Transformation in Zirconia: Lessons Learned and Future Trends. Journal of the American Ceramic Society, 2009. **92**(9): p. 1901-1920.

63. Xia, X., Computational Modelling Study of Yttria-stabilized Zirconia, in Department of Chemistry. 2010, University College London: London. p. 217.

64. DoITPoMS. Electrolyte. 2004-2015 [cited 2017 25/12/2017]; Available from: https://www.doitpoms.ac.uk/tlplib/fuel-cells/sofc_electrolyte.php.

65. Gorelov, V.P., Phase Diagram of the Zirconia-Yttria System in the Region of Low Yttria Content. Tr. Inst. Elektrochim., Ural. Nauchn. Tsentr, Akad. Nauk SSSR, 1978. **26**(69).

66. Ghasemi, R., et al., Comparison of microstructure and mechanical properties of plasma-sprayed nanostructured and conventional yttria stabilized zirconia thermal barrier coatings. Ceramics International, 2013. **39**(8): p. 8805-8813.

67. British Standards Institute Staff, Aluminium Oxide Primarily Used for Production of Aluminium. 1910: B S I Standards.

68. Rankin, G.A. and H.E. Merwin, The ternary system CaO-Al_2O_3-MgO. Journal of the American Chemical Society, 1916. **38**(3): p. 568-588.

69. Rovner, L.H., Diffusion of oxygen in magnesium oxide. 1966: Cornell University.

70. Icon Health Publications, Magnesium Oxide: A Medical Dictionary, Bibliography, and Annotated Research Guide to Internet References. 2004: Icon Health.

71. Gaune-Escard, M. and G.M. Haarberg, Molten Salts Chemistry and Technology. 2014, UK: John Wiley & Sons Ltd.

72. Mishra, B. and D.L. Olson, Molten salt applications in materials processing. Journal of Physics and Chemistry of Solids, 2005. **66**(2–4): p. 396-401.

73. Gaune-Escard, M., Molten Salts: From Fundamentals to Applications. 1 ed. Nato Science Series II:. 2002: Springer Netherlands. 404.

74. Sridharan, K. and T.R. Allen, 12 - Corrosion in Molten Salts, in Molten Salts Chemistry, F.L. Groult, Editor. 2013, Elsevier: Oxford. p. 241-267.

75. Steele, B.C.H. and A. Heinzel, Materials for fuel-cell technologies. Nature, 2001. **414**(6861): p. 345-352.

76. Janz, G.J. and M.R. Lorenz, Solid-Liquid Phase Equilibria for Mixtures of Lithium, Sodium, and Potassium Carbonates. Journal of Chemical & Engineering Data, 1961. **6**(3): p. 321-323.

77. Toshikatsu, K., et al., Density, surface tension, and electrical conductivity of ternary molten carbonate system Li_2CO_3–Na_2CO_3–K_2CO_3 and methods for their estimation. Journal of The Electrochemical Society, 2008. **155**(7): p. F150-F156.

78. Kojima, T., et al., Electrical Conductivity of Molten $Li_2CO_3 – X_2CO_3$ (X: Na, K, Rb, and Cs) and $Na_2CO_3 – Z_2CO_3$ (Z: K, Rb, and Cs). Journal of The Electrochemical Society, 2007. **154**(12): p. F222-F230.

79. Volkov, S.V., Chemical reactions in molten salts and their classification. Chemical Society Reviews, 1990. **19**(1): p. 21-28.

80. Olivares, R.I., C. Chen, and S. Wright, The Thermal Stability of Molten Lithium–Sodium–Potassium Carbonate and the Influence of Additives on the Melting Point. Journal of Solar Energy Engineering, 2012. **134**(4): p. 041002-041002-8.

81. Zhang, L., et al., First spectroscopic identification of pyrocarbonate for high CO_2 flux membranes containing highly interconnected three dimensional ionic channels. Physical Chemistry Chemical Physics, 2013. **15**(31): p. 13147-13152.

82. Exner, F., Ueber den Durchgang der Gase durch Flüssigkeitslamellen. Sitz. Wien. Akad. Wissen. , 1875(70): p. 465.

83. Stefan, J., Über die Beziehung Zwischen der Wärmerstrahlung und Temperatur. Sitzs. Wien. Akad. Wissen. II, 1878(77): p. 371.

84. Wilemski, G., Simple porous electrode models for molten carbonate fuel cells. J. Electrochem. Soc., 1983. **130**(1): p. 117-121.

85. Dubois, P., Carbon dioxide solubility Ann. Chem. (Paris), 1965. **5**: p. 145-186.

86. Kanai, Y., et al., Mass transfer in molten salt and suspended molten salt in bubble column. Chemical Engineering Science, 2013. **100**: p. 153-159.

87. Appleby, A.J. and C. Van Drunen, Solubilities of Oxygen and Carbon Monoxide in Carbonate Melts. Journal of The Electrochemical Society, 1980. **127**(8): p. 1655-1659.

88. Hefter, G.T. and R.P.T. Tomkins, The Experimental Determination of Solubilities. 2003: Wiley.

89. Giddings, J.C., Advances in Chromatography. 1983: Taylor & Francis.

90. Braunstein, J., G. Mamantov, and G.P. Smith, Advances in Molten Salt Chemistry. 2013: Springer US.

91. Janz, G.J. and N.P. Bansal, Molten salts data: Diffusion coefficients in single and multi-component salt systems. J Phys Chem Ref Data 1982. **11**(3): p. 627.

92. Bard, A.J. and L.R. Faulkner, Electrochemical Methods: Fundamentals and Applications, 2nd Edition. 2000: John Wiley & Sons.

93. Diana Mary, W., Chronopotentiometric studies in molten borates and halides, in Northampton College of Advanced Technology. 1968, University of London.

94. Chung, S.J., et al., Dual-Phase Metal−Carbonate Membrane for High-Temperature Carbon Dioxide Separation. Industrial & Engineering Chemistry Research, 2005. **44**(21): p. 7999-8006.

95. Yamaguchi, T., et al., Lithium silicate based membranes for high temperature CO_2 separation. Journal of Membrane Science, 2007. **294**(1): p. 16-21.

96. Fuertes, A.B., D.M. Nevskaia, and T.A. Centeno, Carbon composite membranes from Matrimid and Kapton polyimides for gas separation. Microporous and Mesoporous Materials, 1999. **33**(1): p. 115-125.

97. Poshusta, J.C., et al., Separation of light gas mixtures using SAPO-34 membranes. AIChE Journal, 2000. **46**(4): p. 779-789.

98. Yoshioka, T., et al., Experimental studies of gas permeation through microporous silica membranes. AIChE Journal, 2001. **47**(9): p. 2052-2063.

99. Xomeritakis, G., et al., Anodic alumina supported dual-layer microporous silica membranes. Journal of Membrane Science, 2007. **287**(2): p. 157-161.

100. Dong, X., J. Ortiz Landeros, and Y.S. Lin, An asymmetric tubular ceramic-carbonate dual phase membrane for high temperature CO_2 separation. Chemical Communications, 2013. **49**(83): p. 9654-9656.

101. Patrício, S.G., et al., High performance composite CO_2 separation membranes. Journal of Membrane Science, 2014. **471**: p. 211-218.

102. Marques, F.M.B., et al., On the Model Performance of Composite CO_2 Separation Membranes. Electrochimica Acta, 2016. **210**: p. 87-95.

103. Tong, J., et al., High CO_2 permeation flux enabled by Al_2O_3 modifier and in-situ infiltration of molten carbonate into gd-doped CeO_2 as a CO_2 separation membrane, in Advances in Materials Science for Environmental and Energy Technologies IV. 2015.

104. Ovalle-Encinia, O., H. Pfeiffer, and J. Ortiz-Landeros, $Ce_{0.85}Sm_{0.15}O_2$-$Sm_{0.6}Sr_{0.4}Al_{0.3}Fe_{0.7}O_3$ composite for the preparation of dense ceramic-carbonate membranes for CO_2 separation. Journal of Membrane Science, 2018. **547**: p. 11-18.

105. Tong, J., et al., Electrochemical separation of CO_2 from a simulated flue gas with high-temperature ceramic–carbonate membrane: New observations. Journal of Membrane Science, 2015. **477**(Supplement C): p. 1-6.

106. Lu, B. and Y.S. Lin, Asymmetric Thin Samarium Doped Cerium Oxide–Carbonate Dual-Phase Membrane for Carbon Dioxide Separation. Industrial & Engineering Chemistry Research, 2014. **53**(34): p. 13459-13466.

107. Norton, T.T., J. Ortiz-Landeros, and Y.S. Lin, Stability of La–Sr–Co–Fe Oxide–Carbonate Dual-Phase Membranes for Carbon Dioxide Separation at High Temperatures. Industrial & Engineering Chemistry Research, 2014. **53**(6): p. 2432-2440.

108. Skinner, S.J. and J.A. Kilner, Oxygen ion conductors. Materials Today, 2003. **6**(3): p. 30-37.

109. Stortelder, J.K., Ionic Conductivity in Yttria-Stabilized Zirconia Thin Films grown by Pulsed Laser Deposition in Faculty of Science and Technology,

Inorganic Materials Science,

Mesa+ Institute for Nanotechnology. 2005, University of Twente, Netherlands.

110. Shen, W. and J.L. Hertz, Ionic conductivity of YSZ/CZO multilayers with variable lattice mismatch. Journal of Materials Chemistry A, 2015. **3**(5): p. 2378-2386.

111. Mori, T., et al., Influence of particle morphology on nanostructural feature and conducting property in Sm-doped CeO_2 sintered body. Solid State Ionics, 2004. **175**(1): p. 641-649.

112. Fan, B., J. Yan, and X. Yan, The ionic conductivity, thermal expansion behavior, and chemical compatibility of $La_{0.54}Sr_{0.44}Co_{0.2}Fe_{0.8}O_{3-\delta}$ as SOFC cathode material. Solid State Sciences, 2011. **13**(10): p. 1835-1839.

113. Dutta, S., et al., Structure and microstructure dependent ionic conductivity in 10 mol% Dy_2O_3 doped CeO_2 nanoparticles synthesized by mechanical alloying. Materials Research Bulletin, 2016. **73**: p. 446-451.

114. Rondão, A.I.B., et al., Ionic transport in (nano)composites for fuel cells. International Journal of Hydrogen Energy, 2016. **41**(18): p. 7666-7675.

115. Christie, J.R., A.J. Darnell, and D.F. Dustin, Reaction of molten sodium carbonate with aluminum oxide. The Journal of Physical Chemistry, 1978. **82**(1): p. 33-37.

116. Kale, M.A., C.P. Joshi, and S.V. Moharil, Combustion synthesis of some compounds in the Li_2O-Al_2O_3 system. International Journal of Self-Propagating High-Temperature Synthesis, 2012. **21**(1): p. 19-24.

117. La Ginestra, A., M. Lo Jacono, and P. Porta, The preparation, characterization, and thermal behaviour of some lithium aluminum oxides: Li_3AlO_3 and Li_5AlO_4. Journal of thermal analysis, 1972. **4**(1): p. 5-17.

118. Ferreira, A.S.V., et al., Compositional and microstructural effects in composite electrolytes for fuel cells. International Journal of Energy Research, 2011. **35**(12): p. 1090-1099.

119. Escobedo Bretado, M.A., et al., Hydrogen production by absorption enhanced water gas shift (AEWGS). International Journal of Hydrogen Energy, 2010. **35**(21): p. 12083-12090.

120. Näfe, H. and R. Subasri, Revision of the Data on the Standard Gibbs Free Energy of Formation of Sodium Zirconate. Journal of Chemical Thermodynamics, 2007. **39**: p. 22-27.

121. Duan, Y. and D.C. Sorescu, Density functional theory studies of the structural, electronic, and phonon properties of Li_2O and Li_2CO_3: Applicaton to CO_2 capture reaction. Physical Review B, 2009. **79**(1): p. 014301.

122. Duan, Y., Theoretical Calculating the Thermodynamic Properties of Solid Sorbents for CO_2 Capture Applications, E.A.o.A.A. Meeting, Editor. 2012, National Energy Technology Laboratory.

123. Mendoza-Nieto, J.A., Y. Duan, and H. Pfeiffer, Alkaline zirconates as effective materials for hydrogen production through consecutive carbon dioxide capture and conversion in methane dry reforming. Applied Catalysis B: Environmental, 2018. **238**: p. 576-585.

124. Fauth, D.J., et al., Eutectic salt promoted lithium zirconate: Novel high temperature sorbent for CO_2 capture. Fuel Processing Technology, 2005. **86**(14): p. 1503-1521.

125. Nair, B.N., et al., Processing of Lithium Zirconate for Applications in Carbon Dioxide Separation: Structure and Properties of the Powders. Journal of the American Ceramic Society, 2004. **87**(1): p. 68-74.

126. Ochoa-Fernández, E., et al., Compositional Effects of Nanocrystalline Lithium Zirconate on Its CO_2 Capture Properties. Industrial & Engineering Chemistry Research, 2008. **47**(2): p. 434-442.

127. Ida, J.-i., R. Xiong, and Y.S. Lin, Synthesis and CO_2 sorption properties of pure and modified lithium zirconate. Separation and Purification Technology, 2004. **36**(1): p. 41-51.

128. Xiong, R., J. Ida, and Y.S. Lin, Kinetics of carbon dioxide sorption on potassium-doped lithium zirconate. Chemical Engineering Science, 2003. **58**(19): p. 4377-4385.

129. Budiana, B., et al., Preparation and conductivity measurement of 7-8 mol % YSZ and 12 mol % CSZ for electrolyte SOFC. Journal of Physics: Conference Series, 2016. **739**: p. 012022.

130. Cerisier, P. and F. Roux, A study of the electrical conductivity and transition points of potassium carbonate. Solid State Communications, 1978. **26**(10): p. 661-663.

131. Cerisier, P. and F. Roux, A study of the electrical conductivity and transition points of sodium carbonate. Journal of Solid State Chemistry, 1977. **22**(3): p. 245-251.

132. Wade, J.L., K.S. Lackner, and A.C. West, Transport model for a high temperature, mixed conducting CO_2 separation membrane. Solid State Ionics, 2007. **178**: p. 1530-1540.

133. Rui, Z., et al., Modeling and analysis of carbon dioxide permeation through ceramic-carbonate dual-phase membranes. Journal of Membrane Science, 2009. **345**(1): p. 110-118.

134. Patrício, S.G., et al., Composite CO_2 separation membranes: Insights on kinetics and stability. Journal of Membrane Science, 2017. **541**: p. 253-261.

135. Mardilovich, I.P., E. Engwall, and Y.H. Ma, Dependence of hydrogen flux on the pore size and plating surface topology of asymmetric Pd-porous stainless steel membranes. Desalination, 2002. **144**(1): p. 85-89.

136. Zhu, W., et al., Electrical properties of ceria-carbonate composite electrolytes. Materials Research Bulletin, 2006. **41**(11): p. 2057-2064.

137. Zhao, Y., et al., Quantifying multi-ionic conduction through doped ceria-carbonate composite electrolyte by a current-interruption technique and product analysis. International Journal of Hydrogen Energy, 2012. **37**(10): p. 8556-8561.

138. Rondão, A.I.B., et al., Role of gas-phase composition on the performance of ceria-based composite electrolytes. International Journal of Hydrogen Energy, 2013. **38**(14): p. 5497-5506.

139. Rondão, A.I.B., et al., Impact of ceramic matrix functionality on composite electrolytes performance. Electrochimica Acta, 2013. **109**: p. 701-709.

140. Soares, C.M.C., et al., Relevance of the ceramic content on dual oxide and carbonate-ion transport in composite membranes. International Journal of Hydrogen Energy, 2014. **39**(10): p. 5424-5432.

141. L. Spedding, P., Electrical Conductance of Molten Alkali Carbonate Binary Mixtures. Journal of The Electrochemical Society, 1973. **120**(8).

142. Steele, B.C.H., Appraisal of $Ce_{1-y}Gd_yO_{2-y/2}$ electrolytes for IT-SOFC operation at 500°C. Solid State Ionics, 2000. **129**(1): p. 95-110.

143. Kojima, T., et al., Electrical Conductivity of Molten $Li_2CO_3 – X_2CO_3$ (X: Na, K, Rb, and Cs) and $Na_2CO_3 – Z_2CO_3$ (Z: K, Rb, and Cs). Journal of The Electrochemical Society, 2007. **12**(154).

144. Turner, M.K., Effective Industrial Membrane Processes: Benefits and Opportunities. 2012: Springer Netherlands.

145. Hilal, N., A.F. Ismail, and C. Wright, Membrane Fabrication. 2015: CRC Press.

146. Wu, Z., Dual-layer functional ceramic hollow fibre membranes for partial oxidation of methane in Chemical Engineering. 2012, Imperial College London

147. Norton, T.T., B. Lu, and Y.S. Lin, Carbon dioxide permeation properties and stability of samarium-doped-ceria carbonate dual-phase membranes. Journal of Membrane Science, 2014. **467**: p. 244-252.

148. Wagner, C., Equations for transport in solid oxides and sulfides of transition metals. Progress in Solid-State Chemistry, , 1975. **10**: p. 3-16.

149. Rui, Z., H. Ji, and Y.S. Lin, Modeling and analysis of ceramic–carbonate dual-phase membrane reactor for carbon dioxide reforming with methane. International Journal of Hydrogen Energy, 2011. **36**(14): p. 8292-8300.

150. Millet, J. and R. Buvet, Molten carbonate fuel cell with water injection, in: Proceedings of the Hydrocabon Air Fuel Cells Symposium. 1965, Atlantic City.

151. Newman, J. and K.E. Thomas-Alyea, Electrochemical Systems, ed. E.S. series. 2004: Wiley.

152. Bearman, R.J. and D.L. Jolly, Mass dependence of the self diffusion coefficients in two equimolar binary liquid Lennard-Jones systems determined through molecular dynamics simulation. Molecular Physics, 1981. **44**(3): p. 665-675.

153. Binas, I. and I. Mryglod, Mass-dependence of self-diffusion coefficients in disparate-mass binary fluid mixtures. Condensed Matter Physics, 2009. **12**(4): p. 647-656.

154. Tankeshwar, K., Bulk Viscosity and the Relation between Transport Coefficients. Physics and Chemistry of Liquids, 1991. **24**(1-2): p. 91-101.

155. Tankeshwar, K., Mass dependence of self-diffusion in isotopic fluids. Journal of Physics: Condensed Matter, 1995. **7**(50): p. 9715.

156. Sharma, R., K. Tankeshwar, and K.C. Sharma, Self-diffusion in an isotopic fluid. Physical Review E, 1999. **59**(1): p. 460-468.

157. Zhu, X. and W. Yang, Mixed Conducting Ceramic Membranes: Fundamentals, Materials and Applications. 2016: Springer Berlin Heidelberg.

158. Gibson, I.R., G.P. Dransfield, and J.T.S. Irvine, Sinterability of commercial 8 mol% yttria-stabilized zirconia powders and the effect of sintered density on the ionic conductivity. Journal of Materials Science, 1998. **33**(17): p. 4297-4305.

159. Akedo, J., et al., Advances in Multifunctional Materials and Systems II: Ceramic Transactions. 2014: Wiley.

160. Zhang, Y., et al., New formulas for the tortuosity factor of electrochemically conducting channels. Electrochemistry Communications, 2015. **60**(Supplement C): p. 52-55.

161. Gaudillere, C. and J.M. Serra, Freeze-casting: Fabrication of highly porous and hierarchical ceramic supports for energy applications. Boletín de la Sociedad Española de Cerámica y Vidrio, 2016. **55**(2): p. 45-54.

162. Hu, L., et al., Control of pore channel size during freeze casting of porous YSZ ceramics with unidirectionally aligned channels using different freezing temperatures. Journal of the European Ceramic Society, 2010. **30**(16): p. 3389-3396.

163. Wei, P., et al. Metal supported solid oxide fuel cell by freeze tape casting. in ECS Transactions. 2011.

164. Moon, J.W., et al., Preparation of NiO-YSZ tubular support with radially aligned pore channels. Materials Letters, 2003. **57**(8): p. 1428-1434.

165. Mallick, K.K., Freeze casting of porous bioactive glass and bioceramics. Journal of the American Ceramic Society, 2009. **92**(SUPPL. 1): p. S85-S94.

166. Lichtner, A. Freeze-casting. 2015 [cited 2018; Available from: http://aaronlichtner.com/freeze-casting/.

167. Loeb, S. and S. Sourirajan, Sea Water Demineralization by Means of an Osmotic Membrane, in Saline Water Conversion—II. 1963, AMERICAN CHEMICAL SOCIETY. p. 117-132.

168. Gil, A.M.G., Catalytic Hollow Fibre Membrane Reactors for H_2 Production, in Department of Chemical Engineering 2015, Imperial College London

169. Rezac, M.E., et al., Effect of mild solvent post-treatments on the gas transport properties of glassy polymer membranes. Journal of Membrane Science, 1994. **90**(3): p. 213-229.

170. Jiang, X., et al., CO_2-Tolerant $SrFe_{0.8}Nb_{0.2}O_{3-\delta}$ - Carbonate Dual-Phase Multichannel Hollow Fiber Membrane for CO_2 Capture. Industrial and Engineering Chemistry Research, 2016. **55**(12): p. 3300-3307.

171. Li, K., Ceramic Membranes for Separation and Reaction. 2007: Wiley.

172. Strathmann, H. and K. Kock, The formation mechanism of phase inversion membranes. Desalination, 1977. **21**(3): p. 241-255.

173. Guillen, G.R., et al., Preparation and Characterization of Membranes Formed by Nonsolvent Induced Phase Separation: A Review. Industrial & Engineering Chemistry Research, 2011. **50**(7): p. 3798-3817.

174. Wijmans, J.G., et al., Phase separation phenomena in solutions of polysulfone in mixtures of a solvent and a nonsolvent: relationship with membrane formation. Polymer, 1985. **26**(10): p. 1539-1545.

175. SPIM Optics 101. Theoretical basics. 2014 [cited 2018; Available from: http://openspim.org/SPIM_Optics_101/Theoretical_basics.

176. Reimer, L., Scanning Electron Microscopy: Physics of Image Formation and Microanalysis. 2013: Springer Berlin Heidelberg.

177. Goldstein, J.I., et al., Scanning Electron Microscopy and X-Ray Microanalysis. 2017: Springer New York.

178. Vakgroep META. Scanning Electron Microscope Energy Dispersive X-ray analysis. 2009 [cited 2018; Available from: http://www.vub.ac.be/META/toestellen_sem-edx.php.

179. Stock, S.R., MicroComputed Tomography: Methodology and Applications. 2008: CRC Press.

180. Goertzen, A.L., Development of a combined microPET and microCT system for mouse imaging. 2003: University of California.

181. Mittal, K.L., Contact Angle, Wettability and Adhesion. 2009: CRC Press.

182. Mittal, K.L., Advances in Contact Angle, Wettability and Adhesion. 2013: Wiley.

183. Young, T., An Essay on the Cohesion of Fluids. Philosophical Transactions of the Royal Society of London, 1805. **95**: p. 65-87.

184. Dupré, A. and P. Dupré, Théorie mécanique de la chaleur. 1869: Gauthier-Villars.

185. Nikolopoulos, P., Surface, grain-boundary and interfacial energies in Al_2O_3 and Al_2O_3-Sn, Al_2O_3-Co systems. Journal of Materials Science, 1985. **20**(11): p. 3993-4000.

186. Tsoga, A. and P. Nikolopoulos, Surface and grain-boundary energies in yttria-stabilized zirconia (YSZ-8 mol%). Journal of Materials Science, 1996. **31**(20): p. 5409-5413.

187. Karbassi, M., The Use of Mercury Porosimetry and Scanning Electron Microscopy Techniques to Investigate the Changes in Microstructure of Hardened Portland Cement Pastes Due to Different Methods of Drying. 1985: University of Strathclyde.

188. Westermarck, S., Use of Mercury Porosimetry and Nitrogen Adsorption in Characterisation of the Pore Structure of Mannitol and Microcrystalline Cellulose Powders, Granules and Tablets. 2000: University of Helsinki.

189. Lowell, S., et al., Characterization of Porous Solids and Powders: Surface Area, Pore Size and Density. 2012: Springer Netherlands.

190. Choi, S., Y. Zhang, and Y. Xia, Three-Dimensional Scaffolds for Tissue Engineering: The Importance of Uniformity in Pore Size and Structure. Langmuir, 2010. **26**(24): p. 19001-19006.

191. Vandenabeele, P., Practical Raman Spectroscopy: An Introduction. 2013: Wiley.

192. Gardiner, D.J., et al., Practical Raman Spectroscopy. 2012: Springer Berlin Heidelberg.

193. Wopenka, B. and J.D. Pasteris, Raman intensities and detection limits of geochemically relevant gas mixtures for a laser Raman microprobe. Analytical Chemistry, 1987. **59**(17): p. 2165-2170.

194. Schrötter, H.W. and H.W. Klöckner, Raman Scattering Cross Sections in Gases and Liquids, in Raman Spectroscopy of Gases and Liquids, A. Weber, Editor. 1979, Springer Berlin Heidelberg: Berlin, Heidelberg. p. 123-166.

195. Dawson, P.H., Quadrupole Mass Spectrometry and Its Applications. 2013: Elsevier Science.

196. March, R.E. and J.F. Todd, Quadrupole Ion Trap Mass Spectrometry. 2005: Wiley.

197. LI-COR Inc. LI-840A CO_2/H_2O Gas Analyzer Instruction manual. 2010; Available from: https://www.licor.com/documents/y10gor2jal2p3t8ev4hm.

198. Poole, C.F., Gas Chromatography. 2012: Elsevier.

199. Sparkman, O.D., Z. Penton, and F.G. Kitson, Gas Chromatography and Mass Spectrometry: A Practical Guide. 2011: Elsevier Science.

200. McNair, H.M. and J.M. Miller, Basic Gas Chromatography. 2011: Wiley.

201. Nauman, E.B., Residence Time Theory. Industrial & Engineering Chemistry Research, 2008. **47**(10): p. 3752-3766.

202. Ismail, A.F., K.C. Khulbe, and T. Matsuura, Gas Separation Membranes: Polymeric and Inorganic. 2015, Switzerland: Springer International Publishing. 331.

203. Großberger, S., T. Fey, and G. Lee, Tortuosity of Aligned Channels in Alumina Membranes Produced by Vacuum-Induced Surface Directional Freezing. Materials (Basel, Switzerland), 2017. **10**(4): p. 409.

204. Norton, T.T. and Y.S. Lin, Ceramic–carbonate dual-phase membrane with improved chemical stability for carbon dioxide separation at high temperature. Solid State Ionics, 2014. **263**: p. 172-179.

205. Spedding, P.L., Electrical Conductance of Molten Alkali Carbonate Binary Mixtures. Journal of The Electrochemical Society, 1973. **120**(8): p. 1049-1052.

206. Sherif, S.A., et al., Handbook of Hydrogen Energy. 2014: Taylor & Francis.

207. Korotcenkov, G., Handbook of Gas Sensor Materials: Properties, Advantages and Shortcomings for Applications Volume 2: New Trends and Technologies. 2013: Springer New York.

208. Verkerk, M.J., B.J. Middelhuis, and A.J. Burggraaf, Effect of grain boundaries on the conductivity of high-purity ZrO_2 Y_2O_3 ceramics. Solid State Ionics, 1982. **6**(2): p. 159-170.

209. Ioffe, A.I., et al., Effect of the grain size on the conductivity of high-purity pore-free ceramics Y_2O_8–ZrO_2. Physica Status Solidi (a), 1975. **30**(1): p. 87-95.

210. Cerón, M.R., et al., Surpassing the conventional limitations of CO_2 separation membranes with hydroxide/ceramic dual-phase membranes. Journal of Membrane Science, 2018. **567**: p. 191-198.

211. Fontaine, M.L., et al., CO_2 removal at high temperature from multi-component gas stream using porous ceramic membranes infiltrated with molten carbonates. Energy Procedia, 2013. **37**(Supplement C): p. 941-951.

212. Rui, Z., et al., Ionic conducting ceramic and carbonate dual phase membranes for carbon dioxide separation. Journal of Membrane Science, 2012. **417-418**: p. 174-182.

213. Ahn, H., et al., YSZ-carbonate dual-phase membranes for high temperature carbon dioxide separation. Journal of Industrial and Engineering Chemistry, 2014. **20**(5): p. 3703-3708.

214. Barin, I. and F. Sauert, Thermochemical Data of Pure Substances. 1993: VCH.

215. Feng, Q., et al., Femtosecond laser micromachining of a single-crystal superalloy. Scripta Materialia, 2005. **53**(5): p. 511-516.

216. Luft, A., et al., A study of thermal and mechanical effects on materials induced by pulsed laser drilling. Applied Physics A: Materials Science and Processing, 1996. **63**(2): p. 93-101.

217. Kohara, S., et al., The structure of $LiKCO_3$ studied by ab initio calculations and raman spectroscopy. Journal of Physics and Chemistry of Solids, 1998. **59**(9): p. 1477-1485.

218. Kohlrausch, K.W.F., Ramanspektren, B.a. Erler, Editor. 1943: Leipzig. p. 469.

219. Meekes, H., et al., Raman and infrared spectra of the incommensurate crystal Na_2CO_3. Physical Review B, 1986. **34**(6): p. 4240-4254.

220. Morihiko, M., O. Susumu, and O. Isao, Raman spectroscopic study of vibrational and rotational relaxations of CO_2^{3-} ion in molten Li_2CO_3. The Journal of Chemical Physics, 1990. **92**(2): p. 1515-1516.

Appendix A

Thermodynamic data

The Gibbs free energy of formation of the oxides, hydroxides and carbonates at different temperatures taken from the book of the Thermochemical Data of Pure Substances [214] are summarised in Table A-1.

Table A- 1. Gibbs free energy of formation of the oxides, hydroxides and carbonates at different temperatures [214]**.**

	$\Delta_f G^o$, kJ·mol^{-1}						
T/K	**Li_2CO_3 (s)**	**Na_2CO_3 (s)**	**K_2CO_3 (s)**	**Li_2O (s)**	**Na_2O (s)**	**K_2O (s)**	**CO_2 (g)**
298	-1103.4	-1019.4	-1034.4	-549.5	-365.4	-308.635	-394.6
300	-1074.6	-990.4	-1004.6	-536.3	-350.9	-294.258	-394.9
400	-1045.2	-961.8	-975.0	-522.3	-336.4	-279.982	-395.1
500	-1016.2	-933.9	-945.9	-508.2	-322.2	-265.844	-395.3
600	-987.8	-906.7	-917.3	-494.2	-308.1	-251.855	-395.5
700	-959.7	-879.8	-889.1	-480.3	-294.3	-238.02	-395.7
800	-932.5	-853.3	-861.5	-466.4	-280.6	-224.334	-395.8
900	-1103.4	-1019.4	-1034.4	-549.5	-365.4	-308.635	-394.6
1000	-1074.6	-990.4	-1004.6	-536.3	-350.9	-294.258	-394.9

	$\Delta_f G^o$, kJ·mol^{-1}			
T/K	**LiOH (s)**	**NaOH (s)**	**KOH (s)**	**H_2O (g)**
298	-423.2	-363.8	-362.9	-224.0
300	-407.5	-347.7	-347.2	-219.1
400	-391.4	-332.4	-332.9	-214.1

500	-375.5	-319.4	-319.3	-208.9
600	-361.4	-306.8	-307.1	-203.6
700	-348.8	-294.5	-295.1	-198.2
800	-336.5	-282.4	-283.4	-192.7
900	-423.2	-363.8	-362.9	-224.0
1000	-407.5	-347.7	-347.2	-219.1

Table A- 2 shows the equilibrium constants of reactions taking place for the formation of oxides hydroxide ions calculated using Eq. 2-32.

Table A- 2. The equilibrium constants at different temperatures

	Equilibrium constants		
T / K	$Li_2CO_{3(m)} \rightarrow Li_2O_{(m)} + CO_{2(g)}$	$Na_2CO_{3(m)} \rightarrow Na_2O_{(m)} + CO_{2(g)}$	$K_2CO_{3(m)} \rightarrow K_2O_{(m)} + CO_{2(g)}$
400	2.8E-25	3.3E-35	3.1E-40
500	4.4E-19	2.0E-26	6.0E-30
600	5.6E-15	1.4E-20	4.1E-23
700	4.4E-12	1.8E-16	3.0E-18
800	6.1E-10	2.1E-13	1.2E-14
900	2.7E-08	4.8E-11	7.7E-12
1000	5.0E-07	3.7E-09	1.3E-09
T / K	$Li_2CO_{3(m)} + H_2O_{(g)} \rightarrow 2\ LiOH_{(m)} + CO_{2(g)}$	$Na_2CO_{3(m)} + H_2O_{(g)} \rightarrow 2\ NaOH_{(m)} + CO_{2(g)}$	$K_2CO_{3(m)} + H_2O_{(g)} \rightarrow 2\ KOH_{(m)} + CO_{2(g)}$
400	5.0E-11	1.3E-14	2.6E-17
500	1.3E-08	1.1E-11	1.4E-13

600	5.7E-07	1.3E-09	6.8E-11
700	8.4E-06	7.9E-08	7.1E-09
800	9.9E-05	1.8E-06	3.3E-07
900	9.9E-04	2.0E-05	6.5E-06
1000	6.1E-03	1.5E-04	7.1E-05

Appendix B
Laser drilling

Figure B- 1 shows the SEM images of (110)-oriented YSZ single crystal that has gone through laser processing. Figure B- 1A the 45 μm diameter drilled pore and Figure B- 1B and C show a magnified view of the drilled area and an area far from the drilled pore, respectively. The SEM results showed that the drilled area has significantly changed compared to the polished undrilled region. This indicates that a strong gradient of plastic deformation was induced by laser machining within a region limited to a few microns around the hole. This is an evidence that the material has not maintained its monocrystalline character with the same crystal structure and orientation around the drilled area. The material might have been transformed from monocrystalline to polycrystalline or became amorphous material during laser processing. However, the images indicate that there are no micro-cracks or melting after laser processing.

Feng et al. [215] and Luft et al. [216] have studied in the past the effect of laser drilling on silicon single crystal and they analysed the thermal and mechanical effects on materials induced by laser drilling using a wide range of pulse widths (50 ns to 200 fs) and power densities (10^8 W cm^{-2} to 10^{15} W cm^{-2}). The findings of these studies suggested that the affected heated zones were independent of the duration of pulses and had a maximum width of 5 μm.

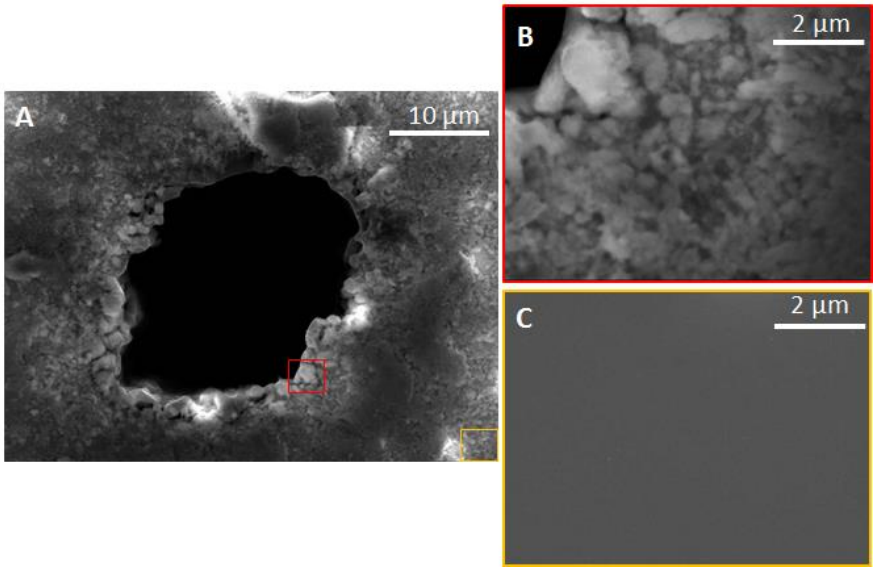

Figure B- 1. SEM images of the drilled (110)-oriented YSZ single crystal. (A) the 45 µm diameter drilled pore, **(B)** a magnified view at the surroundings of the drilled pore and **(C)** a magnified view at an area far from the drilled pore.

Appendix C

Pressure inside the internal gas phase

The Laplace pressure, used to determine the pressure difference in spherical shapes such as bubbles or droplets, depends on the surface tension (γ) and the radius of the sphere (r), and can be calculated by Eq. C- **1**:

$$\Delta P = \frac{2\gamma}{r} \qquad \text{Eq. C- 1}$$

In this work, a gas bubble is formed within the melt (one surface) of the Al_2O_3 single crystal and therefore, the pressure inside the gas bubble P_i (if the external pressure P_o acting on the melt can be assumed to be the atmospheric) will be:

$$P_i = P_o + \frac{2\gamma}{r} \qquad \text{Eq. C- 2}$$

For the ternary eutectic mixture, γ is 220 and 237 dyn cm^{-1} at 450 and 550 °C [77], respectively.

Bubbles studied in this work ranged from 50 – 100 μm diameter, and therefore, the pressure inside the bubbles will be between 1.05 and 1.09 atm.

Capillary meniscus pressure (P_{cap}) can be described for a rectangular capillary as follows:

$$P_{cap} = 2\gamma \cos\vartheta \left(\frac{1}{h_c} + \frac{1}{w_c}\right) \qquad \text{Eq. C- 3}$$

Where,

h_c is the channel height and w_c is the channel width.

The parameters γ and ϑ represent liquid surface tension and contact angle respectively. This meniscus pressure represents the pressure drop across the meniscus.

$$P_{amb} = P_{trapped} - P_{cap} \qquad \text{Eq. C- 4}$$

where P_{amb} is the external pressure applied to the system and $P_{trapped}$ is the pressure inside the trapped-gas volume.

In this work, gas is trapped behind the melt inside the YSZ single crystal and therefore, if θ is the contact angle that the meniscus makes with the surface of the pore as shown in Figure C - 1, the pressure inside the trapped gas will be approximately 1.05 atm.

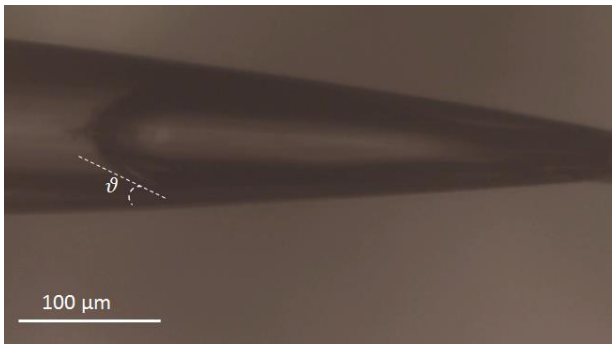

Figure C - 1. Meniscus formed inside the YSZ single crystal and the contact angle with the surface of the pore

Appendix D

Raman spectra of the carbonate mixture

The high temperature stage (Linkam TS1500) was also used for *in situ* Raman measurements. The scattering Raman spectra of the carbonates were collected *in situ* as a function of temperature (in the range of RT- 700 °C) and a controlled atmosphere (Ar or CO_2 was used).

The Raman spectra of the carbonate mixture with temperature -below the melting point of the carbonates- are shown in Figure D- 1. Powder carbonate mixture was placed inside the 100 μm diameter pore of the Al_2O_3 single crystal. Carbonates in the solid state show four basic vibrational modes which are relevant to CO_3^{2-}. The Raman modes in the high shift part of the spectrum (between 1000 and 1100 cm^{-1}) are due to internal modes. The ν_1 stretching vibration of free carbonate ions, CO_3^{2-}, has a frequency of 1063 cm^{-1}. According to previous work on Raman for carbonates the band at 1054 cm^{-1} could be tentatively assigned to the ν_1 symmetric stretching vibration $LiKCO_3$ or Li_2CO_3 [217]. The bands at 1079 and 1089 cm^{-1} may correspond to Na_2CO_3 and K_2CO_3 respectively. The 1079 cm^{-1} band shows a shift in position between RT and 100 °C. This could be due to some composition change by reaction with the atmosphere or to any structural change. The bands at 694 cm^{-1} could be the assigned to the ν_4 torsional mode of the carbonate ion, which was observed at 680 cm^{-1} [218]. The bands in the low shift spectra region may be due to lattice modes in the carbonates [219]. As the temperature increases the bands broaden and shift towards the excitation laser line position, as expected from the expansion of the chemical bonding with temperature increase.

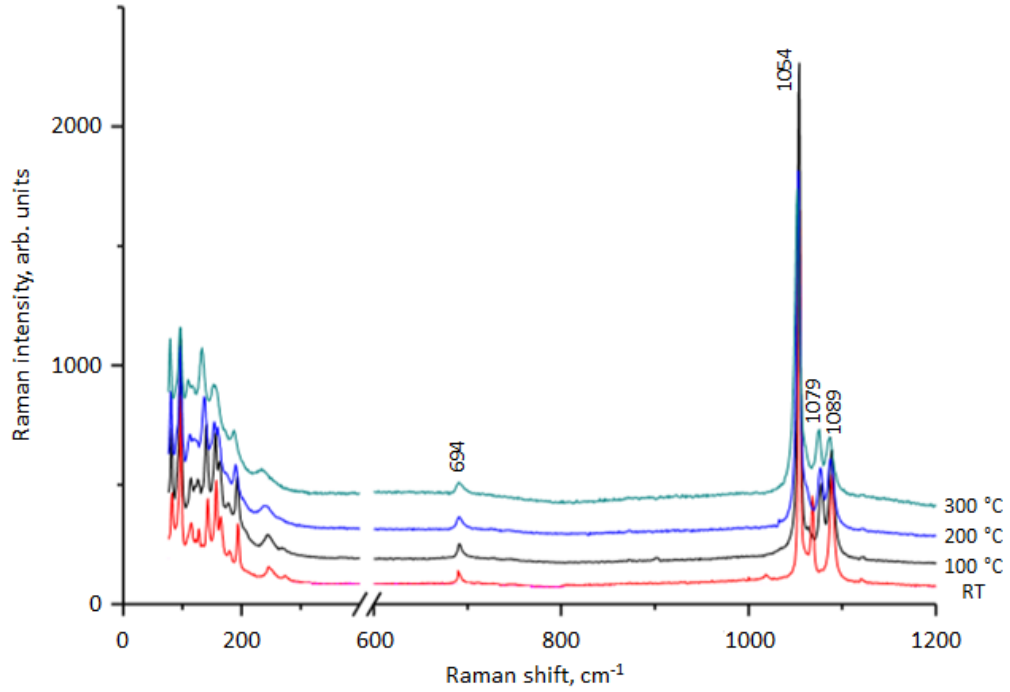

Figure D- 1. Raman spectra of the powder carbonate mixture at room temperature (RT), at 100, 200 and 300 °C in air. Carbonate mixture melts above 400 °C.

The Raman spectra of the molten carbonate mixture at different temperatures under CO_2 and Ar atmosphere were also measured. Figure D- 2 shows the Raman spectra under Ar atmosphere and it is observed that above the melting temperature of the carbonates, the three bands become one broad band at about 1062 cm^{-1} which corresponds to the C=O symmetric stretch of CO_3^{2-} as reported in literature [220]. The band at 602 cm^{-1} observed between 410 and 700 °C is assigned to the YSZ single crystal support. At 700 °C, this band moves to lower frequencies and changes shape which could be attributed to the formation of a second band. After cooling down to room temperature in the same atmosphere (Ar), the single band at 586 cm^{-1}, splits into two bands at room temperature after heating and cooling under pure Argon atmosphere as shown in Figure D- 3. This figure also compares the Raman spectra measured of the fresh carbonates but also the carbonates at room temperature after heating up to 700 °C in pure Argon or CO_2. The band at 586 cm^{-1} recorded in Argon atmosphere could correspond to the Li_2ZrO_3 as seen in Figure D- 4.Figure D- 4 compares the Raman spectrum of a commercially available Li_2ZrO_3 with the spectrum of the carbonate mixture that was heated to 700 °C and cooled down to room temperature in Ar.

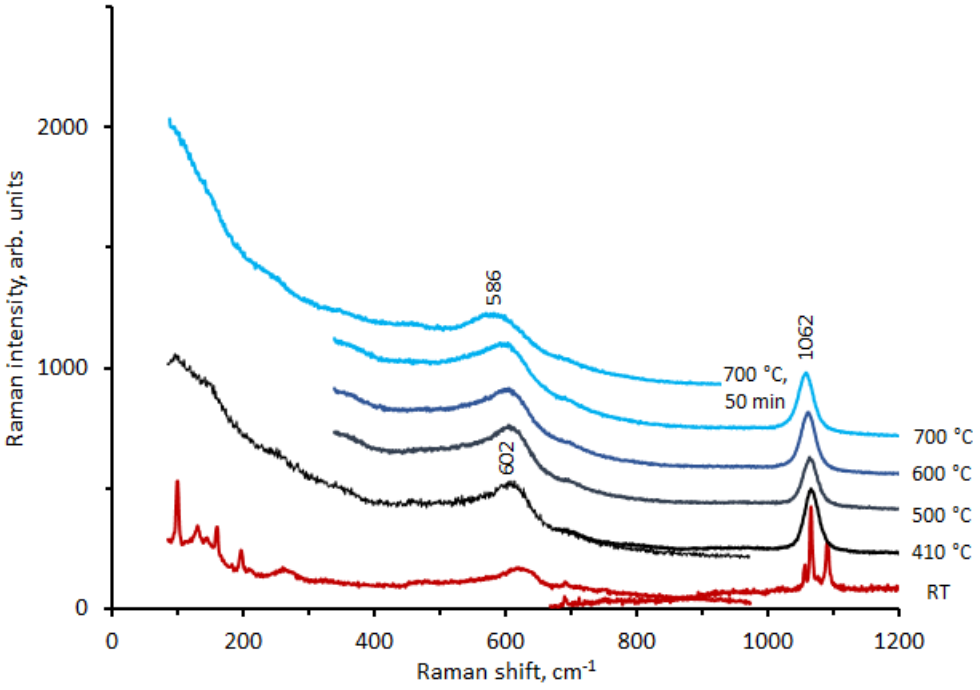

Figure D- 2. Raman spectra of the carbonate eutectic mixture at room temperature (RT), at 410, 500, 600 and 700 °C in Ar. Carbonate mixture melts above 400 °C.

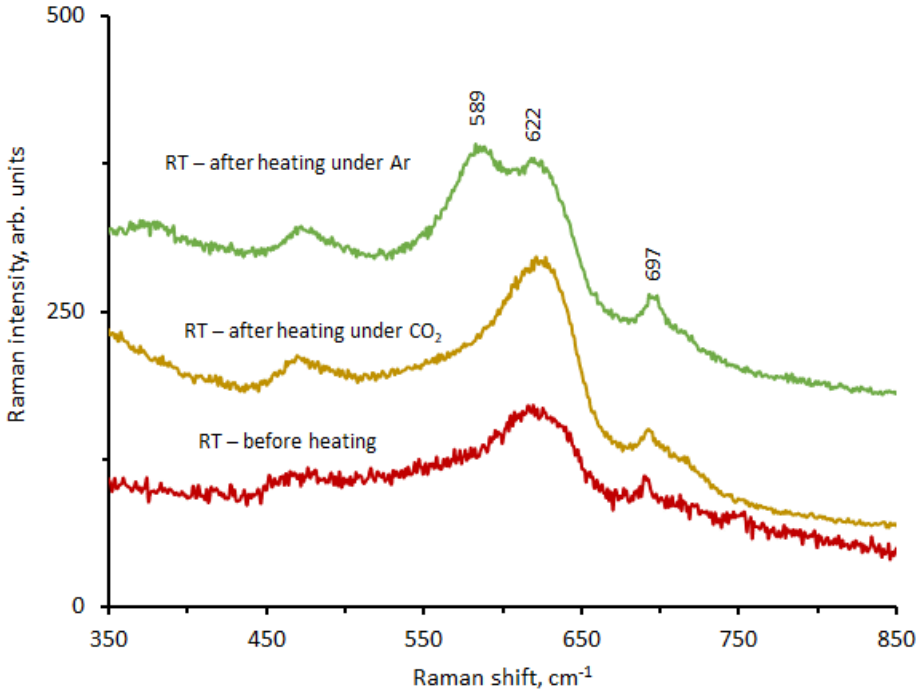

Figure D- 3. Raman spectra of the carbonate mixture at room temperature (RT) before heating and after heating up to 700 °C for more than an hour under Ar and CO_2 atmosphere.

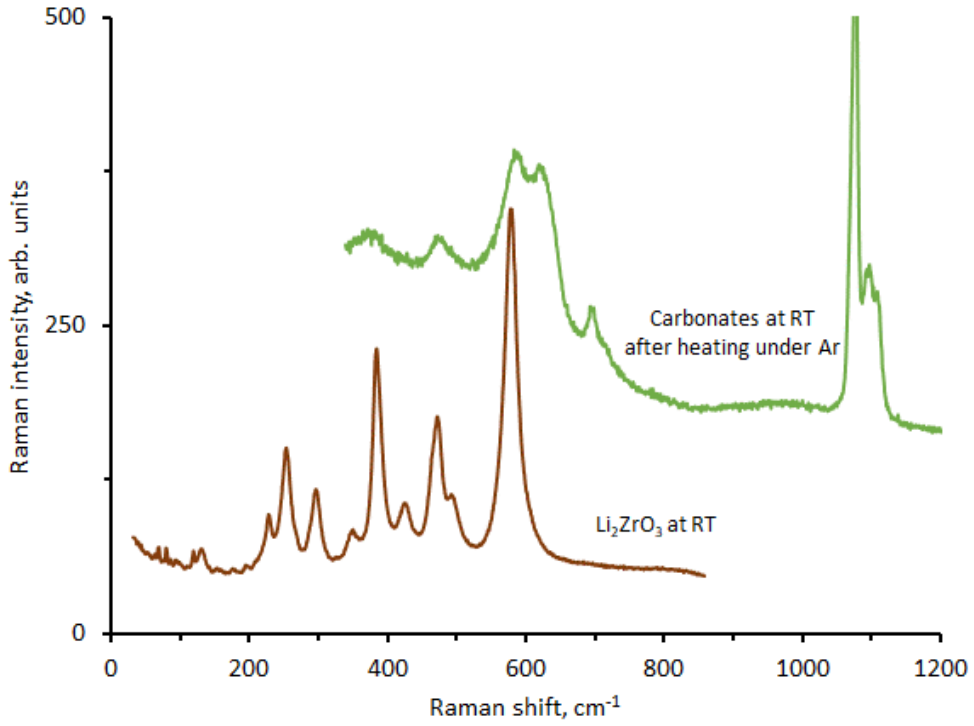

Figure D- 4. Raman spectra of Li_2ZrO_3 and the carbonate mixture at room temperature (RT) after heating up to 700 °C for more than an hour under Ar. The carbonate mixture was melted in the blind pore of the YSZ single crystal.

Figure D- 5 shows the Raman spectra collected from the molten carbonate mixture inside the pore of the YSZ single crystal at different temperatures in Ar atmosphere. As it is shown in this figure, there are no distinguished bands in the region of 1317 and 1582 cm^{-1}, where the pyrocarbonate ion must appear according to what has been reported from a previous work [81]. The band at 1063 cm^{-1} at 700 ˚C corresponds to the carbonate mixture and it can be said that it is not very intense. Therefore, the experiment must be repeated in order to make sure if the formation of pyrocarbonate ion, $C_2O_5^{2-}$, can be observed.

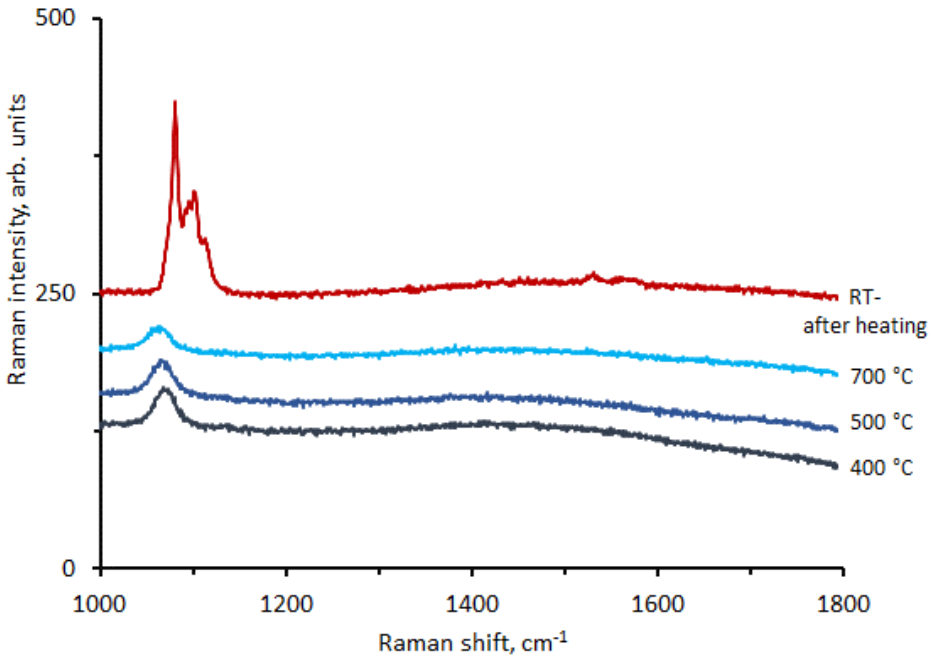

Figure D- 5. Raman spectra of the carbonate eutectic mixture at room temperature (RT), at 410, 500, 600 and 700 °C in Ar. Carbonate mixture melts above 400 °C.

This section shows that when the molten carbonates are exposed to Ar atmosphere, Li_2ZrO_3 is formed. However, this was not observed under CO_2 atmosphere. In the working membrane, pure Ar is usually fed to the permeate side of the membrane and a mixture of CO_2/N_2 is fed to the feed side. This could mean, that Li_2ZrO_3 can be formed on the permeate side of the membrane during operation.

Appendix E

Error analysis for bubble growth/shrinkage in the Al_2O_3 and YSZ single crystal

The variation of the internal gas phase volume was calculated using both computational and manual methods. The uncertainty of the internal gas phase volume is calculated below by manual fitting repeats and comparisons between the computational and manual volumes.

As discussed in Chapter 5.5, bubbles were formed in the 100 μm pore of the Al_2O_3 single crystal. Moreover, the shape and size of the bubbles will have a direct impact on the bubble volume and consequently to the permeation rate. By taking into account the blurry boundaries of the bubbles (approximately an area of 1 μm width around the periphery of the bubble), the fractional uncertainty of the bubble volume ($\frac{\delta V}{V}$ or % error in volume) can be calculated using Eq. E-1:

$$\frac{\delta V}{V} = 3\frac{\delta x}{x/2} \qquad \text{Eq. E-1}$$

Where,

x, is the diameter of the bubble (shown on the 2-D image)

δx, is half of the measured resolution of the blurry boundaries (0.5 μm)

The fractional uncertainty on the permeation rate ($\frac{\delta PR}{PR}$) will then be calculated from the volume differences as shown in Eq. E-2:

$$\frac{\delta PR}{PR} = \sqrt{\frac{\delta V_1^2 + \delta V_2^2}{|V_1 - V_2|}} \qquad \text{Eq. E-2}$$

Where,

V_1 and V_2, are the bubble volumes at times t_1 and t_2 respectively and δV_1 and δV_2 are the errors calculated for each volume using Eq. E-1.

The permeation rate uncertainties are significant according to the calculations shown in Table E-1 and therefore, experiments carried out with the Al_2O_3 single crystal were not used for further calculations and are presented here as a proof of concept.

Table E- 1 is a summary of the errors in volume and permeation rate calculated using Eq. E-1 and Eq. E-2 during the first 180 s of growth/shrinkage of a bubble in the Al_2O_3 single crystal. The manual repeats gave bubble volume uncertainties above 5% for the bubble growth and above 2% for the bubble shrinkage during the first 180 s. The uncertainties decrease with the increase of the initial bubble volume as observed with the bubble growth and shrinkage (permeation starts from a bubble volume of approximately 300 x 10^3 μm^3 for the shrinkage and 15 x 10^3 μm^3 for the growth). The permeation rate uncertainties are significant according to the calculations shown in Table E-1 and therefore, experiments carried out with the Al_2O_3 single crystal were not used for further calculations and are presented here as a proof of concept.

Table E- 1. Uncertainty in the determination of bubble volume and permeation rate during the first 180 s of growth/shrinkage of a bubble in the Al_2O_3 single crystal.

Bubble growth								
Time, s	**Bubble diameter, µm**	**Volume, 10^3 µm^3**	**V/V_o**	**Error in volume, ± 10^3 µm^3**	**% error in volume**	**Permeation rate, 10^{-15} mol s^{-1}**	**Error in permeation rate, ± 10^{-15} mol s^{-2}**	**% error in permeation rate**
0	31.0	15.6	1.0	0.87	5.6	-	-	-
60	34.5	21.5	1.4	1.08	5.0	1.46	0.34	24
120	36.5	25.5	1.6	1.21	4.7	0.98	0.40	41
180	38.2	29.2	1.9	1.32	4.5	0.92	0.44	48
Bubble shrinkage								
Time, s	**Bubble diameter, µm**	**Volume, 10^3 µm^3**	**V/V_o**	**Error in volume, ± 10^3 µm^3**	**% error in volume**	**Permeation rate, 10^{-15} mol s^{-1}**	**Error in permeation rate, 10^{-15} mol s^{-2}**	**% error in permeation rate**
0	83	299.4	1.0	6.25	2.1	-	-	-
60	81.3	281.4	0.9	5.99	2.1	4.45	2.14	48
120	79.5	263.1	0.9	5.73	2.2	4.51	2.05	45
180	77.8	246.6	0.8	5.49	2.2	4.07	1.96	48

As discussed in Chapter 5.6, a carbonate meniscus was formed in the 100 µm pore of the YSZ single crystal and gas was trapped at the closed end of the pore. By taking into account the blurry boundary between the meniscus and the gas phase (approximately an area of 1 µm width on the periphery of the meniscus), the fractional uncertainty of the bubble volume ($\frac{\delta V}{V}$ or % error in volume), which is essentially the error of the volume of the ellipsoid described in Figure 5-12, can be calculated using Eq. E-3:

$$\frac{\delta V}{V} = V_{ellipsoid}\frac{\delta x}{x/2} \qquad \text{Eq. E-3}$$

Where,

x, is the diameter of the bubble (shown on the 2-D image)

δx, is half of the measured resolution of the blurry boundaries (0.5 μm)

The fractional uncertainty on the permeation rate ($\frac{\delta PR}{PR}$) will then be calculated using the same equation as shown before (Eq. E-2).

Table E- 2 is a summary of the errors in volume and permeation rate calculated using Eq. E-3 and Eq. E-2 during the first 180 s of meniscus displacement in the YSZ single crystal. The internal gas phase volume uncertainty is expected to be well below 1% for the time studied as seen in Table E- 2 and from comparisons between the manual and computational volumes (Figure 5-14). The fractional uncertainty on the permeation rate ($\frac{\delta PR}{PR}$) will then be calculated using Eq. E-2. According to the manual fittings, uncertainties in the permeation rate are below 1% for the first 60 s of the meniscus displacement. Permeation rate uncertainties increase over time as there are smaller gas phase volume changes occurring during the same time intervals.

Table E- 2. Uncertainty in the determination of internal gas phase volume and permeation rate during the first 180 s of meniscus displacement in the YSZ single crystal.

Meniscus displacement									
Time, s	x dimension, μm	Volume of ellipsoid, 10^3 μm^3	Volume, 10^3 μm^3	V/V_o	Error in volume, ± 10^3 μm^3	% error in volume	Permeation rate, 10^{-15} mol s^{-1}	Error in permeation rate, 10^{-15} mol s^{-2}	% error in permeation rate
0	95	139.1	635.7	1.00	1.46	0.2	-		
60	88	96.5	352.9	0.56	1.10	0.3	69.76	0.45	1
120	79.5	95.1	343.5	0.54	1.20	0.3	2.32	0.40	17
180	77.8	95.1	337.6	0.53	1.22	0.4	1.46	0.42	29

From the computational analysis, it was found that the effect of the internal gas phase volume uncertainty to the permeation rate is negligible, as the relative range in permeation rates (upper to lower error band) does not change significantly for even higher uncertainties (Figure E- 1). The error bands in permeation rate, were calculated assuming that the error is consistent across the frames (e.g. no variations in contrast between frames), for volume differences equal to

$V_{t_2}(1 + x) - V_{t_1}(1 + x)$, where x= 0.01 or 0.20 for the upper error band and -0.01 or -0.20 for the lower error band respectively.

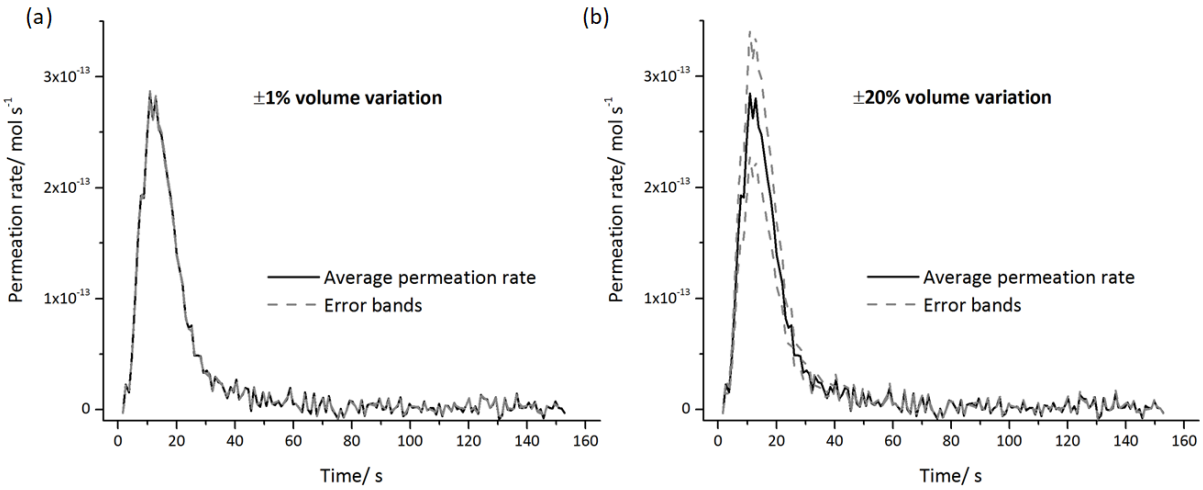

Figure E- 1. Permeation rates versus time for (a) ±1% and (b) ±20% variation of the normalised bubble volume (V/V_o) calculated computationally for the first 150 s of bubble shrinkage at 550 °C. The error bands were calculated for volume differences equal to $\boldsymbol{V_{t_2}(1 + x) - V_{t_1}(1 + x)}$, where (a) $\boldsymbol{x}$ = 0.01 for the upper band and -0.01 for the lower error band and (b) $\boldsymbol{x}$ = 0.20 for the upper band and -0.20 for the lower error band.

The variation of the driving force during visualisation experiments was also calculated considering the uncertainty of the gas phase volume and the residence time distribution inside the chamber. The internal gas phase composition was calculated directly using the internal has phase volume data and Eq. 5-3. The uncertainty of the partial pressure can be estimated by using the limits of both the internal and external gas phase composition, to calculate the minimum and maximum possible driving force.

By assuming ±1% volume variation of the internal gas phase and ±0.005 min decay constant variation according to the residence time distribution graphs for the external gas phase, Figure 5-15 can be shown as Figure E-2. For the first 30 s considered in this work, driving forces uncertainties are insignificant.

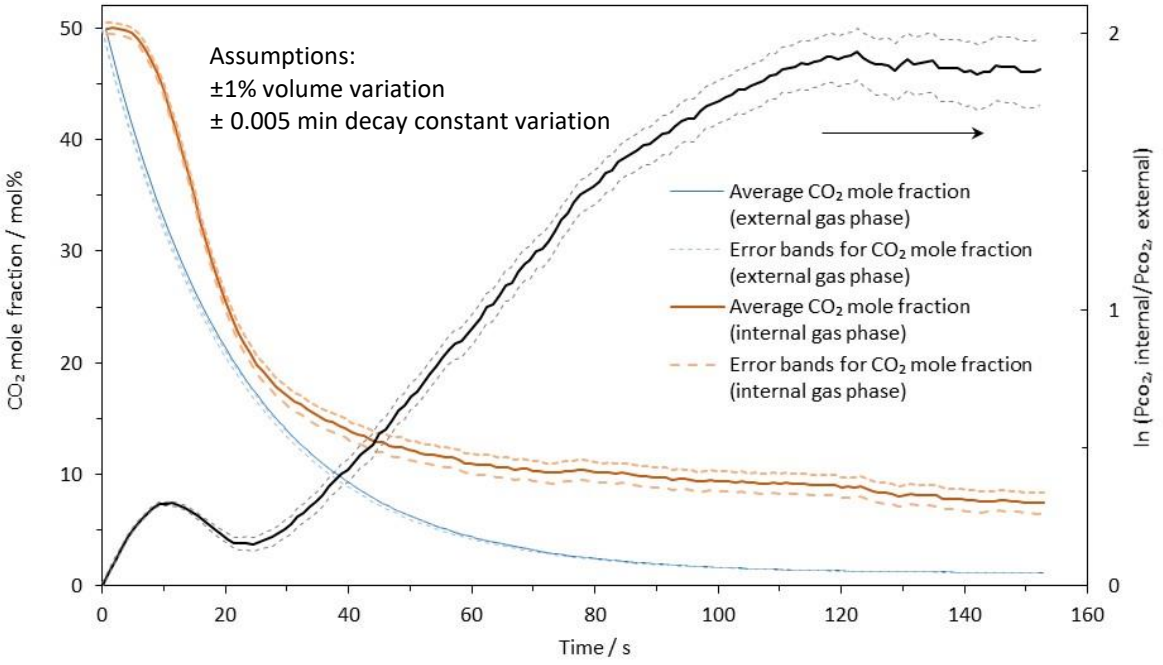

Figure E- 2. Driving force and CO_2 mole fraction changes for the first 150 s of the meniscus displacement at 550 °C. The error bands were calculated using ±1% volume variations for the internal gas phase and ±0.005 min decay constant variation for the external gas phase.

However, when assuming a 3 s time lag between the internal and external gas phase, that could be due to the response time of the analytical equipment or due to relaxation phenomenon following the step change in gas composition, driving force uncertainties become more significant. The uncertainty in the driving force is shown as error bars in Figure 5-16 (orange and blue symbols only).

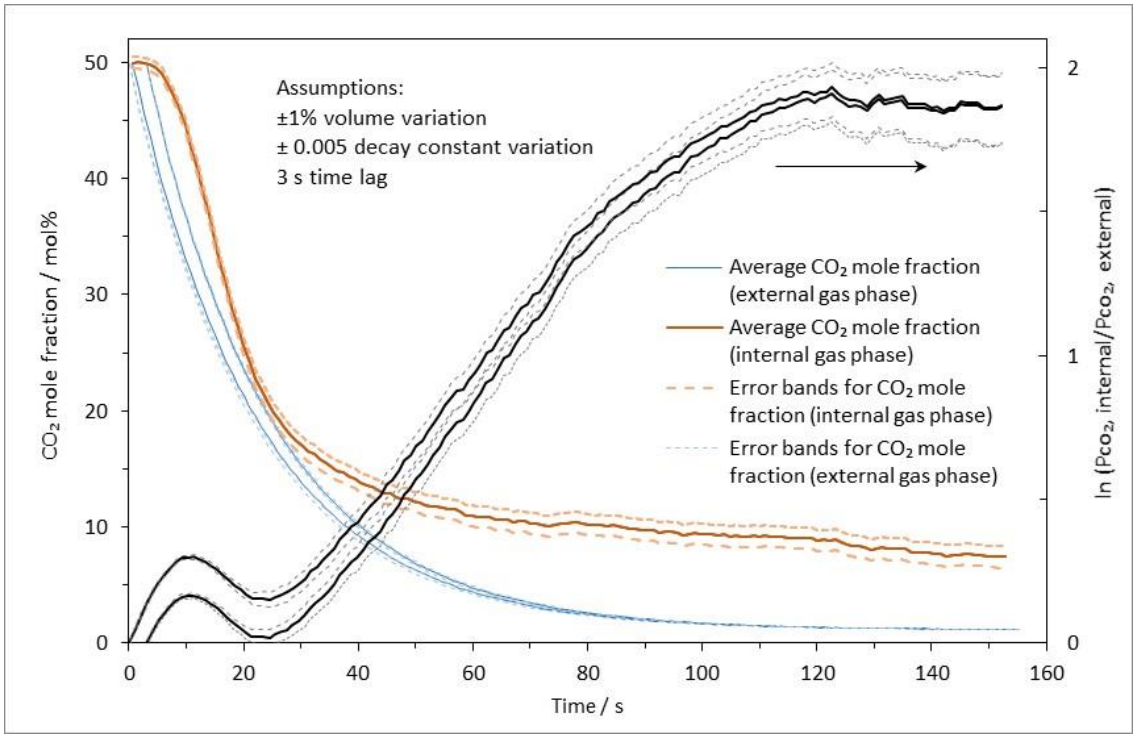
Assumptions:
±1% volume variation
± 0.005 decay constant variation
3 s time lag
Average CO_2 mole fraction (external gas phase)
Average CO_2 mole fraction (internal gas phase)
Error bands for CO_2 mole fraction (internal gas phase)
Error bands for CO_2 mole fraction (external gas phase)
CO_2 mole fraction / mol%
ln (Pco_2, internal/Pco_2, external)
Time / s
0
10
20
30
40
50
0
1
2
0
20
40
60
80
100
120
140
160

Appendix F

Operating conditions for 50 days

Table F- 1 shows the conditions under which the Al_2O_3 closed-end tube membrane was operated with varying temperature, gas phase compositions and water context in chronological order. The membrane was used for approximately 50 days of operation. It is important to emphasize that it is very uncommon for membranes to survive multiple days of operation without cracking and with no detectable leaks during operation. The Al_2O_3 closed-end tube membrane is a very robust membrane.

Table F- 1. Operating conditions for the Al_2O_3 closed-end tube membrane in chronological order. Approximately 50 days of operation.

T ^oC	Duration, h	Feed-chamber gas inlet	Permeate-chamber gas inlet	Feed chamber %CO_2 outlet	Permeate chamber %CO_2 outlet
Heating up with 1 °C min^{-1}					
550	14.0	50% CO_2 /N_2	Ar	50	0.0026
550	3.8	90% CO_2 /N_2	Ar	90	0.0034
550	3.6	50% CO_2 /N_2	Ar	50	0.0026
550	3.5	77% CO_2 /N_2	Ar	77	0.0032
550	3.0	90% CO_2 /N_2	Ar	90	0.0035
550	3.0	25% CO_2 /N_2	Ar	25	0.0020
550	3.2	50% CO_2 /N_2	3.5%H_2O/Ar	50	0.0181
550	4.4	50% CO_2 /N_2	Ar	50	0.0026
550	4.0	50% CO_2 /N_2	3.5%H_2O/Ar	50	0.0183
550	6.1	50% CO_2 /N_2	Ar	50	0.0024
550	8.1	Ar	50% CO_2 /N_2	0.0022	50
550	5.2	Ar	3.5%H_2O/50% CO_2 /N_2	0.0130	50
Heating up with 1 °C min^{-1}					
600	10.6	50% CO_2 /N_2	Ar	50	0.0035
600	4.7	77% CO_2 /N_2	Ar	77	0.0037
600	3.5	90% CO_2 /N_2	Ar	90	0.0041
600	1.6	25% CO_2 /N_2	Ar	25	0.0030
600	8.3	50% CO_2 /N_2	Ar	50	0.0034
600	4.2	50% CO_2 /N_2	3.5%H_2O/Ar	50	0.0275
600	3.0	50% CO_2 /N_2	Ar	50	0.0035
600	4.3	Ar	50% CO_2 /N_2	0.0028	50
600	0.9	Ar	3.5%H_2O/50% CO_2 /N_2	0.242	50
Heating up with 1 °C min^{-1}					

650	12.6	50% CO_2 /N_2	Ar	50	0.0043
650	1.5	77% CO_2 /N_2	Ar	77	0.0047
650	0.5	90% CO_2 /N_2	Ar	90	0.0053
650	1.1	25% CO_2 /N_2	Ar	25	0.0037
650	0.3	50% CO_2 /N_2	Ar	50	0.0043
650	8.6	50% CO_2 /N_2	3.5%H_2O/Ar	50	0.0475
650	0.6	50% CO_2 /N_2	Ar	50	0.0041
650	9.6	Ar	50% CO_2 /N_2	0.0038	50
650	1.2	Ar	3.5%H_2O/50% CO_2 /N_2	0.00435	50
650	0.5	50% CO_2 /N_2	Ar	50	0.0043
Heating up with 1 °C min^{-1}					
700	8.5	50% CO_2 /N_2	Ar	50	0.0067
700	1.2	77% CO_2 /N_2	Ar	77	0.0072
700	1.3	90% CO_2 /N_2	Ar	90	0.0076
700	1.0	25% CO_2 /N_2	Ar	25	0.0059
700	0.2	50% CO_2 /N_2	Ar	50	0.0066
700	3.2	50% CO_2 /N_2	3.5%H_2O/Ar	50	0.0745
700	1.0	50% CO_2 /N_2	Ar	50	0.0065
700	4.8	50% CO_2 /N_2	3.5%H_2O/Ar	50	0.0735
700	2.9	50% CO_2 /N_2	Ar	50	0.0061
700	7.0	Ar	50% CO_2 /N_2	0.0051	50
700	4.3	Ar	3.5%H_2O/50% CO_2 /N_2	0.0690	50
700	8.1	50% CO_2 /N_2	Ar	50	0.0073
700	2.2	77% CO_2 /N_2	Ar	77	0.0079
700	0.7	50% CO_2 /N_2	Ar	50	0.0071
700	1.2	90% CO_2 /N_2	Ar	90	0.0084
700	0.8	50% CO_2 /N_2	Ar	50	0.0069
Cooling down with 1 °C min^{-1}					

Heating up with 1 °C min^{-1}					
550	11.2	50% CO_2 /N_2	Ar	50	0.0023
550	6.5	50% CO_2 /N_2	1000 ppmCO_2/Ar	50	0.1016
550	1.7	90% CO_2 /N_2	1000 ppmCO_2/Ar	90	0.1021
550	0.7	77% CO_2 /N_2	1000 ppmCO_2/Ar	77	0.1019
550	1.2	25% CO_2 /N_2	1000 ppmCO_2/Ar	25	0.1014
550	12.4	50% CO_2 /N_2	380 ppmCO_2/Ar	50	0.0403
550	1.7	77% CO_2 /N_2	380 ppmCO_2/Ar	77	0.0409
550	1.7	90% CO_2 /N_2	380 ppmCO_2/Ar	90	0.0413
550	2.7	25% CO_2 /N_2	380 ppmCO_2/Ar	25	0.0400
550	3.3	50% CO_2 /N_2	Ar	50	0.0023
550	2.6	50% CO_2 /N_2	3.5%H_2O/Ar	50	0.0175
550	7.8	1000 ppmCO_2/Ar	1000 ppmCO_2/Ar	0.1	0.1000
550	1.6	50% CO_2 /N_2	1000 ppmCO_2/Ar	50	0.1016
550	6.5	50% CO_2 /N_2	3.5%H_2O/ 1000 ppmCO_2/Ar	50	0.1100
550	2.2	1000 ppmCO_2/Ar	1000 ppmCO_2/Ar	0.1	0.1000
550	1.1	50% CO_2 /N_2	1000 ppmCO_2/Ar	50	0.1016

550	11.7	50% CO_2 /N_2	Ar	50	0.0022
550	8.9	380 ppmCO_2/Ar	380 ppmCO_2/Ar	0.0380	0.0380
550	1.8	50% CO_2 /N_2	380 ppmCO_2/Ar	50	0.0403
550	0.6	380 ppmCO_2/Ar	380 ppmCO_2/Ar	0.0380	0.0380
550	7.1	50% CO_2 /N_2	3.5%H_2O/ 380 ppmCO_2/Ar	50	0.1120
550	0.9	50% CO_2 /N_2	Ar	50	0.0022
Cooling down with 1 °C min^{-1}					
Heating up with 1 °C min^{-1}					
550	14.4	50% CO_2 /N_2	Ar	50	0.0025
550	2.6	77% CO_2 /N_2	Ar	77	0.0032
550	3.2	90% CO_2 /N_2	Ar	90	0.0034
550	1.4	50% CO_2 /N_2	Ar	50	0.0024
550	2.2	3.5%H_2O/50% CO_2 /N_2	Ar	50	0.0023
550	4.2	25% CO_2 /N_2	Ar	25	0.0015
550	3.4	50% CO_2 /N_2	Ar	50	0.0024
550	10.1	50% CO_2 /N_2	3.5%H_2O/Ar	50	0.0185
550	3.3	50% CO_2 /N_2	Ar	50	0.0025
550	11.3	50% CO_2 /N_2	1.1% CO_2 /N_2	50	1.1013
550	7.2	1.1% CO_2 /N_2	1.1% CO_2 /N_2	1.1	1.1000
550	3.9	90% CO_2 /N_2	1.1% CO_2 /N_2	90	1.1025
550	4.2	77% CO_2 /N_2	1.1% CO_2 /N_2	77	1.1020
550	5.9	25% CO_2 /N_2	1.1% CO_2 /N_2	25	1.1009
550	4.2	50% CO_2 /N_2	1.1% CO_2 /N_2	50	1.1013
550	3.9	50% CO_2 /N_2	380 ppmCO_2/Ar	50	0.0400
550	3.9	380 ppmCO_2/Ar	380 ppmCO_2/Ar	0.0380	0.0380
550	3.4	50% CO_2 /N_2	380 ppmCO_2/Ar	50	0.0401
550	3.9	90% CO_2 /N_2	380 ppmCO_2/Ar	90	0.0414
550	4.3	77% CO_2 /N_2	380 ppmCO_2/Ar	77	0.0410
550	5.7	50% CO_2 /N_2	380 ppmCO_2/Ar	50	0.0401
550	3.3	25% CO_2 /N_2	380 ppmCO_2/Ar	25	0.0395
550	5.1	50% CO_2 /N_2	Ar	50	0.0028
550	8.5	50% CO_2 /N_2	380 ppmCO_2/Ar	50	0.0400
550	11.3	50% CO_2 /N_2	1.1% CO_2 /N_2	50	1.1012
550	4.4	1.1% CO_2 /N_2	1.1% CO_2 /N_2	1.1	1.1000
550	15.5	50% CO_2 /N_2	Ar	50	0.0028
Heating up with 1 °C min^{-1}					
600	10.9	50% CO_2 /N_2	Ar	50	0.0034
600	5.0	3.5%H_2O/50% CO_2 /N_2	Ar	50	0.0034
600	4.4	50% CO_2 /N_2	Ar	50	0.0034
600	4.4	50% CO_2 /N_2	3.5%H_2O/Ar	50	0.0269
Heating up with 1 °C min^{-1}					
650	10.2	50% CO_2 /N_2	Ar	50	0.0041
650	5.4	3.5%H_2O/50% CO_2 /N_2	Ar	50	0.0040
650	4.8	50% CO_2 /N_2	Ar	50	0.0041

650	4.8	50% CO_2 /N_2	3.5%H_2O/Ar	50	0.0471
		Heating up with 1 °C min^{-1}			
700	10.1	50% CO_2 /N_2	Ar	50	0.0067
700	5.4	3.5%H_2O/50% CO_2 /N_2	Ar	50	0.0065
700	4.1	50% CO_2 /N_2	Ar	50	0.0067
700	5.3	50% CO_2 /N_2	3.5%H_2O/Ar	50	0.0739
		Cooling down with 1 °C min^{-1}			
		Heating up with 1 °C min^{-1}			
450	13.5	50% CO_2 /N_2	Ar	50	0.0015
450	1.5	3.5%H_2O/50% CO_2 /N_2	Ar	50	0.0015
450	0.5	50% CO_2 /N_2	Ar	50	0.0016
450	6.1	50% CO_2 /N_2	3.5%H_2O/Ar	50	0.0030
450	1.0	50% CO_2 /N_2	Ar	50	0.0015
		Heating up with 1 °C min^{-1}			
500	10.9	50% CO_2 /N_2	Ar	50	0.0017
500	2.3	3.5%H_2O/50% CO_2 /N_2	Ar	50	0.0017
500	8.5	50% CO_2 /N_2	Ar	50	0.0018
500	2.4	50% CO_2 /N_2	3.5%H_2O/Ar	50	0.0070
500	0.9	50% CO_2 /N_2	Ar	50	0.0016
		Heating up with 1 °C min^{-1}			
550	12.8	50% CO_2 /N_2	Ar	50	0.0026
550	12.0	380 ppmCO_2/Ar	380 ppmCO_2/Ar	0.0380	0.0380
550	9.8	380 ppmCO_2/Ar	3.5%H_2O 439 ppmCO_2/Ar	0.0325	0.0481
550	5.3	380 ppmCO_2/Ar	380 ppmCO_2/Ar	0.0380	0.0380
550	5.9	380 ppmCO_2/Ar	3.5%H_2O 439 ppmCO_2/Ar	0.0324	0.0480
550	4.4	380 ppmCO_2/Ar	380 ppmCO_2/Ar	0.0380	0.0380
550	0.6	50% CO_2 /N_2	Ar	50	0.0026
		Heating up with 1 °C min^{-1}			
700	15.8	50% CO_2 /N_2	Ar	50	0.0071
700	3.0	50% CO_2 /N_2	3.5%H_2O/Ar	50	0.0730
700	4.2	50% CO_2 /N_2	Ar	50	0.0067
700	8.0	1.1% CO_2 /N_2	1.1% CO_2 /N_2	1.1	1.1000
700	5.2	50% CO_2 /N_2	1.1% CO_2 /N_2	50	1.1025
700	1.0	90% CO_2 /N_2	1.1% CO_2 /N_2	90	1.1031
700	1.2	77% CO_2 /N_2	1.1% CO_2 /N_2	77	1.1033
700	0.9	25% CO_2 /N_2	1.1% CO_2 /N_2	25	1.1021
700	1.1	50% CO_2 /N_2	1.1% CO_2 /N_2	50	1.1025
700	9.2	439 ppmCO_2/Ar	439 ppmCO_2/Ar	0.0439	0.0439
700	5.7	439 ppmCO_2/Ar	Ar	0.0435	0.0004
700	2.1	1.1% CO_2 /N_2	Ar	1.1	0.0009
700	1.9	50% CO_2 /N_2	Ar	50	0.0071
700	3.3	50% CO_2 /N_2	439 ppmCO_2/Ar	50	0.0487

700	1.1	90% CO_2 /N_2	439 ppmCO_2/Ar	90	0.0496
700	1.5	50% CO_2 /N_2	439 ppmCO_2/Ar	50	0.0488
700	0.9	90% CO_2 /N_2	439 ppmCO_2/Ar	90	0.0495
700	1.3	77% CO_2 /N_2	439 ppmCO_2/Ar	77	0.0493
700	0.8	25% CO_2 /N_2	439 ppmCO_2/Ar	25	0.0483
700	0.9	50% CO_2 /N_2	439 ppmCO_2/Ar	50	0.0498
700	8.3	439 ppmCO_2/Ar	439 ppmCO_2/Ar	0.0439	0.0439
700	8.5	50% CO_2 /N_2	Ar	50	0.0071
700	3.0	50% CO_2 /N_2	439 ppmCO_2/Ar	50	0.0487
700	2.6	50% CO_2 /N_2	1.1% CO_2 /N_2	50	1.1025
700	6.1	1.1% CO_2 /N_2	1.1% CO_2 /N_2	1.1	1.1000
700	3.3	50% CO_2 /N_2	1.1% CO_2 /N_2	50	1.1025
Cooling down with 1 °C min^{-1}					
Heating up with 1 °C min^{-1}					
550	6.7	50% CO_2 /N_2	Ar	50	0.0031
550	1.1	90% CO_2 /N_2	Ar	90	0.0042
550	0.9	77% CO_2 /N_2	Ar	77	0.0036
550	1.3	25% CO_2 /N_2	Ar	25	0.0027
550	1.1	50% CO_2 /N_2	Ar	50	0.0031
550	1.2	50% CO_2 /N_2	439 ppmCO_2/Ar	50	0.0457
550	4.2	439 ppmCO_2/Ar	439 ppmCO_2/Ar	0.0439	0.0439
550	1.8	90% CO_2 /N_2	439 ppmCO_2/Ar	90	0.0462
550	1.1	77% CO_2 /N_2	439 ppmCO_2/Ar	77	0.0460
550	1.3	25% CO_2 /N_2	439 ppmCO_2/Ar	25	0.0449
550	0.8	50% CO_2 /N_2	1.1% CO_2 /N_2	50	1.1011
550	6.5	1.1% CO_2 /N_2	1.1% CO_2 /N_2	1.1	1.1000
550	2.1	50% CO_2 /N_2	1.1% CO_2 /N_2	50	1.1011
550	6.7	1.1% CO_2 /N_2	1.1% CO_2 /N_2	1.1	1.1000
550	2.3	50% CO_2 /N_2	1.1% CO_2 /N_2	50	1.1011
550	5.2	1.1% CO_2 /N_2	1.1% CO_2 /N_2	1.1	1.1000
550	2.7	90% CO_2 /N_2	1.1% CO_2 /N_2	90	1.1023
550	6.3	1.1% CO_2 /N_2	1.1% CO_2 /N_2	1.1	1.1000
550	2.9	77% CO_2 /N_2	1.1% CO_2 /N_2	77	1.1018
550	5.8	1.1% CO_2 /N_2	1.1% CO_2 /N_2	1.1	1.1000
550	2.9	25% CO_2 /N_2	1.1% CO_2 /N_2	25	1.1008
550	1.1	50% CO_2 /N_2	Ar	50	0.0031
550	1.1	90% CO_2 /N_2	Ar	90	0.0042
550	0.9	77% CO_2 /N_2	Ar	77	0.0036
550	0.7	25% CO_2 /N_2	Ar	25	0.0027
550	1.1	50% CO_2 /N_2	1.1% CO_2 /N_2	50	1.1010
550	5.0	1.1% CO_2 /N_2	1.1% CO_2 /N_2	1.1	1.1000
550	0.9	90% CO_2 /N_2	1.1% CO_2 /N_2	90	1.1023
550	6.7	1.1% CO_2 /N_2	1.1% CO_2 /N_2	1.1	1.1000
550	1.1	77% CO_2 /N_2	1.1% CO_2 /N_2	77	1.1017
550	1.3	25% CO_2 /N_2	1.1% CO_2 /N_2	25	1.1007
550	1.1	50% CO_2 /N_2	439 ppmCO_2/Ar	50	0.0457
550	1.4	90% CO_2 /N_2	439 ppmCO_2/Ar	90	0.0462
550	1.4	77% CO_2 /N_2	439 ppmCO_2/Ar	77	0.0460

550	0.9	25% CO_2 /N_2	439 ppmCO_2/Ar	25	0.0449
550	4.9	439 ppmCO_2/Ar	439 ppmCO_2/Ar	0.0439	0.0439
Heating up with 1 °C min^{-1}					
700	9.4	50% CO_2 /N_2	439 ppmCO_2/Ar	50	0.0492
700	1.1	90% CO_2 /N_2	439 ppmCO_2/Ar	90	0.0450
700	0.9	77% CO_2 /N_2	439 ppmCO_2/Ar	77	0.0498
700	0.8	25% CO_2 /N_2	439 ppmCO_2/Ar	25	0.0488
700	9.3	50% CO_2 /N_2	Ar	50	0.0075
700	1.3	90% CO_2 /N_2	Ar	90	0.0087
700	0.9	77% CO_2 /N_2	Ar	77	0.0083
700	1.3	25% CO_2 /N_2	Ar	25	0.0068
700	2.2	1.1% CO_2 /N_2	1.1% CO_2 /N_2	1.1	1.1
700	3.8	50% CO_2 /N_2	1.1% CO_2 /N_2	50	1.1030
700	1.1	90% CO_2 /N_2	1.1% CO_2 /N_2	90	1.1036
700	1.3	77% CO_2 /N_2	1.1% CO_2 /N_2	77	1.1038
700	0.9	25% CO_2 /N_2	1.1% CO_2 /N_2	25	1.1026
700	2.1	1.1% CO_2 /N_2	1.1% CO_2 /N_2	1.1	1.1
Cooling down with 1 °C min^{-1}					
Heating up with 1 °C min^{-1}					
550	12.8	50% CO_2 /N_2	Ar	50	0.0024
550	5.8	air	air	0.0409	0.0409
550	3.2	air	3.5%H_2O/air	0.0171	0.0639
550	3.3	air	air	0.0409	0.0409
550	3.1	air	3.5%H_2O/air	0.0175	0.0637
550	3.5	air	air	0.0409	0.0409
550	3.3	air	3.5%H_2O/air	0.0171	0.0631
550	3.7	air	air	0.0409	0.0409
Heating up with 1 °C min^{-1}					
600	9.1	air	air	0.0409	0.0409
600	4.0	air	3.5%H_2O/air	0.0170	0.0588
600	5.2	air	air	0.0409	0.0409
600	3.5	air	3.5%H_2O/air	0.0171	0.0579
600	3.2	air	air	0.0409	0.0409
Heating up with 1 °C min^{-1}					
650	5.8	air	air	0.0409	0.0409
650	3.5	air	3.5%H_2O/air	0.0155	0.0580
650	3.7	air	air	0.0409	0.0409
650	3.9	air	3.5%H_2O/air	0.0159	0.0577
650	4.2	air	air	0.0409	0.0409
Cooling down with 1 °C min^{-1}					
Heating up with 1 °C min^{-1}					
550	7.8	50% CO_2 /N_2	Ar	50	0.0026
550	9.1	air	air	0.0409	0.0409
550	3.1	air	3.5%H_2O/air	0.0175	0.0637
550	2.8	air	air	0.0409	0.0409
550	3.2	air	3.5%H_2O/air	0.0170	0.0650

550	3.2	air	air (flow↓)	0.0409	0.0409
550	3.1	air	3.5%H_2O/air (flow↓)	0.0190	0.1380
550	2.8	air	air	0.0409	0.0409
550	3.1	air	3.5%H_2O/air	0.0160	0.0640
550	3.3	air	air	0.0409	0.0409
550	3.3	0.6%H_2O/air	3.5%H_2O/air	0.0330	0.0485
550	3.0	air	air	0.0409	0.0409
550	5.8	50% CO_2 /N_2	Ar	50	0.0024
550	7.5	Ar	Ar	-	-
550	6.7	50% CO_2 /N_2	Ar	50	0.0023
		Heating up with 1 °C min^{-1}			
600	6.1	air	air	0.0409	0.0409
600	3.9	air	3.5%H_2O/air	0.0175	0.0583
600	5.5	air	air	0.0409	0.0409
600	4.0	air	3.5%H_2O/air	0.0172	0.0580
600	2.2	air	air	0.0409	0.0409
		Heating up with 1 °C min^{-1}			
650	7.8	air	air	0.0409	0.0409
650	7.2	air	3.5%H_2O/air	0.0165	0.0575
650	2.2	air	air	0.0409	0.0409
650	3.9	air	3.5%H_2O/air	0.0161	0.0577
650	2.5	air	air	0.0409	0.0409
		Heating up with 1 °C min^{-1}			
700	7.5	air	air	0.0409	0.0409
700	3.7	air	3.5%H_2O/air	0.0150	0.0562
700	2.1	air	air	0.0409	0.0409
700	3.6	air	3.5%H_2O/air	0.0148	0.0566
700	5.8	air	air	0.0409	0.0409
		Cooling down with 1 °C min^{-1}			
		Heating up with 1 °C min^{-1}			
700	12.6	50% CO_2 /N_2	Ar	50	0.0079
700	5.9	air	air	0.0409	0.0409
700	1.6	3.5%H_2O/air	air	0.0780	0.0136
700	2.2	3.5%H_2O/air	3.5%H_2O/air	0.0409	0.0409
700	2.0	air	3.5%H_2O/air	0.0154	0.0670
700	8.1	air	air	0.0409	0.0409
700	3.3	air	3.5%H_2O/air	0.0153	0.0661
700	3.1	3.5%H_2O/air	3.5%H_2O/air	0.0409	0.0409
700	2.7	3.5%H_2O/air	air	0.0552	0.0248
700	4.3	air	air	0.0409	0.0409
		Cooling down with 1 °C min^{-1}			
		Heating up with 1 °C min^{-1}			
700	12.4	50% CO_2 /N_2	Ar	50	0.0076
700	5.9	air	air	0.0409	0.0409
700	4.2	3.5%H_2O/air	3.5%H_2O/air	0.0409	0.0409

700	4.1	air	air	0.0409	0.0409
700	4.4	3.5%H_2O/air	3.5%H_2O/air	0.0409	0.0409
700	4.1	air	air	0.0409	0.0409
700	4.4	3.5%H_2O/air	3.5%H_2O/air	0.0409	0.0409
700	3.9	air	air	0.0409	0.0409
Cooling down with 1 °C min^{-1}					

Appendix G

Long term experiment

The permeation of the membrane was tested continuously over a period of 250 h (Figure G-1). During this period, the temperature, gas phase compositions and water content was varied. The membrane was operated at 550, 600, 650 and 700 °C, the feed-side inlet was varied from 25 to 90%CO_2 /N_2 and for the permeate-side inlet we used Ar, 380 ppm CO_2 /Ar, 1%CO_2 /Ar and 3.5%H_2O/Ar. This experiment was used to prove that CO_2 permeation detected though an Al_2O_3 - carbonate membrane is not a result of CO_2 decomposition of the carbonates in the membrane. It could be argued that the total amount of permeated CO_2 through those membranes is due to the molar hold up of the carbonates. Therefore, the total amount of CO_2 permeated during a long operation is compared to the molar hold up of the carbonates. Over this period, the average permeation rate measured is approximately 1×10^{-9} mol s^{-1}. The molar amount of CO_2 permeated during this time will be 8.3×10^{-4} mol. By comparing this to the molar hold up of the carbonates (0.045 g or 4.5×10^{-4} mol since the average molecular weight of carbonates is 100 g mol^{-1}), it can be proved that the carbonate decomposition cannot account for the CO_2 permeation.

A

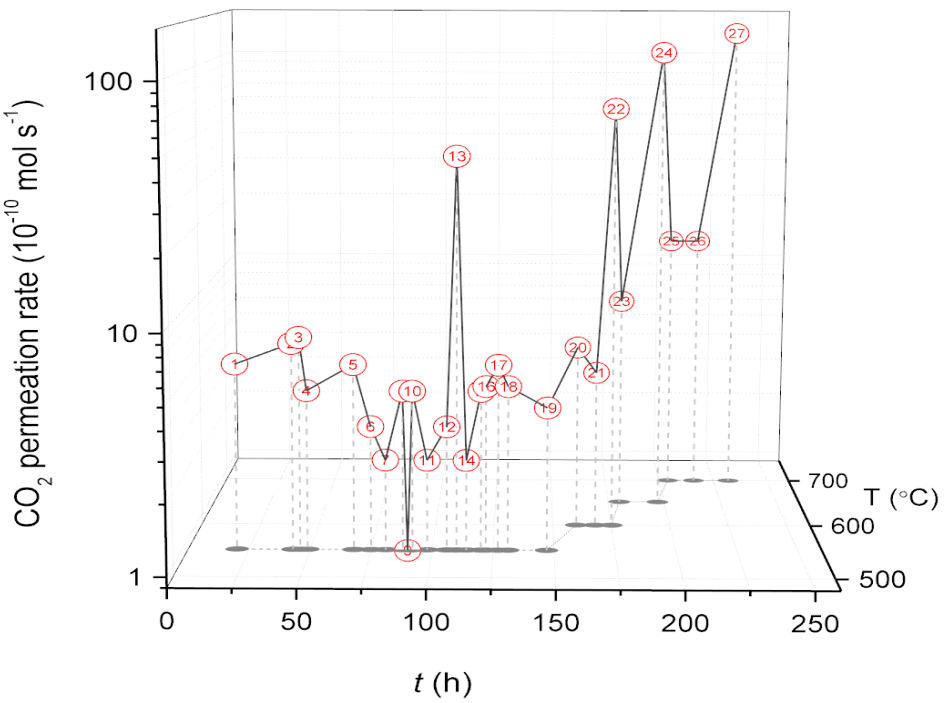

B

Data points	Feed-side gas inlet	Permeate-side gas inlet
1, 5, 17, 20,23, 25, 26	50%CO_2/N_2	Ar
2	77%CO_2/N_2	Ar
3	90%CO_2 /N_2	Ar
4, 21	25%CO_2 /N_2	Ar
6, 12	50%CO_2/N_2	1%CO_2/Ar
7, 11,14	25%CO_2/N_2	1%CO_2/Ar
8	77%CO_2/N_2	1%CO_2/Ar
10	90%CO_2/N_2	1%CO_2/Ar
9	1.1%CO_2/N_2	1%CO_2/Ar
13, 22,24,27	50%CO_2 /N_2	3.5%H_2O/Ar
15	50%CO_2/N_2	439 ppmCO_2/Ar
16, 18	77%CO_2/N_2	439 ppmCO_2/Ar
17	90%CO_2/N_2	439 ppmCO_2/Ar
19	25%CO_2/N_2	439 ppmCO_2/Ar

Figure G- 1. CO_2 permeation rate calculated from the CO_2 mole fraction in the external-chamber gas outlet at 550, 600, 650 and 700 °C over a period of 250h. (A) Permeation rate against time at 550, 600, 650 and 700 °C under **(B)** different gas stream inlets.

Appendix H

The chemical response of the membrane upon subsequent introduction and removal of water in the gas phase

It was observed that upon subsequent introduction and removal of water in the gas phase, CO_2 was produced and consumed respectively. This suggests that the composition of the melt is also changing during these transients. CO_2 evolution upon water introduction may be due to the formation of OH^- in the melt through the reaction $H_2O+CO_3^{2-} \rightleftharpoons CO_2+2OH^-$. Figure H- 1 shows the chemical response of the membrane upon subsequent introduction and removal of water in the gas phase under non-permeating conditions. 3.5% H_2O was introduced in both sides of the membrane and the moles of CO_2 evolved from the melt were obtained through peak integration. If the CO_2 evolution upon water introduction is due to the formation of OH^- in the melt, the mole fraction of OH^- under equilibrium can be estimated. The mole fraction of OH^- was calculated to be 9% in 0.045 g of carbonates. Under symmetrical conditions, water was then removed from both sides and CO_2 was consumed from the melt.

The mole faction of OH^- within the melt can also be calculated thermodynamically using Eq. H-1 (discussed in 2.3.4), by assuming equilibrium at the two interfaces of the membrane. The reaction constant, K_2, was calculated in 2.3.4, and it was found to be equal to 4.5×10^{-5} at 500 °C.

$$K_2 = \frac{[OH^-]^2}{[CO_3^{2-}]}\frac{P_{CO_2}}{P_{H_2O}} \qquad \text{Eq. H-1}$$

By using Eq. H-1 and setting $[CO_3^{2-}]$ equal to 1 (the molen carbonates mainly consist of CO_3^{2-}), the mole faction of OH^- can be calculated on the two interfaces of the membrane; on the hydration side at equilibrium (where $\frac{P_{CO_2}}{P_{H_2O}}$ is approximately 0.01 during uphill experiments) , the mole faction of OH^- will be 6%, and on the carbonation side (where $\frac{P_{CO_2}}{P_{H_2O}}$ is approximately 1 during uphill experiments), the mole faction of OH^- will be around 0.6%.

From the below equations:

$$J_{CO_2} = -\frac{RT}{2F^2L}\frac{\sigma_{CO_3^{2-}}\sigma_{OH^-}}{\sigma_{OH^-}+\sigma_{CO_3^{2-}}} ln\left(\frac{P'_{CO_2}P''_{H_2O}}{P''_{CO_2}P'_{H_2O}}\right) \qquad \text{Eq. H-2}$$

$$\sigma_i = \frac{cF^2 z_i^2 D_i}{RT} \qquad \text{Eq. H-2}$$

$$J_{CO_2} = J_{H_2O} \qquad \text{Eq. H-2}$$

The conductivity of the carbonate ions can be found in Figure 2-5 and knowing that the density and the average molecular weight of the carbonates is 2.3 g cm^{-3} and 100 g mol^{-1} respectively, from Eq. H-2 the H_2O conductivity and flux at 550 °C can be calculated using the mole fraction of hydroxide ions on the hydration side at equilibrium (equal to 6%):

$$\sigma_{OH^-} = \frac{0.06 \cdot 2.3 g\ cm^{-3}}{100\ g\ mol^{-1}} \frac{\left(9.6485 \cdot \frac{10^4\ \text{Coulomb}}{\text{mol}}\right)^2 (-1)^2 \cdot 5.1 \cdot \frac{10^{-10} m^2}{s}}{8.31446 \frac{\text{J}}{(\text{K mol})} (550 + 273)\text{K}} =$$

$$= 0.00345 \frac{mol}{cm^3} 1.36 \cdot 10^6\ s \frac{S}{mol}\ 5.1 \cdot 10^{-10} \frac{m^2}{s} \cdot 10^4 cm^2 m^{-2} = 9.6 \cdot 10^{-3} S/cm$$

$$J_{H_2O} = J_{CO_2} = -\frac{RT}{2F^2 L} \frac{\sigma_{CO_3^{2-}} - \sigma_{OH^-}}{\sigma_{OH^-} + \sigma_{CO_3^{2-}}} ln\left(\frac{P'_{CO_2} P''_{H_2O}}{P''_{CO_2} P'_{H_2O}}\right) =$$

$$= -\frac{8.31446 \frac{\text{J}}{(\text{K mol})} (550 + 273)\text{K}}{2 \left(9.6485 \cdot \frac{10^4\ \text{Coulomb}}{\text{mol}}\right)^2 0.05\ cm} \frac{0.978 \frac{S}{cm} \cdot 9.6 \cdot 10^{-3} \cdot \frac{S}{cm}}{9.6 \cdot 10^{-3} \frac{S}{cm} + 0.978 \frac{S}{cm}} ln\left(\frac{0.02 \cdot 3.5}{0.02 \cdot 0.06}\right)$$

$$\cdot 22400\ \text{mol ml}^{-1} \cdot 60\ \text{s}\ min^{-1} = 3.8 \cdot 10^{-1}\ \text{ml}\ min^{-1} cm^{-2}$$

If the flux of water is approximately 3.8 x 10^{-1} ml min^{-1} cm^{-2} at 550 °C, the permeation rate (for a surface area of carbonates equal to 34 mm^2) will be 3.5 x 10^{-4} mol s^{-1} at 550 °C. If the permeation rate is then compared to the respective experimental value, which is 5 x 10^{-9} mol s^{-1} at 550 °C it can be said that the reactions on the surfaces are slow compared to the bulk ionic diffusion (reaction kinetic limitations) and therefore the mole fraction of OH^- under equilibrium is expected to be a lot lower. Moreover, the diffusion coefficient of OH^-, calculated using the self-diffusion coefficient of CO_3^{2-} differing only in their particle masses, could be a lot higher as the volume, charge and charge distribution of the species may also play a role that was not considered here.

The mole fraction of OH^- under equilibrium was also intended to be identified and measured experimentally using *in situ* Raman spectroscopy. However, OH^- species could not be identified inside the melt when it was exposed to 0.6% H_2O in air under atmospheric pressure

at 500 °C. The analysis of the Raman spectra will not be shown here as these measurements were part of a different project.

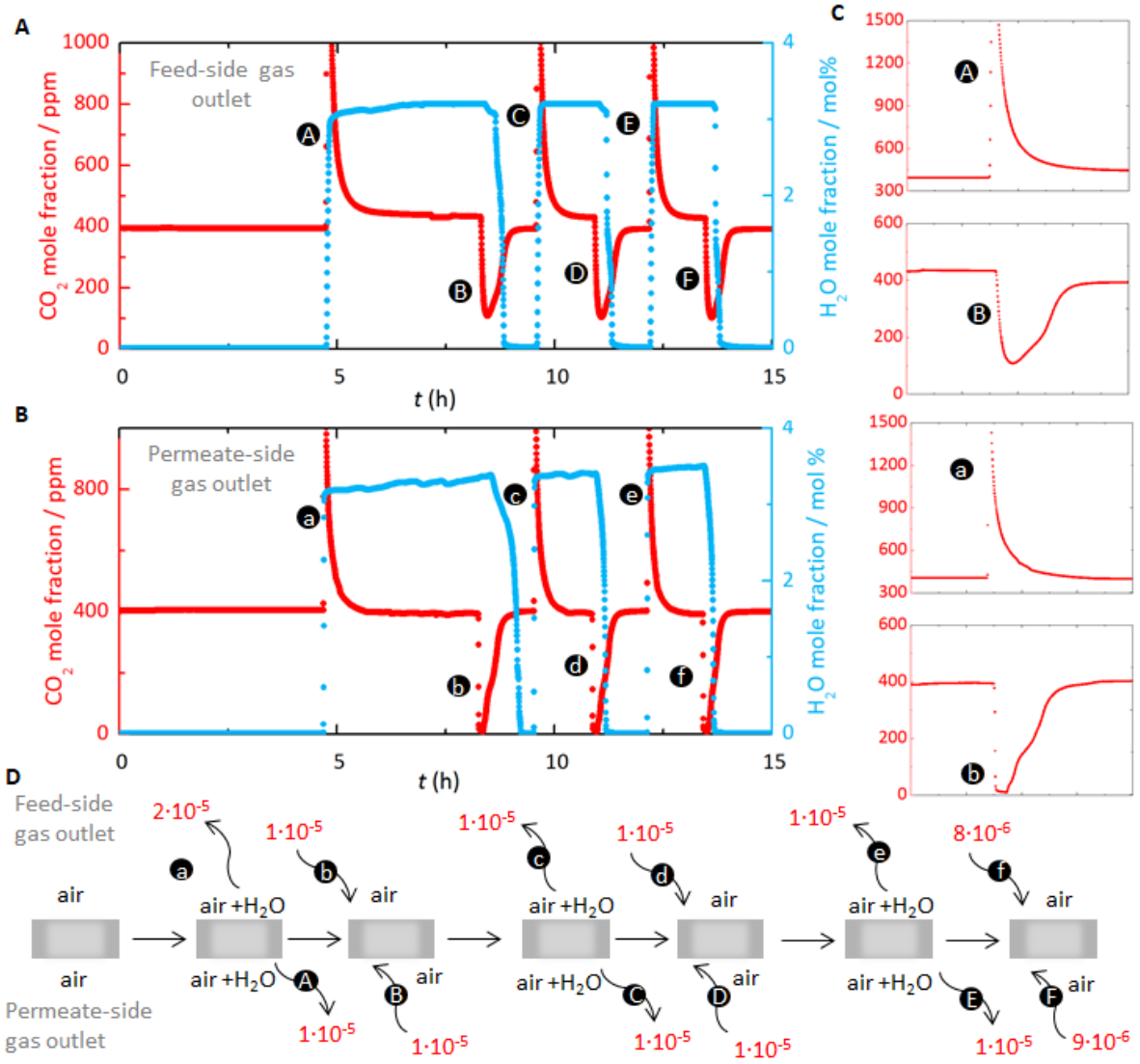

Figure H- 1. The chemical response of the membrane upon subsequent introduction and removal of water in the gas phase under non-permeating conditions. The mole fraction of CO_2 and H_2O **(A)** in the feed-chamber gas outlet and **(B)** in the permeate-chamber gas outlet at 700 °C. **(C)** Magnified view of the some of the peaks of CO_2 evolution and consumption during the introduction and the removal of water respectively. **(D)** Schematic of the membrane showing the moles of CO_2 evolved or consumed on both sides of the membrane upon subsequent introduction and removal of water.